Development of Efficient & Reproducible Perovskite Absorbers for All-Perovskite Triple Junction Tandem Solar Cells

James N. Drysdale

St. Hugh's College

Department of Physics

University of Oxford

A thesis submitted for the degree of

Doctor of Philosophy

Michaelmas 2024

“Everybody talks about the weather, but nobody does anything about it” – Mark Twain

Abstract

The development of efficient and reproducible perovskite absorbers for all-perovskite triple junction tandem solar cells is advanced by this thesis.

Chapter 1 traces the energy advancements that have powered human development throughout history. The burning of fossil fuels since the Industrial Revolution has helped power extraordinary increases in economic development, life expectancy, and global population growth. However, rapid increases in greenhouse gas atmospheric concentrations from burning fossil fuels is raising global average surface temperatures and causing climate change dangerous to humanity today. Sunlight offers the greatest potential to meet our need for increased energy and decreased greenhouse gas emissions. Stable all-perovskite triple junction tandem solar cells offer the promise of higher efficiencies and lower costs than crystalline silicon, the dominant solar cell technology for 70 years, to help solve this challenge.

Chapter 2 explains important physics principles for solar cells, including energy band theory and semiconductor properties. Theoretical and operational fundamentals of solar cells, semiconductor junctions, the operation and characterization of solar cells, and limits to their efficiency are explained. Advantages of perovskites are discussed, including the potential for all-perovskite tandem solar cells to be fabricated at costs 50% lower than crystalline silicon. For perovskites to deliver on the promise of more efficient and lower cost commercial solar cells, however, stability, efficiency, and scalability must improve.

Chapter 3 details the experimental methods used to fabricate and characterize perovskite thin films and solar cells in this thesis.

In Chapter 4, improvements to efficiency, reproducibility, and stability are investigated for a representative middle band gap 1.55 eV $FA_{0.8}Cs_{0.2}PbI_3$ perovskite absorber relevant for all-perovskite triple junction tandem solar cells. A tandem-relevant C_{60}/ALD SnO_2/IZO/Au device stability stack increased solar cell reproducibility. $EDAI_2$ surface passivation and excess PbI_2 perovskite precursor stoichiometry improved the stability of 1.55 eV $FA_{0.8}Cs_{0.2}PbI_3$ single junction perovskite solar cells using the tandem-relevant device stack under 85°C light aging.

In Chapter 5, a novel DMF/DMAX crystallization method was developed to create efficient and reproducible solution-processed ~2 eV (1.97 eV) wide band gap perovskite absorbers and single junction solar cells. The novel 68 mol%:32 mol% stoichiometric mixture of dimethylammonium bromide (DMABr) and dimethylammonium iodide (DMAI) additive salts – DMAX – to a 1.97 eV $FA_{0.9}Cs_{0.1}Pb(Br_{0.68}I_{0.32})_3$ perovskite precursor solution in neat DMF solvent was created to replace DMSO solvent. Perovskite thin films crystallized using DMF/DMAX exhibit larger median apparent grain sizes, more homogeneous morphology, and longer carrier lifetimes. 1.97 eV perovskite single junction solar cells fabricated using DMF/DMAX improved solar cell efficiency, reproducibility, and operational stability compared to DMF/DMSO – achieving near-record 1.42 V open-circuit voltage and 13.7% maximum power point tracked efficiency.

In Chapter 6, non-radiative recombination processes – rather than halide segregation – are shown to dominate V_{OC} losses in the 1.97 eV wide band gap perovskite single junction solar cells. The 20 mV V_{OC} loss from radiative recombination due to halide segregation ($V_{OC,\,rad}$) measured is five times less than the published estimate of ~100 mV loss. These results indicate that, compared to previously published estimates, halide

segregation had a less substantial effect on V_{OC} loss mechanisms in the 1.97 eV perovskite solar cells fabricated using the DMF/DMAX crystallization method.

In Chapter 7, all-perovskite triple junction tandem solar cells with 1.97 eV, 1.61 eV, and 1.25 eV band gap absorbers are optimized with a 0.9 M 1.97 eV perovskite precursor and unique device stack featuring an ICBA electron transport layer for the wide band gap subcell and IZO recombination layers and achieved higher efficiencies with improved steady-state V_{OC} and J_{SC}. The champion all-perovskite triple junction tandem solar cell achieved 27.3% maximum power point tracked efficiency at 1 cm^2 area, the highest efficiency for any known all-perovskite triple junction tandem solar cell published to date and identical to the highest known reported efficiency of 27.3% for a single junction crystalline silicon solar cell. One of the all-perovskite triple junction tandem solar cells was stability tested and retained 99.3% of its initial efficiency after 120 minutes of continuous maximum power point tracking under 1-sun intensity AM 1.5G illumination.

Chapter 8 summarizes improvements to efficiency, reproducibility, and stability that are investigated and achieved in this thesis for three principal areas: 1) representative middle band gap perovskite absorber relevant for all-perovskite triple junction tandem solar cells; 2) all-perovskite triple junction tandem solar cells using a novel crystallization method for the 1.97 eV wide band gap absorber layer involving dimethylammonium bromide and dimethylammonium iodide (DMAX); and 3) all-perovskite triple junction tandem solar cells using a unique device stack incorporating an ICBA electron transport layer and IZO recombination layers with the 1.97 eV wide band gap absorber layer. Future improvements are suggested to achieve all-perovskite triple junction tandem solar cell efficiencies exceeding 30%.

Acknowledgements

From the vanishing glaciers of Montana I have known my whole life to the ancient spires of Oxford that have been home for the last four years, I have tried to not just talk about the weather, but to do something about it. This would not be possible for me without the support of so many incredible people.

I am forever grateful to Professor Henry Snaith for the life-changing opportunity you have given me to come to Oxford and join your world-leading perovskite solar energy research lab. Your passion, knowledge, and leadership make you a joy to have as a supervisor! Thank you for cultivating the wonderfully collaborative, productive, and enthusiastic environment in which we work. I also thank Clare Moloney for keeping our lab and community running smoothly.

I am most grateful to the University of Notre Dame, Fr. Jenkins, Monk Malloy, Sorin Brotters, and Professor Prashant Kamat for the golden years together under The Dome and in your perovskite research lab. My dreams came true at ND and, with your guidance and support, led me to live my dreams at Oxford and beyond. Stay GOLDEN!

Forever grateful to Abbot Thomas Frerking, Abbot Gregory Mohrman, Joe Gleich, and the monks, teachers, coaches, and ChatDBD that nurtured my growth in mind, body, and spirit at Saint Louis Priory – led by Oxford-educated Benedictine monks since 1956. *Laus Tibi Domine!*

I am profoundly thankful to have Dr. Nakita Noel on my side. Thank you for your unbelievable efforts, guidance, and friendship. You have a lifetime supply of huckleberry chocolate bars! I am also grateful to Dr. Bernard Wenger for the opportunity to work as a part-time research and development chemist at Helio Display Materials during the second

year of my DPhil. Thank you for the opportunity to work in a fast-paced, hard-deadline, results-oriented commercial lab – I continue to cheer on all your successes at Helio – and for running a blistering Teddy Hall Relays leg for the Snaith Striders! I thank Professor Ian Shipsey for his passionate leadership of the Department of Physics.

I also express my gratitude to so many members of the Snaith Lab, past and present. Ashley Marshall, thank you for helping to get me up and running upon my arrival at Oxford during the uncertainty of the COVID pandemic. David McMeekin, thank you for being an awesome mentor, friend, and, most importantly, my sieve! Junke Wang and Shuaifeng Hu, thank you for your collaboration and support for the all-perovskite triple junction tandem solar cells project. Joel Smith and Suer Zhou, thank you for being great Oxford teammates on the Office of Naval Research Global project. Jin Yao, thank you for keeping the cluster facility running and with it our ability to fabricate high efficiency tandem solar cells! To our small army of postdoctoral researchers – Grey Christoforo (Go Irish!), Seongrok Seo, Zhongcheng Yuan, Alex Ramadan, Amit Kumar, Melissa McCarthy, Yen Hung-Lin, Sam Teale, James Ball, Krishanu Dey, Manuel Kober-Czerny, and others – for your willingness to provide insight and guidance at every turn. Tino Lukas, Josie Surel, and Philippe Holzhey, thank you for your collaboration and kindness. Ben Putland, Emil Dyrvik, and Harry Sansom, thank you for making Team 2 eV awesome! Augustin Zaininger, a huge thank you for not only fixing everything that breaks in our lab (a job that never ends!) but also enhancing our lab with new equipment and capabilities. Also, you are the best chef in Oxford and a gracious host for everything fun!

I thank my awesome DPhil batchmates in the Snaith Lab – Nicky Evans, Florine Rombach, Akash Dasgupta, Xinyi Shen, and Heon Jin – for your collaboration and fun

times along the way! Starting at Oxford together in the difficult COVID pandemic era brought us closer and has made you all true friends.

I am thankful for the opportunities I have had to continue to run competitively with the Oxford University Cross Country Club. Defeating Cambridge in the Mob Matches and running Varsity Blues at the English National Cross Country Championships have been highlights of my running career! Special thanks to ND forever friends Ryker, Trevor, and Patty for crossing the pond. I must also thank Mike Farrar. You are more than just my lab desk mate, running partner, and one of my best friends – you are truly like a big brother to me!

I am most grateful to my loving parents, Heidi and Douglas, for instilling the values that have made me the person I am: effort, attitude, passion, and purpose. You have always loved me too much to ask too little. I hope that this thesis – a product of a time unlike any before in which we have been an ocean away – honors all that you have given.

I dedicate this thesis to my parents & family, most of all my golden grandparents shining love from above, Melvin & Ruthie Drysdale and Myron & Rosie Noble.

Love Always & Everywhere Forever Together in Our Hearts!

I will continue to do something about the weather and help advance perovskites after these formative years in the Snaith Lab at Oxford. In January, I will join the U.S. National Renewable Energy Laboratory in Golden, Colorado as a postdoctoral researcher under the leadership of Dr. Joe Berry, Dr. Laura Schelhas, Dr. Axel Palmstrom, and Dr. Kai Zhu. I am honored to help develop all-perovskite multijunction tandem solar cells from lab scale to industrial scale and into the wider world.

Cheers & Charge ON!

Table of Contents

Abstract i

Acknowledgements iv

Table of Contents vii

1 Introduction 1

1.1 Energy and Human Development 1

1.2 Climate Change 2

1.3 Solar: A Renewable Energy Solution 3

Chapter 1 References 7

2 Theory and Background 10

2.1 Semiconductor Physics 10

2.1.1 Energy Band Theory 10

2.1.2 Properties of Semiconductors 16

2.2 Solar Cell Fundamentals 18

2.2.1 Absorption, Separation, and Extraction 18

2.2.1.a Absorption 18

2.2.1.b Separation 20

2.2.1.c Extraction 23

2.2.2 Semiconductor Junctions 24

2.2.3 Solar Cell Operation and Characterization 29

2.2.4 Limits to Solar Cell Efficiency 34

2.3 Perovskite Solar Cells 37

2.3.1 Perovskite Structure and Development 38

2.3.2 Advantages of Perovskites....39
2.3.3 Challenges for Perovskites: Stability, Efficiency, Scalability....45
2.3.3.a Stability....45
2.3.3.b Efficiency....47
2.3.3.c Scalability....47
Chapter 2 References....49
3 Experimental Methods....53
3.1 Perovskite Thin Film and Solar Cell Fabrication....53
3.1.1 Substrate Preparation....53
3.1.2 Perovskite Precursor Solution Preparation....54
3.1.2.a Materials....54
3.1.2.b $FA_{0.8}Cs_{0.2}PbI_3$ – 1.55 eV Middle Band Gap Absorber....54
3.1.2.c $FA_{0.9}Cs_{0.1}Pb(Br_{0.68}I_{0.32})_3$ – 1.97 eV Wide Band Gap Absorber....55
3.1.2.d $FA_{0.9}Cs_{0.1}Pb(Br_{0.15}I_{0.85})_3$ – 1.61 eV Middle Band Gap Absorber....55
3.1.2.e $FA_{0.6}MA_{0.3}Cs_{0.1}Pb_{0.5}Sn_{0.5}I_3$ – 1.25 eV Narrow Band Gap Absorber....55
3.1.3 Charge Transport and Surface Passivation Layer Solution Preparation....56
3.1.3.a Charge Transport Layers....56
3.1.3.b Surface Passivation Layers....57
3.1.4 Perovskite Layer Depositions For Both Thin Films and Solar Cells....58

3.1.4.a $FA_{0.8}Cs_{0.2}PbI_3$ – 1.55 eV Middle Band Gap Absorber 58

3.1.4.b $FA_{0.9}Cs_{0.1}Pb(Br_{0.68}I_{0.32})_3$ – 1.97 eV Middle Band Gap Absorber.....58

3.1.4.c $FA_{0.9}Cs_{0.1}Pb(Br_{0.15}I_{0.85})_3$ – 1.61 eV Middle Band Gap Absorber.....59

3.1.4.d $FA_{0.6}MA_{0.3}Cs_{0.1}Pb_{0.5}Sn_{0.5}I_3$ – 1.25 eV Narrow Band Gap Absorber.....59

3.1.5 Hole Transport Layer Deposition 60

3.1.5.a Poly-TPD.....60

3.1.5.b Me-4PACz.....60

3.1.5.c NiO_x.....60

3.1.5.d Al_2O_3 Nanoparticles Wetting Layer 60

3.1.6 Electron Transport Layer Deposition 61

3.1.6.a PCBM.....61

3.1.6.b BCP.....61

3.1.6.c ICBA.....61

3.1.6.d C_{60}.....61

3.1.6.e ALD SnO_2.....62

3.1.6.f Sputtered IZO.....62

3.1.7 1.97 eV and 1.55 eV Perovskite Absorber Surface Passivation Layer Deposition 62

3.1.7.a $EDAI_2$.....62

3.1.7.b $EDABr_2$:$EDAI_2$ (EDAX).....62

3.1.8 Tandem Recombination Layer Deposition 63
3.1.9 Electrode Deposition 63
3.1.10 Encapsulation 64
3.2 Perovskite Thin Film Characterization 64
3.2.1 UV-Visible Absorbance 64
3.2.2 Photoluminescence Quantum Efficiency (PLQE) 64
3.2.3 1-Dimensional X-Ray Diffraction (1D XRD) 65
3.2.4 2-Dimensional X-Ray Diffraction (2D XRD) 65
3.2.5 Grazing Incidence Wide-Angle X-Ray Scattering (GIWAXS) 65
3.2.6 X-Ray Photoelectron Spectroscopy (XPS) 66
3.2.7 Scanning Electron Microscopy (SEM) 66
3.2.8 Time Resolved Photoluminescence Photospectroscopy (TRPL) 66
3.3 Perovskite Solar Cell Characterization 67
3.3.1 Current Density-Voltage (J-V) Characterization 67
3.3.2 External Quantum Efficiency (EQE) 67
3.3.2.a Single Junction Solar Cells 67
3.3.2.b All-Perovskite Triple Junction Solar Cells 68
3.3.2.c dEQE/dE Band Gap Analysis 69
3.3.3 Fourier-Transform Photocurrent Spectroscopy (FTPS) 69
3.3.4 Electroluminescence Quantum Efficiency (ELQE) 70
3.3.5 Cross-Sectional Scanning Electron Microscopy (SEM) 70
3.3.6 Stability Testing 71
Chapter 3 References 72

4 Improved Stability of Efficient and Reproducible 1.55 eV Middle Band Gap Perovskite Absorbers and Single Junction Solar Cells 73

4.1 Introduction 73

4.2 Improved Perovskite Material Stability with Mixed Formamidinium-Cesium A-Site Cation 76

4.3 Fabrication of High Efficiency 1.55 eV Middle Band Gap $FA_{0.8}Cs_{0.2}PbI_3$ Perovskite Solar Cells 79

4.3.1 Tuning of A-Site Cation Composition for $FA_{1-x}Cs_xPbI_3$ Solar Cells 79

4.3.2 DMF/DMSO Solvent System 80

4.3.3 Benzylammonium Thiocyanate Bulk Additive 82

4.3.4 Hole Transport Layer 83

4.3.5 Electron Transport Layer and Top Contact Stack for Champion $FA_{0.8}Cs_{0.2}PbI_3$ 1.55 eV Solar Cell Efficiency and Reproducibility 85

4.4 Improved Stability of 1.55 eV $FA_{0.8}Cs_{0.2}PbI_3$ Perovskite Single Junction Solar Cells Under 85°C Light 89

4.4.1 Further Modifications to Top Contact for Tandem-Relevant Stability Testing 89

4.4.2 $EDAI_2$ Surface Passivation 90

4.4.3 PbI_2 Stoichiometry 92

4.5 Conclusion 100

Chapter 4 References 101

5 Novel Crystallization Method for Fabrication of Efficient and Reproducible 1.97 eV Wide Band Gap Perovskite Absorbers and Single Junction Solar Cells……104

5.1 Introduction……104

5.2 DMF/DMAX Crystallization Method and Thin Film Characterization of 1.97 eV Perovskite Absorbers……109

5.2.1 Development of DMF/DMAX Crystallization Method……109

5.2.2 Material Characterization of Thin Films Fabricated Using DMF/DMAX and DMF/DMSO Crystallization Methods……120

5.3 Single Junction Solar Cell Fabrication and Testing Using 1.97 eV Wide Band Gap Perovskite Absorbers……133

5.3.1 Improving Performance and Reproducibility with DMF/DMAX Crystallization Method Solar Cells……133

5.3.2 Optimization of DMF/DMAX Solar Cells……135

5.3.3 Operational Stability of DMF/DMAX and DMF/DMSO 1.97 eV Solar Cells……141

5.4 Conclusion……143

Chapter 5 References……144

6 V_{OC} Loss Mechanisms in 1.97 eV Wide Band Gap Perovskite Single Junction Solar Cells……146

6.1 Introduction……146

6.2 V_{OC} Loss Mechanism Measurements and Calculations……150

6.2.1 Fourier-Transform Photocurrent Spectroscopy and $V_{OC, rad}$……150

6.2.2 Photoluminescence Quantum Efficiency and $V_{OC, PLQE}$.....155

6.2.3 Electroluminescence Quantum Efficiency and $V_{OC, ELQE}$ 159

6.3 Interpreted Results.....164

6.4 Conclusion.....166

Chapter 6 References.....167

7 All-Perovskite Multijunction Tandem Solar Cells.....169

7.1 Introduction.....169

7.2 All-Perovskite Triple Junction Tandem Solar Cells.....173

7.3 Development of All-Perovskite Tandem Solar Cells.....174

7.3.1 All-Perovskite Double Junction Tandem Solar Cells with 1.97 eV and 1.61 eV Band Gap Absorbers.....175

7.3.2 All-Perovskite Triple Junction Tandem Solar Cells with 1.97 eV, 1.61 eV, and 1.25 eV Band Gap Absorbers, 1.0 M Concentration of 1.97 eV Perovskite Precursor, and Recombination Layer of Au or IZO for 1.61 eV/1.25 eV Subcells.....178

7.3.3 All-Perovskite Triple Junction Tandem Solar Cells with 1.97 eV, 1.61 eV, and 1.25 eV Band Gap Absorbers, 0.8, 0.9, and 1.0 M Concentration of 1.97 eV Perovskite Precursor, and IZO Recombination Layers.....182

7.4 Optimized All-Perovskite Triple Junction Tandem Solar Cell Achieves 27.3% Maximum Power Point Tracked Efficiency at 1cm^2 Area.....183

7.5 Stability Testing of All-Perovskite Triple Junction Tandem Solar Cell.....188

7.6 Conclusion.....190

Chapter 7 References..... 191

8 Conclusion 193

Chapter 1

Introduction

Improved access to energy has powered human development throughout our history. The world today is primarily powered by the burning of fossil fuels that emit greenhouse gases and contribute to climate change impacting people here and now. Solar energy has the potential to harvest enormous quantities of sunlight as a renewable energy technology and power global energy demand while greatly reducing greenhouse gas emissions. Compared to current commercially viable solar cell technologies, all-perovskite triple junction tandem solar cells offer the promise of higher efficiencies and lower costs.

1.1 – Energy and Human Development

At the dawn of human history, energy was only accessible through food and heat from the immediate surrounding environment. For an individual human in a prehistoric hunter-gatherer society, an estimated mere 125 watts of power could be extracted from food resources.[1] Human development forever changed with the First Agricultural Revolution around 10,000 B.C. – marking a shift from nomadic hunting and gathering to settled agriculture.[2] Around this time, humans also domesticated animals that could provide increased muscle to power the First Agricultural Revolution and enable the development of human civilization.[3] One horse provides 746 watts of power – 1 horsepower – about six times that of one human.[4]

The invention and refinement of watermills by the ancient Greeks and Romans starting around 240 B.C. enabled humanity to harvest energy from running water – beyond the confines of human and animal muscle.[5] By the Middle Ages, watermills were producing power at a much larger scale, on the order of a few thousand watts.[6]

Scottish inventor James Watt again forever changed human development with the steam engine, patented in 1769 A.D. The power unit "watts" is named in his honor. By burning coal to heat water, Watt's steam engine used the steam created to push a piston down and pull it back up in a cycle.[7] Watt's steam engine could achieve a power output of 26,000 watts – equal to 35 horses – and was a crucial technological development that helped spur the Industrial Revolution in Britain and around the world.[8]

Since the onset of the Industrial Revolution, the burning of fossil fuel resources – primarily coal, petroleum, and natural gas – has helped power extraordinary increases in economic development, life expectancy, and global population growth from 1 billion people in 1800 to over 8 billion people today.[9,10]

1.2 – Climate Change

"Climate change" refers to the broad range of changes happening to our planet because of long-term warming, including increasing land and ocean temperatures, rising sea levels, melting glaciers and ice sheets, and extreme weather events.[11] 97% of actively publishing climate scientists around the world agree that humans are causing climate change by the emission of greenhouse gases.[12]

The burning of fossil fuels since the Industrial Revolution releases greenhouse gases – primarily carbon dioxide – into the atmosphere. Today, the concentrations of greenhouse gases in the atmosphere are at their highest levels in at least 800,000

years.[13] Greenhouse gases in the atmosphere act as a “thermal blanket” trapping about 90% of the heat from sunlight radiating from Earth back toward the surface of the Earth. This thermal blanket keeps the planet warmed to a life-supporting temperature, without which the Earth would be inhospitable to humans. In general, this greenhouse effect is good, even essential, for life.[14] However, rapid increases in greenhouse gas atmospheric concentrations from burning fossil fuels since the Industrial Revolution is raising global average surface temperatures and causing climate change dangerous to humanity.[15]

Last year, 2023, was the hottest year in recorded history with a global average surface temperature 1.35°C above the pre-industrial average.[16,17] This year, 2024, is on track to be even hotter.[18]

Greenhouse gases in the climate system already have increased the likelihood of severe impacts for people, ecosystems, and economies around the world. More extreme weather events, increased ocean acidification, higher storm surges, and rising sea levels are all happening here and now.[19] In the 2015 Paris Agreement, the world recognized that it is necessary to prevent 2°C global average surface temperature rise above the pre-industrial average to avoid the most catastrophic impacts of climate change.[20]

To help prevent this, the world will need to be powered by more sources, such as solar energy, that emit far less greenhouse gases than fossil fuels. Today, fossil fuels continue to dominate our energy supply – powering 81.5% of global primary energy consumption in 2023.[21]

1.3 – Solar: A Renewable Energy Solution

Powering global energy demand with energy sources that greatly reduce greenhouse gas emissions is an immense challenge.

Global primary energy consumption was reported to be nearly 20 terawatt-years (TWy) in 2023, a new annual record.[21] The combined remaining reserves of all non-renewable energy sources on Earth – coal, petroleum, natural gas, and uranium – are estimated to be around 1,570 TWy.[22] All of these energy sources (except uranium for nuclear power) emit greenhouse gases that contribute to climate change. The combined annual energy potential from renewable sources other than solar – wind, hydro, geothermal, biomass, and tidal – is about 135 TWy, assuming maximum potentials yet to be realized primarily due to cost limitations.[22]

Sunlight offers the highest potential energy of any source on Earth by far. As shown in Figure 1.1, 24,370 TWy of solar energy from sunlight strikes the land surface of the Earth every year – 15 times the total of all non-renewable reserves and 180 times the annual energy potential of all other renewable energy sources combined. In less than eight hours, enough solar energy strikes the terrestrial surface of the Earth to fulfill current global energy demand for an entire year.

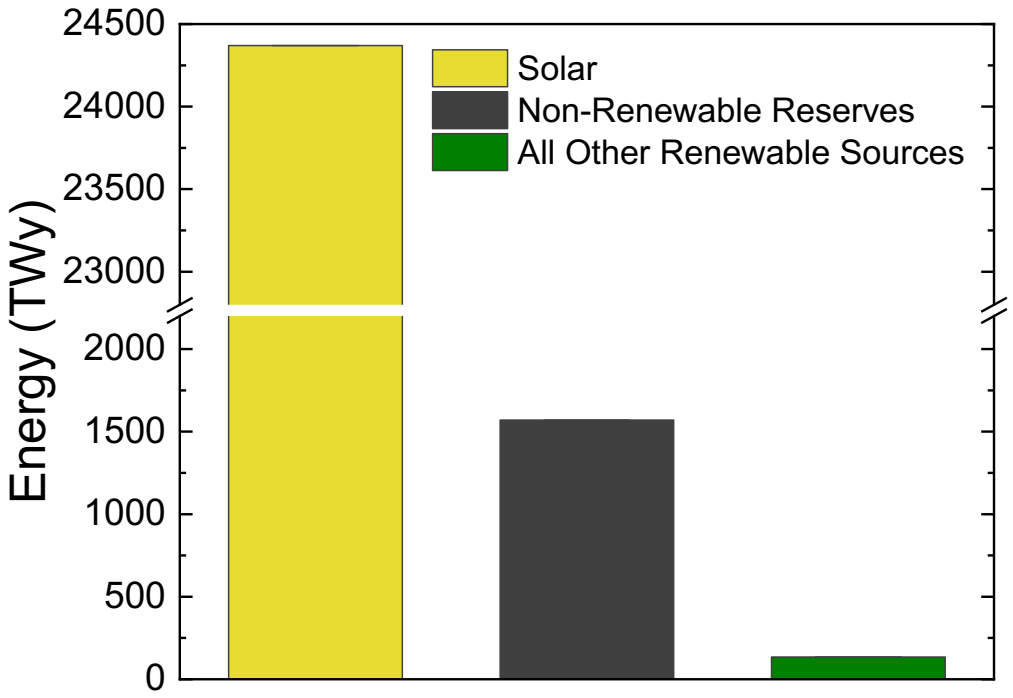

Figure 1.1. The annual energy potential of solar, total estimated energy of non-renewable reserves, and annual energy potential of all other renewable sources. Tsao et al. reported that the average solar flux striking the outer atmosphere of the Earth is 342.5 W/m^2.[23] Of this solar flux, NASA reports that 29% is reflected back into space and a further 23% is absorbed in the atmosphere by gases, dust, and other particles in the atmosphere. The remaining 48% (164.4 W/m^2) is absorbed at the surface of the Earth.[24] Land makes up about 29% of the surface of the Earth. Multiplying the average solar flux that hits the surface of the Earth, the surface area of the Earth, and the fraction that land makes up of the surface of the Earth gives the theoretical potential of terrestrial solar energy on Earth: (164.4 W/m^2) * 4π * (6,378 km)^2 * (106 m^2/km^2) * (10^{-12} TW/W) * 0.29 * 1 year = 24,370 TWy.

Despite this immense potential, solar energy totaled only about 2.5% of global primary energy production in 2023.[21] Crystalline silicon is the dominant current solar cell technology, accounting for about 97% of solar cells manufactured in 2023.[25]

Perovskite solar cells offer advantages compared to crystalline silicon, including superior light absorption, tunable band gaps, lower formation energies, greater defect

tolerance, and lower cost industrially scalable fabrication techniques.[26-31] With the promise of higher efficiencies and lower costs than crystalline silicon, stable all-perovskite triple junction tandem solar cells have the potential to power our world into a better tomorrow.

Chapter 1 References

1. Sørensen, B. *Renewable Energy : Physics, Engineering, Environmental Impacts, Economics and Planning*. Academic Press, 2017.

2. Meyer, S. *The Neolithic Revolution*. Rosen Publishing, 2016.

3. Gupta, A. Origin of Agriculture and Domestication of Plants and Animals Linked to Early Holocene Climate Amelioration. *Current Science*, **87**, 1, (2004).

4. Encyclopaedia Britannica. “Horsepower | Definition, Unit, and Facts.” *Encyclopædia Britannica*, 2019, www.britannica.com/science/horsepower.

5. Wikander, Ö. *Handbook of Ancient Water Technology / Handbook of Ancient Water Technology*. Brill, 2000.

6. Munro, J. Industrial Energy from Water-Mills in the European Economy, 5th to 18th Centuries: The Limitations of Power. *MPRA Paper*, (2002).

7. Scottish Engineering Hall of Fame. “James Watt.” *Scottish Engineering Hall of Fame*, engineeringhalloffame.org/profile/james-watt.

8. The American Society of Mechanical Engineers. “Boulton & Watt Rotative Steam Engine.” *Www.asme.org*, www.asme.org/about-asme/engineering-history/landmarks/111-boulton-watt-rotative-steam-engine.

9. Khan, A. The industrial revolution and the demographic transition. *Business Review*, **1**, (2008).

10. Mohajan, H. The First Industrial Revolution: Creation of a New Global Human Era. *Journal of Social Sciences and Humanities*, **5**, 4, 377–387 (2019).

11. The National Aeronautics and Space Administration. “Questions (FAQ).” *Science.nasa.gov*, science.nasa.gov/climate-change/faq/.

12. Anderegg, W. R. L. et al. Expert Credibility in Climate Change. *Proceedings of the National Academy of Sciences*, **107**, 27, 12107–9 (2010).

13. Lüthi, D. et al. High-resolution carbon dioxide concentration record 650,000-800,000 years before present. *Nature*, **453**, 379-382 (2008).

14. The National Aeronautics and Space Administration. “The Causes of Climate Change.”*Science.nasa.gov*, NASA, science.nasa.gov/climate-change/causes/.

15. Kemp, L. et al. Climate Endgame: Exploring Catastrophic Climate Change Scenarios. *Proceedings of the National Academy of Sciences*, **119**, 34, (2022).

16. World Meteorological Organization. “Climate Change Indicators Reached Record Levels in 2023: WMO.” *World Meteorological Organization*, 19 Mar. 2024, wmo.int/news/media-centre/climate-change-indicators-reached-record-levels-2023-wmo.

17. Lindsey, R. and Dahlman, L. “Climate Change: Global Temperature.” *Climate.gov*, NOAA, 18 Jan. 2024, www.climate.gov/news-features/understanding-climate/climate-change-global-temperature.

18. “Copernicus: Summer 2024 – Hottest on Record Globally and for Europe | Copernicus.” *Copernicus.eu*, 6 Sept. 2024, climate.copernicus.eu/copernicus-summer-2024-hottest-record-globally-and-europe.

19. Intergovernmental Panel on Climate Change. *Climate Change 2014 : Synthesis Report : Contribution of Working Groups I, II and III to the Fifth Assessment Report of the Intergovernmental Panel on Climate Change*. IPCC, 2014.

20. Paris Agreement to the United Nations Framework Convention on Climate Change, Dec. 12, 2015, T.I.A.S. No. 16-1104.

21. Energy Institute. “Statistical Review of World Energy.” *Statistical Review of World Energy*, 2024, www.energyinst.org/statistical-review.

22. Perez, M. and Perez, R. “Update 2022 – a Fundamental Look at Supply Side Energy Reserves for the Planet.” *Solar Energy Advances*, vol. 2, p. 100014, Jan. 2022.

23. Tsao, J., Lewis, N. and Crabtree, G. *Solar FAQs*. Sandia National Laboratories, 20 Apr. 2006, www.sandia.gov/app/uploads/sites/153/2022/02/Solar-FAQs.pdf.

24. The National Aeronautics and Space Administration. “Climate and Earth’s Energy Budget.” *Nasa.gov*, NASA Earth Observatory, 14 Jan. 2009, earthobservatory.nasa.gov/features/EnergyBalance/page4.php.

25. Fraunhofer Institute for Solar Energy Systems. “Photovoltaics Report.” 29 July 2024.

26. Noh, J. H. et al. Chemical Management for Colorful, Efficient, and Stable Inorganic–Organic Hybrid Nanostructured Solar Cells. *Nano Lett.*, **13**, 1764–1769 (2013).

27. Eperon, G. E. et al. Formamidinium lead trihalide: a broadly tunable perovskite for efficient planar heterojunction solar cells. *Energy Environ. Sci.*, **7**, 982–988 (2014).

28. Noel, N. K. et al. Lead-free organic–inorganic tin halide perovskites for photovoltaic applications. *Energy Environ. Sci.*, **7**, 3061–3068 (2014).

29. Che, Q. et al. Controllable Self-Induced Passivation of Hybrid Lead Iodide Perovskites toward High Performance Solar Cells. *Nano Letters*, **14**, 7, 4158-4163 (2014).

30. Afre, R. and Pugliese, D. Perovskite Solar Cells: A Review of the Latest Advances in Materials, Fabrication Techniques, and Stability Enhancement Strategies. *Micromachines*, **15**, 192 (2024).

31. Ibn-Mohammed, T. et al. Perovskite solar cells: An integrated hybrid lifecycle assessment and review in comparison with other photovoltaic technologies. *Renewable and Sustainable Energy Reviews*, **80**, 1321–1344 (2017).

Chapter 2

Theory and Background

This chapter summarizes physics relevant for solar cells, including energy band theory and the properties of semiconductors. Solar cells utilize these semiconductor physics principles to convert sunlight into electrical power. Theoretical and operational fundamentals of solar cells are covered. Absorption of light, separation of charge carriers, and extraction of charge carriers are foundational concepts for understanding the inner workings of solar cells. Semiconductor junctions are explained. The operation and characterization of solar cells are analyzed. Finally, an overview of perovskite semiconductor absorber materials for photovoltaic applications is presented. Advantages and challenges for perovskite solar cells relevant to their real-world implementation as a renewable energy technology are discussed.

2.1 – Semiconductor Physics

2.1.1 – Energy Band Theory

Atoms are the building blocks of matter in our universe. Atoms consist of three subatomic particles: positively charged protons, neutrally charged neutrons, and negatively charged electrons. Protons and usually neutrons form the nucleus of the atom, which is surrounded by a cloud of electrons. Atomic orbitals are three dimensional spaces that predict the location of an electron around an atom with 95% probability.[1] Within each shell of an atom there is a combination of atomic orbitals. The four types of orbitals are sharp, principle, diffuse, and fundamental (s, p, d, f). The spatial distribution of orbitals is

determined by the principal quantum number (n), the angular quantum number (l), and the magnetic quantum number (m_l). n describes the size of the orbital, l the shape of the orbital, and m_l the orientation in space of the orbital.[2] Shapes of s, p, and d atomic orbitals are shown in Figure 2.1.

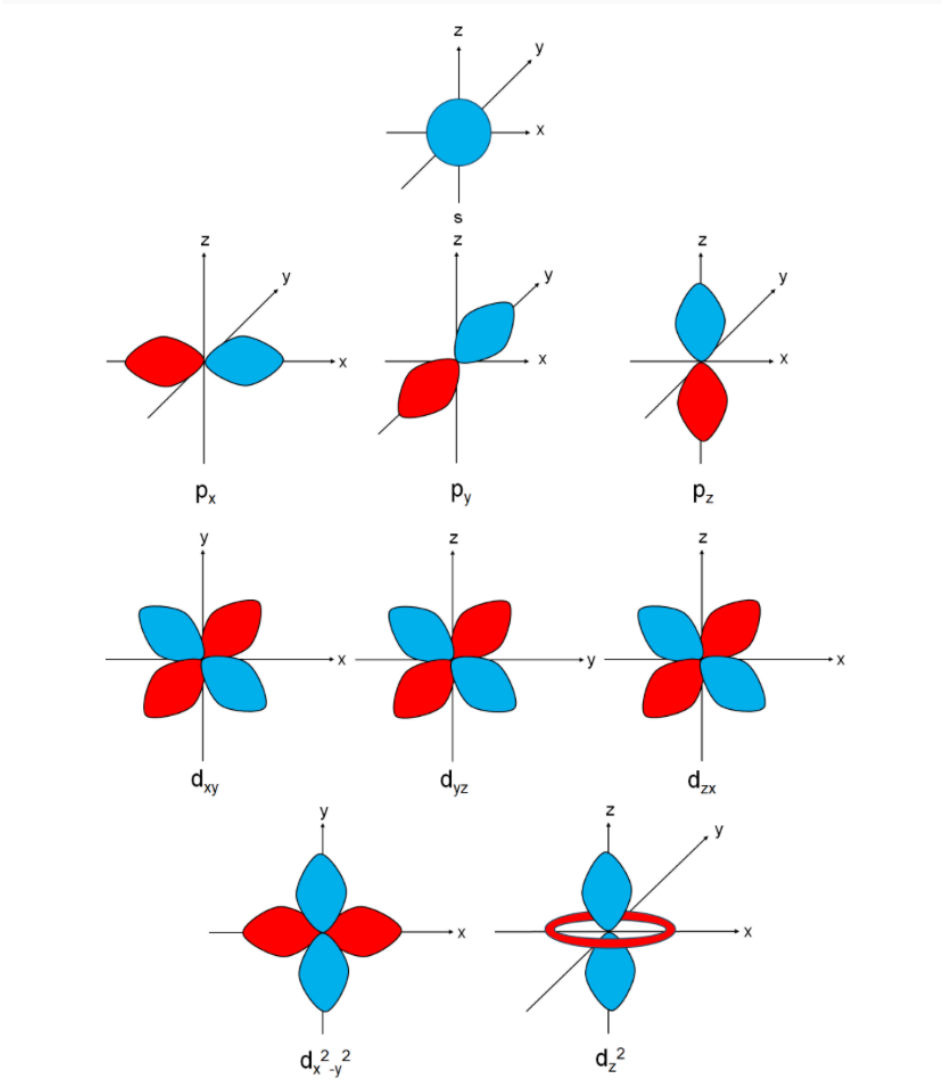

Figure 2.1. s, p, and d atomic orbital surfaces based on different n, l, and m_l quantum numbers. The s atomic orbital is one region of probability that holds a maximum of two electrons total. The p atomic orbitals form a set of three regions of probability that hold a maximum of six electrons total. The d atomic orbitals form a set of five regions of probability that hold a maximum of ten electrons total.

Electrons in the outermost atomic orbitals are called valence electrons. Valence electrons are the farthest away from the positively charged nucleus and thus the least tightly bound, making them eligible to participate in the formation of chemical bonds. When two atoms get close enough to each other, they may share electrons to form such a bond and create a molecule.[3]

The overlap of atomic orbitals via bonding creates molecular orbitals (MOs). The probability distribution of an electron in an atomic orbital is described by the wavefunction, Ψ. The linear combination of atomic orbitals describes their overlapping.[4] If the orbitals of atoms A and B overlap appropriately, electrons can be found in either atomic orbital. The overall Ψ of the molecule formed is a superposition of the atomic orbitals of A and B such that:

$$\Psi_{\pm} = N_{\pm} (\Psi_A \pm \Psi_B) \qquad (2.1)$$

N is the normalization factor. Take the overlap of two neighboring hydrogen atoms (A and B, each with one valence electron from the 1s atomic orbital) to form an H_2 molecule as a simple example. The linear combination of atomic orbitals of the A and B hydrogen atoms produces two probability densities for the two electrons – two molecular orbitals.

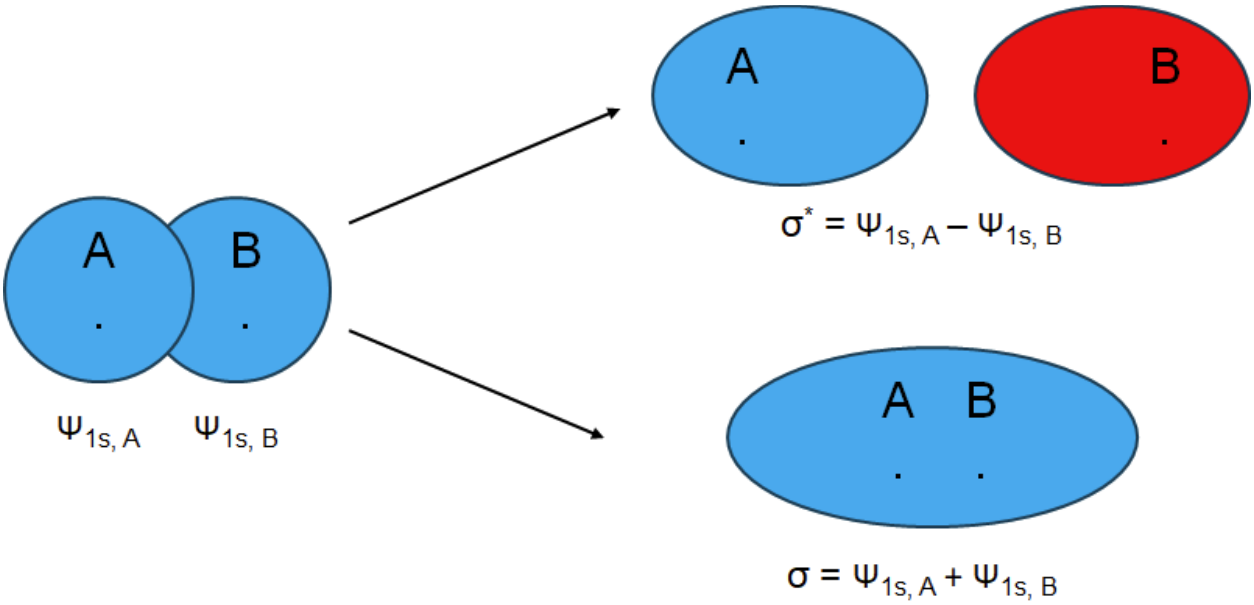

Figure 2.2. The linear combination of two atomic orbitals to form two molecular orbitals, bonding and anti-bonding.

The constructive overlap of atomic orbitals (Ψ_+) generates a bonding molecular orbital (σ) where the electrons reside with opposite spins in the internuclear region between atoms A and B. The destructive overlap of atomic orbitals (Ψ_-) generates an anti-bonding molecular orbital (σ^*) where the electrons are excluded from the internuclear region.[3] The orbital energy diagram in Figure 2.3 illustrates that the H_2 bonding molecular orbital is lower energy than either atomic orbital.

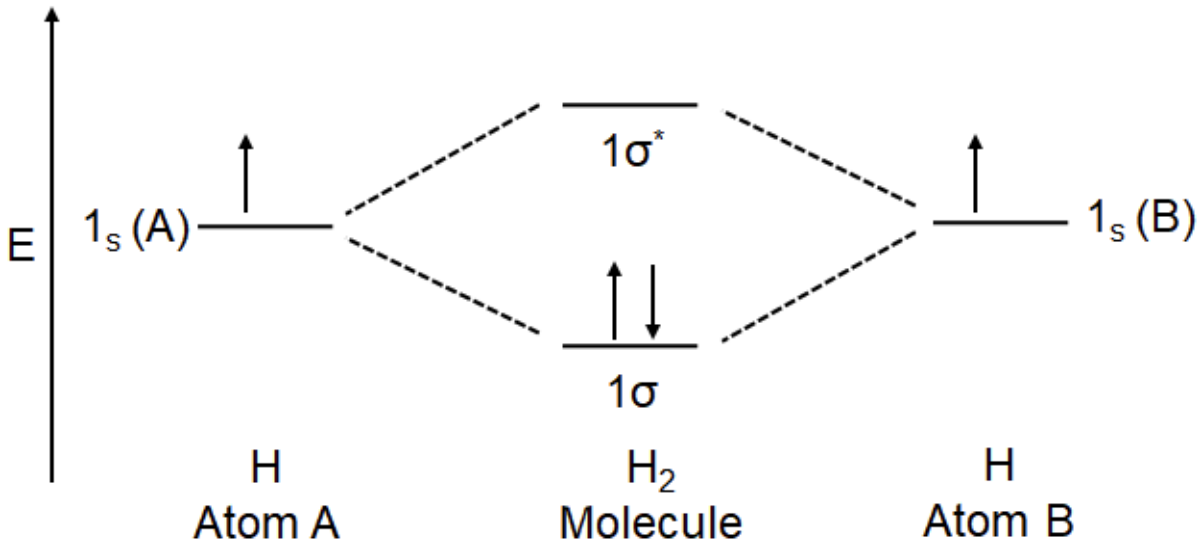

Figure 2.3 Orbital energy diagram for the formation of the H_2 molecule.

As more atoms and atomic orbitals are included in the linear combination, more bonding and anti-bonding molecular orbitals are generated. Molecular orbitals with the same energy become difficult to distinguish with sufficiently complex polyatomic molecules and can at this point be referred to as a band. A crystal lattice has a repeating unit cell grouping of atoms, ions, or molecules in three-dimensional space.[5] The energy bands of a crystal lattice are essentially treated like an infinite set of bonding and anti-bonding molecular orbitals.

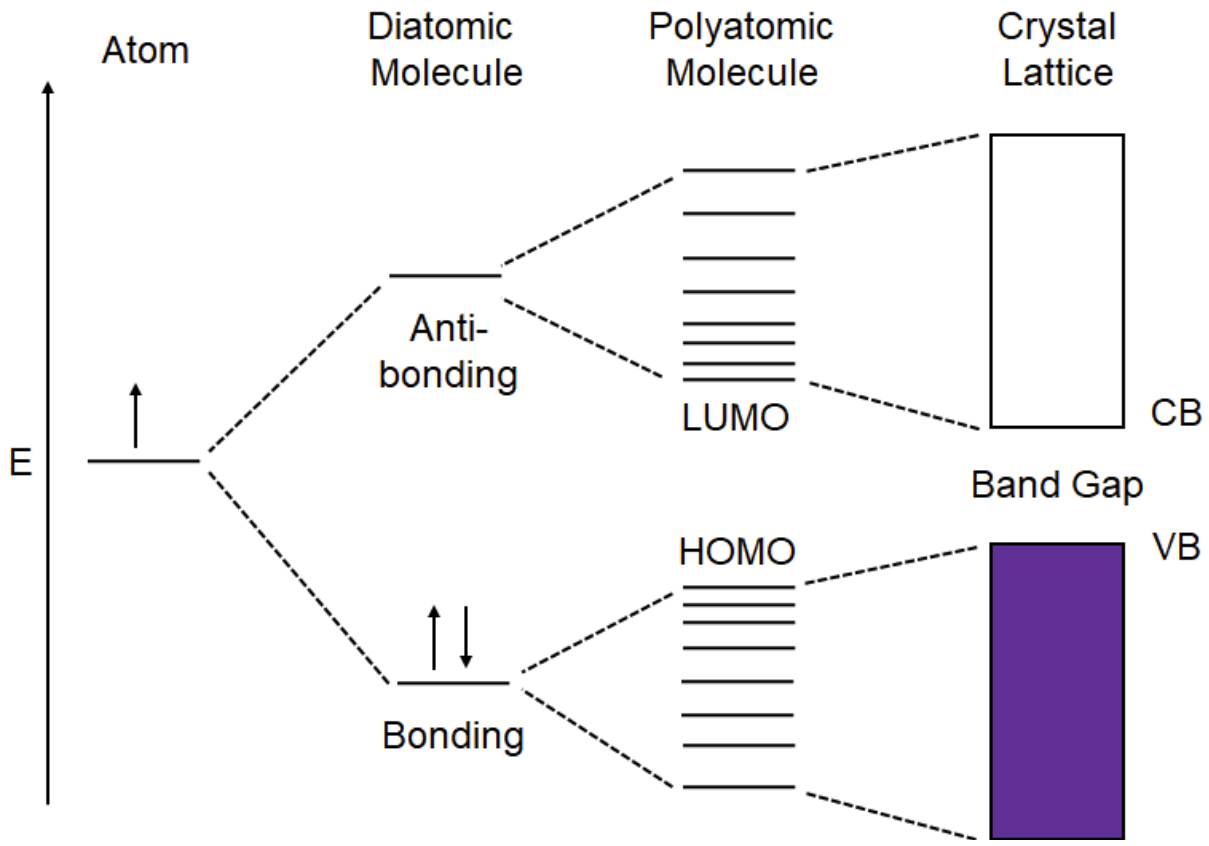

Figure 2.4. Orbital energy diagram for an atom, diatomic molecule, polyatomic molecule, and crystal lattice. The HOMO and LUMO have been demarcated as the highest energy bonding molecular orbital and lowest energy anti-bonding molecular orbital, respectively, for simplicity.

HOMO refers to the highest occupied molecular orbital (the MO with the highest energy in which electrons reside) and LUMO refers to the lowest unoccupied molecular orbital (the MO with the lowest energy in which electrons do not reside). This terminology is often used for organic molecules.

In an energy band context for a crystal lattice, the valence band (VB) and conduction band (CB) edges are analogous to the HOMO and LUMO, respectively. For a crystal lattice, the band of bonding molecular orbitals (VB) is deemed full and the band of anti-bonding molecular orbitals (CB) is deemed empty.[6] The energy difference between

the valence and conduction band edges is called the band gap. If promoted to the empty orbitals in the conduction band, electrons can move through the crystal lattice.[5]

2.1.2 – Properties of Semiconductors

Based on their band structure, materials can be conductors, semiconductors, or insulators. In a conductor (metal), the valence band and conduction band overlap so that there are nearly continuous energy states throughout the band. As such, electrons can move about freely throughout the energy states of the conductor. There is no such continuous energy band for semiconductors and insulators. In a semiconductor, discrete energy bands exist as the valence band (VB) and conduction band (CB). The energy gap between these discrete bands is called the band gap (E_G). Band gap energies for semiconductors are in the 1-3.5 eV range. In an insulator, the band gap energy exceeds 3.5 eV and the VB and CB are separated farther apart.[5]

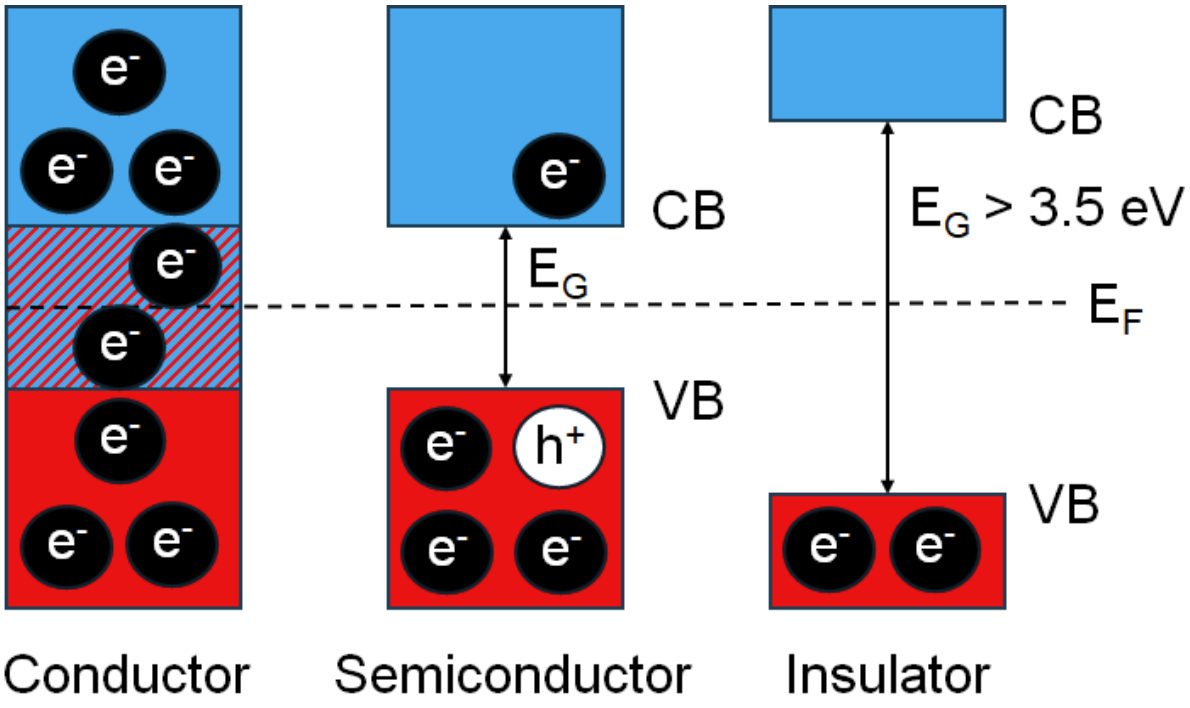

Figure 2.5. Band structures of conductors, semiconductors, and insulators. Energy states for conductors overlap and, as a result, conductors exhibit high conductivity. Energy states for semiconductors are separated by a moderate band gap energy and, as a result, exhibit medium conductivity. The energy states for insulators are separated by a large band gap energy and, as a result, exhibit low conductivity.

Electrons in a semiconductor or an insulator can be promoted from the VB to the CB by an energy transfer with sufficient energy greater than or equal to E_G. This energy transfer can be the result of thermal or electromagnetic energy. If a sufficient energy transfer is applied, an electron in the VB is excited to one of the many empty higher energy states in the CB. The Fermi level (E_F) describes the energy level at which half the electron states are occupied at a given temperature. For an intrinsic semiconductor, the Fermi level is located in the middle of the band gap.[7]

The excited electron becomes a mobile charge carrier and contributes to electrical conduction in the CB. Meanwhile, a positively charged vacancy called a hole is left behind in the VB. Semiconductors are the type of materials necessary for photovoltaic power. The energy of an incident photon from sunlight is described as $E_{photon} = \frac{hc}{\lambda}$, where h is Planck's constant (6.626×10^{-34} J/s), c is the speed of light (3×10^8 m/s), and λ is the wavelength of the photon. For a semiconductor, optical absorption when $E_{photon} \geq E_G$ leads to the excitation of electrons to the CB. The excited electrons in the CB contribute to electrical conduction through photoconductivity.

It is important to note that semiconductor materials are classified as either direct or indirect band gap semiconductors. The energy levels of valence and conduction band edges can change at various crystal momentums. A direct band gap exists if the valence band maximum and conduction band minimum edges are aligned at the same crystal momentum. If $E_{photon} \geq E_G$, a photon can directly excite an electron from the valence band

to the conduction band. An indirect band gap exists if the valence band maximum and conduction band minimum edges are aligned at different crystal momentums. In this case, an electron excited by a photon must also undergo a significant change in its momentum.[8] Conservation of momentum requires this electron to also undergo the absorption of a phonon – which is vibrational mechanical energy in the crystal lattice – for successful excitation from the valence band maximum to the conduction band minimum. Due to this added requirement, light absorption is significantly less probable in indirect band gap semiconductors.[8] For photovoltaic applications, indirect band gap semiconductors require thicknesses 2-3 orders of magnitude greater than their direct band gap counterparts.

2.2 – Solar Cell Fundamentals

2.2.1 – Absorption, Separation, and Extraction

The three processes that need to occur to generate solar power are absorption of light, separation of charge carriers, and extraction of these charge carriers.

2.2.1.a – Absorption

First, incident photon energy must be absorbed to be converted into electrical energy in a solar cell. This occurs in the absorber layer of a solar cell. Perovskite absorber layers are the focus of this thesis. The more photons that are absorbed, the more electrons that can be excited in the semiconductor absorber material and the higher the potential power conversion efficiency of the solar cell.

Photons are absorbed when the incident photon energy (E_P) is equal to the semiconductor band gap energy (E_G). In this situation, the energy from incident photons excites electrons from the valence band to the conduction band of the semiconductor,

where the excited electrons are free to move about and can conduct electricity. When an electron is promoted to the conduction band in this way, it leaves behind a positively charged vacancy referred to as a hole in the valence band.[5]

If E_P is greater than E_G, the incident photons are strongly absorbed by the semiconductor and converted into electrical energy but also result in a thermal energy loss. In this situation, electrons are excited to energy states well above the conduction band edge, rapidly relax back down to the conduction band edge, and convert this excess energy into heat. This excess energy is now a thermal energy loss.

Incident photons also can be reflected or transmitted, however, instead of absorbed. Photons that are reflected or transmitted cannot be converted into electrical energy in a solar cell. In commercial solar cells, reflection is reduced through the application of thin anti-reflection coatings on the surface. Such coatings use a dielectric material so that the photon wave reflected from the anti-reflective coating is out of phase with the photon wave reflected from the surface of the semiconductor. Because these waves are out of phase with respect to one another, they experience destructive interference and there is reduced reflected energy from the solar cell.[9] With reflection taken into account, the remaining incident photons are either absorbed or transmitted.

In general, if the incident photon energy (E_P) is less than the energy of the semiconductor band gap (E_G), the photons will be transmitted through the semiconductor as if it were transparent and not used by the solar cell.[5] With the incident photon energy less than what is required to excite to the conduction band, there are no states (other than a low concentration of trap states caused by defects in the semiconductor) accessible to electrons excited by these photons.

2.2.1.b – Separation

Next, if incident photon energy is successfully absorbed, the second of three processes that must occur to generate solar power is the separation of charge carriers. Upon absorption, photoexcited electron-hole pairs (charge carriers) are separated and either remain separated to be converted into electrical energy or recombine and are unavailable for electrical energy conversion. The ability of solar cells to separate charge carriers and maintain that separation is understood by measuring the rates of recombination processes. Recombination is a fundamental factor of solar cell potential efficiency.

Charge carriers can recombine by three processes: radiative, trap-assisted, and Auger recombination depicted in Figure 2.6.

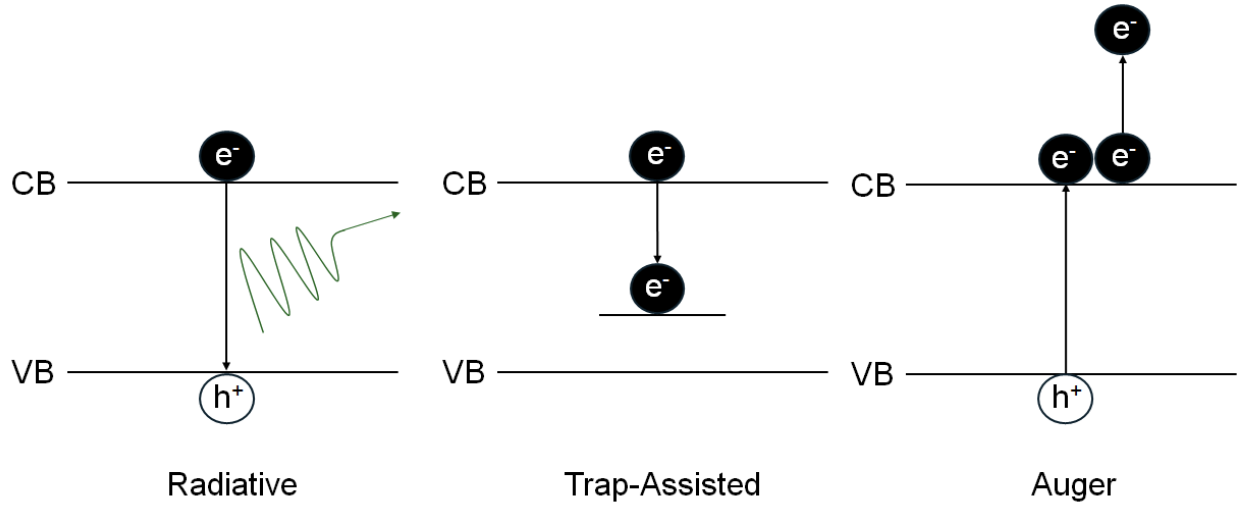

Figure 2.6. Schematics of radiative, trap-assisted, and Auger recombination processes.

First, charge carriers can recombine via radiative recombination, also referred to as band-to-band recombination. Because radiative recombination involves two charge carriers, it is described as a bimolecular recombination process. In this process, an excited electron in the conduction band recombines with a hole in the valence band,

emitting a photon with an energy equivalent to the band gap of the semiconductor material.

The emission of photons by radiative recombination is termed photoluminescence.[10] Photoluminescence quantum efficiency (PLQE) enables the ability to measure the amount of radiative recombination in a given material. PLQE is the ratio of the number of photons emitted to the number of photons absorbed:

$$\text{PLQE} = \frac{\varphi \text{ Emitted}}{\varphi \text{ Absorbed}} \tag{2.2}$$

φ Emitted is the flux of emitted photons and φ Absorbed is the flux of absorbed photons. This is achieved by illuminating the material with a light source of known photon flux and measuring the number of photons emitted from the material with a detector.

Second, charge carriers can recombine via trap-assisted recombination, a non-radiative process also called Shockley-Read-Hall recombination. In this process, an excited electron in the conduction band transitions to an energy level within the band gap called a trap state. Defects in the crystal lattice of the semiconductor material create electronic states within the band gap, referred to as trap states. As a non-radiative process, the energy from trap-assisted recombination is instead lost as a phonon – vibrational mechanical energy that imparts a thermal energy loss.

Trap states can be shallow or deep. A shallow trap state has an energy level close to the conduction band of the semiconductor. As such, it is possible for thermal energy < k_BT to promote the electron from the shallow trap back to the conduction band edge. Shallow traps accordingly have a smaller impact on solar cell performance. A deep trap state, on the other hand, is located farther into the band gap (farther away from the

conduction band). Thermal energy is thus much less likely to promote the electron from a deep trap state back to the conduction band edge. Deep trap states, therefore, have a greater impact on trap-assisted recombination deleterious to solar cell performance. Halide vacancies are major contributors to deep trap state formation in perovskite solar cells.[11] Trap-assisted recombination involves only one type of charge carrier that recombines at the trap state recombination center and so is termed a monomolecular process.

Third, charge carriers can recombine via Auger recombination. In this process, an excited electron in the conduction band transitions back down to the valence band as in radiative recombination. Instead of emitting a photon, however, this energy is released as kinetic energy that is transferred to a second electron in the conduction band, promoting the second electron to a higher energy level in the conduction band. Auger recombination is also non-radiative and termed a trimolecular process due to the involvement of three charge carriers.

These three recombination processes occur in proportion relative to excitation density. At low excitation density, monomolecular trap-assisted recombination dominates. As excitation density increases, however, the trap-assisted recombination rate plateaus as trap states are filled. At this point, bimolecular radiative recombination has a larger impact. At very high excitation density, trimolecular Auger recombination contributes more to the recombination rate.

For perovskite solar cells, Auger recombination usually only occurs under excitation densities many times greater than the 1000 W/m^2 standard solar irradiation for solar cells. In practice, Auger recombination comes into play for concentrated sunlight

conditions, where solar concentrated photovoltaics use mirrors or lenses to generate power fluxes much greater than the AM 1.5G standard of 1000 W/m^2.[12] For this thesis, radiative and trap-assisted recombination are the main relevant processes.

Lifetime (τ) is defined as the amount of time before a charge carrier recombines after excitation. If recombination processes are only considered in the bulk of the absorber material, the total bulk recombination lifetime can be calculated as follows:

$$\frac{1}{\tau} = \frac{1}{\tau,\mathrm{rad}} + \frac{1}{\tau,\mathrm{trap}} + \frac{1}{\tau,\mathrm{Auger}} \qquad (2.3)$$

It is important to note that significant contributions to trap-assisted recombination beyond the bulk come from crystal grain boundaries, surface defects, and interfaces with charge transport layers. Defects between crystalline grains in a semiconductor material create disruptions in the energy band, creating trap states. Impurities from a material interfacing with the semiconductor and/or dangling bonds can create surface defects that induce trap states. Interfaces can also induce non-radiative recombination by mismatched energy level alignment and charge carrier back transfer. Stolterfoht et al. found that charge transport layers that have poor charge selectivity with a perovskite absorber induce non-radiative recombination losses greater than such losses in the bulk perovskite absorber.[13]

2.2.1.c – Extraction

Finally, if incident photon energy is successfully absorbed and the resultant separation of an electron-hole pair is maintained – and not recombined – the third of three processes that must occur to generate solar power is the extraction of charge carriers. Charge carriers must be extracted at electrodes at opposite ends of the solar cell to contribute to the current and generate electrical power.

Charge carriers can move within the semiconductor material through two processes – drift and diffusion. With drift, the existence of an electric field in the semiconductor results in the net movement of carriers where electrons flow in the opposite direction of the field. With diffusion, the presence of a concentration gradient in the semiconductor results in net movement of charge carriers from high carrier concentration to low carrier concentration areas for a more uniform distribution over time.[5] The one-dimensional drift-diffusion equation calculates the combined contribution of these two processes to the overall current density of the solar cell:

$$J(x) = q(n\mu_n + p\mu_p)E_x + q(D_n \frac{dn(x)}{dx} + D_p \frac{dp(x)}{dx}) \quad (2.4)$$

J(x) is the current density of the solar cell in the x-direction, μ_n is the mobility of the electrons, μ_p is the mobility of the holes, E_x is the applied electric field, D_n is the diffusion coefficient for the electrons, and D_p is the diffusion coefficient for the holes.

2.2.2 – Semiconductor Junctions

Absorption of photons, separation of charge carriers, and extraction of these charge carriers are foundational processes for solar cells. The architecture of solar cells is also crucial for effective conversion of sunlight into electricity. The p-n junction is the conventional architecture for crystalline silicon solar cells. A p-n junction is created when a p-type semiconductor with an excess of holes and a n-type semiconductor with an excess of electrons are brought into contact with each other.

Once the p-n junction is formed this way, a concentration gradient exists between the higher concentration of electrons in the n-type semiconductor and the higher concentration of holes in the p-type semiconductor. This driving force causes excited

electrons to diffuse from the n-type into the p-type semiconductor to recombine with holes. Excited holes in turn diffuse from the p-type semiconductor to the n-type semiconductor to recombine with electrons.[5]

As a result of this diffusion, negatively charged donors are formed in the p-type region (holes are filled) and positively charged donors are formed in the n-type region (electrons are filled). These charged donors are immobilized and ultimately create a positively charged region in the n-type semiconductor near the p-n junction and a negatively charged region in the p-type semiconductor near the p-n junction. This region near the p-n junction is referred to as the depletion region (or space charge region).[5]

The resultant charge difference between the p- and n-type semiconductors in the depletion region creates an electric field. Once the system is at equilibrium, the electric field prevents the diffusion of additional charge carriers.[5] This electric field – also referred to as the built-in potential (V_{bi}) of the p-n junction – drives the drift of photoexcited electrons to the n-type side and holes to the p-type side, as shown in Figure 2.7.

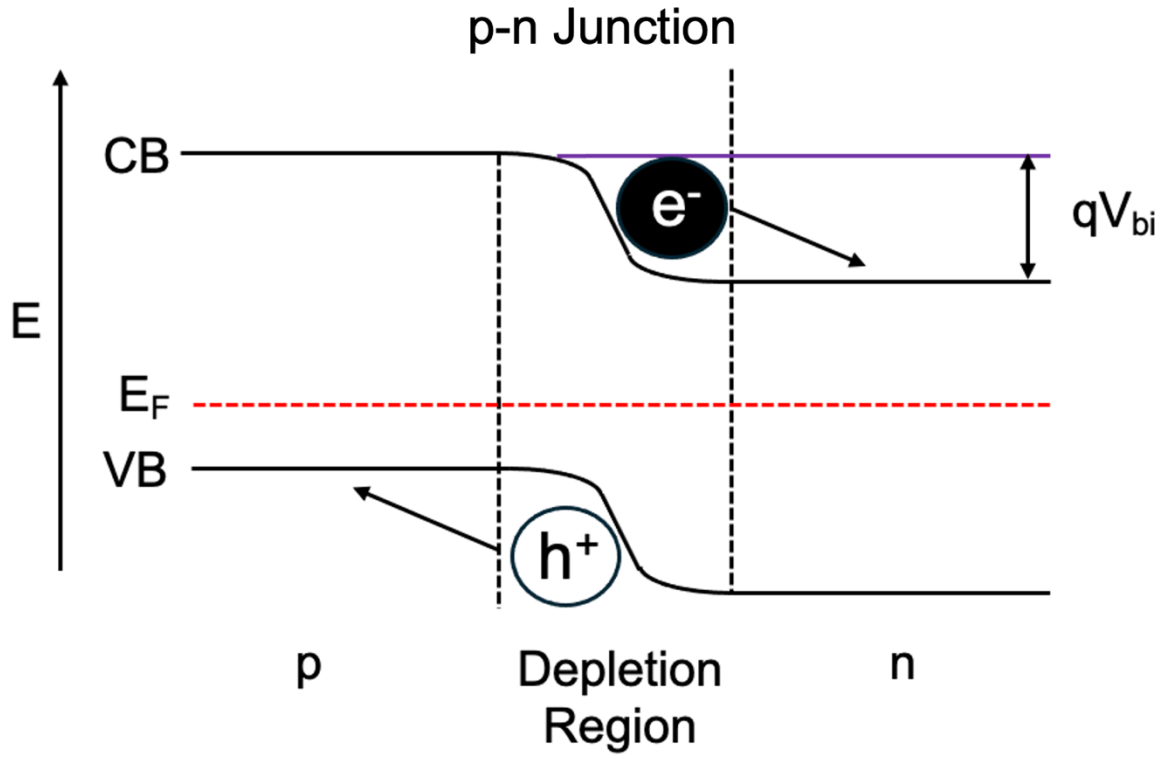

Figure 2.7. Band energy schematic of p-n junction under illumination. Photoexcited electrons are driven to the n-type semiconductor while photoexcited holes are driven to the p-type semiconductor.

In contrast to standard architectures that utilize the p-n junction, the p-i-n architecture places an intrinsic semiconductor absorber material between charge selective contacts. This forms a p-i-n junction. For this thesis, p-i-n architecture is used for all perovskite solar cells fabricated and researched.

Charge selective contacts allow high conductivity for just one type of charge carrier. n-type contacts allow high conductivity for electrons and p-type contacts allow high conductivity for holes. For perovskite solar cells, the n-type contact is referred to as an electron transport layer and the p-type contact is referred to as a hole transport layer.

Solar cells can be subjected to zero, forward, or reverse bias electrical conditions that affect current flow across their junctions. These conditions are illustrated for a p-i-n diode in Figure 2.8.

Under zero bias conditions, electrons from the n-type contact diffuse through the intrinsic absorber toward the p-type contact until a steady-state condition is reached where the Fermi levels of the n- and p-type contacts are aligned, creating an electric field across the intrinsic semiconductor absorber material from the space charge region. This built-in electric field forms a diode.

Under forward bias, the p-type material is connected to a positively charged terminal and the n-type material is connected to a negatively charged terminal. The resultant electric field induces electrons in the n-type material and holes in the p-type material to drift toward the junction. The width of the space charge region decreases and charge carriers can flow across it. Under the forward bias condition, current increases exponentially as a function of voltage.

Under reverse bias, the p-type material is connected to a negatively charged terminal and the n-type material is connected to a positively charged terminal. This bias induces electrons to drift toward the positively charged terminal and holes to drift toward the negatively charged terminal. As such, the width of the space charge region increases, creating a large barrier to charge extraction that inhibits the flow of current (unless under very high reverse bias conditions, where this breaks down). Both p-i-n and p-n junctions are diodes that rectify current – allowing conduction in only one direction.

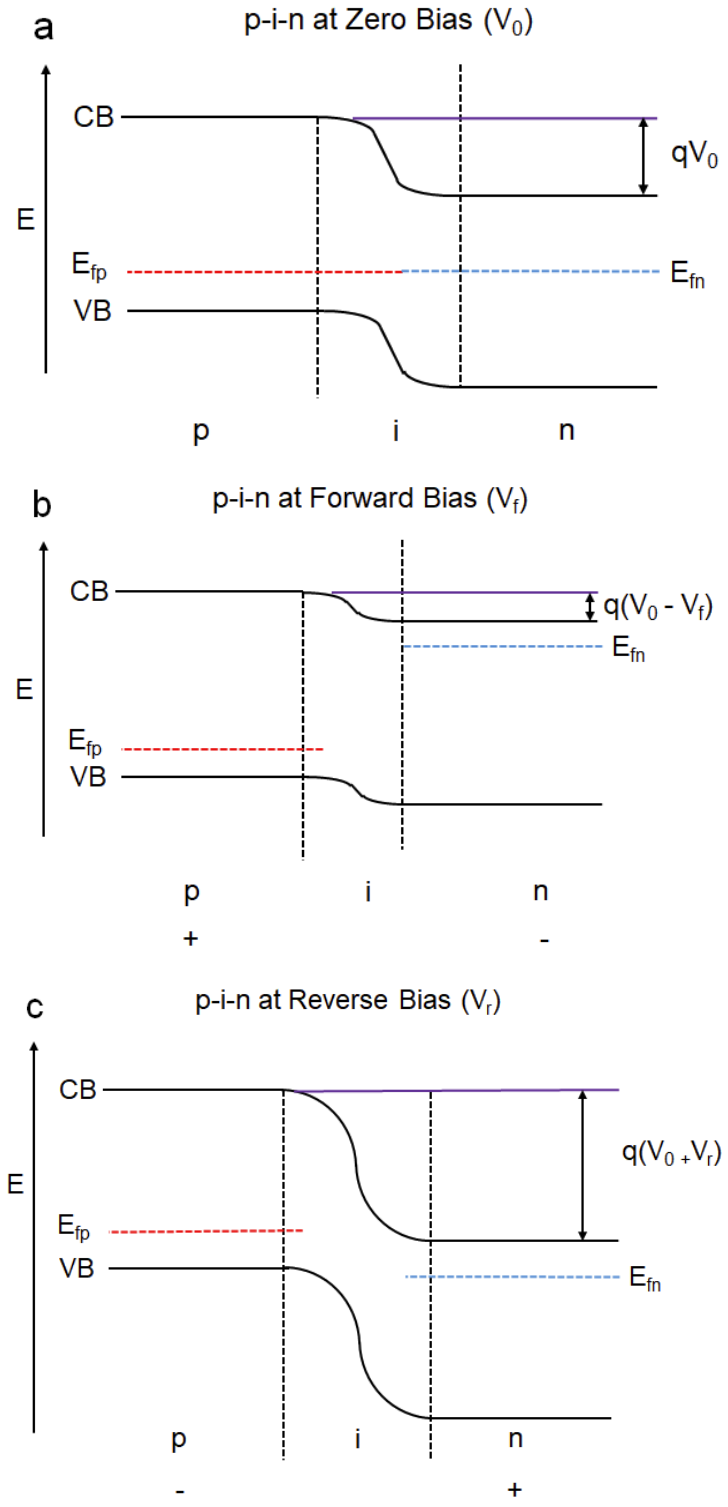

Figure 2.8. Band energy schematic of a p-i-n diode under a) zero b) forward and c) reverse bias.

2.2.3 – Solar Cell Operation and Characterization

To generate power, a solar cell must produce both current and voltage. Because the current generated from a solar cell depends on its area, current is usually described in terms of current density (in the units of mA/cm^2 for this thesis). In the dark, the different energy levels of the p-n or p-i-n junction engenders the solar cell to act as a rectifying diode and so current flows through it under forward bias.[5] This current is called the dark current, J_{dark}. In this situation, the solar cell can be described by the ideal diode equation:

$$J_{dark}(V) = J_0 \left[\exp\left(\frac{qV}{k_B T} - 1\right)\right] \qquad (2.5)$$

J_0 is the dark saturation current – in other words the leakage across the diode in the dark. V is the applied bias.

When light shines on a solar cell and creates charge carriers, the situation changes. A photocurrent that flows in the opposite direction of the dark current is generated. A modified version of the ideal diode equation describes the solar cell under illumination:

$$J(V) = J_{SC} - J_0 \left[\exp\left(\frac{qV}{k_B T} - 1\right)\right] \qquad (2.6)$$

The J_{SC} term is added to the above equation.

When the terminals (contacts) of the solar cell are connected, the voltage difference across them is zero and the current flow from the solar cell therefore reaches its maximum possible value under illumination – the short-circuit current (J_{SC}). When the terminals of the solar cell are disconnected (open-circuit condition), no charge carriers generated in the solar cell can be extracted as there is infinite resistance between the

terminals. As a result, there is zero current and the voltage from the solar cell therefore reaches its maximum possible value under illumination – the open-circuit voltage (V_{OC}). V_{OC} is described as follows:

$$V_{OC} = \frac{k_B T}{q} \ln\left(\frac{J_{SC}}{J_0} + 1\right) \tag{2.7}$$

The current-voltage (J-V) characteristics of the diode can be measured by sweeping the bias voltage and measuring the corresponding current density value at each voltage step. These sweeps are carried out under both illuminated and dark conditions and create J-V curves of the solar cell.

The point on the J-V curve where the product of the voltage and current density is greatest is the maximum power point (MPP) of the solar cell. The maximum power point ("MPP", where V_{MPP} and J_{MPP} intersect on the J-V curve), V_{OC}, J_{SC}, V_{MPP}, and J_{MPP} are demarcated in Figure 2.9.

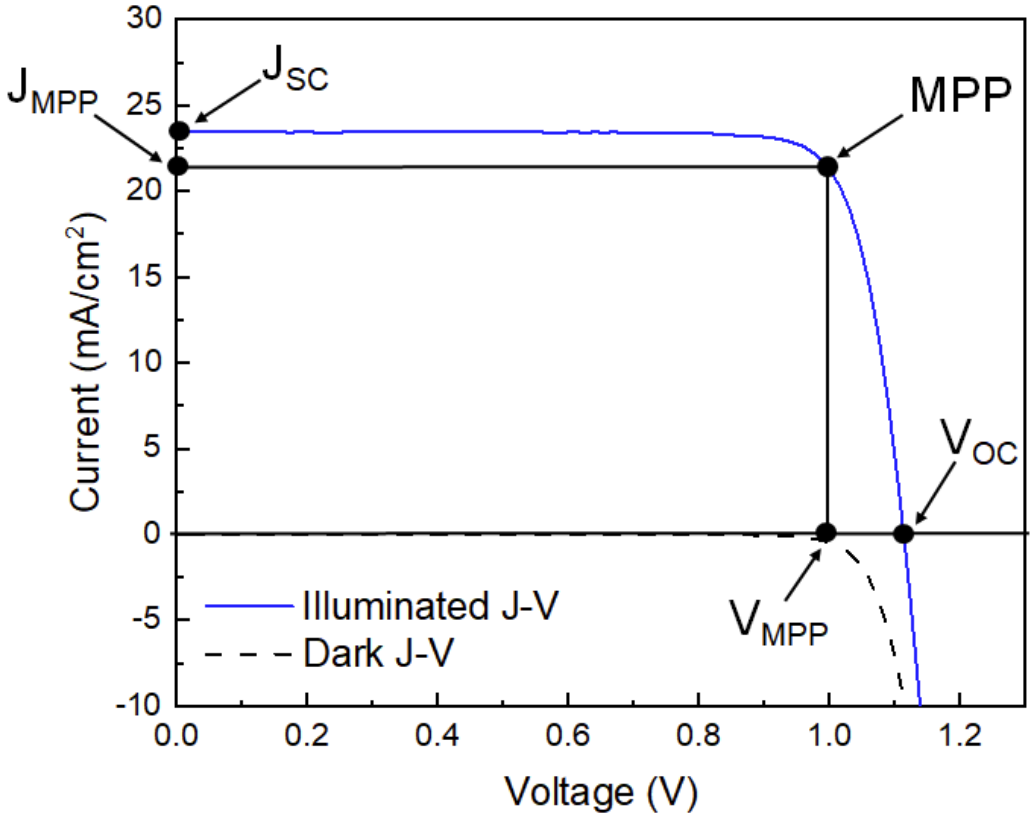

Figure 2.9. J-V curves of an illuminated solar cell and the same solar cell in the dark.

Alternatively, the MPP can be calculated by the product of the V_{OC}, J_{SC}, and fill factor. Fill factor (FF) is a performance parameter important to solar cell characterization. Fill factor is the ratio between the maximum power generated by a solar cell ("maximum power point" = $P_{MPP} = V_{MPP} * J_{MPP}$) and the product of the V_{OC} and J_{SC}.[7]

$$FF = \frac{P_{MPP}}{V_{OC} J_{SC}} \tag{2.8}$$

Fill factor is affected by shunt and series resistances.

Parasitic resistances reduce the efficiency of a solar cell by the dissipation of power in these resistance pathways. Shunt and series resistance are the two key parasitic

resistances. Shunt resistance (R_{SH}) arises from the presence of alternate current pathways in a solar cell that allow charge carriers to bypass the diode. Low shunt resistance is due to some sort of processing defect that creates non-idealities near the junction, such as pinholes in layers of the solar cell. Pinholes within layers can provide direct contact between the absorber and electrodes or between charge transport layers, providing alternate current pathways from the diode.[14] Low R_{SH} lowers solar cell performance and its effect on the J-V curve is noted from the J_{SC} to MPP points. If R_{SH} is very low, the solar cell is effectively at short circuit.

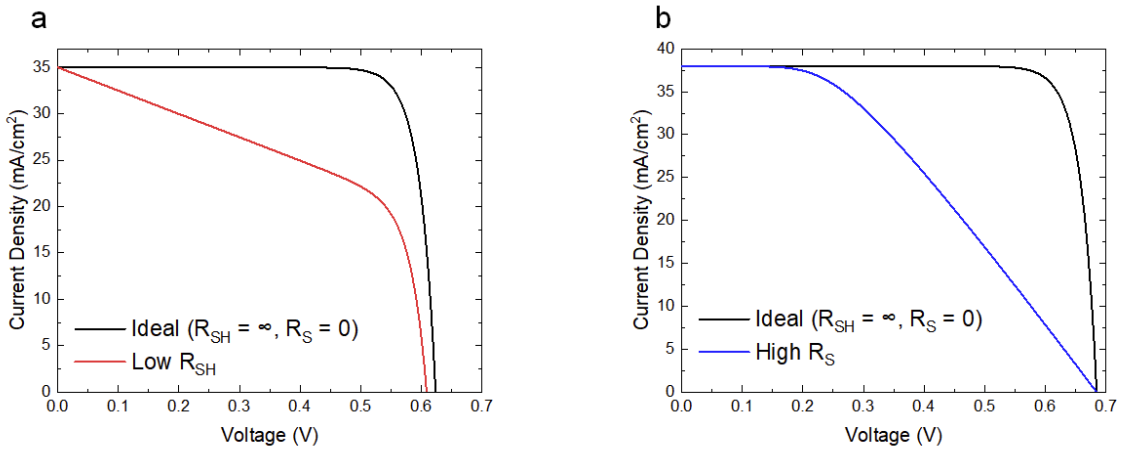

Figure 2.10. An ideal J-V curve and the effect of a) low shunt resistance (R_{SH}) and b) high series resistance (R_S).

Series resistance (R_S), by contrast, is a design parameter rather than a processing defect. R_S is the resistance charge carriers encounter while being extracted at any point in the solar cell. Contributors to series resistance include bulk resistance of the semiconductor material itself, resistance at the metallic electrode contacts and interconnections, and contact resistance between the metallic contacts and charge transport layers.[7] To account for parasitic resistance losses, the ideal diode equation for a solar cell is modified as follows:

$$J(V) = J_{SC} - J_0 \left[\exp\left(\frac{q(V+JR_S)}{nk_BT} - 1\right)\right] - \frac{V+JR_S}{R_{SH}} \qquad (2.9)$$

J is the current density of the solar cell and n is the ideality factor, a description of how well the solar cell follows the ideal diode equation depending on its recombination processes. In reality, solar cells exhibit some degree of non-ideal R_{SH} and R_S. An equivalent circuit diagram of a real solar cell with both shunt and series resistances is shown in Figure 2.11b.

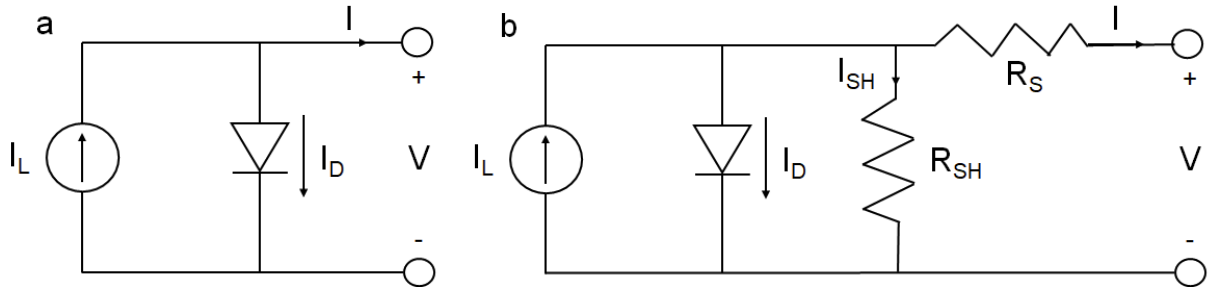

Figure 2.11. Equivalent circuit diagrams of a) an ideal solar cell and b) a real solar cell with series and shunt resistances.

I_L represents the photocurrent when the solar cell is exposed to light. In parallel and flowing in the opposite direction are the dark current (I_D) and current due to shunt resistance R_{SH} (I_{SH}). Series resistance R_S and the voltage across the terminals (V) are also shown. For an efficient solar cell, shunt resistance should be as high as possible and series resistance as low as possible. The ratio between the product of V_{OC}, J_{SC}, and FF and the incident power from sunlight (P_{in}) yields the power conversion efficiency (PCE) of the solar cell.

$$PCE = \frac{V_{OC}\, J_{SC}\, FF}{P_{in}} \qquad (2.10)$$

The PCE of a solar cell is described in terms of percent.

2.2.4 – Limits to Solar Cell Efficiency

The power conversion efficiency limits for solar cells were first calculated with the detailed balance model created by Shockley and Queisser in 1961. This maximum theoretical efficiency value for a given single junction solar cell with a given band gap is called its detailed balance limit. The detailed balance model calculated the maximum theoretical efficiency for a single junction solar cell for any semiconductor material at an ideal band gap of 1.34 eV as ~33.7%.[15] For crystalline silicon, which has a 1.12 eV band gap, the detailed balance limit was calculated as 32.7%. The Shockley and Queisser predictive model made a number of assumptions, however, that have been reconsidered by some in the field resulting in a modified predicted efficiency limit of 29.8% for 1.12 eV band gap crystalline silicon solar cells.[16]

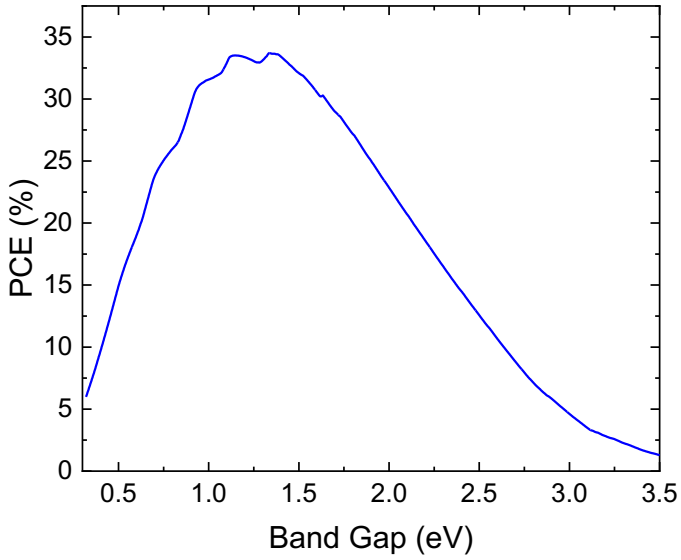

Figure 2.12. The detailed balance limit PCE per band gap energy.

Four assumptions in the Shockley and Queisser model have been reconsidered resulting in a lower predicted theoretical maximum efficiency for crystalline silicon single

junction solar cells.[15] First, all incident photons with an energy greater than that of the band gap of the solar cell are absorbed and create an electron-hole pair. In reality, there are some thermal energy losses from this situation as discussed in Section 2.2.1.a. Additionally, reflection from the surface of the solar cell as well as parasitic absorption from other layers (like a charge transport layer) must be considered even if the absorber was sufficiently thick to theoretically absorb all incident light. Second, the model assumes that all charge carriers recombine radiatively. As covered in Section 2.2.1.b, non-radiative recombination processes occur in real solar cells as a result of defects in the semiconductor bulk crystal or imperfect interfaces. Third, the model assumes that charge carriers have infinite mobilities and all are extracted to an external circuit without any losses. This does not take shunt and series resistance losses discussed in Section 2.2.3 into account. Fourth, the model assumes the incident solar spectrum is equal to a blackbody at 6000 K. While a good approximation for solar radiation outside of the Earth's atmosphere in space (the air-mass 0 spectrum), this does not hold up on the surface of the Earth because some incident photons are absorbed by gases in the atmosphere.

The standard spectrum to approximate solar radiation on the surface of the Earth at sea level is the air-mass 1.5G (AM 1.5G) spectrum. Air-mass is a measurement of how much of the Earth's atmosphere incident sunlight passes through before striking the surface of the Earth.

$$\mathrm{AM} = \frac{1}{\cos\left(\theta_S\right)} \tag{2.11}$$

At a solar zenith angle (θ_S) of 0°, sunlight travels the shortest possible path through the atmosphere to the Earth's surface. This is the AM 1 spectrum. The AM 1.5 spectrum

corresponds to a solar zenith angle of 42.8°, where sunlight travels a distance 50% longer through the Earth's atmosphere compared to the AM 1 condition. The AM 1.5G is a global spectrum that includes scattered and diffuse light and is the standard for terrestrial solar cell testing.[17] Figure 2.13 shows that the original detailed-balance method overestimates the intensity of sunlight at various wavelengths compared to the AM 1.5G spectrum.

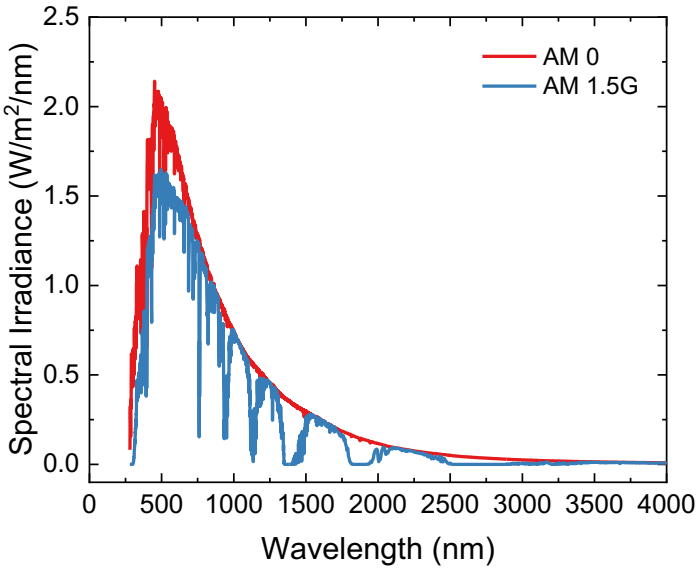

Figure 2.13. AM 0 and AM 1.5G spectra, showing that the original detailed-balance method overestimates the intensity of sunlight at various wavelengths for terrestrial solar cells using the AM 0 spectrum.

Tiedje-Yablonovitch proposed a modified version of the detailed balance model created by Shockley and Queisser. In this model, the AM 1.5G spectrum was used instead of the blackbody radiation spectrum, sub-band gap absorption was considered, and free carrier absorption and Auger recombination were considered in addition to radiative recombination. The maximum radiative recombination-limited power conversion efficiency as a function of solar cell band gap is plotted by Tiedje-Yablonovitch in Figure 2.14.

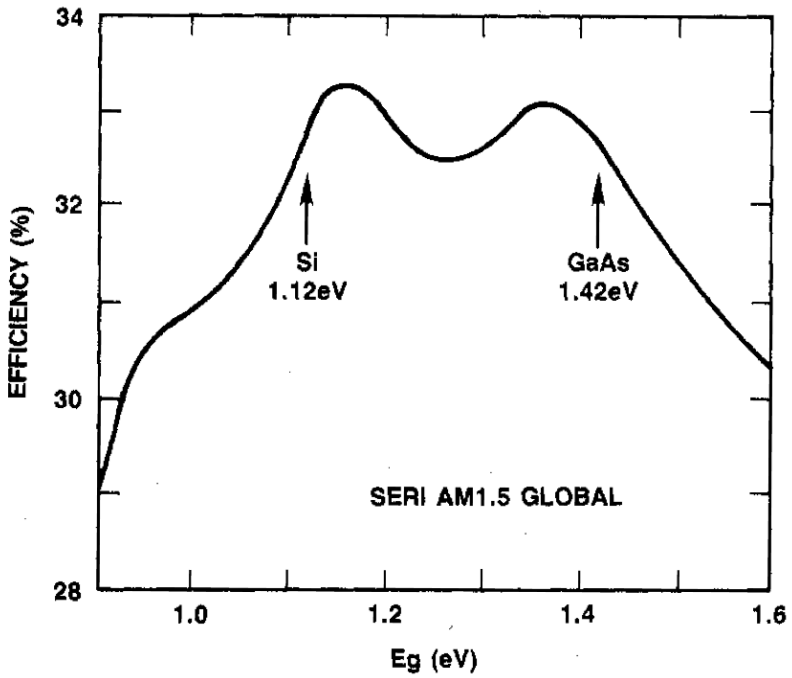

Figure 2.14. Tiedje-Yablonovitch plot of radiative recombination-limited power conversion efficiency of solar cells as a function of band gap. This plot assumes step-function optical absorption under AM 1.5G spectrum irradiation, not taking into account all modified model aspects in the final calculation of the maximum theoretical efficiency limit for crystalline silicon solar cells. Reused with permission from [15]. Copyright 1984 IEEE.

Using all aspects of this modified model, Tiedje-Yablonovitch predicted a maximum theoretical efficiency limit of 29.8% for crystalline silicon solar cells.[15]

2.3 – Perovskite Solar Cells

Perovskites are a class of semiconductor materials with the promise of multijunction tandem efficiencies above the 29.8% modified predicted maximum theoretical efficiency limit of crystalline silicon at lower cost. In practice, the highest reported efficiency for a single junction crystalline silicon solar cell is 27.3%. The champion of the all-perovskite triple junction tandem solar cells fabricated for this thesis matched this efficiency – with an identical maximum efficiency of 27.3% – as detailed in Chapter 7.

2.3.1 – Perovskite Structure and Development

Perovskites are a class of materials with stoichiometry ABX_3, first discovered as $CaTiO_3$ in the Ural Mountains and named after Russian mineralogist Lev Perovski.[18,19] Naturally occurring $(Mg,Fe)SiO_3$ perovskite is the most abundant material in the lower mantle of the Earth and makes up about 38% of the entire volume of our planet.[20] The ABX_3 stoichiometry consists of a monovalent cation A-site, a divalent cation B-site, and monovalent anion X-sites. The ionic radius of the A-site cation is larger than that of the B-site cation. The X-site anion bonds to both the A-site and B-site cations. The ideal perovskite unit cell adopts a cubic structure with the A-site cations at the corners of the cube, the B-site cation in the center of the cube, and the X-site anions surrounding the B-site cation at the face-center positions of the cube, forming an octahedron.[18]

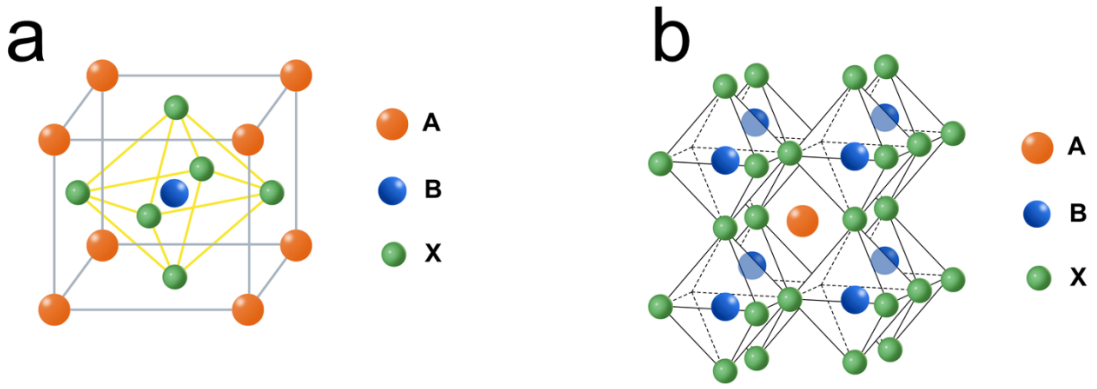

Figure 2.15. a) Unit cell of ABX_3 perovskite b) Same ABX_3 perovskite from different perspective of corner sharing BX_6 octahedra.

From a different perspective, the cubic perovskite structure consists of corner sharing BX_6 octahedra and the A-site cations positioned in cubo-octahedral sites.

While over 90,000 possible three-dimensional perovskites have been calculated to exist, hybrid metal halide perovskites are the subset of focus for photovoltaic applications.[21] Hybrid perovskites utilize both organic and inorganic components. In a hybrid metal halide perovskite, the A-site typically consists of an inorganic cesium (Cs^+), organic formamidinium (FA^+), or organic methylammonium (MA^+) monovalent cation. The B-site is a divalent cation, usually lead (Pb^{2+}) or tin (Sn^{2+}). The X-site is a monovalent halide anion, typically iodide (I^-) or bromide (Br^-).[18] The cations and halides can be (and often are) alloyed in a hybrid metal halide perovskite, such as the $FA_{0.9}Cs_{0.1}Pb(Br_{0.68}I_{0.32})_3$ absorber layer material studied in this thesis at Chapter 5.

While the first hybrid lead halide perovskites were synthesized in 1978,[22] they were not studied for photovoltaic application until 2009. Kojima et al. first used methylammonium lead triiodide ($MAPbI_3$) perovskite nanocrystals as absorbers in dye-sensitized solar cells, reaching just 3.8% PCE.[23] In 2012, a bulk $MAPbI_3$ film was fabricated in a solid-state device architecture to achieve 10.9% PCE.[24] Perovskite solar cell PCEs have improved at the fastest rate in semiconductor history, with a current single junction PCE record of 26.7%.[25] Crystalline silicon solar cells, meanwhile, have existed for 70 years with a single junction PCE record only slightly higher today at 27.3%.[26]

2.3.2 – Advantages of Perovskites

Crystalline silicon dominates the photovoltaic market, accounting for ~97% of solar cells manufactured in 2023.[27] Perovskites, however, have a number of advantages as a solar cell semiconductor material, including superior light absorption, tunable band gaps, lower formation energies, greater defect tolerance, no doping requirements, and adaptable fabrication methods.

Perovskites absorb light more effectively than crystalline silicon. Because perovskites have a direct band gap, they only need absorber layer thicknesses in the range of hundreds of nanometers for solar cells, about three orders of magnitude less than crystalline silicon. Crystalline silicon has an indirect band gap and requires a thickness in the range of hundreds of micrometers to be effective in solar cells (see Section 2.1.1). As a result, crystalline silicon requires more material to achieve light absorption equivalent to thinner perovskite absorbers. Perovskites also have higher absorption coefficients and relatively long diffusion lengths exceeding 1 μm, resulting in their excellent absorption and charge carrier extraction properties.[29]

Perovskites have a band gap with a range of 1.22-3.5 eV, providing greater maximum theoretical efficiencies than crystalline silicon by enabling different perovskites to absorb different portions of the AM 1.5G spectrum effectively.[29-31] Crystalline silicon has a fixed band gap at 1.12 eV, limiting the spectrum it can absorb.[7] The band gap of a perovskite can be easily modified within its range by altering the ABX_3 composition. By changing the composition of the A-site cation (Cs^+, FA^+, MA^+, or a mix), the B-site cation (Pb^{2+}, Sn^{2+}, or a mix), and/or the X-site halide (I^-, Br^-, Cl^-, or a mix), the perovskite band gap can be tuned from approximately 1.22-3.5 eV.

The fabrication of perovskite absorbers with different band gaps allows for the creation of a multijunction solar cell that stacks these absorbers together to effectively absorb more portions of the solar spectrum than one junction could alone. Perovskite band gap absorbers can be narrow, middle, and wide. If the band gaps are tuned appropriately, a perovskite multijunction tandem solar cell could achieve an efficiency

greater than the 33.7% detailed balance limit for a single junction solar cell of any kind of semiconductor material, as discussed in Section 2.2.4.

For this thesis, all-perovskite multijunction tandem solar cells have been fabricated using narrow, middle, and wide band gap perovskite absorbers. For the narrow band gap absorbers, mixed B-site Pb-Sn materials (typically 1:1 Pb:Sn ratio) around 1.25 eV are used. For the middle and wide band gap absorbers, neat lead mixed iodide-bromide halide perovskites ($APb(I_xBr_{1-x})_3$) that can be tuned between 1.48-2.35 eV are used.

The champion of these all-perovskite triple junction tandem solar cells achieved a maximum power point tracked efficiency of 27.3% at 1 cm^2 area, as detailed in Chapter 7.

Perovskites also have low formation energies and are far more defect tolerant than crystalline silicon. A typical hybrid metal halide perovskite can be effectively crystallized with low-temperature solution processing around 100-200°C while crystalline silicon requires processing temperatures of at least 850°C.[7,18]

Crystalline silicon must be purified from its base silicon dioxide (SiO_2 or quartz sand) input to produce a material of sufficient quality for solar cells. This is typically done with the Siemens process, in which trichlorosilane ($HSiCl_3$) gas is created upon exposure of metallurgical silicon to hydrogen chloride (HCl). The $HSiCl_3$ gas is decomposed onto rods of silicon heated at 850-1050°C, depositing silicon atoms on these rods to create purified, polycrystalline silicon.[7]

While polycrystalline silicon solar panels exist, monocrystalline silicon dominates production today. Monocrystalline silicon is created chiefly through the Czochralski process. In this process, purified polycrystalline silicon is melted in a crucible at a

temperature around 1500°C. At this point, boron impurities can be incorporated for p-doped silicon or phosphorus impurities for n-doped silicon. A seed crystal is mounted on a rotating rod and dipped into the molten silicon. The rotating rod is pulled slowly upward to meticulously form a large cylindrical column called an ingot that is used to make wafers for solar panels.[32]

Perovskite absorbers do not require the costly and energy intensive Siemens and Czochralski processes. Perovskite absorbers also do not require the expensive p-doping and n-doping that crystalline silicon needs to form a p-n junction.

Perovskite absorbers are more defect tolerant than crystalline silicon, allowing perovskites to function effectively in solar cells at crystalline quality lower than crystalline silicon. Perovskite absorbers can have a defect density one million times greater than crystalline silicon and still exhibit comparable PCE values in solar cells.[33] This defect tolerance enables perovskite absorbers to be fabricated using lower cost methods than crystalline silicon.[34]

Perovskites are more adaptable in their fabrication than crystalline silicon. While crystalline silicon wafers are produced from a solid-state, energy-intensive set of processes, perovskite absorbers can be crystallized in a variety of ways. Solutions of perovskite inks can be easily made by dissolving inexpensive precursor powders in solvents. The fact that the perovskite precursor can exist in solution form opens the door for a variety of low-cost industrial fabrication techniques. These include dip coating, bar coating, inkjet printing, or slot-die coating for sheet-to-sheet or roll-to-roll processing.[35] Perovskite precursors can also be thermally evaporated, although the record research-scale perovskite solar cells are solution-processed.[25]

Overall, these advantages provide the potential for perovskite solar cells to be fabricated at substantially lower cost with shorter energy payback times than crystalline silicon. Energy payback time (EPT) is the amount of time a solar panel must operate to produce the same amount of energy that was needed to make it. Standard crystalline silicon panels have an EPT of 1.52 years and a greenhouse gas emission factor (GHGEF) of 24.6 g CO_2-eq/kWh for their production. Perovskite-based tandem panels have been simulated to exhibit a decreased EPT. Double junction perovskite-perovskite tandem panels have an estimated EPT of just 0.35 years – less than 25% of crystalline silicon – and a GHGEF of just 10.69 CO_2-eq/kWh. While perovskite-on-silicon double junction tandem panels also offer the promise of high efficiency, they only have a slightly lower estimated EPT of 1.44 years and nearly doubled GHGEF of 46.38 CO_2-eq/kWh compared to crystalline silicon.[36] EPT and GHGEF can be lowered even more for all-perovskite tandem panels if processed on flexible substrates instead of rigid glass.

A 2021 National Renewable Energy Laboratory (NREL) report found that all-perovskite tandem solar cells can achieve the lowest module minimum sustainable prices (MSPs) of existing solar cell technologies studied. NREL defined MSP as a 15% gross margin. NREL estimated that developing a double junction perovskite tandem module at 30% efficiency could drop MSP to as low as $0.18/W at larger scale production. Crystalline silicon had an MSP of $0.25-0.27/W, as much as 50% higher.[37]

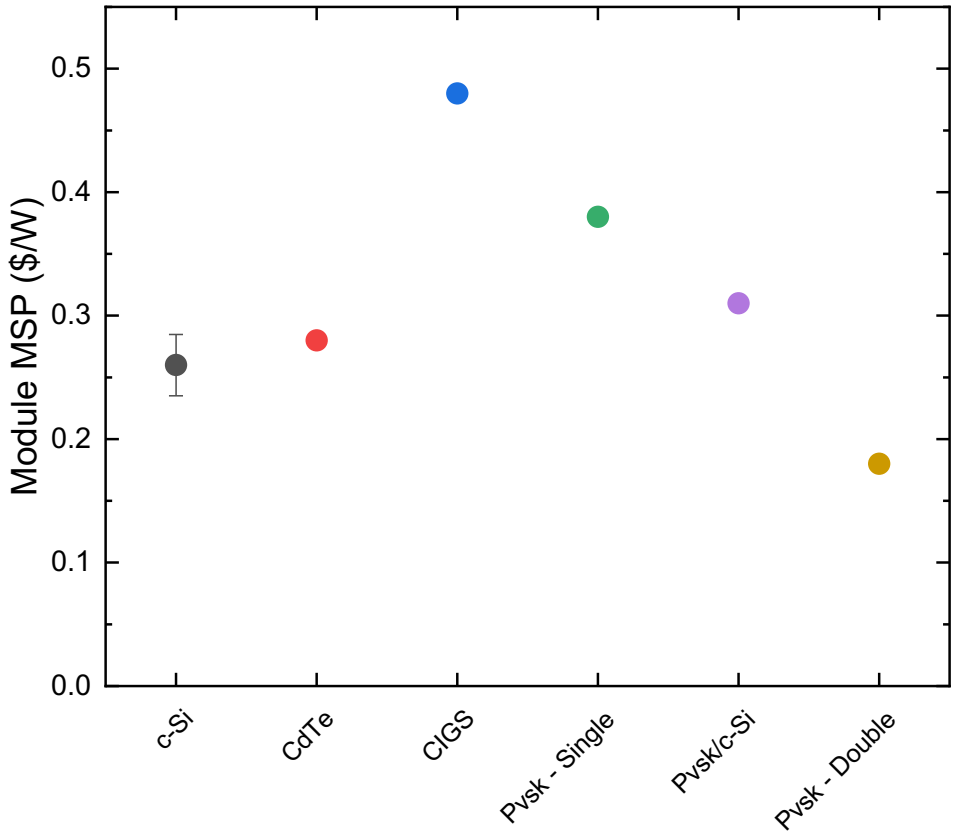

Figure 2.16. Module MSP in United States Dollars per Watt-peak: $0.25-0.27/W for crystalline silicon (c-Si, 20.5% module efficiency), $0.28/W for cadmium telluride (CdTe, 18% module efficiency), $0.48/W for copper indium gallium selenide (CIGS, 16% module efficiency), $0.38/W for perovskite single junction (Pvsk – Single), $0.31/W for perovskite-on-silicon tandem (Pvsk/c-Si) and $0.18/W for perovskite double junction tandem (Pvsk-Double).

NREL calculated the MSP for a single junction sheet-to-sheet perovskite module to be $0.38/W at 16% efficiency at small scale production. NREL also determined a number of module MSPs for perovskite multijunction tandem technologies. NREL approximated a module MSP of $0.31/W for perovskite-on-silicon tandem modules in early production based on pilot results. As noted, double junction perovskite tandem modules were found to have the lowest potential module MSP of $0.18/W.[37]

Although not among the NREL technologies studied and not part of the NREL report, because all-perovskite triple junction tandem solar cells have higher theoretical efficiencies than all-perovskite double junction tandem solar cells, all-perovskite triple junction tandem solar cells have the potential for even lower module MSP.

2.3.3 – Challenges for Perovskites: Stability, Efficiency, Scalability

For perovskites to deliver on the promise of more efficient and cost-effective commercial solar cells, stability, efficiency, and scalability must improve.

2.3.3.a – Stability

Perovskite solar cells are less stable than crystalline silicon, at present. While the industry standard limited power warranty for a crystalline silicon module is 25 years, high efficiency perovskite solar cells offer a usable lifetime on the order of weeks, months, or at most a few years.[38]

Perovskite absorbers can be degraded by moisture, oxygen, heat, and light. Moisture from humidity in air can act as a catalyst for degradation processes of perovskite material, such as methylammonium lead triiodide ($MAPbI_3$ or $CH_3NH_3PbI_3$):

$$CH_3NH_3PbI_3\ (s) \Leftrightarrow PbI_2\ (s) + CH_3NH_3I\ (aq) \qquad (2.12)$$

While initially reversible, the creation of enough PbI_2 to phase segregate at grain boundaries of hydrate crystals may cause the perovskite degradation process to become irreversible.[39]

Oxygen in the air can cause photoexcited electrons in the perovskite absorber to be oxidized, creating the superoxide O_2^-. This superoxide may deprotonate organic A-site cations to form water and volatile methylamine gas, irreversibly degrading the perovskite.[40,41] Narrow band gap lead-tin perovskite absorbers that utilize the Sn^{2+} cation

for the B-site are very unstable in the presence of oxygen, rapidly oxidizing to Sn^{4+}. The Sn^{4+} is undesirable because it causes the Pb-Sn perovskite to become heavily p-doped and reduce the diffusion lengths of electron carriers, dramatically lowering solar cell performance.[31]

Perovskite absorbers also can be unstable under heat. Because perovskites such as $MAPbI_3$ often have low formation energies, endothermic transitions back to constituent components can be driven at relatively low temperatures like 85°C, degrading the perovskite absorber.[42]

Light also can affect perovskite absorbers, inducing a phenomenon called halide segregation in mixed halide perovskites, in which narrower band gap iodide-rich domains form in the absorber. While halide segregation is reversible in the dark and not considered a long-term stability issue, the iodide-rich domains can potentially act as trap sites that reduce open-circuit voltage in perovskite solar cells during their operation under light.[43] The combined presence of light and oxygen also can lead to the photooxidation of iodide ions and resultant degradation of the perovskite absorber.[44] The combination of heat and light is a particularly harsh stressor for perovskite solar cells, as discussed in Chapter 4.

The hole transport layer, electron transport layer, and electrode layer also are susceptible to degradation pathways in perovskite solar cells. Organic molecules for hole transport layers can require unstable dopants. Electron transport layers can degrade under ultraviolet light. Metallic top contact electrodes like silver (as is commonly used in commercial crystalline silicon solar panels today) can react with chemical species that escape from the perovskite absorber or diffuse themselves into the device stack below, creating shunt pathways that harm perovskite solar cell performance and stability.[45]

2.3.3.b – Efficiency

Fabricating all-perovskite tandem solar cells of 30% or higher efficiency is required to exceed the 29.8% modified practical limit of crystalline silicon. While all-perovskite triple junction tandem solar cells offer a potential efficiency estimated as high as 36.6%,[46] the highest published result – prior to this thesis – is 25.1%.[47]

As detailed in Chapter 7, the champion all-perovskite triple junction tandem solar cell fabricated for this thesis achieved 27.3% maximum power point tracked efficiency at 1 cm^2 area. This 27.3% efficiency is the highest of any known all-perovskite triple junction tandem solar cell published to date and identical to the highest reported efficiency of 27.3% for a single junction crystalline silicon solar cell.

Higher efficiencies from all-perovskite triple junction tandem solar cells are needed and potentially possible. Continuous, high voltage output from ~2 eV wide band gap absorber top subcells and quality recombination layers for monolithic, 2-terminal architectures are some of the challenges that must be addressed to achieve higher efficiencies for all-perovskite triple junction tandem solar cells, as discussed in Chapters 5, 6, and 7.

2.3.3.c – Scalability

Fabricating perovskite solar cells at scale is a challenge that must be met to achieve widespread adoption similar to crystalline silicon. Perovskites are more adaptable in their fabrication than crystalline silicon and industrial scale fabrication is developing.

Promisingly, perovskite precursors can exist in solution form allowing a variety of low-cost industrially scalable fabrication techniques. These include slot-die coating for roll-to-roll processing, dip coating, bar coating, and inkjet printing.[35]

In 2023, Beynon et al. created the first perovskite solar cell under ambient conditions in an open space, pioneering the possibility of low-cost production.[48] These single junction perovskite solar cells were made in a fully roll-to-roll printable device architecture, including a top electrode produced from carbon ink, using slot-die coating that produced 20 meter long flexible substrates.

The layers printed on 20 meter long flexible substrates were diced into smaller segments, achieving a champion 10.8% stabilized PCE at 0.15 cm^2 active area. Weerasinghe et al. further advanced development with the fabrication of entirely roll-to-roll perovskite large-area modules through serially connected individual cells, achieving 11% PCE at 49.5 cm^2 active area.[49]

The development of low-cost, high-throughput roll-to-roll perovskite processing is a promising pathway to scalable fabrication and widespread adoption of perovskite solar cells, yet efficiencies must continue to improve.

Chapter 2 References

1. Housecroft, C. E. and Constable, E. C. *An Introduction to Organic, Inorganic and Physical Chemistry*. Pearson Education Ltd. 2010.

2. Purdue University. *Quantum Numbers and Electron Configurations*. 2020, chemed.chem.purdue.edu/genchem/topicreview/bp/ch6/quantum.html.

3. Landskron, K. "3.1: Introduction into Molecular Orbital Theory." *Chemistry LibreTexts*, 20 Aug. 2020, chem.libretexts.org/Bookshelves/Inorganic_Chemistry/Inorganic_Coordination_Chemistry_(Landskron)/03%3A_Molecular_Orbitals/3.01%3A_Formation_of_Molecular_Orbitals_From_Atomic_Orbitals.

4. Atkins, P., de Paula, J. and Keeler, J. *Atkin's Physical Chemistry*. Oxford University Press. 2018.

5. Nelson, J. *The Physics of Solar Cells*. Imperial College Press. 2013.

6. ScienceDirect. "HOMO/LUMO Gap - an Overview | ScienceDirect Topics." 2023, www.sciencedirect.com/topics/chemistry/homo-lumo-gap.

7. Smets, A., Jager, K., Isabella, O., Van Swaaij, R., and Zeman, M. *Solar Energy*. Bloomsbury Publishing, 2016.

8. University of Cambridge. "DoITPoMS - TLP Library Introduction to Semiconductors – Direct and Indirect Band Gap Semiconductors." 2018, www.doitpoms.ac.uk/tlplib/semiconductors/direct.php.

9. Gandham, B., Hill, R., Macleod, H.A., and Bowden, M. "Antireflection Coatings on Solar Cells." *Solar Cells*, **1**, no. 1, pp. 3–22, (1979).

10. de Mello, J. C., Wittmann, H. F. and Friend, R. H. An improved experimental determination of external photoluminescence quantum efficiency. *Advanced Materials*, **9**, 230–232 (1997).

11. Luo, D. et al. Minimizing non-radiative recombination losses in perovskite solar cells. *Nat. Rev. Mater.* **5**, 44–60 (2020).

12. Lin, Q. et al. Hybrid Perovskites; Prospects for Concentrator Solar Cells. *Adv. Sci.* **5**, 1700792 (2018).

13. Stolterfoht, M. et al. The Impact of Energy Alignment and Interfacial Recombination on the Internal and External Open-Circuit Voltage of Perovskite Solar Cells. *Energy & Environmental Science*, **12**, 9, 2778–88 (2019).

14. Kaienburg, P. et al. How Contact Layers Control Shunting Losses from Pinholes in Thin-Film Solar Cells. *J. Phys. Chem. C* **122**, 48, 27263-27272 (2018).

15. Shockley, W. and Queisser, H.J. Detailed Balance Limit of Efficiency of pn Junction Solar Cells. *J. Appl. Phys.* **32**, 510 (1961).

16. Tiedje, T., Yablonovitch, E., Cody, G. D. and Brooks, B. G. Limiting efficiency of silicon solar cells*. IEEE Trans. Electron Devices* **31**, 711–716 (1984).

17. National Renewable Energy Laboratory. *Reference Air Mass 1.5 Spectra*. www.nrel.gov/grid/solar-resource/spectra-am1.5.html.

18. Manser, J. S., Christians, J. A., and Kamat, P. V. Intriguing Optoelectronic Properties of Metal Halide Perovskites. *Chem. Rev.* **116**, 12956–13008 (2016).

19. Miyasaka, T. *Perovskite Photovoltaics and Optoelectronics: From Fundamentals to Advanced Applications*. WILEY-VCH. 2021.

20. Sharp, T. Bridgmanite – named at last. *Science*. **346**, 6213 (2014).

21. Filip, M.R. and Giustino, F. The geometric blueprint of perovskites. *Proceedings of the National Academy of Sciences*, **115**, 5397–5402 (2018).

22. Weber, D. CH3NH3PbX3, ein Pb(II)-System mit kubischer Perowskitstruktur CH3NH3PbX3, a Pb(II)-System with Cubic Perovskite Structure. Zeitschrift für Naturforschung B **33**, 1443–1445, (1978).

23. Kojima, A., Teshima, K., Shirai, Y. and Miyasaka, T. Organometal Halide Perovskites as Visible-Light Sensitizers for Photovoltaic Cells. *J. Am. Chem. Soc.*, **131**, 6050–6051 (2009).

24. M. M. Lee, et al. Efficient hybrid solar cells based on meso-superstructured organometal halide perovskites. *Science*, **338**, 643–647 (2012).

25. Green, M.A. et al. Solar cell efficiency tables (Version 64). *Prog Photovolt Res Appl*. **32**, 425-441 (2024).

26. Bellini, E. *Longi Announces 27.30% Efficiency for Heterojunction Back Contact Solar Cell*. PV Magazine International, 8 May 2024, www.pvmagazine.com/2024/05/08/longi-announces-27-30-efficiency-for-heterojunction-back-contact-solar-cell/.

27. Fraunhofer Institute for Solar Energy Systems. “Photovoltaics Report.” 29 July 2024.

28. Stranks, S. D. et al. Electron-Hole Diffusion Lengths Exceeding 1 Micrometer in an Organometal Trihalide Perovskite Absorber. *Science* **342**, 341–344 (2013).

29. Noh, J. H. et al. Chemical Management for Colorful, Efficient, and Stable Inorganic–Organic Hybrid Nanostructured Solar Cells. *Nano Lett.* **13**, 1764–1769 (2013).

30. Eperon, G. E. et al. Formamidinium lead trihalide: a broadly tunable perovskite for efficient planar heterojunction solar cells. *Energy Environ. Sci.* **7**, 982–988 (2014).

31. Noel, N. K. et al. Lead-free organic–inorganic tin halide perovskites for photovoltaic applications. *Energy & Environmental Science* **7**, 3061–3068 (2014).

32. Warden, G. et al. Recent developments on manufacturing and characterization of fused quartz crucibles for monocrystalline silicon for photovoltaic applications. *Open Ceramics*, **13**, 100321 (2023).

33. Che, Q. et al. Controllable Self-Induced Passivation of Hybrid Lead Iodide Perovskites toward High Performance Solar Cells. *Nano Letters*, **14**, 7, 4158-4163 (2014).

34. Afre, R. and Pugliese, D. Perovskite Solar Cells: A Review of the Latest Advances in Materials, Fabrication Techniques, and Stability Enhancement Strategies. *Micromachines*, **15**, 192 (2024).

35. Ibn-Mohammed, T. et al. Perovskite solar cells: An integrated hybrid lifecycle assessment and review in comparison with other photovoltaic technologies. *Renewable and Sustainable Energy Reviews* **80**, 1321–1344 (2017).

36. Tian, X. et al. Life cycle energy use and environmental implications of high-performance perovskite tandem solar cells. *Science Advances*, **6**, 31, eabb0055 (2020).

37. Smith, B. et al. *Photovoltaic (PV) Module Technologies: 2020 Benchmark Costs and Technology Evolution Framework Results.* National Renewable Energy Laboratory (2021).

38. Meng, L., You, J., and Yang, Y. Addressing the stability issue of perovskite solar cells for commercial applications. *Nature Communications*, **9**, 5265 (20188).

39. Leguy, M. A. et al. Reversible hydration of CH3NH3PbI3 in films, single crystals, and solar cells. *Chemistry of Materials*, **27**, 9, 3397–3407, (2015).

40. Senocrate, A. et al. Interaction of oxygen with halide perovskites. *Journal of Materials Chemistry A*, 6, 23, 10847–10855 (2018).

41. Aristidou, N. et al. The role of oxygen in the degradation of methylammonium lead trihalide perovskite photoactive layers. *Angewandte Chemie International Edition*, **54**, 28, 8208–8212 (2015).

42. Kim, N. et al. Investigation of Thermally Induced Degradation in $CH_3NH_3PbI_3$ Perovskite Solar Cells using *In-situ* Synchrotron Radiation Analysis. *Scientific Reports*, **7**, 4645 (2017).

43. Brennan, M. C., et al. Light-induced anion phase segregation in mixed halide perovskites. *ACS Energy Letters*, **3**, 1, 204–213 (2017).

44. Aristidou, N. et al. Fast oxygen diffusion and iodide defects mediate oxygen-induced degradation of perovskite solar cells. *Nature Communications*, **8**, 15218 (2017).

45. Svanstrom, S. et al. Degradation Mechanism of Silver Metal Deposited on Lead Halide Perovskites. *ACS Appl. Mater. Interfaces*, **12**, 6, 7212-7221 (2020).

46. Höranter, M. et al. The Potential of Multijunction Perovskite Solar Cells. *ACS Energy Lett*., **2**, 10, 2506-2513 (2017).

47. Wang, J. et al. Halide homogenization for low energy loss in 2-eV-bandgap perovskites and increased efficiency in all-perovskite triple-junction solar cells. *Nature Energy*, **9**, 70-80 (2023).

48. Beynon, D., Parvazian, E., Hooper, K., McGettrick, J., Patidar, R., Dunlop, T., Wei, Z., Davies, P., Garcia-Rodriguez, R., Carnie, M., Davies, M., and Watson, T. All-Printed Roll-to-Roll Perovskite Photovoltaics Enabled by Solution-Processed Carbon Electrode. *Adv. Mater.* **35**, 2208561 (2023).

49. Weerasinghe, H. et al. The first demonstration of entirely roll-to-roll fabricated perovskite solar cell modules under ambient room conditions. *Nature Communications*, **15**, 1656 (2024).

Chapter 3

Experimental Methods

This chapter describes the materials and methods used to fabricate and characterize the perovskite thin films and solar cells detailed in this thesis. For this thesis, all-perovskite triple junction tandem solar cells were fabricated using: 1) a novel crystallization method for the 1.97 eV wide band gap absorber layer involving dimethylammonium bromide and dimethylammonium iodide (DMAX) and 2) a unique device stack incorporating an ICBA electron transport layer and IZO recombination layers with the 1.97 eV band gap absorber.

3.1 – Perovskite Thin Film and Solar Cell Fabrication

3.1.1 – Substrate Preparation

Bare glass, indium doped tin oxide (ITO), and fluorine doped tin oxide (FTO) substrates were all cleaned and prepared according to the same method. ITO (30 x 30 m, 10 ohm/sq, Latech) and FTO (30 x 30 mm, 15 ohm/sq, Latech) substrates were pre-etched. Substrates were cleaned using the following method: 15 minutes sonication in DECON-90 solution (1% volume in deionized water), followed by scrubbing of substrates with soap and deionized water, further 10 minutes sonication in DECON-90 solution, 10 minutes sonication in deionized water, 10 minutes sonication in acetone, and 10 minutes sonication in IPA. The substrates were dried with nitrogen and UV ozone treated for 30 minutes directly before use.

3.1.2 – Perovskite Precursor Solution Preparation

3.1.2.a – Materials

Lead iodide (PbI_2, perovskite grade, 99.99% trace metals basis) was purchased from Tokyo Chemical Industries Ltd. Lead bromide ($PbBr_2$, 98+%) was purchased from ThermoScientific. Cesium iodide (CsI, 99.9% trace metals basis) was purchased from Alfa-Aesar. Formamidinium bromide (FABr, >99.99%), benzylammonium thiocyanate (BzSCN), dimethylammonium bromide (DMABr), and dimethylammonium iodide (DMAI) were purchased from Greatcell Solar Materials. Ethanol (anhydrous 99.997%) was purchased from VWR. Ethylenediammonium dibromide ($EDABr_2$, 98%) and ethylenediammonium diiodide ($EDAI_2$, 98%) were purchased from Sigma-Aldrich. N,N-Dimethylformamide (DMF, anhydrous 99.8%), dimethyl sulfoxide (DMSO, anhydrous >99.9%), methyl acetate (anhydrous 99.5%), anisole (anhydrous 99.7%), toluene (anhydrous 99.8%), ethyl acetate (anhydrous 99.8%), chlorobenzene (anhydrous 99.8%), and 2-propanol (IPA, anhydrous 99.5%) solvents were purchased from Sigma-Aldrich.

3.1.2.b – $FA_{0.8}Cs_{0.2}PbI_3$ – 1.55 eV Middle Band Gap Absorber

The $FA_{0.8}Cs_{0.2}PbI_3$ perovskite precursor solution was prepared at 1.4 M concentration containing 192.6 mg FAI, 72.2 mg CsI, and 651.9 mg PbI_2 (1 mol% excess PbI_2 unless otherwise stated) per 1 mL of 3:1 DMF:DMSO. Benzylammonium thiocyanate was added to the bulk perovskite at a concentration of 0.2 mol% excess relative to the 1.4 M concentration of the perovskite. The perovskite precursor solution was then stirred overnight. Before use, the solution was filtered with a 0.22 μm PTFE filter.

3.1.2.c – $FA_{0.9}Cs_{0.1}Pb(Br_{0.68}I_{0.32})_3$ – 1.97 eV Wide Band Gap Absorber

The $FA_{0.9}Cs_{0.1}Pb(Br_{0.68}I_{0.32})_3$ perovskite precursor solution was prepared at 1.0 M concentration (or 0.9 M for optimal concentration as the top subcell absorber for all-perovskite triple junction tandems) containing 26.0 mg CsI, 112.5 mg FABr, 209.2 mg $PbBr_2$, and 198.2 PbI_2 per 1 mL of solvent. For the DMF/DMAX solvent system, 30 mol% excess – relative to the perovskite precursor concentration – of DMAX (where "DMAX" = 68% DMABr + 32% DMAI by molar mass; 25.7 mg DMABr and 16.6 mg DMAI per 1 mL DMF) was added to the bulk perovskite and the entire solution was dissolved in neat DMF solvent. The DMF/DMAX perovskite precursor solution was stirred for 1 hour and then filtered with a 0.22 μm PTFE filter before use. For the DMF/DMSO solvent system, the perovskite precursor solution was dissolved in 4:1 DMF:DMSO volume ratio solvent, stirred overnight, and filtered with a 0.22 μm PTFE filter before use.

3.1.2.d – $FA_{0.9}Cs_{0.1}Pb(Br_{0.15}I_{0.85})_3$ – 1.61 eV Middle Band Gap Absorber

1.5 M perovskite precursor solution was prepared by mixing CsI, FAI, $PbBr_2$, and PbI_2 subject to the stochiometric ratio in 4:1 DMF:DMSO volume ratio solvent, stirred overnight, and filtered with a 0.22 μm PTFE filter before use.

3.1.2.e – $FA_{0.6}MA_{0.3}Cs_{0.1}Pb_{0.5}Sn_{0.5}I_3$ – 1.25 eV Narrow Band Gap Absorber

The $FA_{0.6}MA_{0.3}Cs_{0.1}Pb_{0.5}Sn_{0.5}I_3$ perovskite precursor solution was prepared by mixing CsI (48.06 mg, 0.185 mmol), FAI (190.89 mg, 1.11 mmol), MAI (88.23 mg, 0.555 mmol), SnI_2 (334.58 mg, 0.925 mmol), PbI_2 (426.43 mg, 0.925 mmol), SnF_2 (14.50 mg, 0.0925 mmol), and NH_4SCN (2.82 mg, 0.037 mmol) in a solvent mixture of 0.25 mL DMSO and 0.75 mL DMF to reach a concentration of 1.85 M. 2.5 mol% of glycine hydrochloride was added as additive according to the procedure developed by Hu et al.[1]

0.5 mg/mL Sn(0) powder was added to the perovskite precursor solution to scavenge the potential Sn(IV) introduced by oxidation of Sn(II).[2] The precursor solutions were stirred at 45°C for about 40 minutes and filtered through a 0.22 μm PTFE filter before use.

3.1.3 – Charge Transport and Surface Passivation Layer Solution Preparation

3.1.3.a – Charge Transport Layers

[4-(3,6-dimethyl-9*H*-carbazol-9-yl)butyl]phosphonic acid (Me-4PACz, >99.0%) was purchased from Tokyo Chemical Industries Ltd. Me-4PACz solution was prepared as a 1 mg/mL stock in anhydrous ethanol and stirred overnight. This stock solution was then diluted to 0.33 mg/mL before use.

Poly(4-butylphenyl-diphenyl-amine) (Poly-TPD, 99+% trace metal analysis) was purchased from 1-Material Inc. 1 mg/mL Poly-TPD solution was prepared in toluene, stirred at 80°C overnight, and filtered with a 0.22 μm PTFE filter before use.

Nickel oxide nanoparticles (NiO_X) were purchased from Avantama and diluted in 1:10 ethanol, v:v.

MPA-CPA ((2-(4-(bis(4-methoxyphenyl)amino)phenyl)-1-cyanovinyl)phosphonic acid was purchased from Dyenamo. 1 mg/mL MPA-CPA solution was prepared in ethanol.

Aluminum oxide (Al_2O_3, nanoparticles, <50 nm particle size (DLS), 20 weight % in 2-propanol) was purchased from Sigma-Aldrich. For use as a wetting layer, diluted Al_2O_3 nanoparticle solution was prepared by adding 50 μL Al_2O_3 nanoparticles solution to 7.5 mL IPA to give a 1:150 volume ratio solution.

[6,6]-phenyl-C_{61}-butyric acid methyl ester (PCBM) was purchased from Solenne. PCBM solution was prepared 20 mg/mL in chlorobenzene, stirred overnight, and filtered with 0.22 μm PTFE filter before use.

1′,1″,4′,4″-Tetrahydro-di[1,4]methanonaphthaleno[1,2:2′,3′,56,60:2″,3″] [5,6]fullerene-C_{60} (ICBA, 99%, HPLC) was purchased from Sigma-Aldrich. ICBA solution was prepared at 5 mg/mL concentration in neat chlorobenzene, stirred overnight, filtered with 0.22 μm PTFE filter, and diluted to 1 mg/mL concentration before use.

Bathocuproine (BCP, 98%) was purchased from Alfa-Aesar. BCP solution was prepared 0.5 mg/mL in IPA, stirred at 75°C overnight, and filtered with 0.22 μm PTFE filter before use.

3.1.3.b – Surface Passivation Layers

$EDAI_2$ surface passivation stock solution was prepared at a concentration of 1 mol% (relative to the 1.4 M $FA_{0.8}Cs_{0.2}PbI_3$ perovskite precursor solution) or 14 mM in IPA, stirred overnight, and filtered with a 0.22 μm PTFE filter before use. For the stability optimized 0.5 mol% (7 mM) concentration, the filtered 1 mol% (14 mM) $EDAI_2$ stock solution was diluted 1:1 in IPA.

EDAX surface passivation (where “EDAX” = 68% $EDABr_2$ + 32% $EDAI_2$ by molar mass) stock solution was prepared at a concentration of 0.5 mg/mL in 1:1 toluene:IPA volume ratio solvent, stirred at 70°C for 2-3 hours, and filtered after cooling with a 0.22 μm PTFE filter before use.

3.1.4 – Perovskite Layer Depositions For Both Thin Films and Solar Cells

3.1.4.a – $FA_{0.8}Cs_{0.2}PbI_3$ – 1.55 eV Middle Band Gap Absorber

The perovskite precursor solution was spin-coated in a nitrogen-filled glovebox at 1000 rpm (250 rpm/s ramp) for 10s, followed by 5000 rpm (1000 rpm/s ramp) for 35s, with 300 µL of the solution dynamically spin-coated 5s into the program. 150 µL of anisole was dropped as an antisolvent 20s before the end of the program. Films were then annealed at 130°C for 20 minutes.

3.1.4.b – $FA_{0.9}Cs_{0.1}Pb(Br_{0.68}I_{0.32})_3$ – 1.97 eV Middle Band Gap Absorber

For the DMF/DMAX crystallization method, 250 µL of the perovskite precursor solution was statically deposited on the substrate and then spin-coated at 6000 rpm (2000 rpm/s ramp) for 45s in a nitrogen-filled glovebox. 325 µL of methyl acetate was dropped as an antisolvent 5s after the start of the program. Films were then first annealed at 100°C for 5 minutes in the nitrogen-filled glovebox designed to remove the DMF solvent. At this point, the perovskite films remained in a yellow-ish polytype intermediate phase. Upon cooling, the films were transferred to a preheated hot plate inside a compressed air-filled drybox set at ~20% relative humidity and annealed at 160°C for 10 minutes to allow full crystallization to the cubic 3C phase.

For the DMF/DMSO crystallization method, 250 µL of the perovskite precursor solution was statically deposited on the substrate and then spin-coated at 6000 rpm (2000 rpm/s ramp) for 35s in a nitrogen-filled glovebox. 325 µL of ethyl acetate was dropped as an antisolvent 10s after the start of the program. The films were then annealed at 110°C for 30 minutes.

3.1.4.c – $FA_{0.9}Cs_{0.1}Pb(Br_{0.15}I_{0.85})_3$ – 1.61 eV Middle Band Gap Absorber

200 µL of the perovskite precursor was spin-coated at 1000 rpm for 10 s (500 rpm/s ramp) and 5000 rpm for 30 s (2500 rpm/s ramp). 150 µL anisole was dropped on the film 5 seconds before the end of the spinning program. The film was immediately annealed at 100 °C for 10 min. For the interfacial passivation layer, a solution, with 0.5 mg $EDAI_2$ and 1 mg PEAI added to 1 mL IPA, was spin-coated onto the as-prepared perovskite films and followed up with 5 min thermal annealing under 100 °C.

3.1.4.d – $FA_{0.6}MA_{0.3}Cs_{0.1}Pb_{0.5}Sn_{0.5}I_3$ – 1.25 eV Narrow Band Gap Absorber

200 µL of the room temperature precursor solution was applied to the substrate. A two-step spin coating program was used. The substrate was spin-coated at 1000 rpm for 10 s (200 rpm/s ramp) and 4000 rpm for 40 s (1000 rpm/s ramp). 500 µL of chlorobenzene was quickly dripped onto the surface of the spinning substrate 20 seconds before the end of the procedure. The substrate was then immediately annealed on a 100°C hot plate for 10 minutes, followed by annealing at 65 °C for over 10 minutes to avoid glovebox vapor ingress of the as-prepared films, then the films were cooled down to room temperature for the following processes. The post-treatment was done by dripping PPCPTA (piperazine and C60 pyrrolidine tris-acid) solution dynamically while spinning the as-prepared perovskite films.[3] The substrate was spin-coated at 4000 rpm for 20 s (1333 rpm/s ramp). Following spin-coating, the films were immediately annealed again at 100°C for about 5 minutes. The samples were then moved under a nitrogen atmosphere to a vacuum deposition chamber for ETL deposition.

3.1.5 – Hole Transport Layer Deposition

3.1.5.a – Poly-TPD

200 μL of 1 mg/mL Poly-TPD was dynamically spin-coated onto the substrates at 2000 rpm (2000 rpm/s ramp) for 20s under ambient atmosphere. Subsequently, the substrates were annealed on a hot plate at 130°C for 10 minutes.

3.1.5.b – Me-4PACz

In a nitrogen-filled glovebox, 250 μL of 0.33 mg/mL Me-4PACz SAM solution was statically deposited onto the substrate, and after 5s spun at 3000 rpm (600 rpm/s ramp) for 30s. The substrates were then annealed at 100°C for 10 minutes.

3.1.5.c – NiOx

NiO_X (diluted in 1:10 ethanol, v:v, Avantama) was spin-coated at 3000 rpm for 30s (1000 rpm/s ramp) under ambient atmosphere without any post-treatment. 1 mg/mL MPA-CPA was spin-coated inside a nitrogen-filled glovebox at 3000 rpm for 30s (1000 rpm/s ramp) and the substrates were annealed at 100°C for about 10 minutes.

3.1.5.d – Al_2O_3 Nanoparticles Wetting Layer

Because the hole transport layer surface has a strongly hydrophobic nature, a Al_2O_3 nanoparticles solution was deposited as a wetting layer for perovskite solution deposition thereafter. Upon cooling of the Me-4PACz or Poly-TPD HTL, 500 μL of Al_2O_3 nanoparticles solution (1:150 dilution in IPA) was statically deposited in a nitrogen-filled glovebox and then spun at 5000 rpm (5000 rpm/s ramp) for 20s, followed by a 2 minute anneal at 100°C.

3.1.6 – Electron Transport Layer Deposition

3.1.6.a – PCBM

For solution-processed electron transport layers, 100 µL of PCBM was statically spin-coated in a nitrogen-filled glovebox at 2000 rpm (200 rpm/s ramp) for 30s and then annealed at 100°C for 4-5 minutes.

3.1.6.b – BCP

For the solution-processed method, after PCBM films were spun and cooled, BCP was dynamically spin-coated in a nitrogen-filled glovebox at 5000 rpm (5000 rpm/s ramp) for 20s and annealed at 100°C for 1 minute. For the evaporated method, 5-6 nm BCP was thermally evaporated at a rate of 0.1 Å/s in an Angstrom Engineering cluster chamber at < 1 x 10^{-7} mbar pressure.

3.1.6.c – ICBA

150 µL of ICBA was statically spin-coated in a nitrogen-filled glovebox at 2000 rpm (200 rpm/s ramp) for 20s and then annealed at 100°C for 4-5 minutes.

3.1.6.d – C_{60}

In lieu of solution-processed PCBM, C_{60} (Buckminsterfullerene, Alfa Aesar, sublimed, 99.9+%) was thermally evaporated at a rate of 0.2 Å/s in an Angstrom Engineering cluster chamber at < 1 x 10^{-7} mbar pressure. Solution-processed solar cells were sealed in a nitrogen environment in the nitrogen-filled glovebox and transported to the cluster facility. For 1.55 eV solar cells, 25 nm C_{60} was thermally evaporated. For 1.97 eV, 1.61 eV, and 1.25 eV solar cells, 20 nm C_{60} was thermally evaporated.

3.1.6.e – ALD SnO_2

After C_{60} deposition, the substrates were transferred to an atomic layer deposition (ALD) system (Picosun) to deposit 20 nm of SnO_2 using precursors of tetrakis(dimethylamino) tin (IV) (TDMASn, Pegasus Chemicals, 99.9999%) and deionized (DI) water. The TDMASn source was held at 80°C and the DI water source was held at 20°C. ~140 cycles of 1.6 s of TDMASn pulse/8.4 s purging/1s of DI water pulse/9s of purging per cycle were run to deposit 20 nm of ALD SnO_2. The chamber temperature was held at 90°C for the 1.97 eV wide band gap and 1.25 eV narrow band gap absorbers. The chamber temperature was held at 100°C for the 1.55 eV and 1.61 eV middle band gap absorbers.

3.1.6.f – Sputtered IZO

For $FA_{0.8}Cs_{0.2}PbI_3$ solar cell stability batches, the substrates were then transferred to a sputtering system where 100 nm of indium doped zinc oxide (IZO) was sputtered at 90°C at a rate of ~1 Å /s on top of ALD SnO_2 before top metal electrode evaporation.

3.1.7 – 1.97 eV and 1.55 eV Perovskite Absorber Surface Passivation Layer Deposition

3.1.7.a – $EDAI_2$

For $FA_{0.8}Cs_{0.2}PbI_3$ solar cell stability batches, 100 µL of 0.5 mol% (7 mM) $EDAI_2$ surface treatment was dynamically spin-coated in a nitrogen-filled glovebox at 5000 rpm (5000 rpm/s ramp) for 20s and annealed at 100°C for 5 minutes.

3.1.7.b – $EDABr_2$:$EDAI_2$ (EDAX)

150 µL of EDAX surface treatment was statically spin-coated onto the substrates in a nitrogen-filled glovebox and immediately spun at 4000 rpm (1333 rpm/s ramp) for 20s and annealed at 100°C for 3 minutes.

3.1.8 – Tandem Recombination Layer Deposition

Recombination layers for multijunction perovskite tandem solar cells were deposited using a shadow mask with either gold or sputtered IZO. 1 nm of gold was thermally evaporated in an Angstrom Engineering cluster chamber under < 1 x 10^{-7} mbar pressure at a rate of 0.01 Å/s. 10 nm of indium doped zinc oxide (IZO) was sputtered at room temperature in an Angstrom Engineering cluster sputtering chamber at < 1 x 10^{-7} mbar pressure at a rate of approximately 0.8-1 Å/s. IZO was the far superior recombination layer material for all-perovskite tandem solar cells explored in this thesis.

3.1.9 – Electrode Deposition

After removing the substrates to air for scratching, the top metal electrode was deposited in a Kurt J. Lesker Nano36 evaporation chamber. 100 nm of silver (Ag) was thermally evaporated under < 4 x 10^{-6} mbar pressure at a rate of 0.2-1.0 Å/s. For solar cell stability batches, 100 nm of gold (Au) was thermally evaporated under < 2 x 10^{-6} mbar pressure at a rate of 0.01-0.7 Å/s. Alternatively, 3.5 nm of chromium (Cr) was evaporated under < 2 x 10^{-6} mbar pressure at a rate of 0.1 Å/s before 100 nm Au (referred to as chrome-gold, Cr-Au). Solar cells were stored overnight in a nitrogen-filled glovebox before testing. All materials were deposited using a shadow mask to ensure an electrode pattern compatible with our in-house solar simulator measurement setup. The pattern used was either 4 pixels per substrate or 6 pixels per substrate. For the 4-pixel pattern, there were 3 active areas of 0.25 cm^2 and 1 active area of 1 cm^2. For the 6-pixel pattern, there were 6 active areas of 0.25 cm^2.

3.1.10 – Encapsulation

Encapsulation of all thin films and solar cells was conducted using an epoxy glue (Everlight Eversolar AB341) and glass cover slip (AMG, Korea). First, all material outside the perimeter of the rectangular glass cover slips was removed via scratching. This was to ensure that all glue deposited was in direct contact with the glass coverslip for proper encapsulation. For thin films, the edge-encapsulation method was employed by depositing glue around the perimeter of the perovskite material and then placing an edge-ridged glass coverslip on top of the glue. The glue was cured for 3 minutes under a UV light. For solar cells, the full area encapsulation method was employed by depositing glue over the entire solar cell area (including active areas for measurement) and then placing a flat glass coverslip on top of the glue. The glue was also cured for 3 minutes under a UV light.

3.2 – Perovskite Thin Film Characterization

3.2.1 – UV-Visible Absorbance

Absorbance measurements were measured using a Cary 50 Bio UV-visible spectrophotometer. Measurements were taken in the 300-900 nm range.

3.2.2 – Photoluminescence Quantum Efficiency (PLQE)

Samples were measured inside an integrating sphere and illuminated via 445 nm laser (ThorLabs LP1600MM) coupled to an optical fiber feedthrough. The laser spot size on the sample was 0.15 cm^2. The laser power was adjusted to 1-sun equivalent for the appropriate band gap based on values published by Kirchartz et al.[4] This was 42.64 mW/cm^2 for 1.97 eV band gap and 76.05 mW/cm^2 for 1.55 eV band gap perovskite samples. A second fiber was used for light collection from the sphere, connecting to a

Maya2000 Pro spectrometer. PLQE values were determined using the method published by DeMello et al. and calculated with a Python program created by Dr. Bernard Wenger, University of Oxford.[5]

3.2.3 – 1-Dimensional X-Ray Diffraction (1D XRD)

1-dimensional X-ray diffraction patterns were obtained using a Panalytical X'Pert Pro X-ray diffractometer, with a copper K-α source at (λ = 1.54 Å). The generator setting was 40 kV and 40 mA. Samples were fixed into holders using plasticine and care was taken to align the surfaces of films as close as possible with the holder rims. Each sample was typically scanned 7 times repeatedly for 15 minutes (for a total of 1 hour 45 minutes) and the summed intensity for the 7 scans was plotted.

3.2.4 – 2-Dimensional X-Ray Diffraction (2D XRD)

In-situ 2-dimensional X-Ray Diffraction spectrum measurements were conducted using a Rigaku SmartLab X-ray diffractometer with a CuKα1 and a HyPix-3000 2D hybrid pixel array detector and operated at 40 kV. 2D one-shot XRD spectra were measured every minute from 9.75 to 15.36° without moving the 2D detector. Each 2D spectrum was folded to generate the plotted 1D XRD. An Anton Paar heating stage was employed together with the Rigaku SmartLab diffractometer for the annealing. Samples were spin-coated, sealed in an air-tight container, and directly measured on the Rigaku Smartlab.

3.2.5 – Grazing Incidence Wide-Angle X-Ray Scattering (GIWAXS)

In-situ grazing-incidence wide-angle X-ray scattering (GIWAXS) data was acquired at the I07 undulator beamline at Diamond Light Source. Solutions were deposited using an in-situ blade coater contained in an N_2 environment incorporating a syringe driver, coating surface, motorized blade, integrated hotplate, and an N_2 outlet

directed at the sample acting as an air knife. Solutions were deposited onto cleaned glass substrates, and coated with a blade with a shim height of 100 um and coating speed of 9 mm/s. Monochromatic X-rays with energy 10 keV were incident on the sample at a grazing angle of 1°, with scattering collected by a Pilatus 2M (DECTRIS) hybrid photon-counting detector at a distance of 365 mm, calibrated using an LaB6 standard. 2D detector images were acquired every 0.2s as samples were annealed. Data reduction was performed using scripts based on the pyFAI and pygix libraries.[6]

3.2.6 – X-Ray Photoelectron Spectroscopy (XPS)

XPS measurements were taken at 1-5 nm probing depth using monochromatic aluminum K-alpha X-rays at 1487 eV, 200 W, and 10 kV. Measurements conducted at Hydra station, Helmholtz-Zentrum Berlin.

3.2.7 – Scanning Electron Microscopy (SEM)

SEM images were taken using an FEI Quanta 600 microscope with an acceleration voltage of 5 kV, a spot size of 3.5-4, and a working distance of 10-15 mm. Samples were held in place with conductive carbon tape. Apparent grain size analysis was conducted via measuring the diameters of grains in an SEM image using ImageJ software.

3.2.8 – Time Resolved Photoluminescence Photospectroscopy (TRPL)

To measure the time-resolved photoluminescence a TimeHarp300 (Picoquant) was used, where a PMT detector (dead time < 95 ps) is coupled to single-photon counting electronics (TimeHarp260 nano). A monochromator was used to only measure the photoluminescence at a wavelength of 632 nm. A 398 nm excitation laser was used with a repetition rate of 3 MHz and a fluence of 0.53 nJ/cm^2. The spot size was estimated to be 3.4 x 10^3 cm^2. The pile-up rate was below 0.01%, which allowed the measurement of

single photons. To reduce the illumination time, which leads to halide segregation, 5 different spots on the sample were measured for 60 seconds each at the low fluence mentioned. Then, the average of these datasets was calculated and used for the TRPL decays, as well as to determine the photoluminescence lifetimes.

3.3 – Perovskite Solar Cell Characterization

3.3.1 – Current Density-Voltage (J-V) Characterization

Solar cells were tested under simulated AM 1.5G solar irradiation at 100 mW/cm^2 (equivalent to 1000 W/m^2) irradiance with a Wavelabs Sinus-220 (light-emitting diode array) solar simulator. The Wavelabs solar simulator was calibrated with a silicon reference cell (Fraunhofer ISE). Current density-voltage characterization was performed in air using a Keithley 2400 source meter, with a scan rate of 0.3 V/s. p-i-n inverted architecture solar cell J-V curves were measured with a reverse bias scan (from V_{OC} to J_{SC} range) first and a forward scan (from J_{SC} to V_{OC} range) second. Typically, steady-state open-circuit voltage was measured over 30 seconds, steady-state short-circuit current over 5 seconds, and maximum power point tracked efficiency for at least 30 seconds. Solar cells in the solar simulator were actively cooled during measurement by a nearby fan to maintain an operating temperature around 25°C.

3.3.2 – External Quantum Efficiency (EQE)

3.3.2.a – Single Junction Solar Cells

External quantum efficiency measurements were performed using a custom-built system. The monochromatic illumination source was provided using a 250 W halogen lamp and monochromator (Princeton Instruments Acton SP2150, FA2448 filter wheel), which was chopped (Thorlabs MC2000B-EC) at 280 Hz and focused to a spot size on the

sample that was smaller than the pixel defined by the evaporated rear electrode. The pixel was selected using a home-built multiplexer, and its AC current signal due to the chopped monochromatic illumination was converted to a voltage using a 50 Ω resistor. The amplitude of this voltage signal was measured using a lock-in amplifier (Stanford Research Systems SR830). The absolute value of EQE was calculated based on the ratio of this voltage signal to that of a signal generated by a reference Si photodiode of known EQE (Newport 818-UV/DB or Thorlabs FDS100-CAL) under the same illumination conditions as the test solar cell. The solar cell was unmasked and measured in ambient conditions.

3.3.2.b – All-Perovskite Triple Junction Solar Cells

To create an accurate EQE spectrum for an all-perovskite triple junction solar cell, the EQE response of each subcell must be measured under the appropriate conditions. To measure the EQE response from the 1.97 eV wide band gap subcell, the 1.61 eV middle band gap and 1.25 eV narrow band gap subcells were biased to their open-circuit voltage conditions with two LED lights at the wavelength of 740 and 850 nm, respectively. To measure the EQE response from the 1.61 eV wide band gap subcell, the 1.97 eV wide band gap and 1.25 eV narrow band gap subcells were biased to their open-circuit voltage conditions with two LED lights at the wavelength of 455 and 850 nm, respectively. To measure the EQE response from the 1.25 eV narrow band gap subcell, the 1.97 eV wide band gap and 1.61 eV middle band gap subcells were biased to their open-circuit voltage conditions with two LED lights at the wavelength of 455 and 740 nm, respectively. LED light sources were purchased from Mightex. Like the single junction solar cells, the all-

perovskite triple junction tandem solar cells were unmasked and measured in ambient conditions.

3.3.2.c – dEQE/dE Band Gap Analysis

The first derivative of the single junction solar cell EQE spectrum (dEQE) was plotted as a function of energy (eV). The energy value corresponding to the peak with the highest dEQE intensity value is the dEQE/dE band gap of the solar cell.

3.3.3 – Fourier-Transform Photocurrent Spectroscopy (FTPS)

Fourier-transform photocurrent spectroscopy (FTPS) was measured on a custom-built system with a Bruker Vertex 80v Fourier Transform Interferometer, an AM 1.5G filtered xenon lamp, and using perovskite solar cells with an active area of 0.25 cm^2 as the photodetector. Prior to measurements, the xenon lamp was calibrated such that an incident power of 1-sun intensity (AM 1.5G, 1000 W/m^2) was irradiated on the tested solar cell. External Quantum Efficiency (EQE) spectra obtained were calibrated against the spectral response of a certified Si reference Cell from Newport. Unencapsulated perovskite solar cells were held in open-circuit condition in air with a relative humidity of ~45%, with measurements taken at a discrete interval of time under constant xenon lamp illumination. To increase sensitivity and dynamic range (up to 5 orders of magnitude in photocurrent) of all spectra below the bandgap, above-bandgap illumination were filtered out with a 610 nm color filter. To extract Urbach energy (E_u) each EQE spectrum was fitted in the Urbach-tail spectral region, near the absorption edge, with the equation:

$$\mathrm{EQE} = \exp\left(\frac{\mathrm{hv} - \mathrm{E_0}}{\mathrm{E_U}}\right),$$

where $\mathrm{E_0}$ is a constant.

3.3.4 – Electroluminescence Quantum Efficiency (ELQE)

Electroluminescence external quantum efficiency (EQE_{EL} or ELQE) of the 1.97 eV band gap solar cell was measured in the following setup in a nitrogen-filled glovebox at room temperature in the dark. An Ocean Insight QE Pro spectrometer and an integrating sphere coupled with fiber were used for the EL spectrum collection and a Keithley 2400 was used to drive the solar cells with current. The system was calibrated by a standard light source (HL-3P-INT-CAL Radiometrically Calibrated Tungsten Halogen Light Sources) for the absolute spectral response of the spectrometer. The EQE_{EL} values were calculated from the associated emission peaks:

$$\mathrm{EQE_{EL}} = \frac{\mathrm{N_{photon}(V)}}{\mathrm{N_{charges}(V)}} * 100\% = \int \frac{\phi_\lambda * \lambda * \mathrm{e}}{\mathrm{h} * \mathrm{c} * \mathrm{J} * \mathrm{A}}\, d\lambda * 100\%$$

where N_{photon} and $N_{charges}$ are emitted photons and injected charge carriers, respectively, Φ_λ (μW/nm) is the spectral flux, h is Planck's constant (6.626×10^{-34} J/s), c is the speed of light in vacuum (3.0×10^8 m/s), J (mA/cm^2) is the current density, e is the elementary charge (1.602×10^{-19} C), and A is the working area of the solar cell in cm^2.

3.3.5 – Cross-Sectional Scanning Electron Microscopy (SEM)

A cross-sectional SEM image of an all-perovskite triple junction solar cell was recorded by a FEI Quanta 3D FEG microscopy setup. A 5-kV electron beam with a spot size of 3 and a secondary electron detector were used. The working distance was 13.8 mm and dwell time for single-pass image acquisition was 5 μs. Focusing and alignment were conducted at different areas than those imaged to minimize electron beam-induced damage.

3.3.6 – Stability Testing

Thin films and solar cells were subjected to stability testing under the accelerated aging protocol of combined heat and light. Using an Atlas SunTest XLS+ aging box, samples were illuminated by a xenon lamp source pulsed at an average irradiance of 765 W/m^2 in the 300-800 nm spectral range with a temperature control set at 85˚C on a Black Standard at open-circuit condition (for solar cells) – hereafter referred to as “85°C light” aging in this thesis. The $FA_{1-x}Cs_xPbI_3$ half-stacks covered in Section 4.2 were aged in a similar Atlas SunTest XLS+ box but with a temperature control set at 65˚C on a Black Standard because the 85°C light setup was not available for use at that time. Unless otherwise stated, all thin films and solar cells were encapsulated according to the method described in Section 3.1.10 for 85°C light aging. Solar cells were periodically taken out of the Atlas SunTest XLS+ aging box, allowed to cool to room temperature, measured in the solar simulator, and then put back into the aging box for solar cell stability experiments.

Chapter 3 References

1. Hu, S. et al. Optimized carrier extraction at interfaces for 23.6% efficient tin-lead perovskite solar cells. *Energy Environ. Sci.* **15**, 2096-2107 (2022).

2. Lin, R. et al. Monolithic all-perovskite tandem solar cells with 24.8% efficiency exploiting comproportionation to suppress Sn(ii) oxidation in precursor ink. *Nature Energy*, **4**, 864-873 (2019).

3. Hu, S. et al. Synergistic Surface Modification of Tin-Lead Perovskite Solar Cells. *Adv. Mater.*, **35**, 2208320 (2023).

4. Kirchartz, T. et al. Photoluminescence-Based Characterization of Halide Perovskites for Photovoltaics. *Advanced Energy Materials*, **10**, 1904134 (2020).

5. de Mello, J. C., Wittmann, H. F. and Friend, R. H. An improved experimental determination of external photoluminescence quantum efficiency. *Advanced Materials*, **9**, 230–232 (1997).

6. Ashiotis, G. et al. The fast azimuthal integration Python library: pyFAI. *J. Appl. Cryst.* **48**, 510–519 (2015).

Chapter 4

Improved Stability of Efficient and Reproducible 1.55 eV Middle Band Gap Perovskite Absorbers and Single Junction Solar Cells

4.1 – Introduction

For practical and widespread use, solar cells must be stable and efficient. The dominant crystalline silicon solar technology used today has 20% efficiencies with an industry standard limited power warranty of 25 years. Perovskite solar cells are not yet as stable as crystalline silicon, with current operational stability lasting for weeks, months, or a few years at most.

All-perovskite triple junction tandem solar cells have three absorbers with three different band gaps: wide, middle, and narrow. An absorber is the layer of the solar cell that absorbs light and generates photoexcited charge carriers to produce electrical power.

In this chapter, improved stability is achieved for a representative middle band gap perovskite absorber in efficient and reproducible single junction solar cells.

Improvements to perovskite crystallization of wide band gap absorbers, resulting in increased efficiencies for all-perovskite triple junction tandem solar cells, are detailed in Chapters 5, 6, and 7.

For all-perovskite triple junction tandem solar cells to survive aging conditions experienced in the field, the stability of each perovskite absorber subcell – wide, middle, and narrow – must be improved. The combination of heat and light is a particularly harsh

aging condition for perovskite solar cells of different band gaps.[1-3] The consensus ISOS-L-2 stability protocol combines elevated temperature (65°C or 85°C) and 1-sun intensity illumination stressors at open-circuit load conditions to age perovskite solar cells.[4] In the Snaith Lab, this aging condition can be most closely replicated by subjecting perovskite solar cells to 85°C temperature (relative to a Black Standard) and 765 W/m^2 average irradiance (from a xenon lamp in the 300-800 nm spectral range) at open-circuit, hereafter referred to as 85°C light aging. Aging was conducted at open-circuit primarily because it was not available to do so at maximum power point due to complexity of the equipment setup in the Snaith Lab. Most notably, the irradiance intensity from the xenon lamp source was pulsed (with an average value of 765 W/m^2) so maximum power point tracking could not reliably be conducted at a constant irradiance intensity that would be required.

This chapter investigates advancements to improving the stability of efficient and reproducible 1.55 eV middle band gap perovskite single junction solar cells under 85°C light aging. It is shown that creating a mixed formamidinium-cesium (FACs) A-site with sufficient cesium content improves the material stability of $FA_{1-x}Cs_xPbI_3$ perovskite films.

Novel elements of the work detailed in this chapter include the incorporation of a benzylammonium thiocyanate bulk additive into $FA_{0.8}Cs_{0.2}PbI_3$ 1.55 eV perovskite solar cells for improved efficiency and reproducibility, the development of a tandem-relevant C_{60}/ALD SnO_2/IZO/Au top contact device stack that demonstrated improved performance and promise for stability in $FA_{0.8}Cs_{0.2}PbI_3$ single junction solar cells under 85°C light aging, and the discovery of significant enhancement to $FA_{0.8}Cs_{0.2}PbI_3$ thin film and solar cell stability under 85°C light aging with the combination of $EDAI_2$ surface passivation and excess PbI_2 perovskite precursor stoichiometry.

The $FA_{0.8}Cs_{0.2}PbI_3$ absorber fabricated yields efficient 1.55 eV perovskite solar cells relevant for middle band gap subcell application, with improved stability. The incorporation of a benzylammonium thiocyanate bulk additive into $FA_{0.8}Cs_{0.2}PbI_3$ 1.55 eV perovskite solar cells is shown to enhance their efficiency and reproducibility. The use of a compact and conductive ALD SnO_2 top contact – crucial for fabrication of solution-processed, monolithic all-perovskite triple junction tandem solar cells – in conjunction with a C_{60} electron transport layer yields even higher maximum power point tracked efficiencies, achieving a champion maximum power point tracked efficiency of 21.2%.

All-perovskite triple junction solar cells subsequently fabricated for this thesis, using a different middle band gap subcell absorber, achieved the highest champion maximum power point tracked efficiency of 27.3%, as discussed in Chapter 7.

The further development of a sputtered indium doped zinc oxide (IZO) buffer layer and gold (Au) electrode as additional top contacts improves 1.55 eV perovskite single junction solar cell reproducibility in a device stability stack that can be useful in all-perovskite triple junction tandems.

$EDAI_2$ surface passivation and excess PbI_2 perovskite stoichiometry are shown to improve the stability of 1.55 eV $FA_{0.8}Cs_{0.2}PbI_3$ single junction solar cells under 85°C light aging in a tandem-relevant C_{60}/ALD SnO_2/IZO/Au top contact device stack. $FA_{0.8}Cs_{0.2}PbI_3$ is a representative perovskite composition for middle band gap subcell absorbers and these stability enhancements may be transferrable to perovskites with similar band gaps.

Methylammonium lead triiodide ($MAPbI_3$, 1.48 eV) and formamidinium lead triiodide ($FAPbI_3$, 1.53 eV) perovskites are candidates for middle band gap subcell

absorbers in all-perovskite triple junction tandem solar cells but suffer from thermal or phase instabilities. Methylammonium cations are volatile, particularly at temperatures such as 85°C and higher, and therefore $MAPbI_3$ perovskite solar cells quickly degrade under such conditions. Formamidinium cations are less volatile and $FAPbI_3$ solar cells exhibit improved thermal stability over $MAPbI_3$.[5] It is acutely challenging, however, to keep $FAPbI_3$ in the desired photo-active, black α-phase due to its phase instability at temperatures below 150°C. At room temperature, the α-phase $FAPbI_3$ has been shown to degrade to photo-inactive, yellow δ-phase $FAPbI_3$.[6] Degradation to this photo-inactive δ-phase results in reduced photo-absorption and charge carrier extraction, harming solar cell performance.[7]

The introduction of cesium into the A-site cation of the perovskite absorber to create mixed formamidinium-cesium lead triiodide ($FA_{1-x}Cs_xPbI_3$) materials is shown to improve phase stability over a wider temperature range, including room temperature.[8] In addition, a mixed FACs A-site cation has been shown to improve thermal and photostability of perovskite absorbers.[9] $FA_{1-x}Cs_xPbI_3$ compositions offer the promise of improved stability under combined heat and light for middle band gap subcell absorber applications in all-perovskite triple junction tandem solar cells.

4.2 – Improved Perovskite Material Stability with Mixed Formamidinium-Cesium A-Site Cation

To test the effect of A-site cation composition on perovskite material under combined heat and light stability, $FA_{1-x}Cs_xPbI_3$ thin films with 0-30% cesium A-site compositions in 5% increments were aged. The thin films were aged unencapsulated under 65°C light (the 85°C light aging setup was not available at this time in the Snaith

Lab) for UV-visible absorbance measurements to track material stability. Photos of the half-stacks with aging time are displayed in Figure 4.1, with severe degradation visible within 29 hours for $FAPbI_3$ and $FA_{0.95}Cs_{0.05}PbI_3$ compositions. Higher cesium compositions, such as $FA_{0.8}Cs_{0.2}PbI_3$, were significantly more stable under 65°C light.

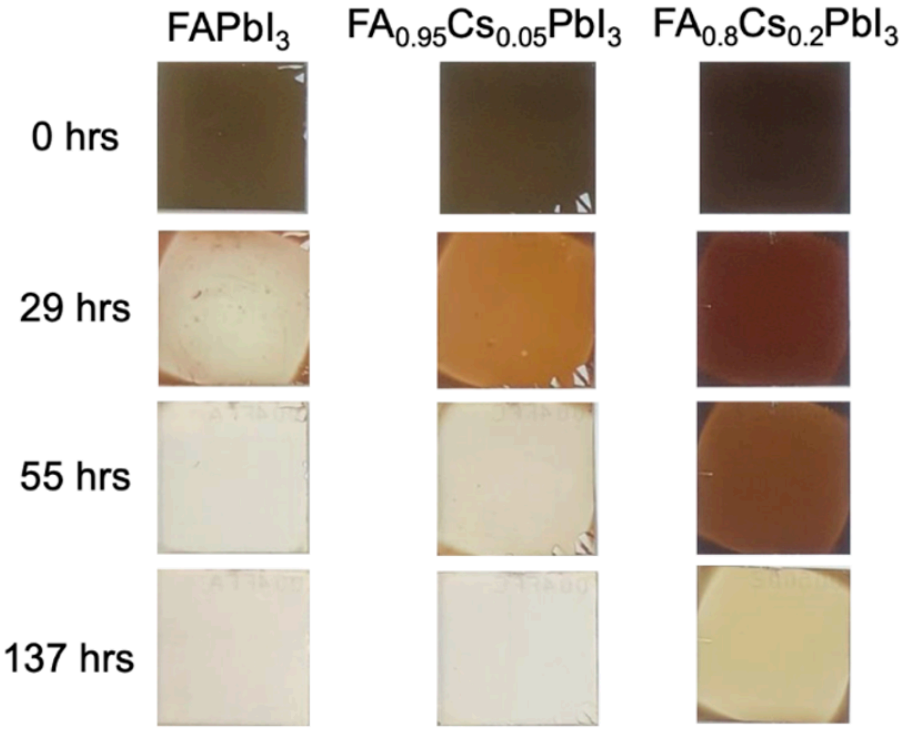

Figure 4.1. Photos of $FAPbI_3$, $FA_{0.95}Cs_{0.05}PbI_3$, and $FA_{0.8}Cs_{0.2}PbI_3$ thin films at different 65°C light aging time points. The $FA_{0.8}Cs_{0.2}PbI_3$ thin film exhibited less degradation.

Individual UV-visible absorbance plots for the thin films of each cesium composition in Figure 4.2 illustrate less degradation in absorbance with aging time for cesium A-site compositions ≥ 10%. Incorporating at least 10% cesium into the A-site cation was shown to improve perovskite material stability under combined heat and light.

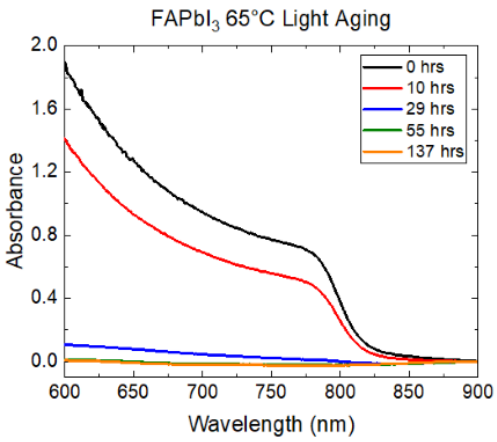
FAPbI3 65°C Light Aging
Absorbance
Wavelength (nm)
0 hrs
10 hrs
29 hrs
55 hrs
137 hrs

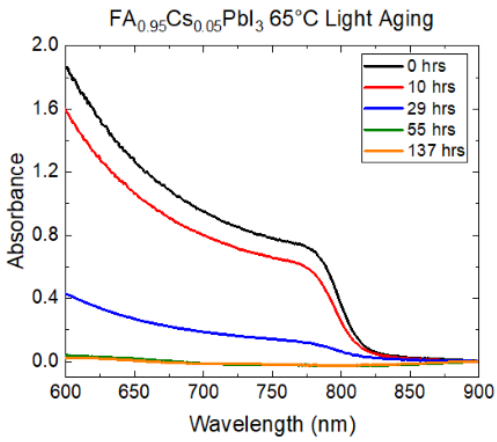
FA0.95Cs0.05PbI3 65°C Light Aging
Absorbance
Wavelength (nm)
0 hrs
10 hrs
29 hrs
55 hrs
137 hrs

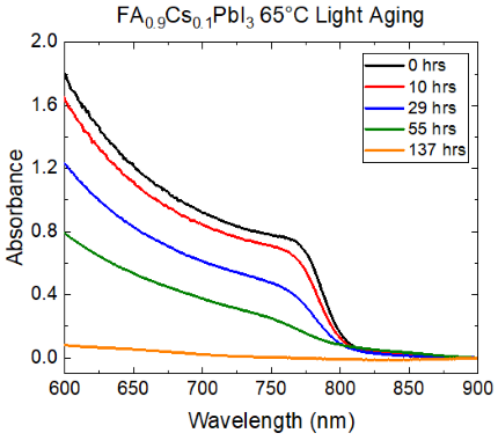
FA0.9Cs0.1PbI3 65°C Light Aging
Absorbance
Wavelength (nm)
0 hrs
10 hrs
29 hrs
55 hrs
137 hrs

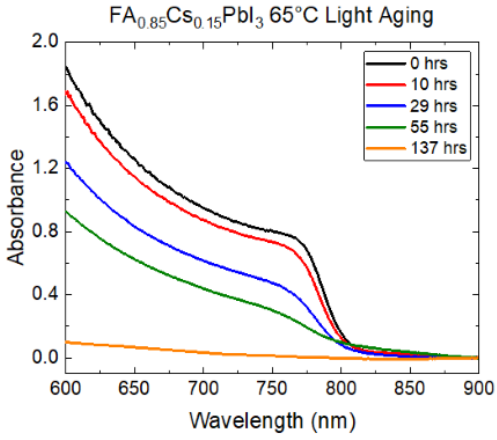
FA0.85Cs0.15PbI3 65°C Light Aging
Absorbance
Wavelength (nm)
0 hrs
10 hrs
29 hrs
55 hrs
137 hrs

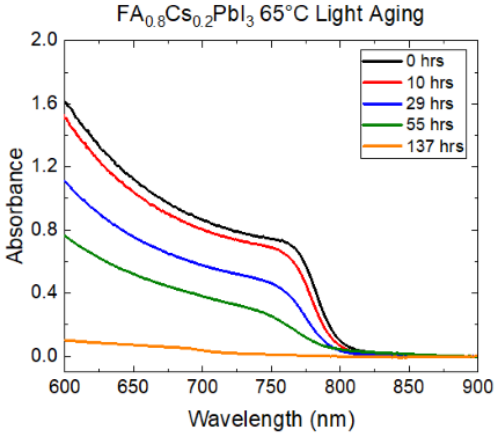
FA0.8Cs0.2PbI3 65°C Light Aging
Absorbance
Wavelength (nm)
0 hrs
10 hrs
29 hrs
55 hrs
137 hrs

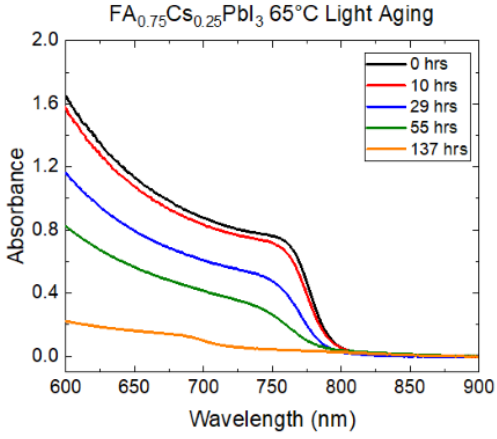
FA0.75Cs0.25PbI3 65°C Light Aging
Absorbance
Wavelength (nm)
0 hrs
10 hrs
29 hrs
55 hrs
137 hrs

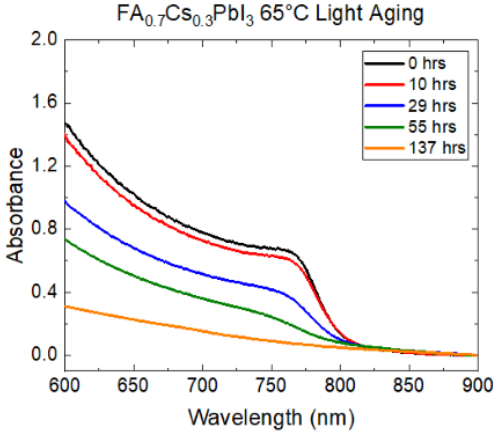
FA0.7Cs0.3PbI3 65°C Light Aging
Absorbance
Wavelength (nm)
0 hrs
10 hrs
29 hrs
55 hrs
137 hrs

Figure 4.2. UV-visible absorbance spectra of $FA_{1-x}Cs_xPbI_3$ thin films under 65°C light aging for 137 hours. $FAPbI_3$ and $FA_{0.95}Cs_{0.05}PbI_3$ thin films show near complete degradation at 29 hours while A-site compositions with cesium content ≥ 10% do not. Higher cesium compositions exhibit less material degradation over time.

4.3 – Fabrication of High Efficiency 1.55 eV Middle Band Gap $FA_{0.8}Cs_{0.2}PbI_3$ Perovskite Solar Cells

4.3.1 – Tuning of A-Site Cation Composition for $FA_{1-x}Cs_xPbI_3$ Solar Cells

With increased material stability under combined heat and light, $FA_{1-x}Cs_xPbI_3$ perovskite solar cells with A-site cesium compositions ≥ 10% were fabricated. The 20% cesium composition yielded the best solar cell performance with noticeably highest steady-state fill factor, as shown in Figure 4.3, and from these results $FA_{0.8}Cs_{0.2}PbI_3$ was selected as the perovskite composition for use in solar cells fabricated and tested in this chapter.

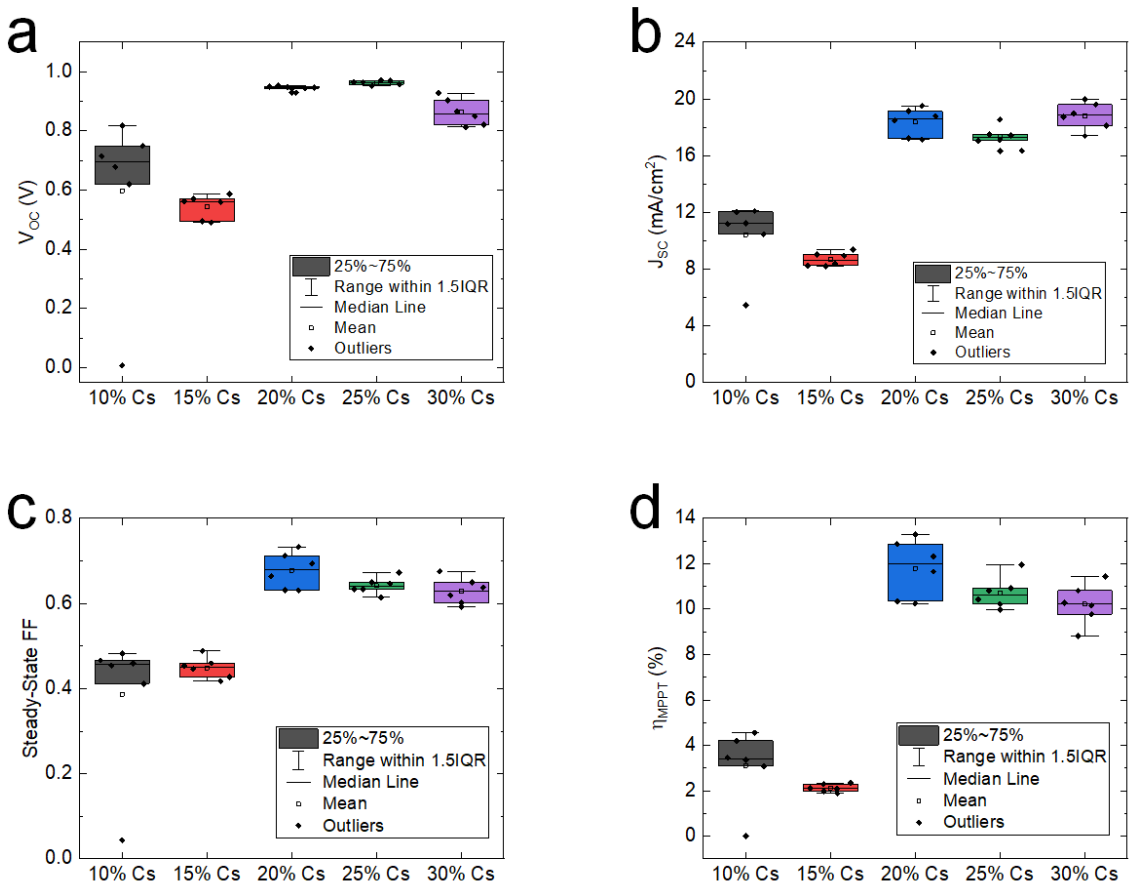

Figure 4.3. 10-30% cesium A-site composition $FA_{1-x}Cs_xPbI_3$ solar cell performance parameter statistics. Device stack: FTO/Poly-TPD/Al_2O_3 nanoparticles/$FA_{1-x}Cs_xPbI_3$/PCBM/BCP/Au. Steady-state a) open-circuit voltage b) short-circuit current c) fill factor and d) maximum power point tracked efficiency. All performance parameters clearly improved with cesium compositions > 15%. The 20% cesium composition solar cells yielded highest maximum power point tracked efficiency with noticeably greatest steady-state J_{SC} and fill factor. 6 solar cells of 0.25 cm^2 area were fabricated for each condition.

4.3.2 – DMF/DMSO Solvent System

A standard 4:1 DMF:DMSO solvent ratio was used for perovskite precursor solutions to fabricate the $FA_{1-x}Cs_xPbI_3$ thin films and solar cells discussed in this chapter up to this point. Significant enhancements to steady-state V_{OC} and fill factor were achieved, however, with an increase in DMSO content to the DMF/DMSO solvent

systems. Decreasing the DMSO content reduced steady-state V_{OC} and fill factor. The optimal DMF/DMSO solvent ratio was 3:1, as shown in Figure 4.4.

This optimal 3:1 DMF:DMSO solvent ratio was used to fabricate the $FA_{0.8}Cs_{0.2}PbI_3$ single junction solar cells in the rest of this chapter. As noted, a novel DMF/DMAX crystallization method was created to fabricate 1.97 eV wide band gap absorbers in all-perovskite triple junction tandem solar cells, as detailed in Chapters 5 and 7.

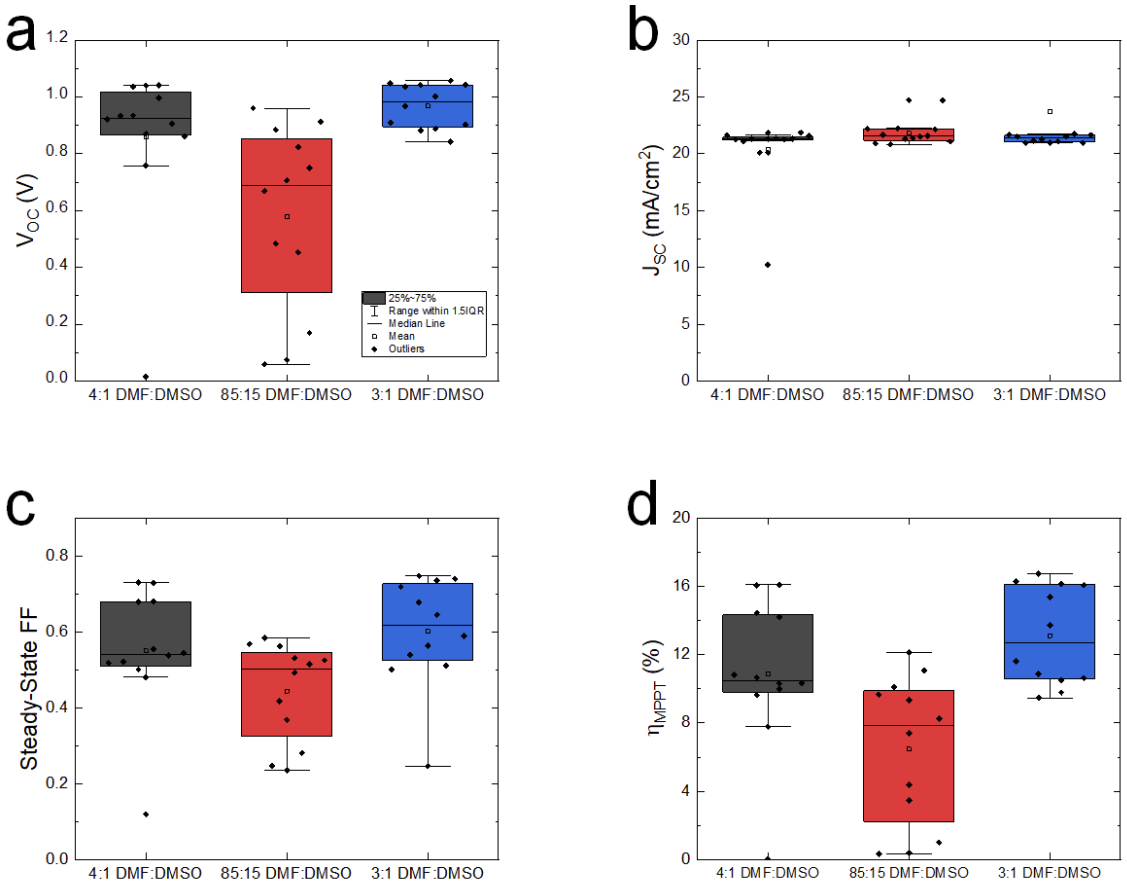

Figure 4.4. Various DMF:DMSO solvent ratios for $FA_{0.8}Cs_{0.2}PbI_3$ solar cell performance parameter statistics. Device stack: FTO/Poly-TPD/Al_2O_3 nanoparticles/$FA_{0.8}Cs_{0.2}PbI_3$/PCBM/BCP/Au. Steady-state a) open-circuit voltage b) short-circuit current c) fill factor and d) maximum power point tracked efficiency. Increasing DMSO content to a 3:1 DMF:DMSO ratio improved steady-state V_{OC} and fill factor, increasing solar cell efficiency. This optimal 3:1 DMF:DMSO solvent ratio was used

in $FA_{0.8}Cs_{0.2}PbI_3$ solar cells for the rest of this study. 12 solar cells of 0.25 cm^2 area were fabricated for each condition.

4.3.3 – Benzylammonium Thiocyanate Bulk Additive

A series of benzylammonium salts, some of which have been previously shown to effectively passivate defects and improve charge carrier extraction in perovskites, were screened.[10-12] Five bulk additives were respectively introduced to solutions of $FA_{0.8}Cs_{0.2}$ PbI_3 perovskite precursor. These additives were benzylammonium iodide, benzylammonium bromide, benzylammonium chloride, benzylamine, and benzylammonium thiocyanate (BzSCN), each added at a concentration of 0.2 mol% excess relative to the perovskite precursor solution. As shown in Figure 4.5, each additive showed some improvement to specific performance parameters as compared to the no bulk additive control solar cells. BzSCN additive solar cells reproducibly achieved steady-state V_{OC} values greater than the control and had the highest maximum power point tracked efficiency of the study, reaching 17.1% as compared to the control maximum of 15.7%.

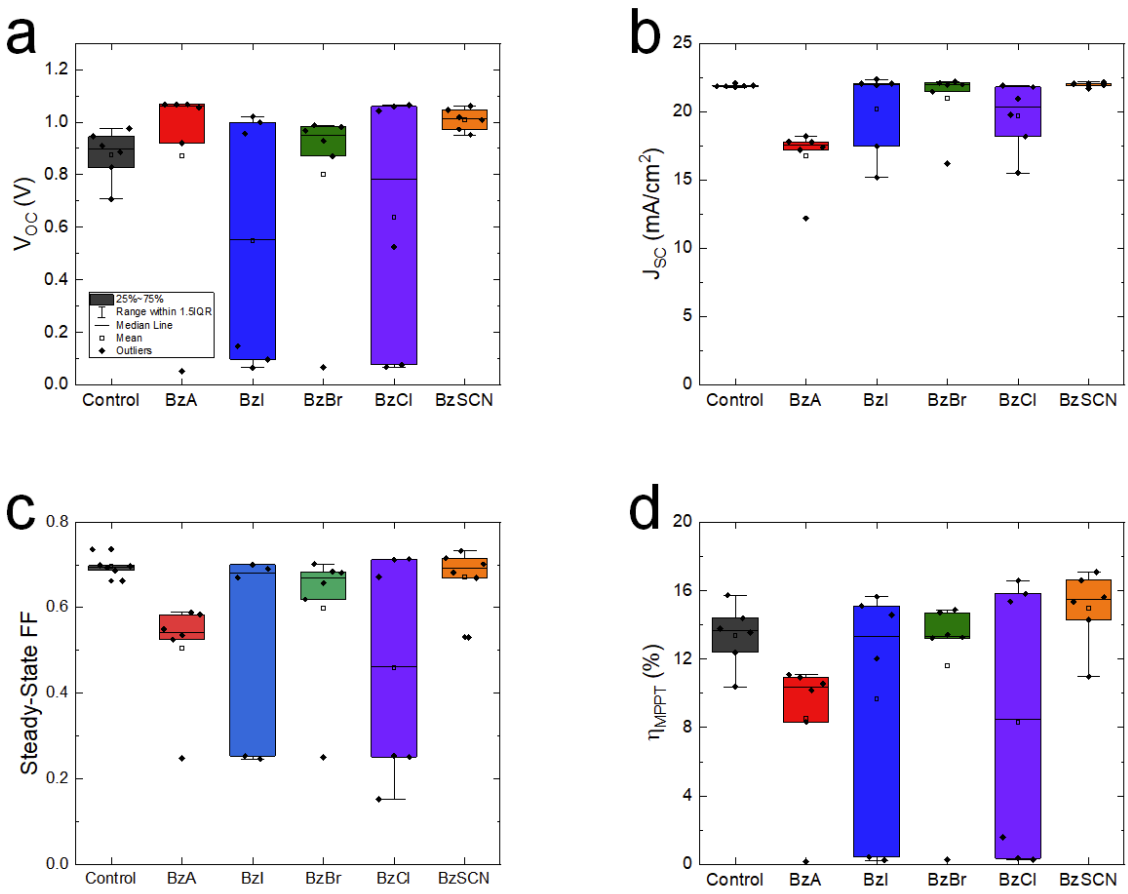

Figure 4.5. Control (no bulk additive), benzylamine (BzA), benzylammonium iodide (BzI), benzylammonium bromide (BzBr), benzylammonium chloride (BzCl), and benzylammonium thiocyanate (BzSCN) bulk additive (0.2 mol% concentration for all) screened for $FA_{0.8}Cs_{0.2}PbI_3$ solar cell performance parameter statistics. Device stack: FTO/Poly-TPD/Al_2O_3 nanoparticles/ $FA_{0.8}Cs_{0.2}PbI_3$ + bulk additive/PCBM/BCP/Ag. Steady-state a) open-circuit voltage b) short-circuit current c) fill factor and d) maximum power point tracked efficiency. Compared to the control, BzSCN solar cells consistently improved steady-state V_{OC}, without also harming steady-state J_{SC} or fill factor, for the champion maximum power point tracked efficiency of the batch. 6 solar cells of 0.25 cm^2 area were fabricated for each condition.

4.3.4 – Hole Transport Layer

To further improve the performance of $FA_{0.8}Cs_{0.2}PbI_3$ solar cells, a Me-4PACz hole transport layer (HTL) was investigated. Poly-TPD typically requires the thermally unstable F4-TCNQ dopant to function effectively as a hole transport layer while Me-4PACz does not use such dopants. In addition, Me-4PACz has been shown to reduce

non-radiative recombination at the interface with the perovskite absorber, improving open-circuit voltage.[13] Figure 4.6 shows that the combination of the BzSCN bulk additive with a Me-4PACz HTL improved $V_{OC.}$ This principal improvement in V_{OC} may be due to better energetic alignment with the 1.55 eV perovskite absorber – yielding a maximum power point tracked efficiency of 18.4%, the highest for a $FA_{0.8}Cs_{0.2}PbI_3$ 1.55 eV single junction solar cell so far in this chapter.

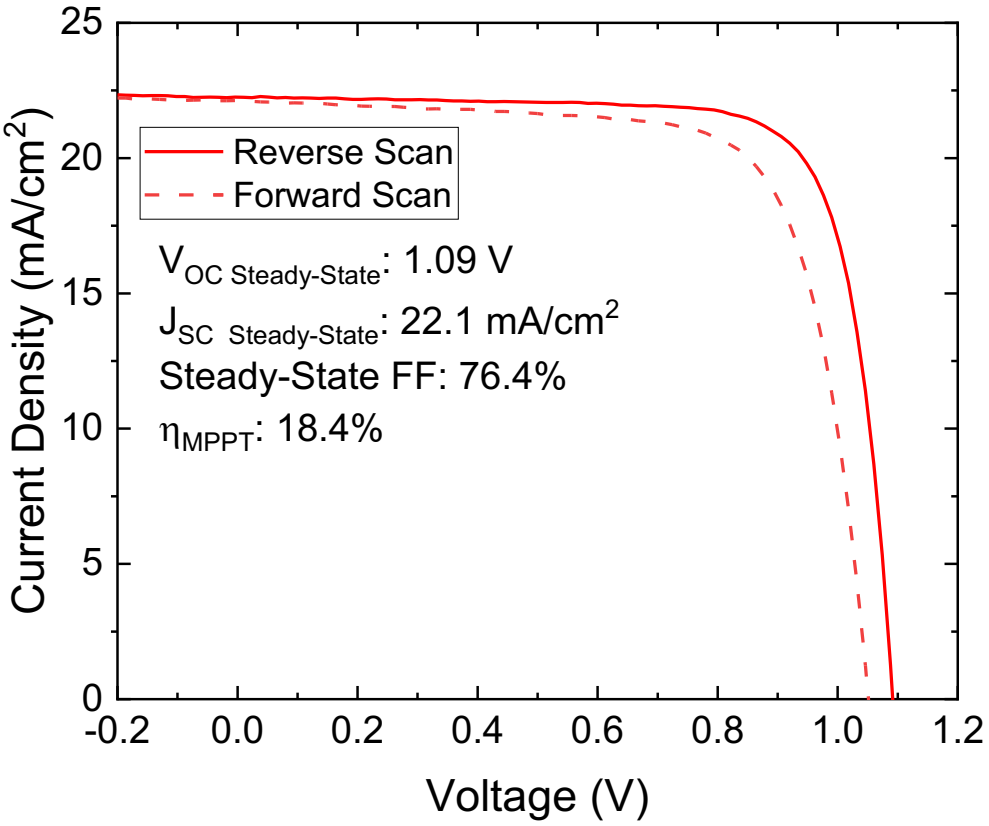

Figure 4.6. Champion J-V curve of a $FA_{0.8}Cs_{0.2}PbI_3$ solar cell with Me-4PACz HTL, characterized by a substantial boost to steady-state V_{OC} and maximum power point tracked efficiency. Device stack: FTO/Me-4PACz/Al_2O_3 nanoparticles/ $FA_{0.8}Cs_{0.2}PbI_3$ + BzSCN bulk additive/PCBM/BCP/Cr-Au.

4.3.5 – Electron Transport Layer and Top Contact Stack for Champion $FA_{0.8}Cs_{0.2}PbI_3$ 1.55 eV Solar Cell Efficiency and Reproducibility

Up to this point in this chapter, the only top contact stack between the perovskite absorber and electrode explored was PCBM/BCP – with PCBM as the electron transport layer (ETL) and BCP as a buffer layer to prevent recombination between the PCBM and top metal electrode for efficient solar cell performance. Buckminsterfullerene (C_{60}), however, is a promising alternate ETL due to its higher electron mobility and conductivity than PCBM.[14]

In addition, C_{60} is thermally evaporated while PCBM is typically deposited via spin-coating at lab-scale. The more controlled process of thermal evaporation enables the opportunity for improved conformality of C_{60} as an ETL on top of a perovskite absorber in a p-i-n architecture solar cell, offering the potential of higher efficiency and reproducibility.[15]

The use of a compact and conductive metal oxide layer as a top contact between the ETL and the metal electrode also offers a number of advantages. Published literature has shown that the use of a compact and conductive metal oxide such as tin oxide (SnO_2) as a top contact with quality electron extraction can improve perovskite solar cell efficiency, reproducibility, and stability.[16-18] These metal oxide layers can be deposited using atomic layer deposition (ALD), an industrially scalable technique that can deliver uniform layer coverage at relatively low processing temperatures around 50-100°C.[19-20]

Furthermore, a compact layer like atomic layer deposition tin oxide (ALD SnO_2) can protect perovskite subcells in monolithic all-perovskite multijunction tandem architectures. If an ALD SnO_2 top contact layer has sufficient density and thickness, it can protect a perovskite subcell from processing damage of subsequent layers in a

monolithic all-perovskite multijunction tandem. For example, ALD SnO_2 can protect perovskite subcell absorbers from sputtering damage (for a recombination layer like indium doped zinc oxide) and dissolution from solvents like DMF and DMSO used in the fabrication of subsequent solution-processed perovskite absorbers. ALD SnO_2 is a quality compact metal oxide top contact candidate for subcells in all-perovskite triple junction tandem solar cells.

$FA_{0.8}Cs_{0.2}PbI_3$ single junction solar cells incorporating C_{60} and ALD SnO_2 as the top contact stack, replacing PCBM and BCP, before the silver (Ag) electrode were fabricated and tested. C_{60} was used as the electron transport layer. A conductive ALD SnO_2 layer was used to fabricate the $FA_{0.8}Cs_{0.2}PbI_3$ solar cells in a tandem-relevant stack. ALD SnO_2 has the ability to transport charges and also protect the perovskite subcell absorbers from damage due to sputtering or solvents from subsequent depositions of layers required for tandem solar cells. Figure 4.7 shows solar cell performance parameters for a 15-30 nm range of C_{60} ETL thicknesses before the 20 nm ALD SnO_2 top contact, highlighting the improved efficiency and reproducibility of these solar cells with a C_{60}/ALD SnO_2/Ag top contact stack.

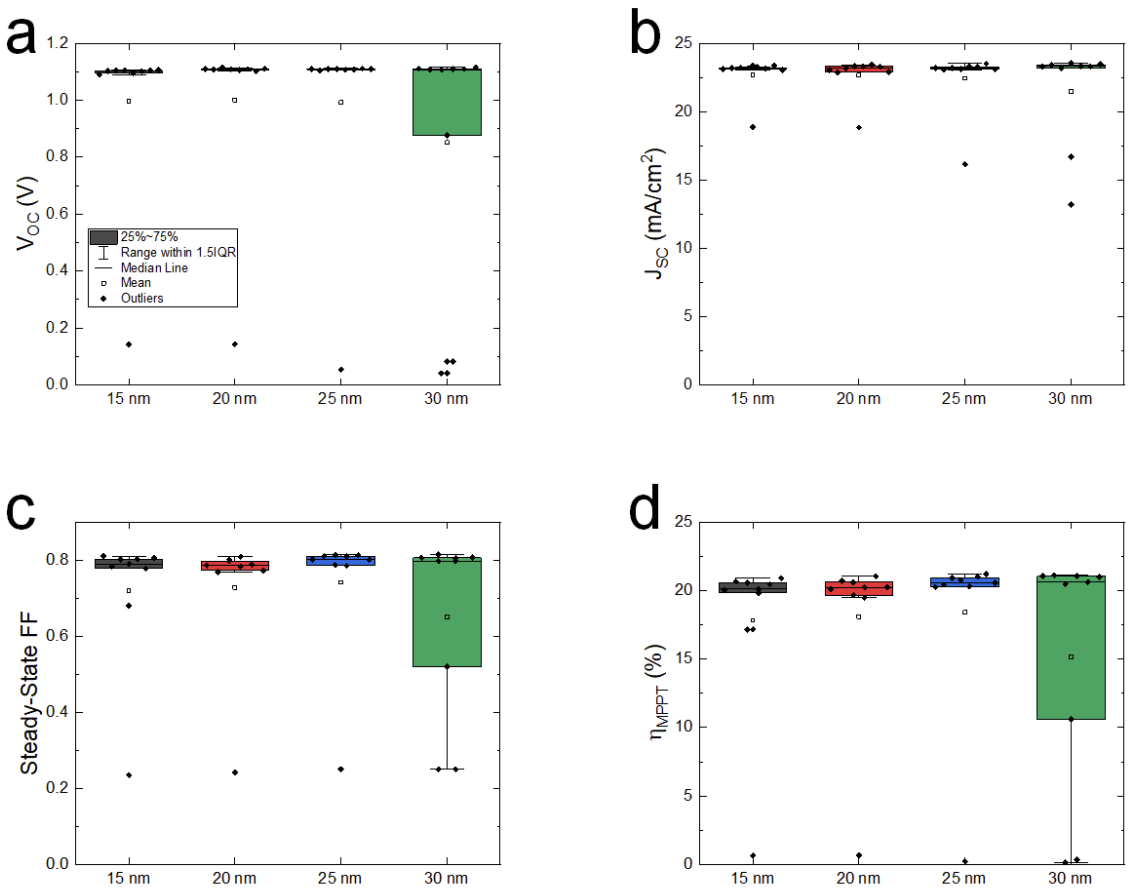

Figure 4.7. C_{60} electron transport layer thickness solar cell performance parameter statistics. Device stack: FTO/Me-4PACz/Al_2O_3 nanoparticles/ $FA_{0.8}Cs_{0.2}PbI_3$ + BzSCN bulk additive/C_{60}/ALD SnO_2/Ag. Steady-state a) open-circuit voltage b) short-circuit current c) fill factor and d) maximum power point tracked efficiency. The C_{60}/ALD SnO_2/Ag top contact stack yielded solar cells with excellent efficiency and reproducibility. 9 solar cells of 0.25 cm^2 area were fabricated for each condition.

The 25 nm C_{60}/ALD SnO_2/Ag top contact stack yielded the champion solar cell with 21.2% maximum power point tracked efficiency at 0.25 cm^2 area, as shown in Figure 4.8. Only a reduction in steady-state fill factor was observed for the 1 cm^2 area champion compared to 0.25 cm^2 area champion. As illustrated in Figure 4.8, the external quantum efficiency (EQE) spectra of both champion solar cells were nearly identical with an EQE value ≥ 90% for much of the visible spectrum. dEQE/dE analysis confirmed a 1.55 eV band gap value for $FA_{0.8}Cs_{0.2}PbI_3$ solar cells.

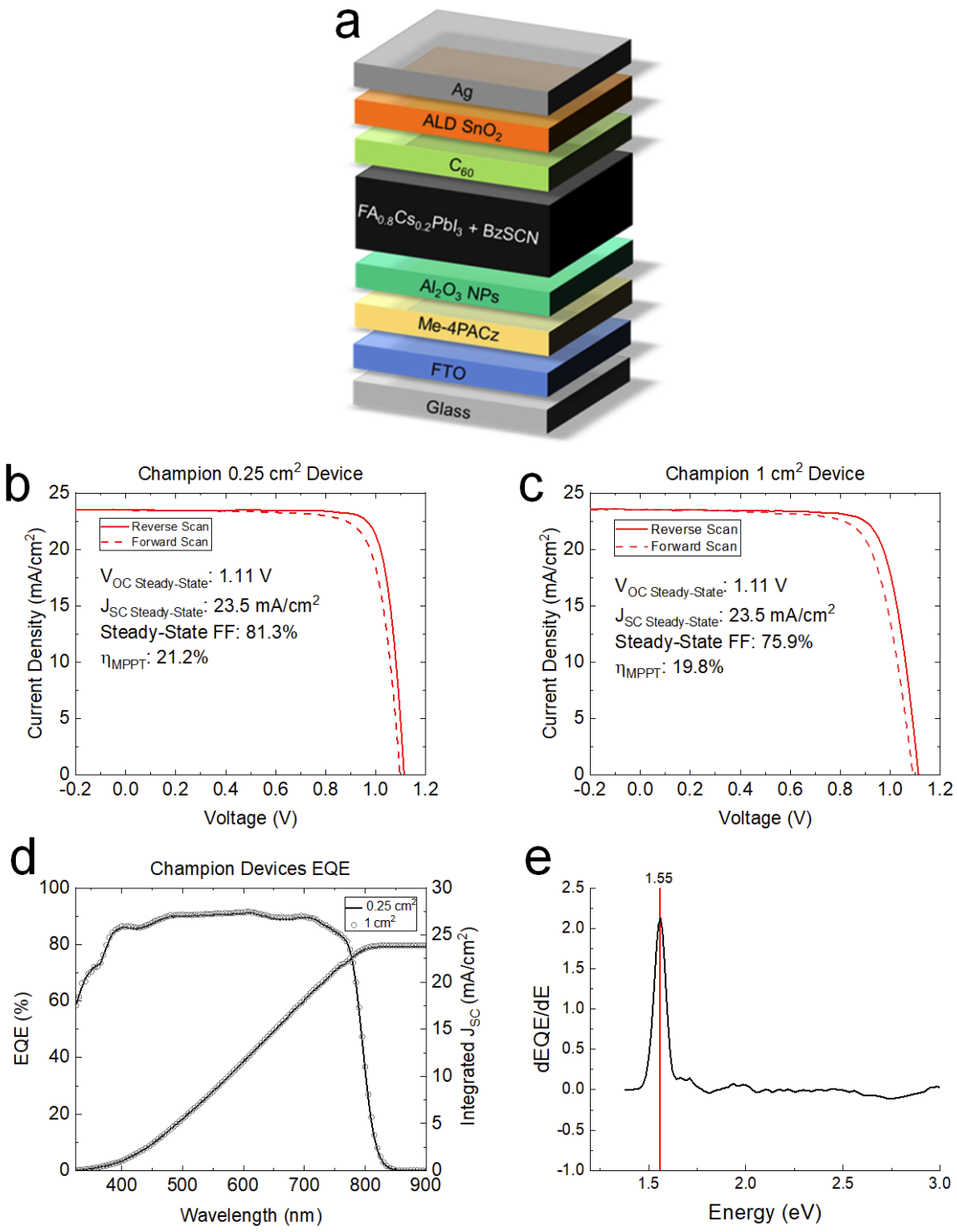

Figure 4.8. a) Device stack for 1.55 eV champion solar cells: FTO/Me-4PACz/Al_2O_3 nanoparticles/$FA_{0.8}Cs_{0.2}PbI_3$ + BzSCN bulk additive/25 nm C_{60}/20 nm ALD SnO_2/Ag. b) J-V curve of champion 0.25 cm^2 area solar cell c) J-V curve of champion 1 cm^2 area solar cell d) External quantum efficiency (EQE) spectrum and integrated current density

of champion 0.25 and 1 cm^2 area solar cells shown in Figures 4.8b and 4.8c. e) dEQE/dE band gap analysis of 0.25 cm^2 area champion confirms a band gap of 1.55 eV.

4.4 – Improved Stability of 1.55 eV $FA_{0.8}Cs_{0.2}PbI_3$ Perovskite Single Junction Solar Cells Under 85°C Light

4.4.1 – Further Modifications to Top Contact for Tandem-Relevant Stability Testing

Silver metal electrodes can react with chemical species that escape from the perovskite absorber or diffuse themselves into the device stack underneath, creating shunt pathways that harm perovskite solar cell performance and stability.[21] Gold (Au) is less reactive than silver and has been used to improve stability in perovskite solar cells at research-scale. However, gold can still diffuse into layers underneath and degrade perovskite solar cells over time.[22] A chrome-gold (Cr-Au) metal electrode, where the chrome may act as a buffer layer to prevent gold diffusion, has been used in perovskite solar cells with improved stability under heat and light.[23]

For this study, however, persistent shunting of $FA_{0.8}Cs_{0.2}PbI_3$ solar cells from the Cr-Au electrode occurred, hampering solar cell efficiency and reproducibility. This may be attributable to issues with Cr reacting with exposed regions of perovskite. Because Cr forms very conformally, this may then introduce shunting pathways through the solar cell, reducing the diode blocking of the cell.[24]

As a substitute for chrome, a 100 nm layer of indium doped zinc oxide (IZO) was sputtered on top of ALD SnO_2 before the evaporation of a gold metal electrode. Sputtered IZO is a candidate material for use as a recombination layer to fabricate efficient all-perovskite multijunction solar cells. Additionally, sputtered IZO has been reported to

increase thermal stability in lead-tin perovskite single junction solar cells when used as a capping electrode on top of ALD SnO_2.[25]

The C_{60}/ALD SnO_2/IZO/Au top contact stack was used for the stability testing of $FA_{0.8}Cs_{0.2}PbI_3$ 1.55 eV single junction solar cells in this thesis.

4.4.2 – $EDAI_2$ Surface Passivation

To improve stability of $FA_{0.8}Cs_{0.2}PbI_3$ 1.55 eV solar cells under 85°C light, $EDAI_2$ surface passivation was applied on top of the perovskite absorber before evaporating the C_{60} ETL. $EDAI_2$ surface passivation has been shown to improve the perovskite absorber/electron transport layer interface for improved V_{OC}.[26,27]

For this thesis, $FA_{0.8}Cs_{0.2}PbI_3$ 1.55 eV absorbers were treated with and without 7 mM $EDAI_2$ surface passivation in solar cells to determine if potential interfacial improvements could improve stability under 85°C light. Figure 4.9 shows that solar cells without $EDAI_2$ surface passivation degraded sharply after the first 24 hours of 85°C light aging, with the median maximum power point tracked efficiency dropping to 6% (~37% of the efficiency measured before aging). Solar cells with $EDAI_2$ surface passivation fared much better under 85°C light aging.

After 24 hours, the median maximum power point decreased to 13.5% (~67% of the efficiency measured before aging). $EDAI_2$-passivated solar cells maintained a greater percentage of their initial median maximum power point tracked efficiency after 231 hours of aging than their non-passivated counterparts after the first 24 hours. The $EDAI_2$ surface passivation slowed the decline of both steady-state V_{OC} and fill factor of the solar cells during 85°C light aging. This indicates an improvement in the perovskite absorber/electron transport layer interface, in agreement with published literature.[26,27]

As shown in Figure 4.9, $FA_{0.8}Cs_{0.2}PbI_3$ solar cells passivated with $EDAI_2$ also demonstrated improved stability under 85°C light. Changes to stability under 85°C light were not discussed in these publications.[26,27] It is postulated that $EDAI_2$ may act as a barrier layer to prevent or slow down iodide halide migration from the $FA_{0.8}Cs_{0.2}PbI_3$ perovskite absorber into the C_{60} electron transport layer, reducing loss to open-circuit voltage and fill factor over time and therefore increasing the overall solar cell stability and performance under 85°C light aging.

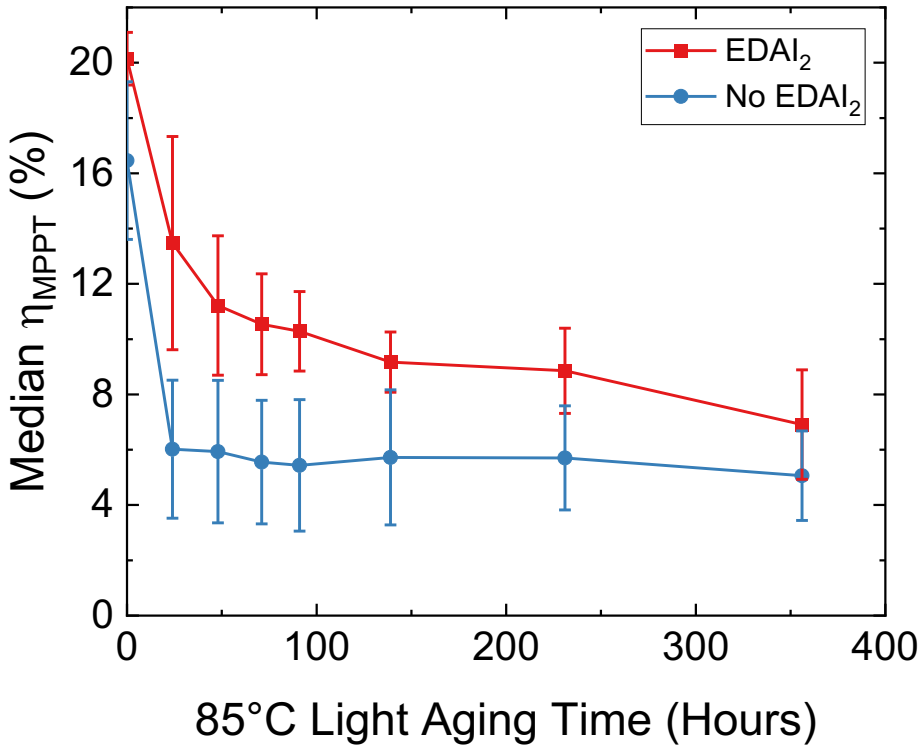

Figure 4.9. Median maximum power point tracked efficiency of solar cells with and without $EDAI_2$ surface passivation under 85°C light aging. Device stack: FTO/Me-4PACz/Al_2O_3 nanoparticles/$FA_{0.8}Cs_{0.2}PbI_3$ + BzSCN bulk additive/$EDAI_2$ (if applicable)/C_{60}/ALD SnO_2/Sputtered IZO/Au. All solar cells were full area, on-cell encapsulated. Median absolute deviation is shown in error bars. $EDAI_2$-passivated solar cells demonstrated significantly enhanced stability under 85°C light. 18 solar cells of 0.25 cm^2 area were fabricated and tested for each condition.

4.4.3 – PbI_2 Stoichiometry

Excess PbI_2 in the perovskite precursor stoichiometry may improve initial perovskite solar cell efficiency by passivating deep level traps at perovskite grain boundaries and improving charge transfer at the perovskite absorber/electron transport layer interface.[28-30] But, reports have highlighted that excess PbI_2 in the perovskite precursor stoichiometry may lead to poor solar cell stability under illumination due to the photolysis of unreacted PbI_2 into metallic lead and iodine.[31] Up to this point in the study, all $FA_{0.8}Cs_{0.2}PbI_3$ perovskite thin films and solar cells were fabricated using 1 mol% excess PbI_2 stoichiometry in the precursor. The effect of PbI_2 stoichiometry on 85°C light stability, however, was unclear.

To test the effect on stability of PbI_2 perovskite precursor stoichiometry for $FA_{0.8}Cs_{0.2}PbI_3$, five different PbI_2 perovskite precursor stoichiometries were examined under 85°C light aging: 5 mol% deficient, 1 mol% deficient, stoichiometric, 1 mol% excess, and 5 mol% excess PbI_2. $FA_{0.8}Cs_{0.2}PbI_3$ solar cells were fabricated with 5 mol% deficient, 1 mol% deficient, stoichiometric, 1 mol% excess, and 5 mol% excess PbI_2 stoichiometries – all utilizing the optimized $EDAI_2$ surface passivation – and tested under 85°C light aging. A sharp decline in solar cell performance over the first 48 hours of 85°C light aging was observed for all PbI_2 stoichiometries. This was mostly attributable to a loss in steady-state V_{OC} and fill factor, indicating that the degradation route is likely related to the interfaces between the perovskite absorber and charge transport layers.[32] A loss of steady-state J_{SC}, on the other hand, would likely indicate degradation of the perovskite absorber itself with less material able to absorb light and generate photoexcited charges.[33]

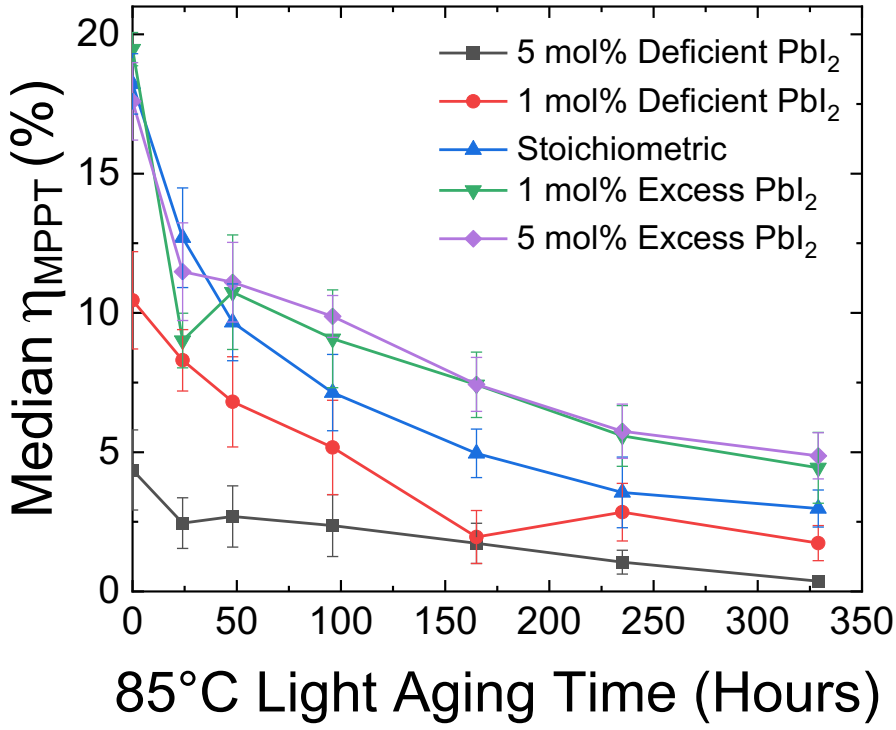

Figure 4.10. Median maximum power point tracked efficiency of solar cells with different PbI_2 stoichiometries under 85°C light aging. Median absolute deviation is shown in error bars. Device stack: FTO/Me-4PACz/Al_2O_3 nanoparticles/$FA_{0.8}Cs_{0.2}PbI_3$ + BzSCN bulk additive/$EDAI_2$/C_{60}/ALD SnO_2/Sputtered IZO/Au. All solar cells were full area, on-cell encapsulated. PbI_2 excess solar cells exhibit improved stability. 9 solar cells of 0.25 cm^2 area were fabricated and tested for each condition.

As shown in Figure 4.11, the 1 and 5 mol% excess PbI_2 solar cells retained noticeably more steady-state J_{SC} than the stoichiometric solar cells after hundreds of hours under 85°C light aging.

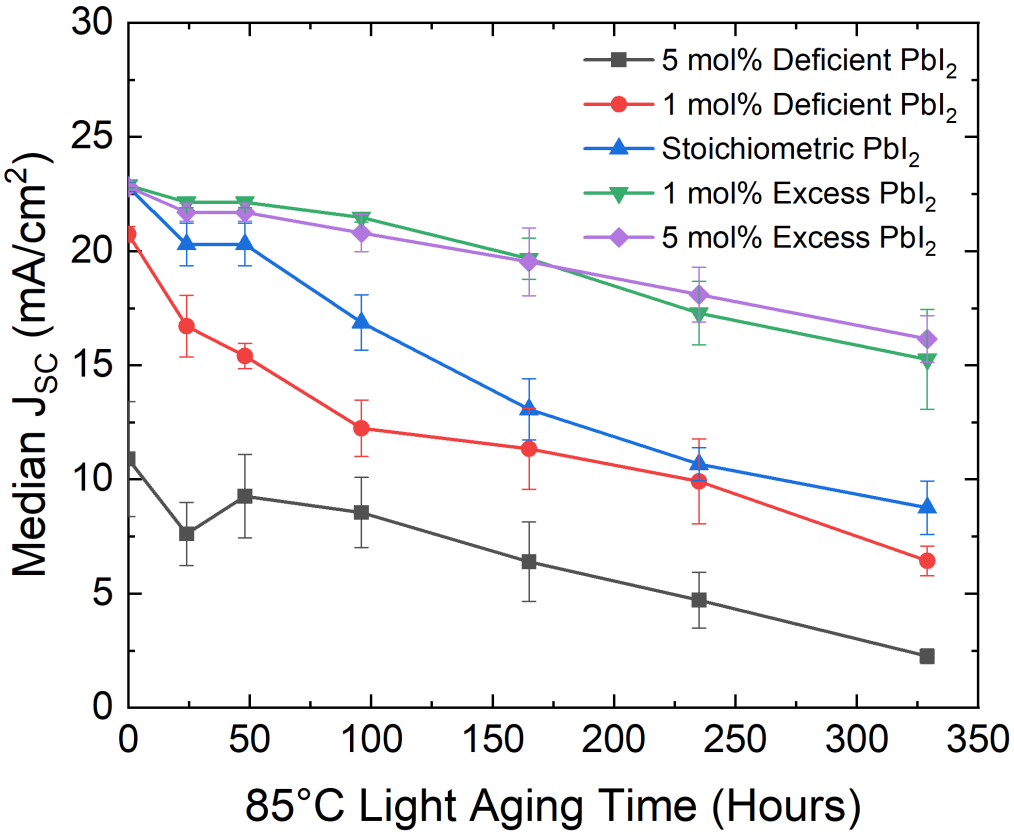

Figure 4.11. Median steady-state J_{SC} of solar cells with different PbI_2 stoichiometries under 85°C light aging. Median absolute deviation is shown in error bars. PbI_2 excess solar cells retain the most steady-state J_{SC} during aging by a significant margin. 9 solar cells of 0.25 cm^2 area were fabricated and tested for each condition.

Table 4.1 confirms that the median J_{SC} ratio at t_{329}/t_0 hours is greatest for the solar cells with PbI_2 excess stoichiometry.

PbI_2 Stoichiometry	t_{329}/t_0 Hours Median J_{SC} Ratio (%)
5 mol% Deficient	20.7
1 mol% Deficient	31.0
Stoichiometric	38.4
1 mol% Excess	66.7
5 mol% Excess	70.8

Table 4.1. Ratio in percentage of median steady-state J_{SC} of solar cells with different PbI_2 stoichiometries after 329 hours of 85°C light aging compared to 0 hours (before aging). 1 mol% and 5 mol% excess PbI_2 solar cells exhibited substantially less median steady-state J_{SC} loss.

J-V curves for a high performing solar cell for each of the stoichiometric, 1 mol% excess, and 5 mol% excess PbI_2 stoichiometries are presented in Figure 4.12. While all three solar cells produced ~23 mA/cm^2 J_{SC} at t_0, the 1 mol% and 5 mol% excess PbI_2 solar cells retained significantly more of this initial value over time. After 329 hours of 85°C light aging, the J_{SC} values were as follows: 11.4 mA/cm^2 (stoichiometric), 19.7 mA/cm^2 (1 mol% excess), and 15.8 mA/cm^2 (5 mol% excess) extracted from the data shown in Figure 4.12 d, h, and l, respectively.

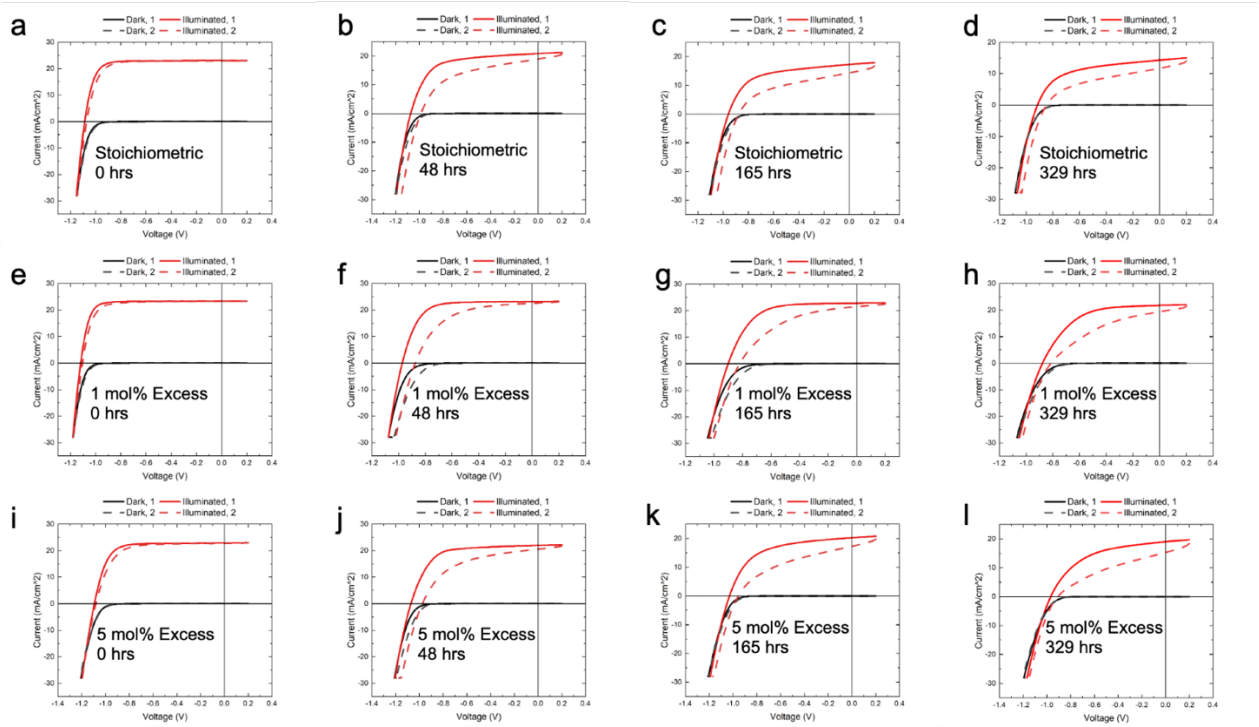

Figure 4.12. J-V curves of a sample solar cell with stoichiometric (a-d), 1 mol% excess (e-h), and 5 mol% excess (i-l) PbI_2 at various 85°C light aging points. The solar cells with PbI_2 excess stoichiometry exhibited significantly less steady-state J_{SC} loss over time for improved stability.

To determine if there was significant $FA_{0.8}Cs_{0.2}PbI_3$ perovskite absorber material degradation, XRD scans of pristine perovskite half-stacks with the five PbI_2 stoichiometries were compared with XRD scans of perovskite films aged under 85°C light taken from deconstructed solar cells. Comparison between XRD peaks for the half-stacks in Figure 4.13a and b show that, despite significant overall solar cell performance loss after 329 hours of 85°C light aging, there was little structural change in the perovskite absorber itself for the excess PbI_2 half-stacks.

Orthorhombic $CsPbI_3$ (δ-$CsPbI_3$) phases were detected for the PbI_2-deficient half-stacks. These phases also were weakly present for the aged stoichiometric sample, indicating some degradation from its initial cubic phase. This material degradation to

some δ-$CsPbI_3$ phases with poor optical and electrical properties could be the cause for the large decrease in steady-state J_{SC} for stoichiometric PbI_2 solar cells over time.[34]

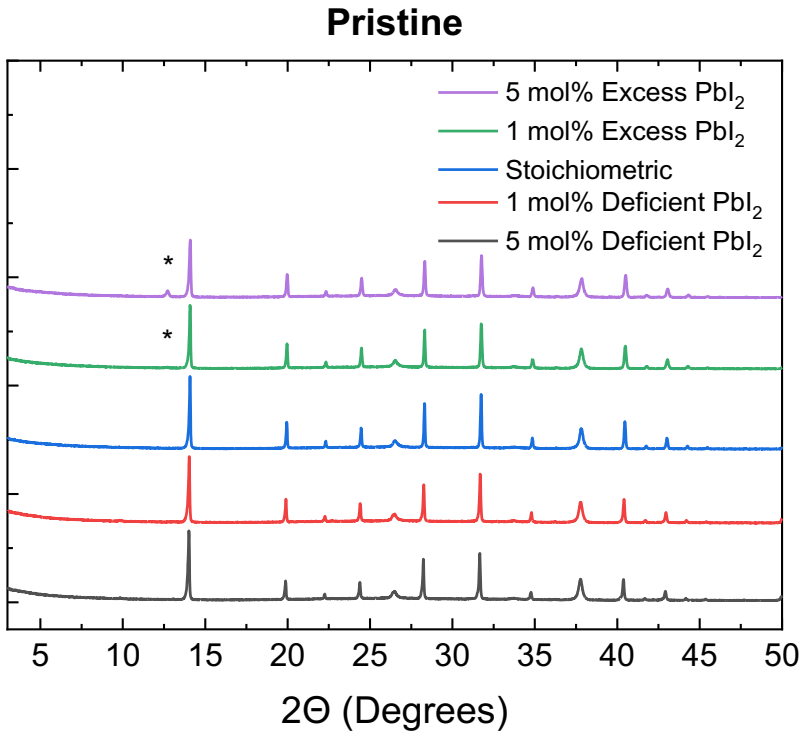

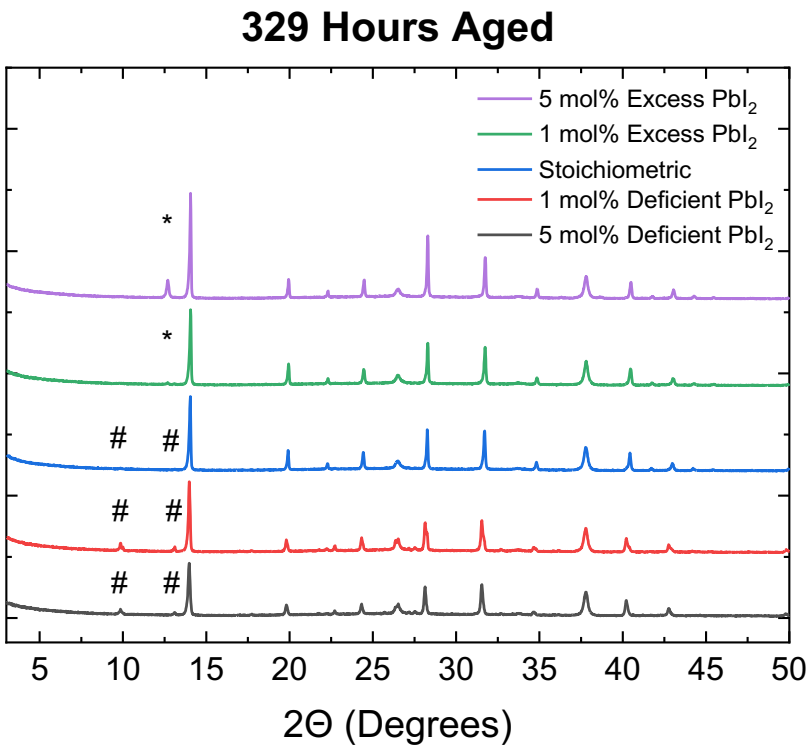

Figure 4.13. a) XRD patterns of pristine perovskite half-stacks. The * denotes PbI_2. PbI_2 peaks are present for both 1 mol% and 5 mol% excess PbI_2 samples, as expected. b) XRD patterns of perovskite layers from encapsulated solar cells that were aged under 85°C light for 329 hours. The encapsulation glue, top electrode, and glass cover slip were removed for measurement. The * denotes PbI_2 while the # denotes δ-$CsPbI_3$ phases. The PbI_2 peak grows in both PbI_2 excess samples but more strongly for 5 mol% excess. δ-$CsPbI_3$ phases grow significantly in intensity for 1 mol% and 5 mol% deficient PbI_2 samples and weakly for the stoichiometric sample after 329 hours of 85°C light aging.

To investigate whether the $EDAI_2$ surface passivation improved the stability of the perovskite absorber itself, as opposed to improving the perovskite absorber/C_{60} ETL interface in a complete solar cell, a thin film with and without $EDAI_2$ surface passivation was fabricated per PbI_2 stoichiometric condition. All thin films were edge-encapsulated, aged under 85°C light, and periodically taken out of the aging setup for UV-visible absorbance measurements presented in Figure 4.14.

1 mol% and 5 mol% excess PbI_2 thin films surface passivated with $EDAI_2$ exhibited almost no shift or change in absorption onset in UV-visible absorbance spectra over 720 hours of 85°C light aging. PbI_2 excess stoichiometry, combined with $EDAI_2$ surface passivation, markedly improved perovskite absorber stability under 85°C light aging.

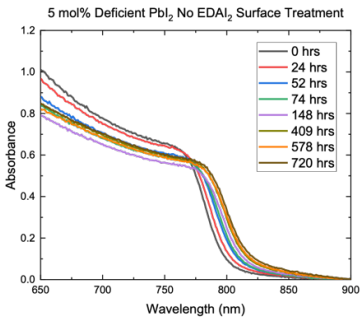
5 mol% Deficient PbI2 No EDAI2 Surface Treatment
Absorbance
Wavelength (nm)
0 hrs
24 hrs
52 hrs
74 hrs
148 hrs
409 hrs
578 hrs
720 hrs

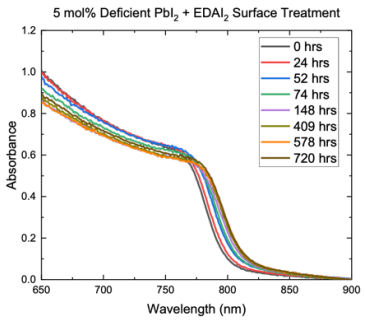
5 mol% Deficient PbI2 + EDAI2 Surface Treatment
Absorbance
Wavelength (nm)
0 hrs
24 hrs
52 hrs
74 hrs
148 hrs
409 hrs
578 hrs
720 hrs

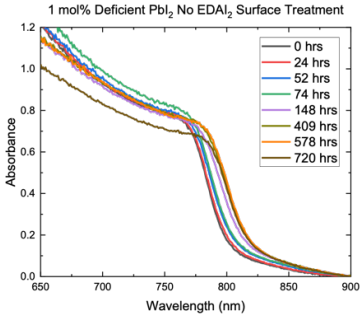
1 mol% Deficient PbI2 No EDAI2 Surface Treatment
Absorbance
Wavelength (nm)
0 hrs
24 hrs
52 hrs
74 hrs
148 hrs
409 hrs
578 hrs
720 hrs

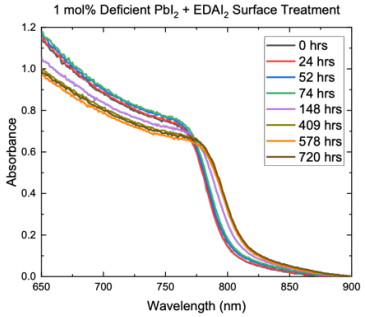
1 mol% Deficient PbI2 + EDAI2 Surface Treatment
Absorbance
Wavelength (nm)
0 hrs
24 hrs
52 hrs
74 hrs
148 hrs
409 hrs
578 hrs
720 hrs

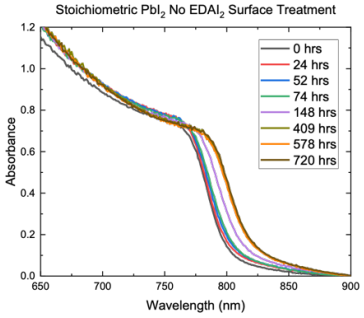
Stoichiometric PbI2 No EDAI2 Surface Treatment
Absorbance
Wavelength (nm)
0 hrs
24 hrs
52 hrs
74 hrs
148 hrs
409 hrs
578 hrs
720 hrs

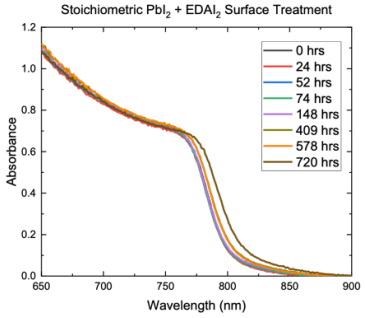
Stoichiometric PbI2 + EDAI2 Surface Treatment
Absorbance
Wavelength (nm)
0 hrs
24 hrs
52 hrs
74 hrs
148 hrs
409 hrs
578 hrs
720 hrs

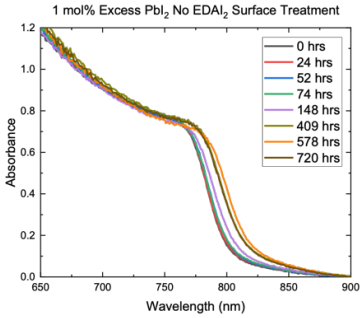
1 mol% Excess PbI2 No EDAI2 Surface Treatment
Absorbance
Wavelength (nm)
0 hrs
24 hrs
52 hrs
74 hrs
148 hrs
409 hrs
578 hrs
720 hrs

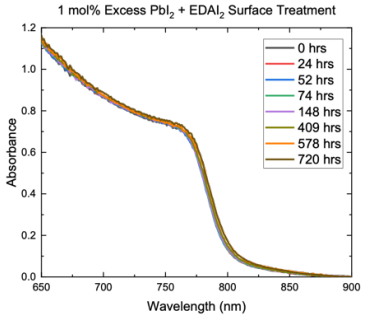
1 mol% Excess PbI2 + EDAI2 Surface Treatment
Absorbance
Wavelength (nm)
0 hrs
24 hrs
52 hrs
74 hrs
148 hrs
409 hrs
578 hrs
720 hrs

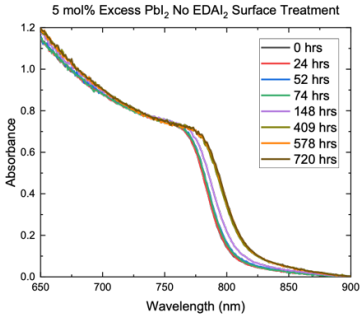
5 mol% Excess PbI2 No EDAI2 Surface Treatment
Absorbance
Wavelength (nm)
0 hrs
24 hrs
52 hrs
74 hrs
148 hrs
409 hrs
578 hrs
720 hrs

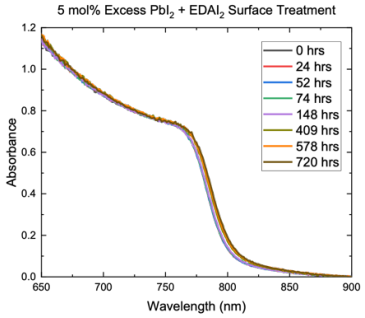
5 mol% Excess PbI2 + EDAI2 Surface Treatment
Absorbance
Wavelength (nm)
0 hrs
24 hrs
52 hrs
74 hrs
148 hrs
409 hrs
578 hrs
720 hrs

Figure 4.14. UV-visible absorbance plots of $FA_{0.8}Cs_{0.2}PbI_3$ thin films with and without $EDAI_2$ surface passivation for different PbI_2 stoichiometries under 85°C light aging. All PbI_2 deficient thin films exhibited poor material stability with strong red shifts over time, indicative of material degradation. $EDAI_2$ surface passivation strongly reduced material degradation for PbI_2 excess thin films.

4.5 – Conclusion

For this thesis, 1.55 eV $FA_{0.8}Cs_{0.2}PbI_3$ single junction perovskite solar cells were studied as a representative middle band gap subcell absorber relevant for all-perovskite triple junction solar cells. Improvements to efficiency, reproducibility, and stability were achieved.

The incorporation of a benzylammonium thiocyanate bulk additive and the use of a C_{60}/ALD SnO_2 top contact device stack yielded efficient and reproducible $FA_{0.8}Cs_{0.2}PbI_3$ solar cells, with a maximum power point tracked efficiency of 21.2% reached. Further modification to a C_{60}/ALD SnO_2/IZO/Au device stability stack increased solar cell reproducibility in a tandem-relevant context. $EDAI_2$ surface passivation and excess PbI_2 perovskite precursor stoichiometry improved the stability of 1.55 eV $FA_{0.8}Cs_{0.2}PbI_3$ single junction perovskite solar cells in a tandem-relevant C_{60}/ALD SnO_2/IZO/Au top contact device stack under 85°C light aging. For perovskite absorbers with similar band gaps to $FA_{0.8}Cs_{0.2}PbI_3$, these stability enhancements may be transferrable.

Building on the advancements from the work detailed in this chapter, a similar mixed $EDAI_2$/$EDABr_2$ surface passivation and the C_{60}/ALD SnO_2 top contact device stack were used for 1.97 eV wide band gap single junction perovskite solar cells fabricated in Chapter 5 with high efficiency and reproducibility. C_{60}/ALD SnO_2/IZO top contacts were used in all-perovskite triple junction solar cells subsequently fabricated for this thesis, achieving a champion maximum power point tracked efficiency of 27.3%.

Chapter 4 References

1. Tyagi, P. et al. Multivariate approach for studying the degradation of perovskite solar cells. *Solar Energy,* **193**, 12-19 (20219).

2. Duong, T. et al. Light and elevated temperature induced degradation (LeTID) in perovskite solar cells and development of stable semi-transparent cells. *Solar Energy Materials and Solar Cells*, **188**, 27-36 (2018).

3. Le, T. et al. Tailoring Wetting Processes of Organic Hole-Transport Interlayers for Slot-Die-Coated Perovskite Solar Cells. *Sol. RRL*, 2400437 (2024).

4. Khenkin. M.V. et al. Consensus statement for stability assessment and reporting for perovskite photovoltaics based on ISOS procedures. *Nature Energy*, **5**, 35-49 (2020).

5. Noman, M. et al. 26.48% efficient and stable $FAPbI_3$ perovskite solar cells employing $SrCu_2O_2$ as hole transport layer. *RSC Adv.*, **13**, 1892 (2023).

6. Zheng, Z. et al. Development of formamidinium lead iodide-based perovskite solar cells: efficiency and stability. *Chem. Sci.*, **13**, 2167-2183 (2022).

7. Frohna, K. et al. Nanoscale Chemical Heterogeneity Dominates the Optoelectronic Response of Alloyed Perovskite Solar Cells. *Nat. Nanotechnol.*, **17**, 2, 190-196 (2022).

8. Charles, B. et al. Phase Behavior and Substitution Limit of Mixed Cesium-Formamidinium Lead Triiodide Perovskites. *Chem. Mater.*, **32**, 6, 2282-2291 (2020).

9. McMeekin, D. et al. A mixed-cation lead mixed-halide perovskite absorber for tandem solar cells. *Science*, **351**, 6292, 151-155 (2016).

10. Oliver, R. D. J. et al. Thermally Stable Passivation toward High Efficiency Inverted Perovskite Solar Cells. *ACS Energy Lett.*, **5**, 11, 3336-3343 (2020).

11. Klug, M. T. et al. Metal composition influences optoelectronic quality in mixed-metal lead–tin triiodide perovskite solar absorbers. *Energy Environ. Sci.*, **13**, 1776–1787 (2020).

12. Bowman, A. R. et al. Microsecond Carrier Lifetimes, Controlled p-Doping, and Enhanced Air Stability in Low-Bandgap Metal Halide Perovskites. *ACS Energy Lett.*, **4**, 2301–2307 (2019).

13. Suo, J. et al. The Dual Use of SAM Molecules for Efficient and Stable Perovskite Solar Cells. *Adv. Energy Mater.* 2400205 (2024).

14. Liang, P. et al. Roles of Fullerene-Based Interlayers in Enhancing the Performance of Organometal Perovskite Thin-Film Solar Cells. *Adv. Energy Mater.*, **5**, 1402321 (2015).

15. Said, A. et al. Sublimed C_{60} for efficient and repeatable perovskite-based solar cells. *Nat. Commun.*, **15**, 708 (2024)

16. Lee, Y. et al. Efficient planar perovskite solar cells using passivated tin oxide as an electron transport layer. *Adv. Sci.*, **5**, 6 (2018).

17. Jeong, S. et al. Atomic layer deposition of a SnO_2 electron-transporting layer for planar perovskite solar cells with a power conversion efficiency of 18.3%. Chem. Commun., **55**, 17, 2433-2436 (2019).

18. Wang, H. Hydrogen peroxide-modified SnO_2 as electron transport layer for perovskite solar cells with efficiency exceeding 22%. *J. Power Sources*, **481**, 229160 (2021).

19. Ren, N. et al. 50°C low-temperature ALD SnO_2 driven by H_2O_2 for efficient perovskite and perovskite/silicon tandem solar cells. *Appl. Phys. Lett.*, **121**, 3, (2022).

20. Xing, Z. et al. Atomic layer deposition of metal oxides in perovskite solar cells: present and future. *Small Methods*, **4**, 12, 2000588 (2020).

21. Svanstrom, S. et al. Degradation Mechanism of Silver Metal Deposited on Lead Halide Perovskites. *ACS Appl. Mater. Interfaces*, **12**, 6, 7212-7221 (2020).

22. Kim, H. et al. Managing the lifecycle of perovskite solar cells: Addressing stability and environmental concerns from utilization to end-of-life. *eScience*, **2**, 100243 (2024).

23. Lin, Y. et al. A piperidinium salt stabilizes efficient metal-halide perovskite solar cells. *Science*, **369**, 6499, 96-102 (2020).

24. Kumar, V. et al. A Dense Conformal Electrode Array for High Spatial Resolution Stimulation of Electrosensory Systems. *Adv. Mater. Technol.*, **8**, 2200354 (2023).

25. Prasanna, R. et al. Design of low bandgap tin–lead halide perovskite solar cells to achieve thermal, atmospheric and operational stability. *Nature Energy*, **4**, 939-947 (2019).

26. Hu, S. et al. A Universal Surface Treatment for p–i–n Perovskite Solar Cell. *ACS Appl. Mater. Interfaces*, **14**, 50, 56290–56297 (2022).

27. Pan, Y. et al. Surface chemical polishing and passivation minimize non-radiative recombination for all-perovskite tandem solar cells. *Nature Communications*, **15**, 7335 (2024).

28. Chen, Q. et al. Controllable self-induced passivation of hybrid lead iodide perovskites toward high performance solar cells. *Nano Lett.*, **14**, 4158-4163 (2014).

29. Chen, Y. et al. Mechanism of PbI_2 in Situ Passivated Perovskite Films for Enhancing the Performance of Perovskite Solar Cells. *ACS Appl. Mater. Interfaces*, **11**, 44101-44108 (2019).

30. Cao, D.H. et al. Remnant PbI_2, an unforeseen necessity in high-efficiency hybrid perovskite-based solar cells? *APL Mater.*, **2** (2014)

31. Roose, B. et al. Critical Assessment of the Use of Excess Lead Iodide in Lead Halide Perovskite Solar Cells. *. Phys. Chem. Lett.*, **11**, 16, 6505–6512 (2020).

32. Stolterfoht, M. et al. The Impact of Energy Alignment and Interfacial Recombination on the Internal and External Open-Circuit Voltage of Perovskite Solar Cells. *Energy & Environmental Science*, **12**, 9, 2778–88 (2019).

33. Bi, E. et al. Efficient Perovskite Solar Cell Modules with High Stability Enabled by Iodide Diffusion Barriers. *Joule*, **3**, 11 (2019).

34. Ke, F. et al. Preserving a robust $CsPbI_3$ perovskite phase via pressure-directed octahedral tilt. *Nature Communications*, **12**, 461 (2021).

Chapter 5

Novel Crystallization Method for Fabrication of Efficient and Reproducible 1.97 eV Wide Band Gap Perovskite Absorbers and Single Junction Solar Cells

5.1 – Introduction

This chapter details a novel crystallization method developed to create efficient and reproducible solution-processed ~2 eV (1.97 eV) wide band gap perovskite absorbers and single junction solar cells. The novel crystallization method, involving the addition of a mixture of dimethylammonium bromide (DMABr) and dimethylammonium iodide (DMAI) salts – "DMAX" – to a 1.97 eV $FA_{0.9}Cs_{0.1}Pb(Br_{0.68}I_{0.32})_3$ perovskite precursor solution in neat DMF solvent, is presented. The DMAX salts replace the DMSO solvent used in standard perovskite precursor solutions dissolved in DMF and DMSO solvents. The crystallization using the DMF/DMAX method is slowed and driven through an intermediate phase during a two-step annealing process.

After annealing, thin films crystallized using the DMF/DMAX crystallization method exhibit larger median apparent grain sizes, more homogeneous morphology, and longer carrier lifetimes compared to DMF/DMSO control thin films. Thin films crystallized using both DMF/DMAX and DMF/DMSO methods are characterized by 1D-XRD, 2D-XRD, GIWAXS, XPS, SEM, and TRPL measurements.

1.97 eV single junction solar cells are fabricated and tested. Compared to the DMF/DMSO control, the DMF/DMAX crystallization method improves solar cell median maximum power point tracked efficiency, reproducibility, and operational stability. The champion 1.97 eV single junction perovskite solar cell fabricated using the DMF/DMAX crystallization method achieves near-record 1.42 V steady-state open-circuit voltage and 13.7% maximum power point tracked efficiency.

The stability of DMF/DMAX and DMF/DMSO 1.97 eV single junction perovskite solar cells is tested with 30 minutes of continuous maximum power point tracking under 1-sun intensity AM 1.5G illumination. The DMF/DMAX solar cell retains 93.4% of its initial efficiency, compared to 82.1% for the DMF/DMSO solar cell, demonstrating superior operational stability.

As detailed in previous thesis work conducted in the Snaith Lab by Dr. Emil Dyrvik, University of Oxford, ~2 eV single junction perovskite solar cells fabricated using the traditional DMF/DMSO crystallization method suffered from serious reproducibility issues.[1] Compared to the DMF/DMSO control, the DMF/DMAX crystallization method delivered more reproducible 1.97 eV single junction perovskite solar cells as shown by the more consistent performance parameter results achieved using DMF/DMAX.

2 eV wide band gap perovskite absorbers are crucial for implementation as wide band gap top subcell absorbers in p-i-n architecture all-perovskite triple junction tandem solar cells because these 2 eV wide band gap subcell absorbers must produce the highest voltage of the three subcells to achieve higher efficiencies. Using a top subcell absorber with a band gap in the 1.95-2.05 eV range, Hörantner et al. calculated theoretical

maximums for all-perovskite triple junction tandem solar cell performance of 33% and 36.6% power conversion efficiency (PCE), as shown in Figures 5.1 and 5.2.[2]

For the 33% PCE theoretical maximum shown in Figure 5.1, Hörantner et al. used existing performance parameters in the calculation. For the 36.6% PCE theoretical maximum shown in Figure 5.2, Hörantner et al. boosted the efficiency by assuming in the calculation significant improvements to the recombination layers, charge transport layers, and perovskite absorbers themselves beyond what has been scientifically published. This theoretical estimation assumed the ~2.0 eV perovskite solar cell achieved an open-circuit voltage greater than 1.5 V, which has yet to be achieved in the field.

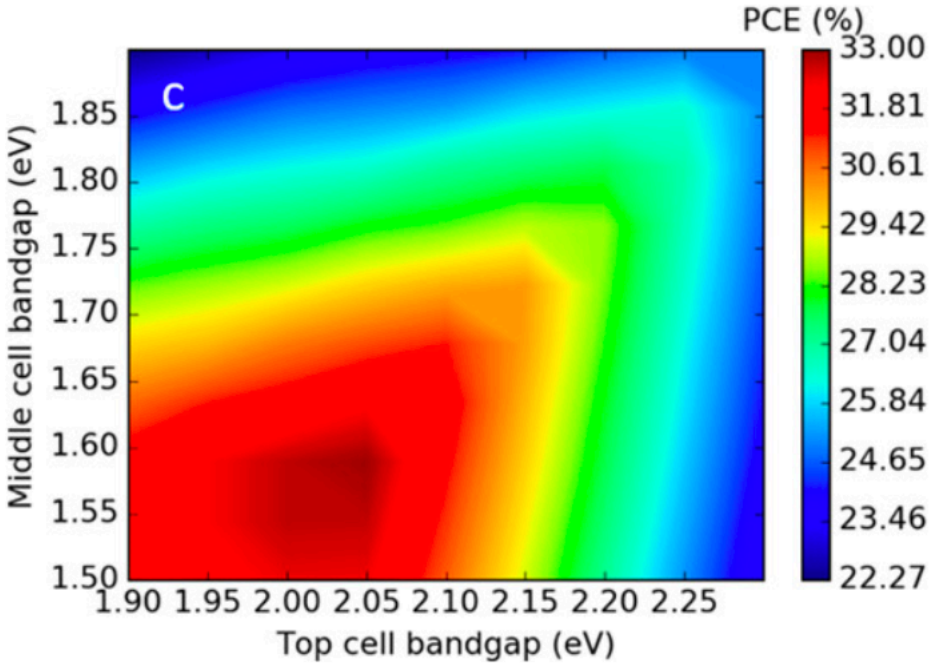

Figure 5.1. Theoretical all-perovskite triple junction tandem solar cell power conversion efficiency based on band gap combinations for top and middle subcells, assuming a 1.22 eV narrow band gap bottom subcell. Adapted with permission from [2]. Copyright 2017 American Chemical Society.

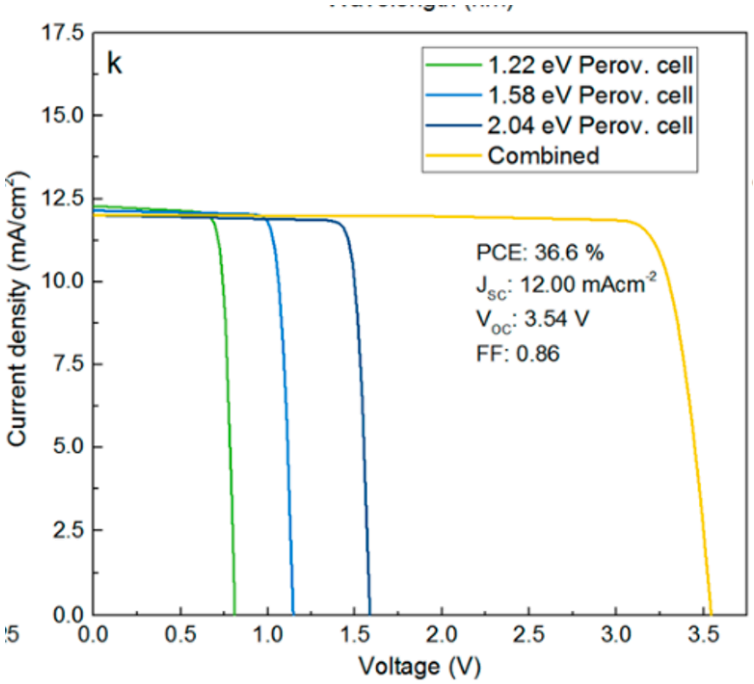

Figure 5.2. J-V curves of theoretical 36.6% PCE all-perovskite triple junction tandem, 1.22 eV narrow band gap single junction, 1.58 eV middle band gap single junction, and 2.04 eV wide band gap single junction solar cells. Adapted with permission from [2]. Copyright 2017 American Chemical Society.

Although 2 eV wide band gap perovskite absorbers are necessary for all-perovskite triple junction tandem solar cells, they remain relatively unexplored compared to their middle and narrow band gap perovskite absorber counterparts. To date, 2 eV perovskite solar cells exhibit significantly lower open-circuit voltage performance relative to theoretical expectation and can suffer from poor reproducibility due to a lack of halide heterogeneity in the bulk and at interfaces.[3,4] The reported V_{OC} of high-performance ~2 eV (1.94-2.05 eV) perovskite single junction solar cells are shown in Table 5.1, with only one published result achieving V_{OC} values greater than 1.4 V.

Composition	Band Gap (eV)	V_{OC} (V)	Publication Year	Institution
$FA_{0.83}Cs_{0.17}Pb(Br_{0.7}I_{0.3})_3$	1.94	1.27	2019[5]	University of Oxford
$FAPb(Br_{0.73}I_{0.27})_3$	2.00	1.35	2022[6]	Korea University
$FA_{0.70}Cs_{0.15}MA_{0.15}Pb(Br_{0.85}I_{0.15})_3$	2.05	1.27	2022[7]	KAUST
$MAPb(Br_{0.35}I_{0.5}\ Cl_{0.15})_3$	1.96	1.28	2023[8]	Seoul National University
$Rb_{0.15}Cs_{0.85}Pb(Br_{0.583}I_{0.417})_3$	2.01	1.312	2023[9]	University of Toronto
$FA_{0.8}Cs_{0.2}Pb(Br_{0.7}I_{0.3})_3$	2.00	1.325	2023[10]	Hanyang University
$FA_{0.85}Cs_{0.15}Pb(Br_{0.6}I_{0.4})_3$	1.97	1.44	2023[3]	University of Toronto

Table 5.1. High-performance ~2 eV band gap solar cell V_{OC} values published to date. All V_{OC} values are from single junction solar cells with the corresponding perovskite composition. Only one ~2 eV composition has achieved a V_{OC} value greater than 1.4 V.

To realize the efficiency potential of all-perovskite triple junction solar cells, a 2 eV band gap top subcell must produce V_{OC} greater than 1.5 V. Yet, to date, only one published result has exceeded even 1.4 V. Controlling crystallization kinetics via changes to the perovskite precursor solution offers an opportunity to improve 2 eV perovskite material quality and reproducibility and therefore enhance all-perovskite triple junction tandem solar cell efficiency.

5.2 – DMF/DMAX Crystallization Method and Thin Film Characterization of 1.97 eV Perovskite Absorbers

5.2.1 – Development of DMF/DMAX Crystallization Method

Perovskite precursor solutions are typically crystallized from a DMF/DMSO solvent system. However, DMF/DMSO presents challenges to reproducibility and stability. The DMF/DMAX solvent system was created to address these challenges. 1.97 eV wide band gap perovskite absorbers and single junction solar cells fabricated using the novel DMF/DMAX crystallization method resulted in more efficient, reproducible, and operationally stable solar cells than those fabricated using DMF/DMSO.

For the standard DMF/DMSO crystallization method, the “antisolvent” quench method is often used to induce crystallization during spin-coating. An antisolvent is a solvent that perovskite precursor materials do not dissolve in appreciably. The dripping of an antisolvent on top of a liquid perovskite film during spin-coating induces nucleation of perovskite-DMSO complexes on the order of seconds, quickly creating a series of intermediate phases.[11] Annealing at sufficient temperature after spin-coating provides the thermodynamic drive to fully crystallize the perovskite as desired.

While simple to implement, the DMF/DMSO solvent system introduces several challenges for perovskites of various band gaps. Perovskites crystallized from DMF/DMSO solvent systems are often characterized by relatively small grain sizes, more grain boundaries, and relatively high defect densities.[12] These offer more potential pathways for undesirable trap-assisted recombination, harming solar cell performance. In addition, significant amounts of DMSO solvent can remain trapped in a crystallized perovskite film, even after annealing, due to its high 189°C boiling point and strong

interaction with PbI_2.[13] Trapped solvents like DMSO can absorb moisture more readily at perovskite grain boundaries, decreasing the stability of the perovskite absorber and reducing its performance in solar cells more quickly.[14]

To combat the challenges created by DMSO, substitutes have been explored. Replacing DMSO with a different solvent, such as NMP, has been reported to improve perovskite solar cell stability.[15] The replacement of DMSO with dimethylammonium chloride (DMACl) salts is particularly encouraging. McMeekin et al. have shown that DMACl salts control perovskite intermediate precursor phases for a thermodynamically-driven crystallization kinetics process, slowing the rate of perovskite crystallization from seconds (with DMF/DMSO) to tens of minutes.[12]

DMA^+ cations from the DMACl induce intermediate 2H, 4H, and 6H polytype phases during spin-coating. Upon ~170°C higher temperature annealing, DMACl is largely removed and the perovskite is fully crystallized to the desired 3C cubic phase. Slowing the rate of crystallization from the DMF/DMACl system was found to improve perovskite material crystallinity and reproducibility.[12]

Perovskite solar cells produced using the DMF/DMACl crystallization method have exhibited a substantial boost in their stability. The champion DMF/DMACl solar cell by McMeekin et al. retained 80% of its efficiency after 1,410 hours under illumination at 65°C in air.

For this thesis, the DMF/DMACl crystallization method was first explored for 1.97 eV wide band gap perovskite absorbers. The 1.97 eV perovskite precursor, however, did not dissolve in the DMF/DMACl solvent system – potentially due to the precipitation of CsCl.

A novel 68 mol%:32 mol% stoichiometric mixture – with a similar chemical structure to DMACl – of dimethylammonium bromide (DMABr) and dimethylammonium iodide (DMAI) additive salts (hereafter referred to as DMAX) was created as a replacement.

DMAX salts were added to the DMF solvent in various amounts to examine the effect on material properties. 0-100 mol% excess DMAX amounts relative to the stoichiometry of the $FA_{0.9}Cs_{0.1}Pb(Br_{0.68}I_{0.32})_3$ perovskite were added to precursor solutions. These precursor solutions were spin-coated on FTO/Me-4PACz/Al_2O_3 nanoparticles to create perovskite half-stacks. After spin-coating, all half-stacks were annealed at 160°C for 10 minutes in nitrogen. Photographs of the 0-100 mol% excess DMAX range half-stacks are presented in Figure 5.3.

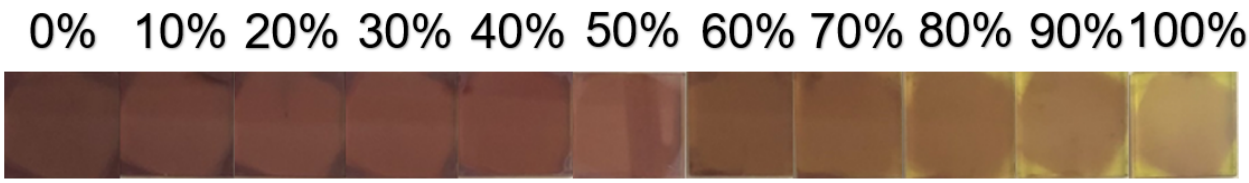

Figure 5.3. Series of photographs of FTO/Me-4PACz/Al_2O_3 nanoparticles/$FA_{0.9}Cs_{0.1}Pb(Br_{0.68}I_{0.32})_3$ perovskite half-stacks spin-coated with various amounts of DMAX additive, where percentages are expressed in excess mol% amounts of DMAX relative to lead added to the bulk of the perovskite. Up to 50 mol% excess DMAX, the fully annealed half-stacks appeared smooth and uniform. From 60 mol% excess DMAX onwards, the half-stacks appeared increasingly hazy and inhomogeneous. Light yellow regions near the edges of the 80-100 mol% excess DMAX half-stack are present, indicative of PbI_2 regions.

Notable visible changes to the smoothness and uniformity of the half-stacks occur with more excess DMAX content, including increasing haziness, inhomogeneity, and yellowing. Characterization techniques that probe beyond the visible, however, are needed to better understand these changes.

1D-XRD measurements were taken of the 0-100 mol% excess DMAX half-stacks to probe crystalline orientation. As shown in Figure 5.4, the (100) peak increases in intensity from 0 mol% to a maximum value at 60 mol% excess DMAX.

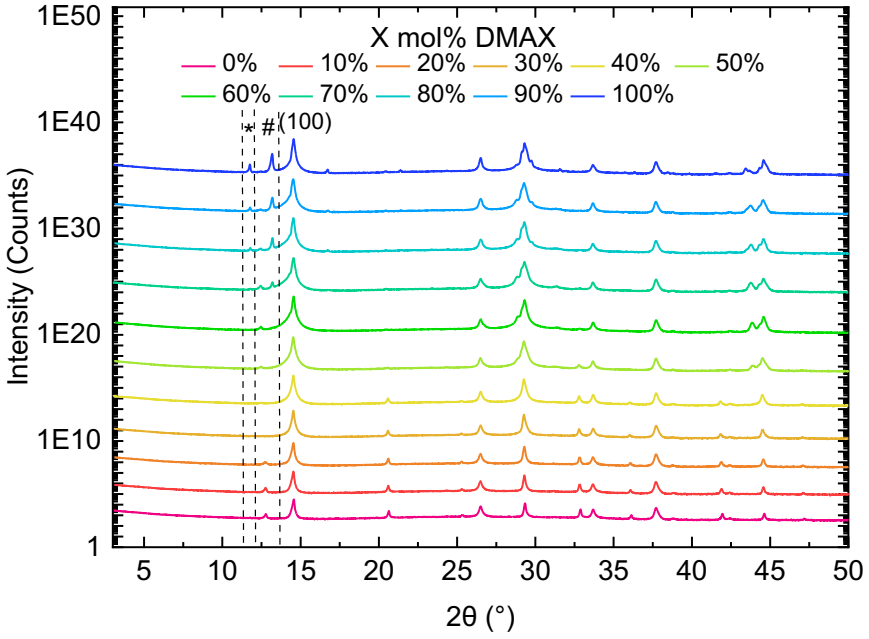

Figure 5.4. 1D-XRD patterns of 0-100 mol% excess DMAX $FA_{0.9}Cs_{0.1}Pb(Br_{0.68}I_{0.32})_3$ half-stacks on a logarithmic scale. (100) orientation peak intensity increases strongly from 0 mol% DMAX to a maximum value at 60 mol% DMAX. * denotes PbI_2 present in the 80, 90, and 100 mol% (and weakly in the 70 mol%) excess DMAX samples. # denotes possible residual DMAX or intermediate phases seemingly present in all except the 30 and 40 mol% excess DMAX samples.

The (100) peak corresponds to the situation in which the perovskite crystals in the film lie perpendicular to the substrate in a highly ordered manner. A PbI_2 peak is clearly present for the 80, 90, and 100 mol% excess DMAX samples, matching up with the visible yellow regions noted in Figure 5.3.

UV-visible absorbance measurements of 0-100 mol% excess DMAX half-stacks are presented in Figure 5.5, highlighting a decrease in absorption onset intensity with increasing DMAX content.

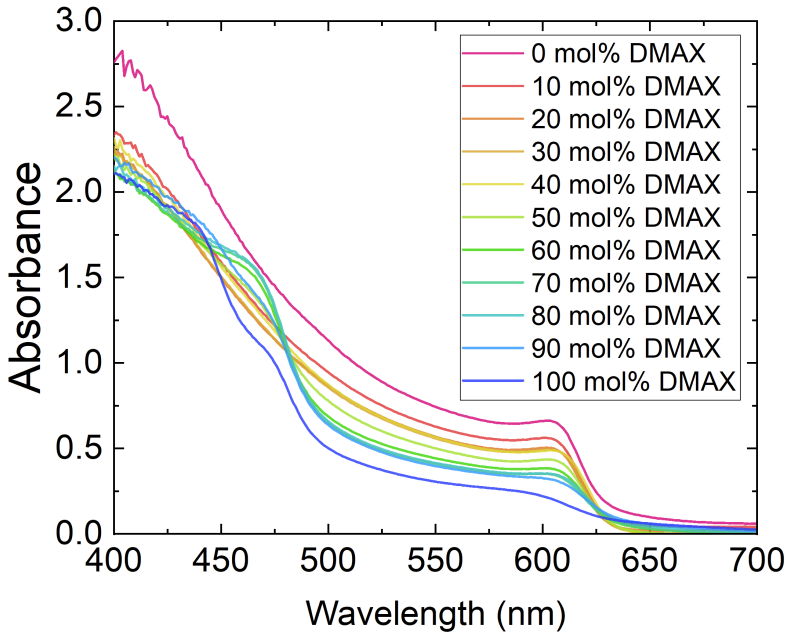

Figure 5.5. UV-visible absorbance spectra of 0-100 mol% excess DMAX range. Absorption onset intensity values decrease as excess DMAX additive amounts increase. Residual DMAX material may be present in a feature between 450-475 nm for the 60 and 70 mol% excess DMAX samples.

In addition, a feature between 450-475 nm is seen for the 60, 70, and 80 mol% DMAX samples. While a feature in this region could be indicative of PbI_2,[16] no strong PbI_2 peak is present for the 60 and 70 mol% excess DMAX samples in the 1D-XRD. Instead, this feature in the UV-visible absorbance spectrum may be residual DMAX material that was not removed during 160°C annealing, appearing to correlate with other signals noted in the 1D-XRD measurements.

Top-down SEM images were taken of 0-100 mol% excess DMAX half-stacks, as presented in Figure 5.6, to analyze film morphology. Pinholes and small apparent grain sizes were clearly visible in the 0 mol% excess DMAX sample (just the perovskite in neat DMF solvent). This was expected given there were neither DMAX salts nor DMSO solvent to help slow down the perovskite crystallization rate for more uniform film

formation. Pinholes and small grains persisted in the 10 mol% excess DMAX sample. For 20 mol% excess DMAX, small grains but fewer pinholes were observed. At 30 mol% excess DMAX, grain sizes increased while grain boundaries appeared rougher. The perovskite surface appeared to flatten compared to lower excess DMAX samples. Apparent grain sizes increased strongly with 40 mol% excess DMAX. The grains in this sample, however, appeared to have grown on top of each other, potentially a result of competition between nuclei during crystallization. DMAX salts may have annealed out at different rates at such high excess amounts, resulting in increased texturing and possibly rougher topography between perovskite grains at the surface. This behavior was observed for the 50-100 mol% excess DMAX samples as well. Very large voids ~1 μm in diameter were apparent for the 50 mol% excess DMAX sample.

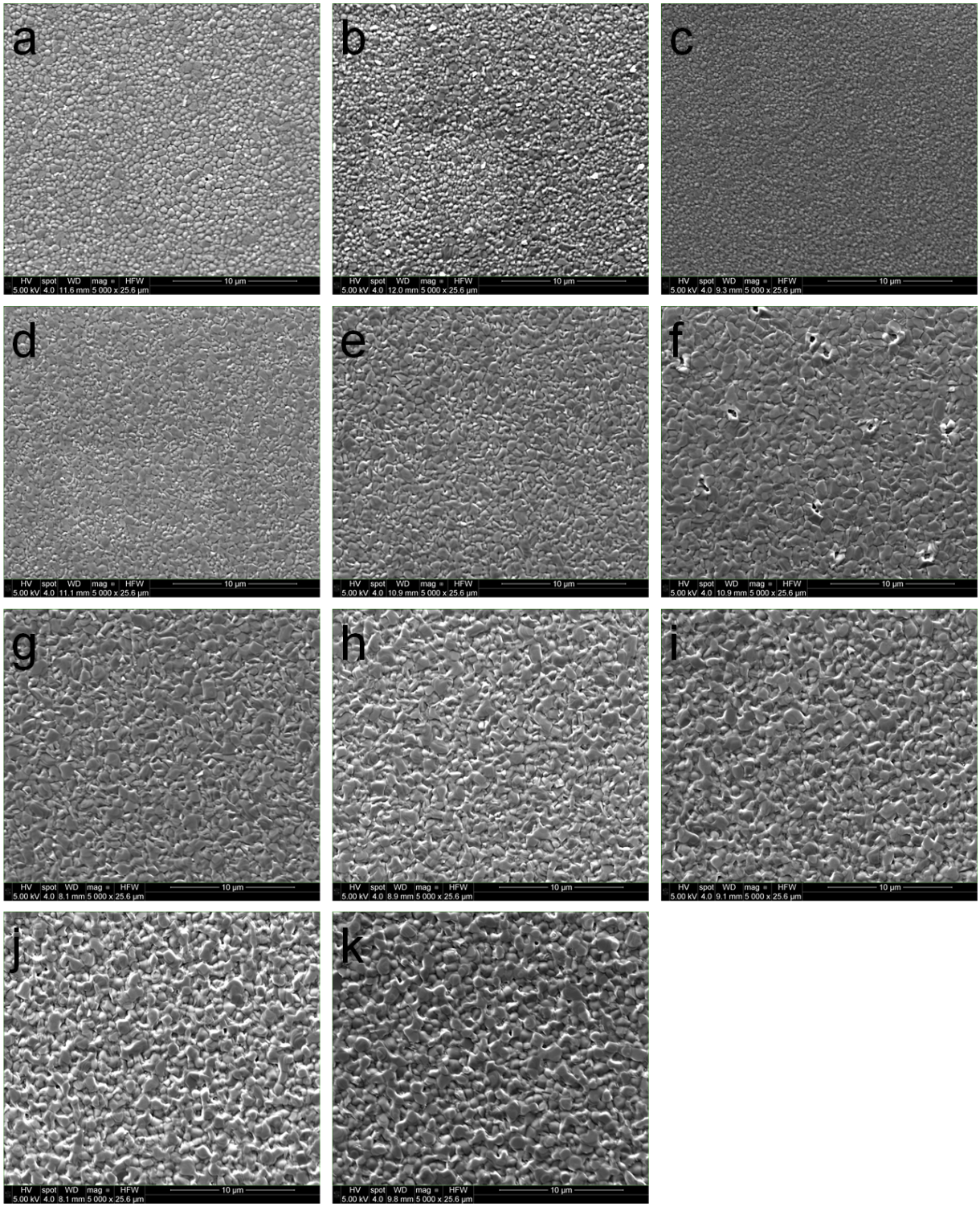

Figure 5.6. Top-down SEM images of FTO/Me-4PACz/Al_2O_3 nanoparticles/$FA_{0.9}Cs_{0.1}Pb(Br_{0.68}I_{0.32})_3$ perovskite half-stacks spin-coated with excess DMAX additive in the following amounts:

a) 0 mol% b) 10 mol% c) 20 mol% d) 30 mol% e) 40 mol% f) 50 mol% g) 60 mol% h) 70 mol% i) 80 mol% j) 90 mol% k) 100 mol%. SEM images taken with assistance from Dr. Amit Kumar, University of Oxford.

In addition, PbI_2 appeared to form in increasing abundance between perovskite grains for the 80, 90, and 100 mol% DMAX samples, respectively. This aligns with the PbI_2 peaks observed for these samples in 1D-XRD measurements as seen in Figure 5.4.

SEM images also allow for quantitative analysis of apparent grain sizes of the perovskite thin films. The grain size is referred to as “apparent” because only the top surface of the thin film is imaged. The median apparent grain sizes for all 0-100 mol% excess DMAX thin films are presented in Table 5.2.

mol% Excess DMAX (%)	Median Apparent Grain Size (nm)
0	293
10	319
20	306
30	395
40	634
50	694
60	827
70	778

80	670
90	714
100	735

Table 5.2. Calculated median apparent grain size for each half-stack. Grain sizes were calculated by measuring the diameter of 80 grains in every SEM image with ImageJ analysis software.

Statistical distributions of the 80 apparent grain sizes measured per sample are presented in Figure 5.7. The median apparent grain size mostly increased with larger excess amounts of DMAX until reaching a maximum value at 60 mol%.

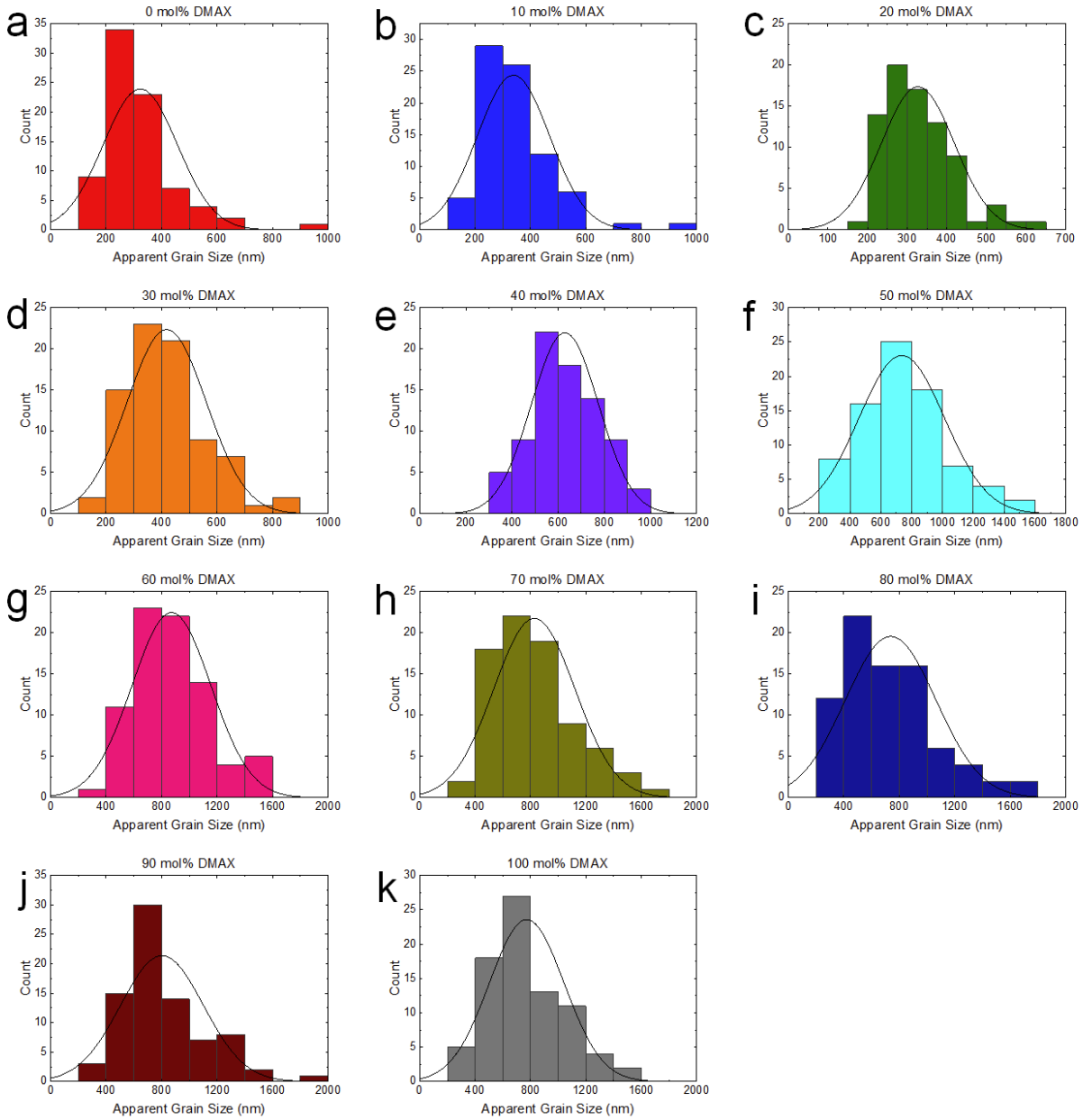

Figure 5.7. Distributions of median apparent grain sizes with excess DMAX additive in the following amounts: a) 0 mol% b) 10 mol% c) 20 mol% d) 30 mol% e) 40 mol% f) 50 mol% g) 60 mol% h) 70 mol% i) 80 mol% j) 90 mol% k) 100 mol%. A normal distribution curve is applied to each chart.

The increasing trend of median apparent grain size largely corresponded with the increasing trend of (100) orientation in 1D-XRD measurements of the same samples. While median apparent grain size grew beyond 30 mol% excess compositions, it was coupled with seemingly rougher topography between perovskite grains at the surface.

30 mol% and 40 mol% excess DMAX half-stacks showed the most promise for solar cells based on their relatively homogeneous morphology and large apparent grain size from SEM, seemingly PbI_2 and residual DMAX-free signals in 1D-XRD, and quality UV-visible absorbance spectra. As such, 30 mol% and 40 mol% excess DMAX additive amounts were tested in a batch of solar cells. Each DMAX additive amount was annealed under two conditions – a 2 step anneal of 100°C for 5 minutes in N_2 and 160°C for 10 minutes in ~20% RH air (similar to the optimal DMF/DMACl procedure for McMeekin et al.) and a 1 step anneal of 160°C for 10 minutes in N_2. The results are shown in Figure 5.8, with a clear optimal condition of 30 mol% excess DMAX and 2 step annealing.

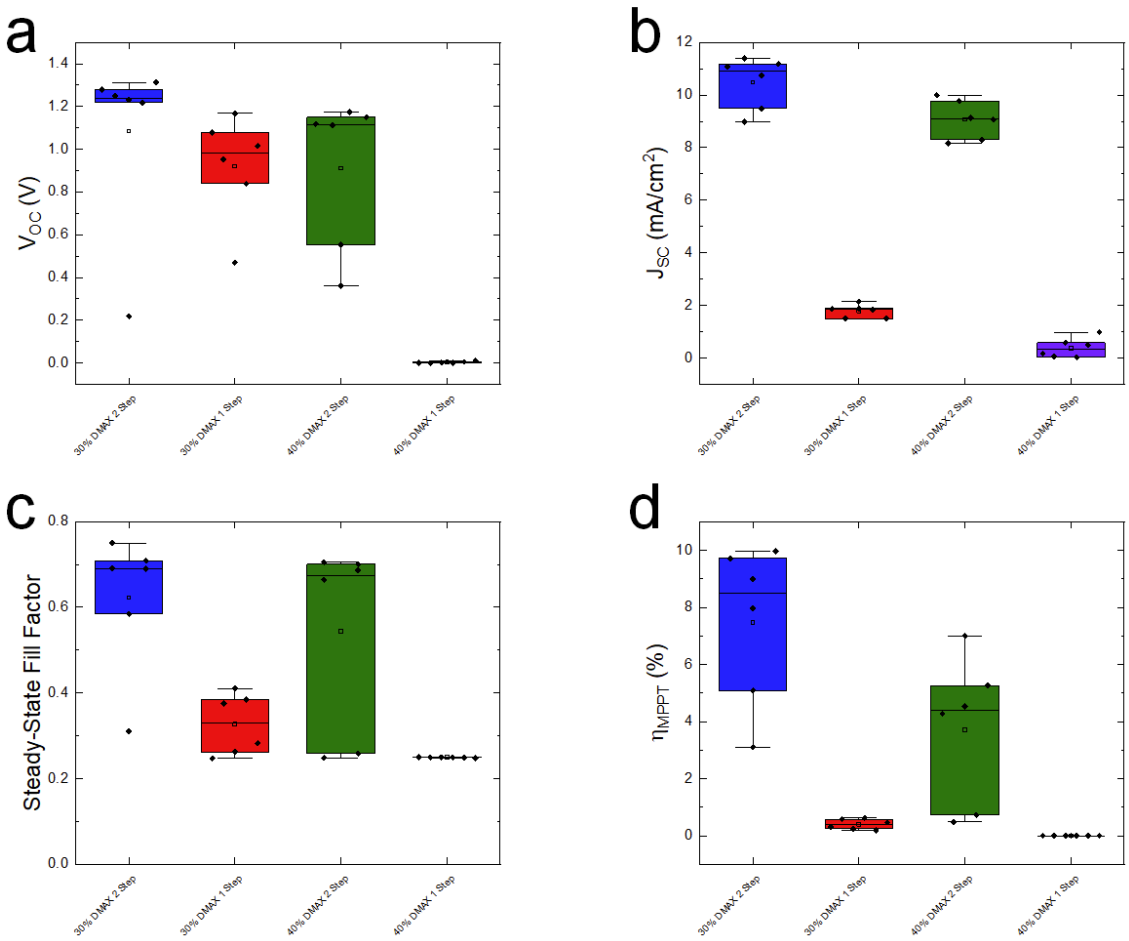

Figure 5.8. Solar cell performance parameter statistics of steady-state a) open-circuit voltage b) short circuit current c) fill factor and d) maximum power point tracked efficiency.

Device stack: FTO/Me-4PACz/Al_2O_3 nanoparticles/ $FA_{0.9}Cs_{0.1}Pb(Br_{0.68}I_{0.32})I_3$/PCBM/BCP/Ag. The solar cells with 30 mol% excess DMAX and a 2 step annealing process (100°C 5 minutes in N_2 and 160°C 10 minutes in ~20% RH air) exhibited greatly enhanced steady-state V_{OC}, J_{SC}, and fill factor for the highest overall performance. 6 solar cells of 0.25 cm^2 area were fabricated and measured per condition.

The $FA_{0.9}Cs_{0.1}Pb(Br_{0.68}I_{0.32})_3$ perovskite exhibited tolerance to oxygen and moisture in the air during crystallization from a DMF/DMAX solvent system. These 30 mol% excess DMAX and two step annealing conditions were used for all DMF/DMAX thin films and DMF/DMAX 1.97 eV wide band gap solar cell absorbers in this thesis.

5.2.2 – Material Characterization of Thin Films Fabricated Using DMF/DMAX and DMF/DMSO Crystallization Methods

To probe the effect on material quality of the novel DMF/DMAX crystallization method compared to the standard DMF/DMSO method, $FA_{0.9}Cs_{0.1}Pb(Br_{0.68}I_{0.32})_3$ perovskite thin films were fabricated and tested using a variety of characterization techniques. Compared to standard DMF/DMSO, the DMF/DMAX thin films exhibited larger median apparent grain sizes, more homogeneous morphology, and longer carrier lifetimes.

1D-XRD measurements were taken of fully annealed thin films made using both the DMF/DMAX and DMF/DMSO crystallization methods. As shown in Figure 5.9, there were no significant differences between the XRD plots, indicating a similar composition after complete annealing.

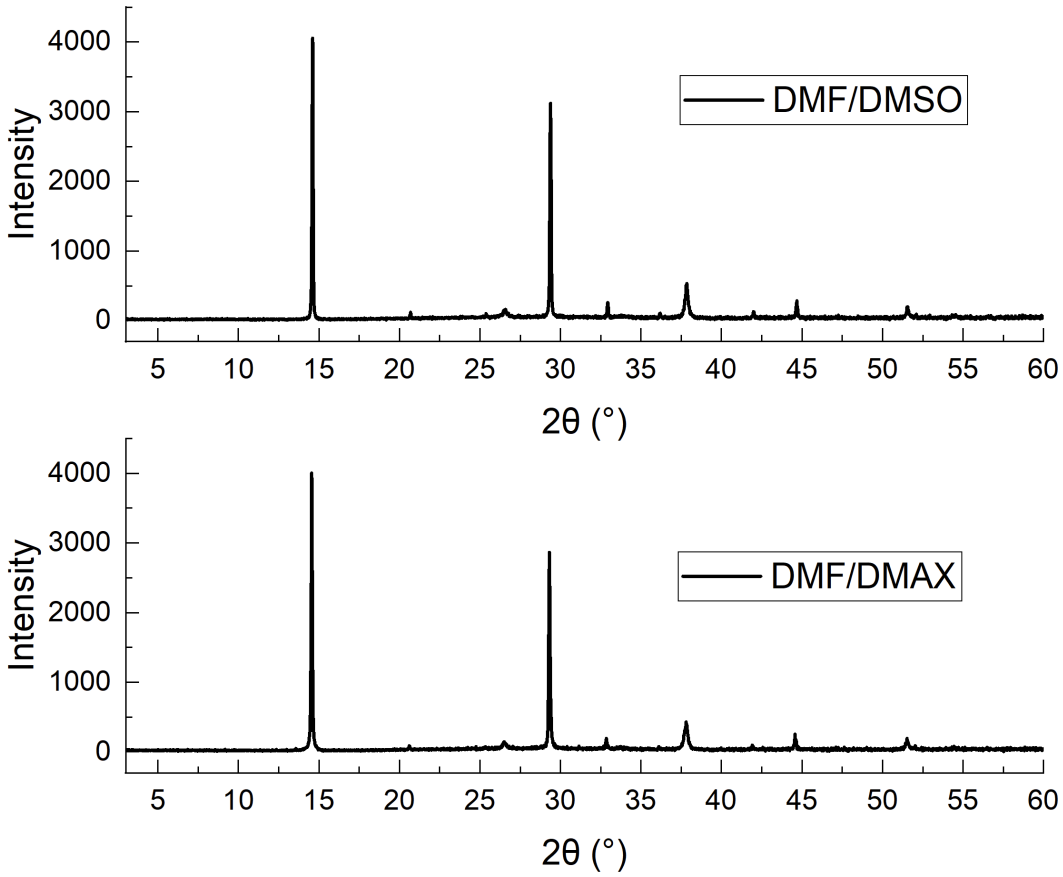

Figure 5.9. 1D-XRD plots of 1.97 eV half-stacks fabricated using the DMF/DMSO and DMF/DMAX crystallization methods. There are no significant discrepancies present in peaks, positions, or intensities. The fully crystallized half-stacks from each crystallization method indicate the same 1.97 eV composition as desired.

Such 1D-XRD measurements, however, do not show what is occurring during the annealing process to reach the final crystallized state from either DMF/DMAX or DMF/DMSO solvent systems.

2D-XRD measurements, where the diffraction angles are detected repeatedly during in-situ annealing, provide insight after the thin film has been spin-coated and antisolvent-quenched and until it has been fully annealed. 2D-XRD in-situ annealing plots are shown in Figure 5.10, with each sample annealed according to the optimal procedure for solar cell performance.

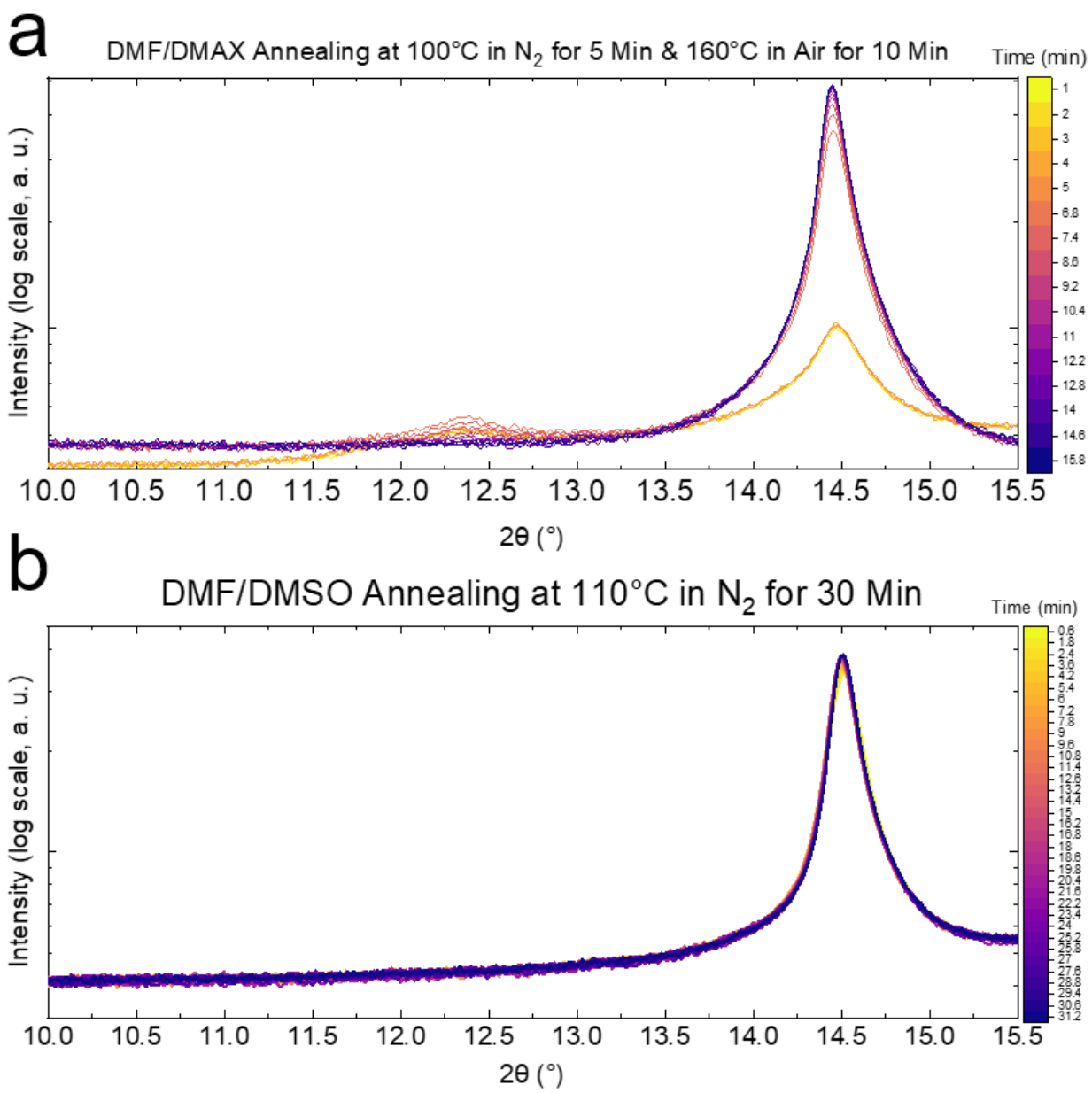

Figure 5.10. 2D-XRD Rigaku measurements for in-situ perovskite thin films fabricated using the a) DMF/DMAX and b) DMF/DMSO crystallization methods. Measurements performed by Dr. Philippe Holzhey, University of Oxford.

During the 100°C 5 minute N_2 first annealing step, the DMF/DMAX sample exhibited a peak at a diffraction angle around 2θ = 12.4°, indicative of a 2H-6H polytype intermediate phase. A perovskite 3C cubic peak around 2θ = 14.5° was also present at this time but weakly compared to the DMF/DMSO sample. Upon the 160°C 10 minute

drybox air second annealing step, the intermediate phase peak completely disappeared and the perovskite 3C cubic peak grew by about an order of magnitude in intensity. This was indicative that the DMF/DMAX sample was thermodynamically driven out of an intermediate phase to the desired fully crystalline cubic phase. Meanwhile, the DMF/DMSO sample exhibited a perovskite 3C cubic peak around $2\theta = 14.6°$ immediately that only slightly increased in intensity over 30 minutes of 110°C N_2 annealing. These results led to further investigation into the intermediate stages of the DMF/DMAX and DMF/DMSO crystallization methods.

Thin films were prepared by drop-casting precursor solutions from both DMF/DMAX and DMF/DMSO solvent systems for snapshots of intermediate stages of these crystallization methods. The thin films were neither antisolvent quenched nor annealed. The thin films were sealed in a nitrogen atmosphere and transported for 1D-XRD measurement with minimal air exposure before measurement. The 1D-XRD measurements of the unquenched and unannealed thin films are presented in Figure 5.11. The DMF/DMSO sample exhibited a DMSO solvent peak at $2\theta = 9.5°$. The presence of the DMSO peak at this stage has been reported to be undesirable for final crystalline quality.[17]

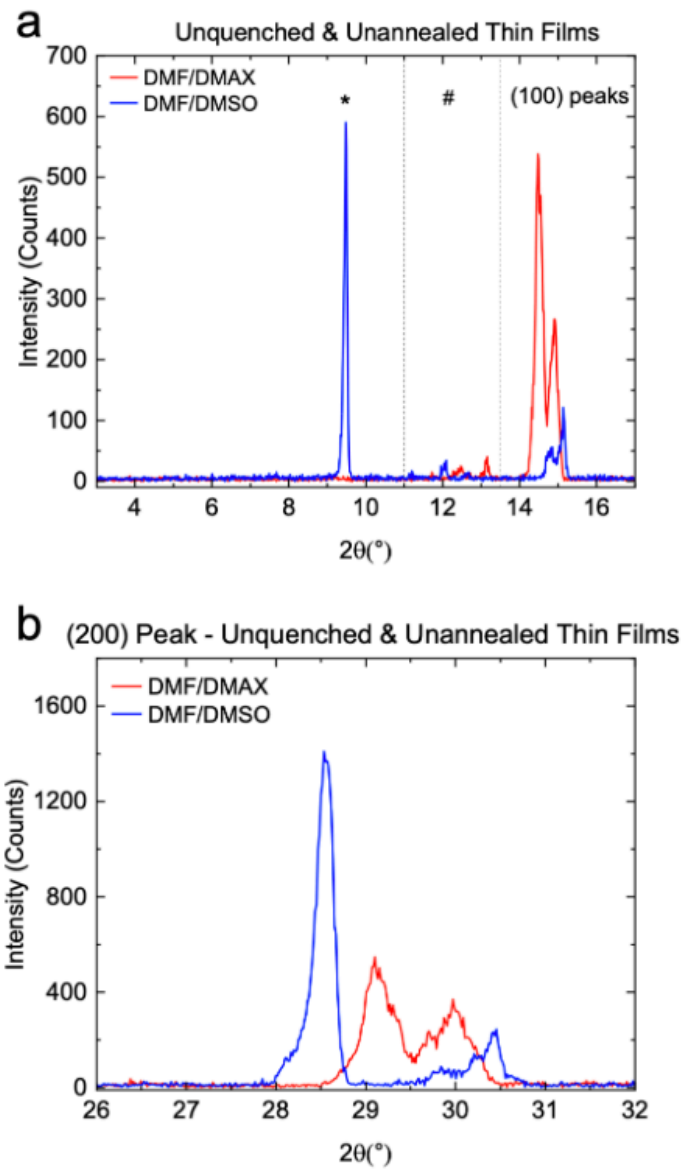

Figure 5.11. 1D-XRD plots of drop-casted 1.97 eV thin films without antisolvent quenching or annealing in DMF/DMAX and DMF/DMSO solvent systems with focus around the a) intermediates and (100) peak and b) (200) peak. * designates the DMSO solvent peak. # designates possible perovskite intermediate polytypes in both samples, in addition to possible $DMAPbX_3$ materials in the DMF/DMAX sample. Splitting of both the (100) and (200) orientation peaks into doublets corresponding to iodide and bromide regions is observed for the DMF/DMAX and DMF/DMSO samples.

Splitting of the (100) and (200) orientation peaks into doublets was present in both DMF/DMAX and DMF/DMSO samples. This phenomenon is indicative that iodide and bromide elements were present in different regions from the beginning of perovskite

precursor solution deposition. This peak splitting is consistent with the existence of such iodide and bromide rich regions in mixed halide perovskites reported in literature.[18]

In addition, thin films were spin-coated and antisolvent-quenched according to optimal recipes for both DMF/DMAX and DMF/DMSO crystallization methods. These thin films were not annealed. They then were sealed in a nitrogen atmosphere and transported for 1D-XRD measurement with minimal air exposure before measurement. The 1D-XRD measurements of the antisolvent-quenched and unannealed thin films are presented in Figure 5.12. Upon antisolvent quenching of the DMF/DMSO sample, only a perovskite peak was residual at both (100) and (200) orientation peaks. Upon antisolvent quenching of the DMF/DMAX sample, an intermediate perovskite polytype persisted along with continued peak splitting at both (100) and (200) orientation peaks.

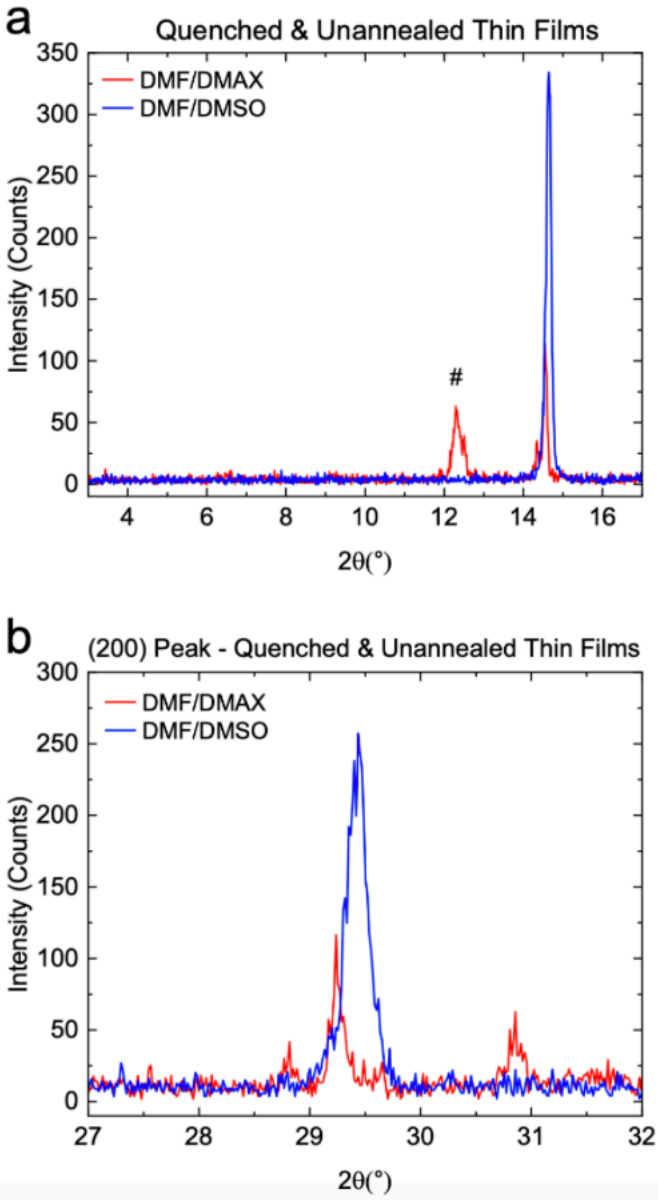

Figure 5.12. 1D-XRD plots of 1.97 eV thin films antisolvent-quenched and unannealed fabricated using the DMF/DMAX and DMF/DMSO crystallization methods with focus around the a) (100) peak and b) (200) peak. # designates the intermediate perovskite polytype peak at 2θ = 12.4° also observed in 2D-XRD in-situ annealing measurements for the DMF/DMAX sample. The DMSO solvent peak disappears and the iodide and bromide rich peaks merge at the (100) and (200) peaks for the DMF/DMSO sample. The peak splitting persists at these peaks for the DMF/DMAX sample.

These 1D-XRD measurements show the DMF/DMSO crystallization method is antisolvent quenching-controlled. Antisolvent quenching did not similarly induce full crystallization for the DMF/DMAX method. Instead, the DMF/DMAX crystallization

method is thermodynamically-controlled by a two-step annealing process as confirmed by the 2D-XRD in-situ annealing measurements presented in Figure 5.10. Although the DMF/DMAX films exhibited more halide heterogeneity initially, Figure 5.9 confirms that the iodide and bromide regions present as split peaks at the (100) and (200) orientations at intermediate stages have merged into a standard single perovskite upon complete annealing. Halide exchange during full crystallization therefore appears to be controlled by annealing for DMF/DMAX thin films and antisolvent quenching for DMF/DMSO.

In-situ GIWAXS measurements of DMF/DMSO and DMF/DMAX 2 eV thin films shown in Figure 5.13 provide further insight into these crystallization methods. For the DMF/DMSO sample, the (100) perovskite peak at 2θ = ~14.8° (~1.00 A^{-1} Q-space) was present before annealing. This indicates a direct crystallization from antisolvent quenching. For the DMF/DMAX sample, the (100) perovskite peak only appeared upon annealing, increasing in intensity upon exposure to 160°C temperature used for full annealing of such films.

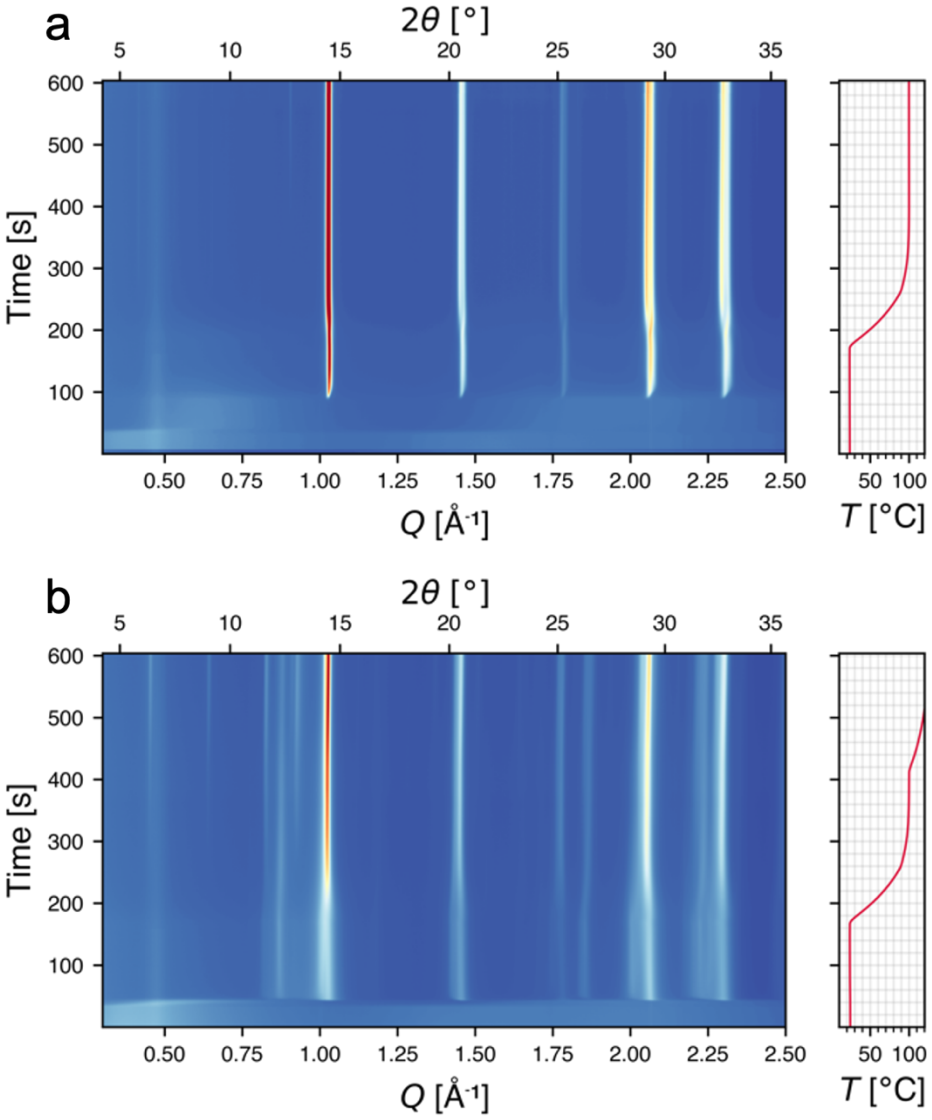

Figure 5.13. In-situ GIWAXS plots for a) DMF/DMSO and b) DMF/DMAX samples. Temperature over time is plotted to the right of both graphs to indicate the annealing temperature of each film over 600 seconds. The (100) perovskite peak detected around 14.8° 2θ (1.00 Q-space) is present before (and during) annealing for DMF/DMSO. The same peak only appears after annealing for DMF/DMAX, increasing in intensity upon annealing up to 160°C. These measurements provide further evidence that the DMF/DMSO crystallization is antisolvent-controlled while the DMF/DMAX crystallization is annealing-controlled. GIWAXS measurements and plotting were performed by Dr. Joel A. Smith, University of Oxford.

As shown from the 1D-XRD of unannealed films in Figures 5.11 and 5.12, it appears that the DMF/DMSO sample crystallized from a solvated phase and the

DMF/DMAX sample crystallized from a solid intermediate phase. The GIWAXS results confirm that the DMF/DMSO crystallization method is antisolvent-dependent while the DMF/DMAX crystallization method is annealing-dependent. 2D-XRD showed that the DMF/DMAX intermediate phase disappears completely – coupled with a strong growth of the fully crystallized cubic phase – over a period of 10 minutes at 160°C in air.

The GIWAXS results support that the DMF/DMAX solid intermediate phase is likely less sensitive to processing conditions, including antisolvent, before annealing. The annealing-dependent nature of the DMF/DMAX crystallization method makes it primed to improve 2 eV perovskite material reproducibility in both thin films and solar cells because temperature can be more easily controlled than other variables like antisolvent quenching.

XPS measurements of fully annealed DMF/DMSO and DMF/DMAX samples were conducted to probe the presence of Pb 4f, Br 3d, I 3d, and N 1s chemical species. The samples exhibit near complete signal overlap for these species. Although they employ different crystallization methods, both end materials have the same chemical species signals in their XPS spectra and are therefore essentially the same in final composition.

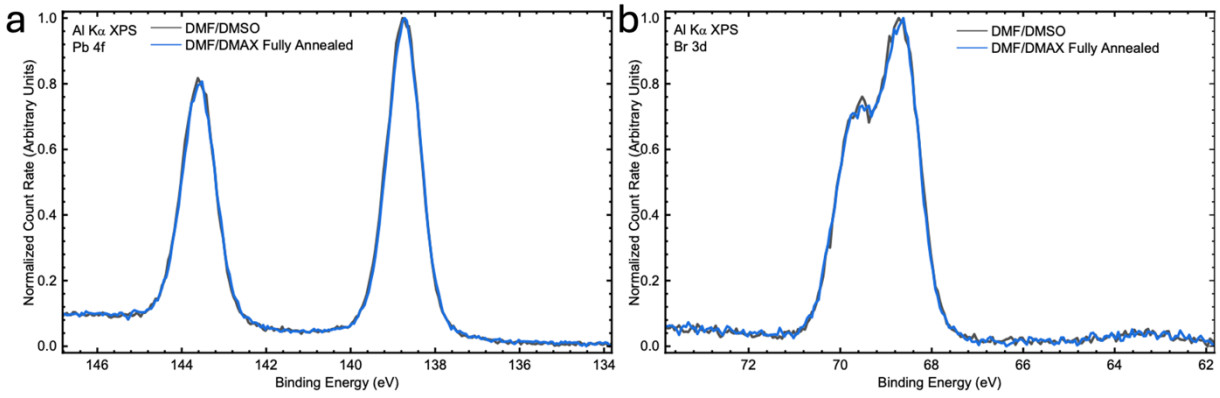

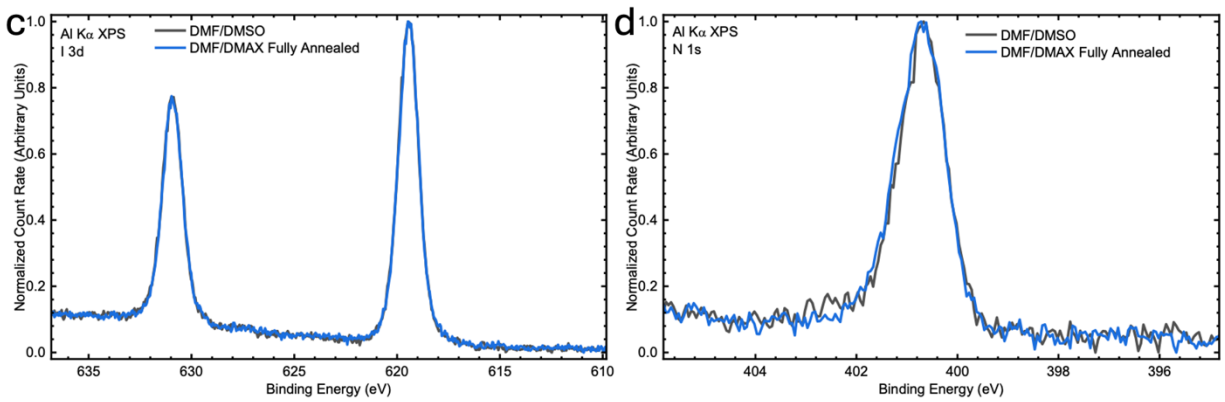

Figure 5.14. XPS measurements of the surface of DMF/DMSO and DMF/DMAX films at 1-5 nm probing depth for a) Pb 4f b) Br 3d c) I 3d and d) N 1s chemical species. Compared to the DMF/DMSO sample, there are no new peaks or significant shifts for the fully annealed DMF/DMAX sample, indicating similar final chemical compositions for both samples. XPS measurements and plots created by Michael A. Anderson and Xiodan Wang, Helmholtz Zentrum Berlin, and Dr. Krishanu Dey, University of Oxford.

Top-down SEM images were taken of fully annealed DMF/DMAX and DMF/DMSO half-stacks. As seen in Figure 5.15, the DMF/DMAX half-stack exhibited improved homogeneity across the surface. The significant contrast between dark and bright regions in the DMF/DMSO half-stack are potentially indicative of increased grain topography and heterogeneity across the film. Compared to the DMF/DMSO control, the more homogeneous morphology of the DMF/DMAX half-stack demonstrates more reproducible crystalline growth. In addition to improved and more reproducible morphology, the DMF/DMAX half-stack produced a 67% increase in median apparent grain size.

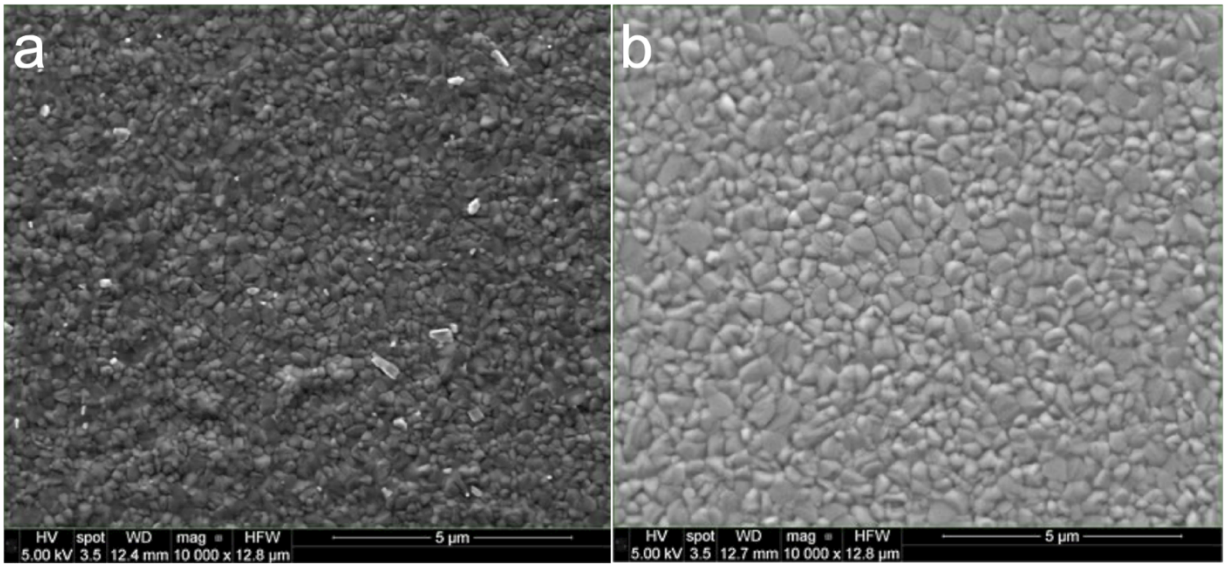

Figure 5.15. Top-down SEM images of half-stacks fabricated using a) DMF/DMSO and b) DMF/DMAX crystallization methods. Median apparent grain size is increased from 255 nm for DMF/DMSO to 425 nm for the DMF/DMAX sample. Grain sizes were calculated by measuring the diameter of 80 grains in each image with ImageJ analysis software. SEM images taken with assistance from Dr. Amit Kumar, University of Oxford.

Time resolved photoluminescence (TRPL) spectroscopy measurements of DMF/DMAX and DMF/DMSO half-stacks were conducted to assess carrier lifetime. Figure 5.16 illustrates that the DMF/DMAX half-stack had an improved rate of TRPL decay and carrier lifetime compared to DMF/DMSO. The longer carrier lifetime is indicative of reduced rates of non-radiative recombination in the DMF/DMAX half-stack, potentially due to the presence of fewer trap states in the bulk.[19]

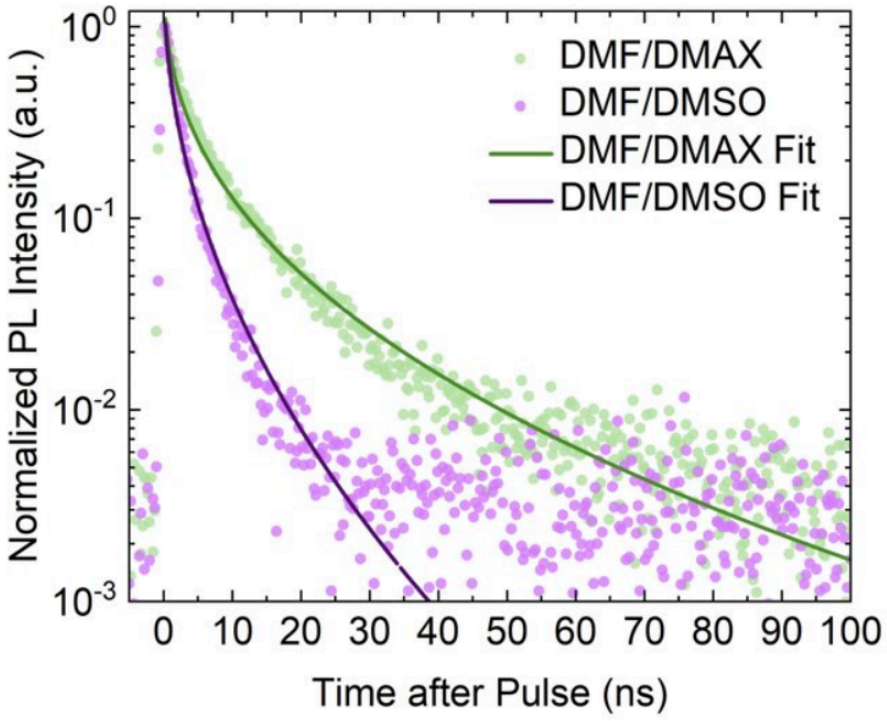

Figure 5.16. TRPL lifetime decays for half-stacks fabricated using the DMF/DMAX and DMF/DMSO crystallization methods. The DMF/DMAX half-stack had a 1/e carrier lifetime of 4.2 ns while the DMF/DMSO half-stack had a carrier lifetime of 2.8 ns. TRPL measurements and carrier lifetime calculations conducted with assistance from Dr. Manuel Kober-Czerny, University of Oxford.

Overall, these tests indicate thin films crystallized using the DMF/DMAX method improved material quality by exhibiting larger median apparent grain sizes, more homogeneous morphology, and longer carrier lifetimes compared to DMF/DMSO.

5.3 – Single Junction Solar Cell Fabrication and Testing Using 1.97 eV Wide Band Gap Perovskite Absorbers

5.3.1 – Improving Performance and Reproducibility with DMF/DMAX Crystallization Method Solar Cells

While the DMF/DMAX thin films demonstrated a number of significant material improvements over DMF/DMSO, the novel DMF/DMAX crystallization method had not yet been compared to DMF/DMSO in perovskite solar cells. Perovskite single junction solar cells were fabricated and tested using 1.97 eV wide band gap absorbers made using both DMF/DMAX and DMF/DMSO crystallization methods. The spincoating parameters, antisolvent, and antisolvent quench parameters such as timing and volume for the DMF/DMSO crystallization method were optimized and followed according to previous thesis work conducted in the Snaith Lab by Dr. Emil Dyrvik, University of Oxford.[1]

Testing showed that the 1.97 eV perovskite single junction solar cells fabricated using DMF/DMAX improved in both performance and reproducibility compared to DMF/DMSO, as seen in Figure 5.17. For the DMF/DMAX 1.97 eV perovskite single junction solar cells, every median performance parameter is higher than the solar cells using DMF/DMSO. The performance parameters for the DMF/DMAX 1.97 eV perovskite single junction solar cells also are more consistent than those using DMF/DMSO, demonstrating improved reproducibility of these solar cells fabricated using the DMF/DMAX crystallization method.

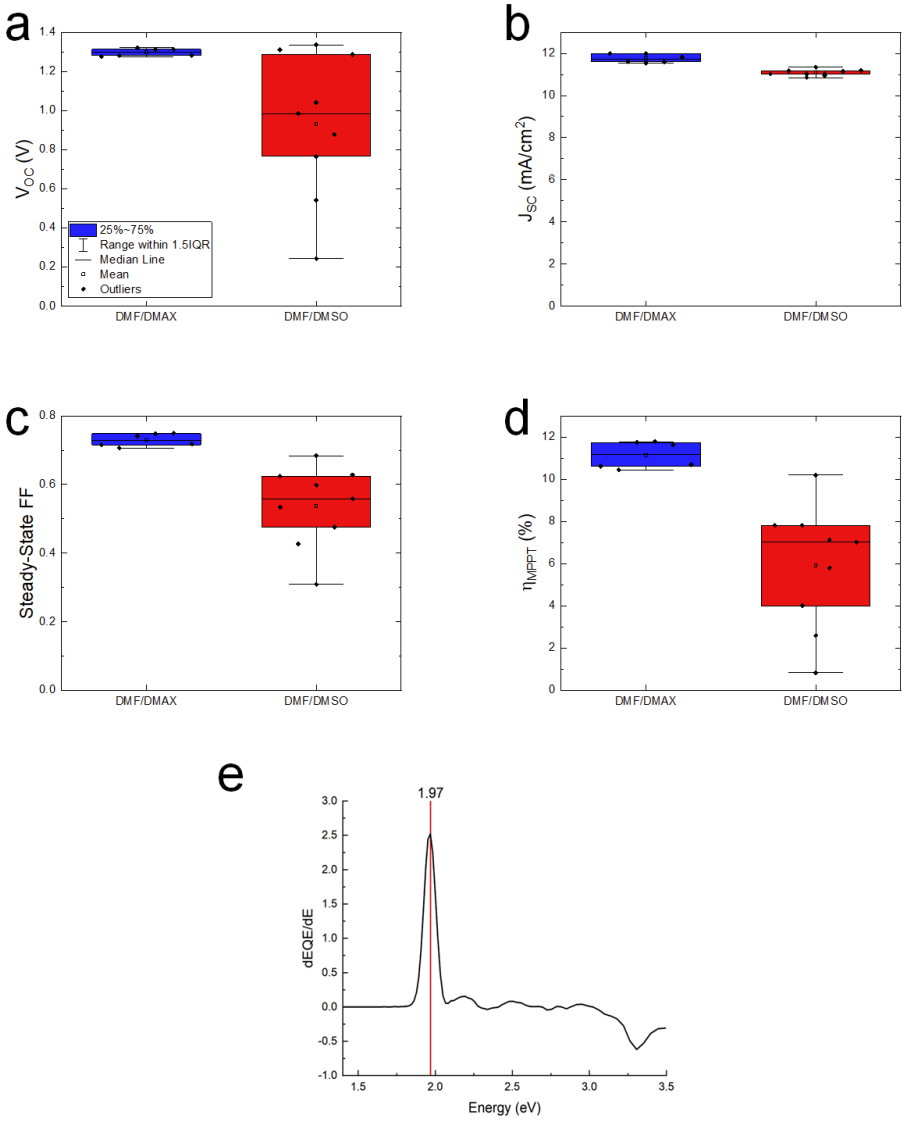

Figure 5.17. Solar cell performance parameter statistics of steady-state a) open-circuit voltage b) short circuit current c) fill factor and d) maximum power point tracked efficiency. Device stack: FTO/Me-4PACz/Al_2O_3 nanoparticles/ $FA_{0.9}Cs_{0.1}Pb(Br_{0.68}I_{0.32})I_3$/$C_{60}$/BCP/Ag. The solar cells with 30 mol% excess DMAX and a 2 step annealing process (100°C 5 minutes in N_2 and 160°C 10 minutes in ~20% RH air) exhibited greatly enhanced steady-state V_{OC}, J_{SC}, and fill factor for the highest overall performance. 6 DMF/DMAX solar cells and 9 DMF/DMSO solar cells of 0.25 cm^2 area were fabricated and measured.
e) dEQE/dE analysis from an EQE spectrum of a DMF/DMAX solar cell calculated a 1.97 eV band gap.

5.3.2 – Optimization of DMF/DMAX Solar Cells

After demonstrating the potential of more efficient and reproducible perovskite single junction solar cells with 1.97 eV wide band gap absorbers made using the DMF/DMAX crystallization method, surface passivation was explored with the aim of further optimization by improving open-circuit voltage. Hu et al. reported improved V_{OC} with $EDAI_2$ surface passivation.[20] Because this study explored a triiodide Pb-Sn perovskite composition, $EDAI_2$, $EDABr_2$, and a 50:50 mol% mix of $EDAI_2$ and $EDABr_2$ surface passivation were screened to better examine the possible effects on the mixed-halide 1.97 eV perovskite composition.

Each surface passivation solution was prepared at 0.5 mg/mL concentration in 1:1 toluene:IPA solvent, stirred at 70°C for 2-3 hours, and after cooling filtered with a 0.22 μM PTFE filter before use. Each surface passivation material was spin-coated at 4000 rpm, 20 seconds, 1333 rpm/second conditions. Each film was then annealed at 100°C for 3 minutes in N_2. Figure 5.18 shows that the best overall performance came from the mixed $EDAI_2$/$EDABr_2$ surface passivation.

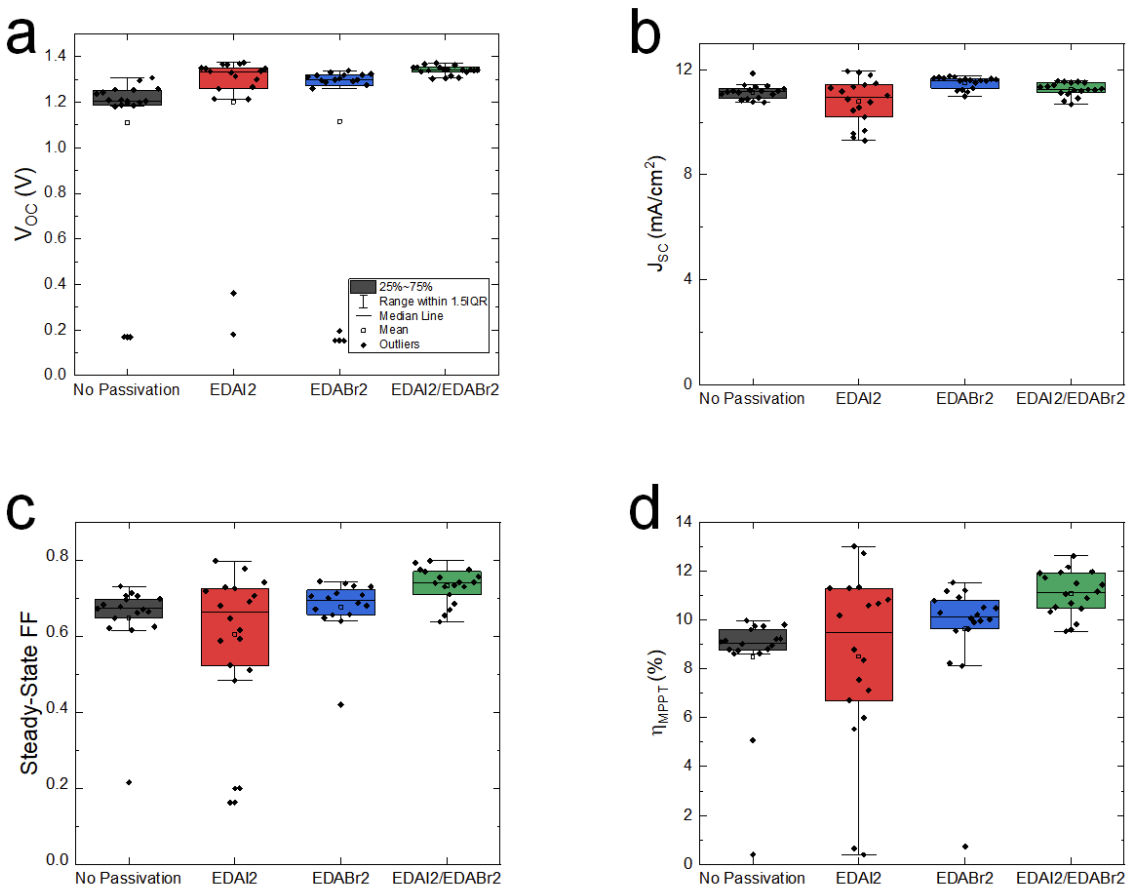

Figure 5.18. Performance parameter statistics for $EDAX_2$ surface passivation screening for $FA_{0.9}Cs_{0.1}Pb(Br_{0.68}I_{0.32})I_3$ solar cells. Device stack: FTO/Me-4PACz/Al_2O_3 nanoparticles/ $FA_{0.9}Cs_{0.1}Pb(Br_{0.68}I_{0.32})I_3$/$C_{60}$/BCP/Ag. Steady-state a) open-circuit voltage b) short-circuit current c) fill factor and d) maximum power point tracked efficiency. The solar cells with mixed $EDAI_2$/$EDABr_2$ surface passivation exhibited the best overall performance. 18 solar cells of 0.25 cm^2 area were fabricated and measured per condition.

The mixed $EDAI_2$/$EDABr_2$ surface passivation material generated solar cells with the greatest median steady-state V_{OC} and fill factor values with improved overall solar cell performance and yield. Passivating the perovskite absorber/ETL interface can boost V_{OC} in 1.97 eV band gap solar cells.

Next, the mixture of $EDABr_2$ and $EDAI_2$ surface passivation materials itself was explored in more detail. A 68:32 mol% $EDABr_2$:$EDAI_2$ mixture, exactly correlating with the bromide:iodide stoichiometry of the 1.97 eV perovskite, was included.

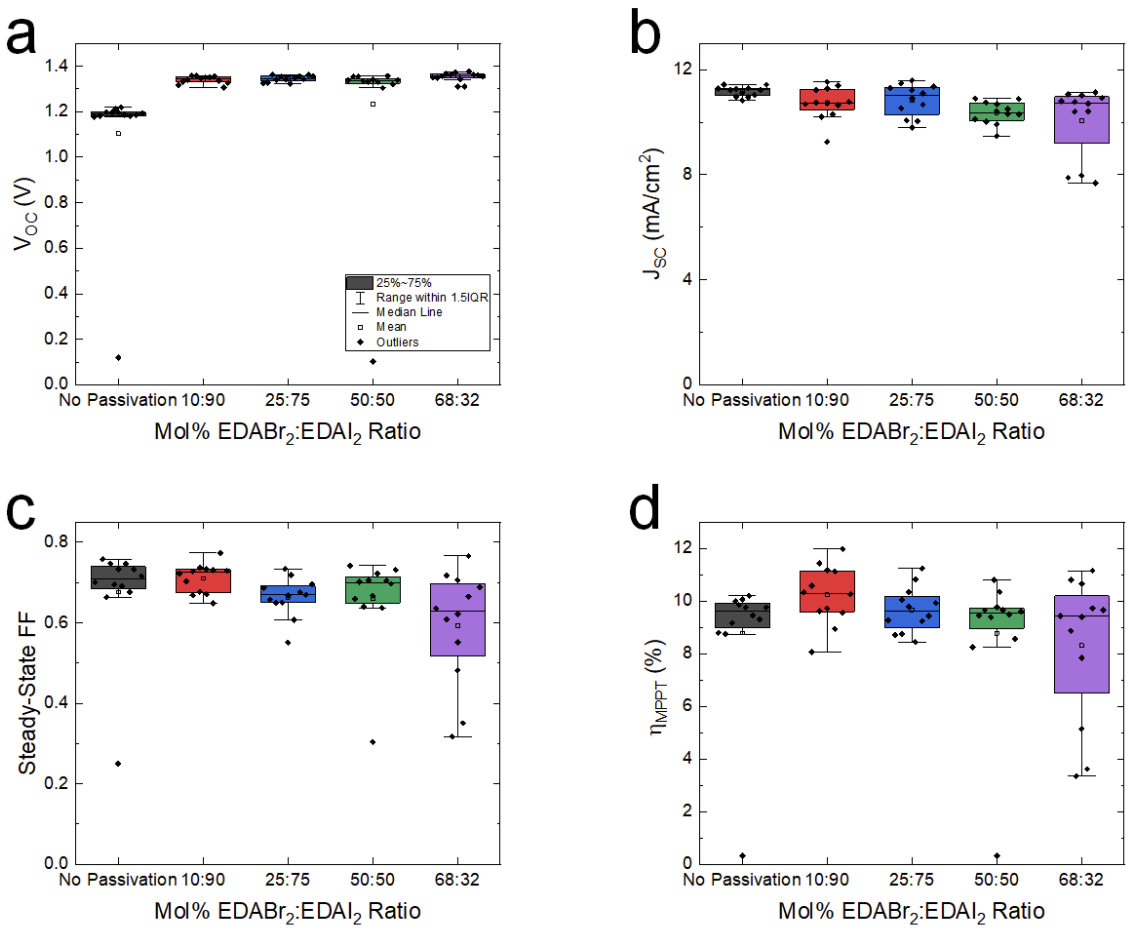

Figure 5.19. Performance parameter statistics for $EDABr_2$:$EDAI_2$ surface passivation screening for $FA_{0.9}Cs_{0.1}Pb(Br_{0.68}I_{0.32})I_3$ solar cells. Device stack: FTO/Me-4PACz/Al_2O_3 nanoparticles/ $FA_{0.9}Cs_{0.1}Pb(Br_{0.68}I_{0.32})I_3$/$EDABr_2$:$EDAI_2$/$C_{60}$/BCP/Ag. Steady-state a) open-circuit voltage b) short-circuit current c) fill factor and d) maximum power point tracked efficiency. The solar cells with mixed $EDAI_2$/$EDABr_2$ surface passivation exhibited the best steady-state open-circuit voltage. 12 solar cells of 0.25 cm^2 area were fabricated and measured per condition.

Solar cells passivated with the 68:32 mol% $EDABr_2$:$EDAI_2$ mixture produced the greatest median steady-state V_{OC}. Almost half of the 68:32 mol% $EDABr_2$:$EDAI_2$ solar cells produced a steady-state V_{OC} exceeding 1.36 V, the highest value achieved to this point in the study.

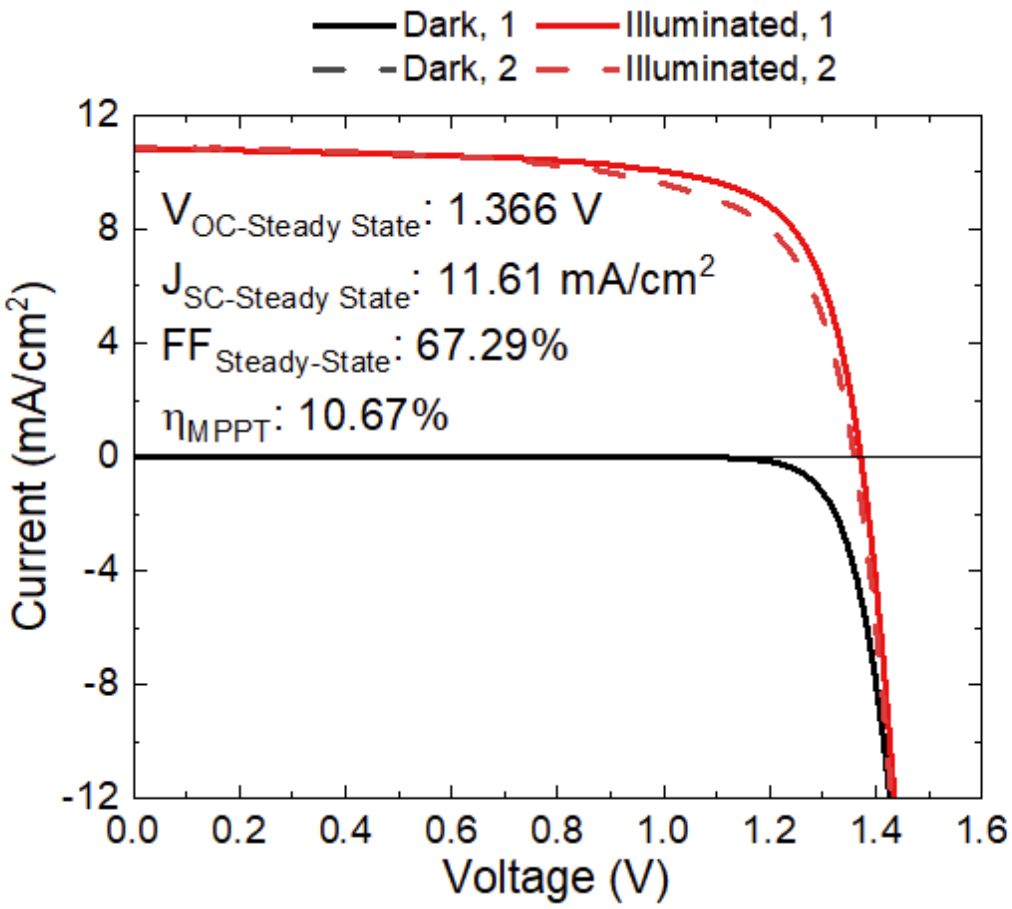

Figure 5.20. Representative J-V curve of a 68:32 mol% $EDABr_2$:$EDAI_2$ surface passivation solar cell. Although a lower steady-state fill factor was observed, the steady-state V_{OC} > 1.36 V was the highest value achieved using surface passivation to this point.

While the overall performance yield was less consistent with the 68:32 mol% ratio, the demonstration of highest V_{OC} was compelling. The high performance demonstrated with the 68:32 mol% $EDABr_2$:$EDAI_2$ ("EDAX") ratio was sought to be further improved with changes to the top contact device stack, namely the introduction of an ICBA electron transport layer sandwiched between the perovskite absorber and C_{60} layers.

As Figure 5.21 shows, an ICBA electron transport layer improved steady-state open-circuit voltage. A 1 mg/mL ICBA layer and subsequent 20 nm C_{60} layer yielded enhanced solar cell performance, largely from increased steady-state short-circuit and fill

factor. The 1 mg/mL concentration appeared to improve the energetic alignment between the perovskite absorber and electron transport layer stack, boosting solar cell efficiency.

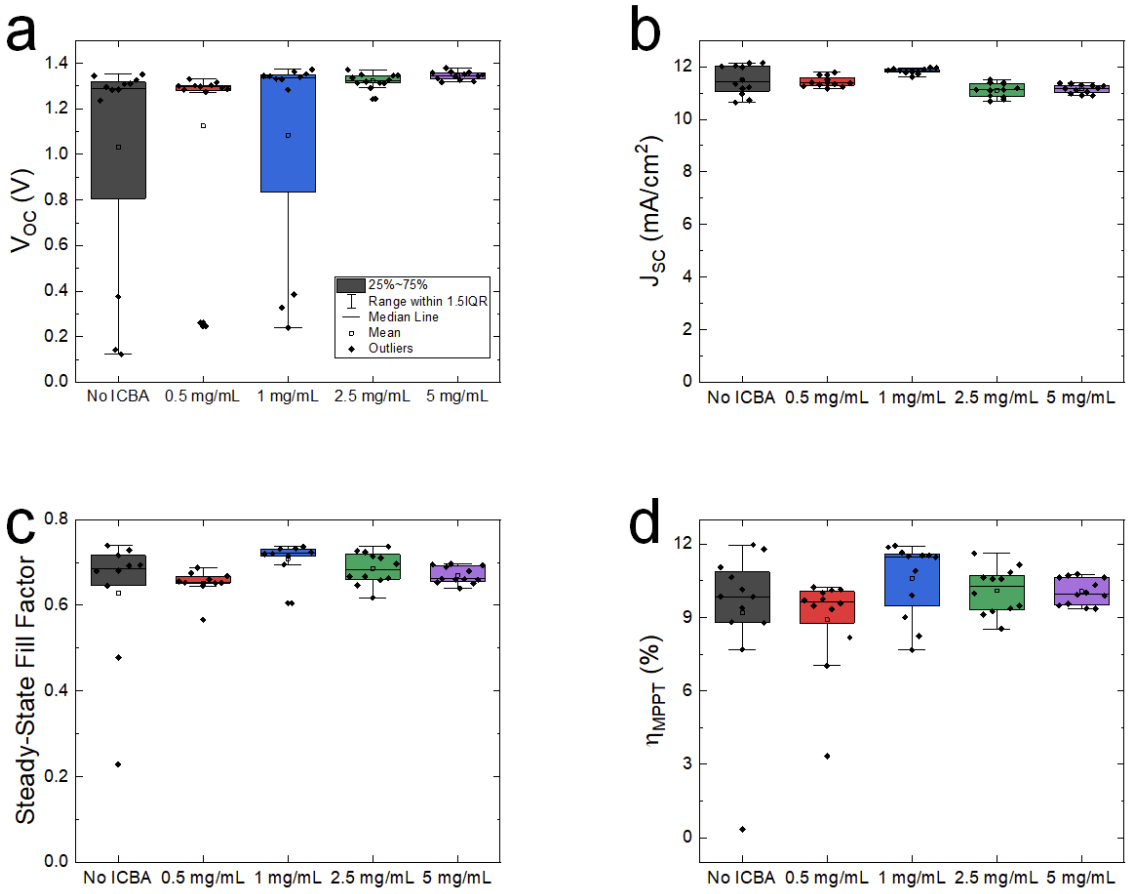

Figure 5.21. Solar cell performance statistics of steady-state a) open-circuit voltage b) short circuit current c) fill factor and d) maximum power point tracked efficiency. Device stack: FTO/Me-4PACz/Al_2O_3 NPs/$FA_{0.9}Cs_{0.1}Pb(Br_{0.68}I_{0.32})I_3$/EDAX/ICBA/$C_{60}$/BCP/Ag. The solar cells with a 1 mg/mL ICBA electron transport layer exhibited enhanced median steady-state J_{SC} and fill factor for the highest overall performance. 12 solar cells of 0.25 cm^2 area were fabricated and measured per condition.

The champion DMF/DMAX 1.97 eV perovskite single junction solar cell utilizing the 1 mg/mL ICBA electron transport layer achieved near-record 1.42 V steady-state open-circuit voltage and 13.7% maximum power point tracked efficiency, as detailed in Figure 5.22.

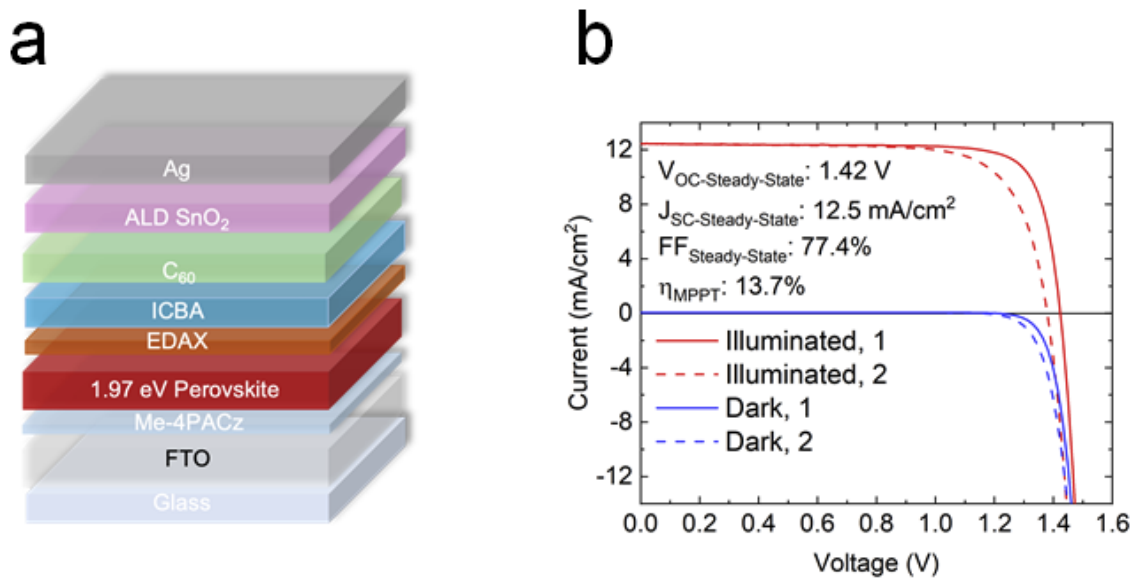

Figure 5.22. Champion DMF/DMAX 1.97 eV perovskite single junction solar cell a) device stack and b) J-V curve. The solar cell recorded 1.42 V steady-state open-circuit voltage, 12.5 mA/cm^2 steady-state short-circuit current, 77.4% steady-state fill factor, and 13.7% maximum power point tracked efficiency.

Based on the detailed balance limit, the performance parameters of this champion are more than 80% of the theoretical maximums for V_{OC}, J_{SC}, and FF and 58.9% of the theoretical maximum efficiency, as shown in Table 5.3.

Solar Cell Parameter	Champion Solar Cell	Theoretical Maximum (Detailed Balance)	Champion:Theoretical Ratio
V_{OC}	1.42 V	1.655 V	85.8%
J_{SC}	12.5 mA/cm^2	15.26 mA/cm^2	81.9%
FF	77.4%	92.1%	84.0%
Efficiency	13.7%	23.25%	58.9%

Table 5.3. Open-circuit voltage, short-circuit current, fill factor, and efficiency parameters for the champion 1.97 eV wide band gap single junction solar cell. Theoretical maximum values are based on detailed balance calculations for a 1.97 eV single junction solar cell illuminated by the AM 1.5G spectrum at 1-sun intensity at 25°C cell temperature. The calculations assume radiative emission from both the front and rear of the solar cell.

Champion solar cell statistics are from the steady-state measurements noted in Figure 5.22.

The overall efficiency of the champion 1.97 eV perovskite single junction solar cell with the absorber fabricated using the DMF/DMAX crystallization method is more than half of the theoretical maximum. The leading driver for efficiency loss was J_{SC}. While J_{SC} could have potentially been boosted by increasing the concentration of the perovskite precursor solution, doing so would have made the absorber layer thicker. Increasing the thickness of the absorber could induce optical losses in all-perovskite triple junction tandems, potentially increasing parasitic absorption by the 1.97 eV wide band gap top subcell and harming the performance of the subcells below. As such, the absorber layer thickness was not increased. V_{OC} losses in the champion 1.97 eV solar cell totalled 235 mV, lower than those of most reported ~2 eV wide band gap single junction solar cells.

V_{OC} values exceeding 1.4 V, achieved using DMF/DMAX to fabricate these 1.97 eV perovskite solar cells, demonstrated a performance improvement.

5.3.3 – Operational Stability of DMF/DMAX and DMF/DMSO 1.97 eV Solar Cells

The operational stability of DMF/DMAX and DMF/DMSO 1.97 eV perovskite single junction solar cells were tested with 30 minutes of continuous maximum power point tracking under 1-sun intensity AM 1.5G illumination. The optimal device stack for performance was used for both DMF/DMAX and DMF/DMSO solar cells tested.

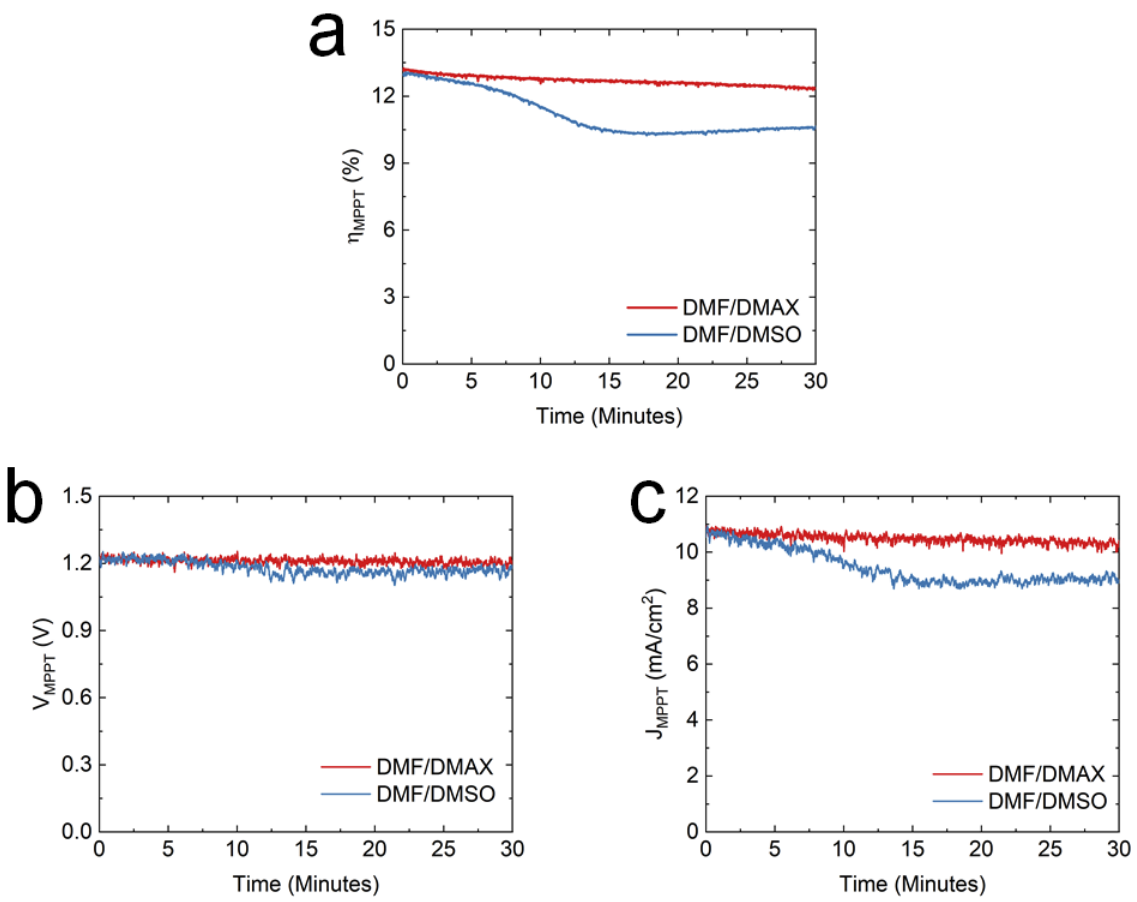

Figure 5.23. a) Unencapsulated DMF/DMAX and DMF/DMSO 1.97 eV perovskite single junction solar cells continuously operated at maximum power point under 1-sun intensity AM 1.5G illumination for 30 minutes. b) The voltage at maximum power point (V_{MPPT}) for the solar cells. c) The current density at maximum power point (J_{MPPT}) for the solar cells.

The DMF/DMAX 1.97 eV perovskite single junction solar cell retained 93.4% of its initial efficiency, compared to only 82.1% for the DMF/DMSO solar cell, demonstrating superior operational stability. The significant drop in maximum power point tracked efficiency for the DMF/DMSO solar cell is largely attributed to a current decay at this condition not observed in the DMF/DMAX solar cell. The improved material properties in the perovskite absorber fabricated using the thermodynamically-controlled DMF/DMAX crystallization method may be the primary reason for this improved operational stability. Longer carrier lifetimes measured by TRPL indicate reduced rates of non-radiative

recombination, potentially due to the presence of fewer trap states and defects in the bulk. Larger median apparent grain sizes, as well as improved morphological homogeneity, reduce the number of grain boundaries and therefore sites for non-radiative recombination or regions for trapped solvents to induce degradation. These improved material properties may explain the enhanced operational stability observed for the DMF/DMAX solar cell.

5.4 – Conclusion

A novel DMF/DMAX crystallization method was developed to create efficient and reproducible solution-processed 1.97 eV wide band gap perovskite absorbers and single junction solar cells. DMAX salts replace the DMSO solvent used in standard perovskite precursor solutions dissolved in DMF and DMSO for the purpose of avoiding reproducibility issues for ~2 eV band gap perovskites fabricated using the standard DMF/DMSO crystallization method. The perovskite thin films crystallized using the DMF/DMAX method exhibit larger median apparent grain sizes, more homogeneous morphology, and longer carrier lifetimes compared to DMF/DMSO. The 1.97 eV perovskite single junction solar cells fabricated using DMF/DMAX demonstrated improved median maximum power point tracked efficiency (with champion 1.42 V steady-state open-circuit voltage and 13.7% maximum power point tracked efficiency), reproducibility, and operational stability compared to DMF/DMSO. The 1.97 eV perovskite absorbers made using the novel DMF/DMAX crystallization method in this chapter were subsequently incorporated as the top subcells in the all-perovskite triple junction tandem solar cells detailed in Chapter 7.

Chapter 5 References

1. Dyrvik, Emil Grove. *Wide-Bandgap Halide Perovskite Materials for Photovoltaic and Optoelectronic Applications*. Print. 2023.

2. Höranter, M. et al. The Potential of Multijunction Perovskite Solar Cells. *ACS Energy Lett*., **2**, 10, 2506-2513 (2017).

3. Wang, J. et al. Halide homogenization for low energy loss in 2-eV-bandgap perovskites and increased efficiency in all-perovskite triple-junction solar cells. *Nature Energy*, **9**, 70-80 (2023).

4. Huang, T. et al. Performance-limiting formation dynamics in mixed-halide perovskites. *Sci. Adv.,* **7**, eabj1799 (2021).

5. McMeekin, D.P. et al. Solution-Processed All-Perovskite Multi-Junction Solar Cells. *Joule*, **3**, 1-15 (2019).

6. Choi, K. et al. Suppressing Halide Segregation in Wide-Band-Gap Mixed-Halide Perovskite Layers through Post-Hot Pressing. *ACS Appl. Mater. Interfaces*, **14**, 24341–24350 (2022).

7. Isikgor, F.H. et al. Monolithic Perovskite–Perovskite–Organic Triple-Junction Solar Cells with a Voltage Output Exceeding 3 V. *ACS Energy Lett.*, **7**, 4469-4471 (2022).

8. Choi, Y.J. et al. Atomic Layer Deposition-Free Monolithic Perovskite/Perovskite/Silicon Triple-Junction Solar Cells. *ACS Energy Lett.,* **8**, 7, 3141–3146, (2023).

9. Wang, Z. et al. Suppressed phase segregation for triple-junction perovskite solar cells. *Nature*, **618**, 74–79 (2023).

10. Cheng, J. et al. Wide-Band-Gap (2.0 eV) Perovskite Solar Cells with a V_{OC} of 1.325 V Fabricated by a Green-Solvent Strategy," *ACS Appl. Mater. Interfaces*, **15**, 23077–23084 (2023).

11. Rong, Y. et al. Solvent engineering towards controlled grain growth in perovskite planar heterojunction solar cells. *Nanoscale*, **7**, 10595–10599 (2015).

12. McMeekin, D.P. et al. Intermediate-phase engineering via dimethylammonium cation additive for stable perovskite solar cells. *Nature Materials*, **22**, 73-83 (2023).

13. Kwang, Z. et al. Solvent-modulated reaction between mesoporous PbI_2 film and CH_3NH_3I for enhancement of photovoltaic performances of perovskite solar cells. *Elctrochemica Acta*, **266**, 118-129 (2018).

14. Zhou, Y. et al. Effect of Solvent Residue in the Thin-Film Fabrication on Perovskite Solar Cell Performance. *ACS Appl. Mater. Interfaces*, **14**, 25, 28729–28737 (2022).

15. Zhi, L. et al. Dissolution and recrystallization of perovskite induced by *N*-methyl-2-pyrrolidone in a closed steam annealing method. *J. Energy Chem.*, **30**, 78-83 (2019).

16. Eze, V. et al. Air-assisted flow and two-step spin-coating for highly efficient $CH_3NH_3PbI_3$ perovskite solar cells. *Jpn. J. Appl. Phys.*, **55**, 02BF08 (2016).

17. Dang, H. et al. Multi-cation Synergy Suppresses Phase Segregation in Mixed-Halide Perovskites. *Joule*, **3**, 17, 1746-1764 (2019).

18. Zhao, Y. et al. Strain-activated light-induced halide segregation in mixed-halide perovskite solids. *Nature Communications*, **11**, 6328 (2020).

19. Chen, J. et al. Carrier dynamic process in all-inorganic halide perovskites explored by photoluminescence spectra. *Photonics Research*, **9**, 2 (2021).

20. Hu, S. et al. A Universal Surface Treatment for p–i–n Perovskite Solar Cell. *ACS Appl. Mater. Interfaces*, **14**, 50, 56290–56297 (2022).

Chapter 6

V_{OC} Loss Mechanisms in 1.97 eV Wide Band Gap Perovskite Single Junction Solar Cells

6.1 – Introduction

2 eV wide band gap perovskite absorbers are crucial to the efficiency of p-i-n architecture all-perovskite triple junction tandem solar cells because high voltage from these 2 eV wide band gap subcells is necessary to achieve higher efficiencies. The most important solar cell performance parameter for a 2 eV wide band gap subcell is open-circuit voltage because it must be the largest voltage contributor among the three perovskite subcells to create high efficiency triple junction tandem solar cells. For real-world implementation, the 2 eV wide band gap subcells also must maintain high voltage output during continuous operation to maintain high efficiency of the all-perovskite triple junction tandem solar cells.

This chapter investigates and quantifies the effects of several open-circuit voltage loss mechanisms during operation for 1.97 eV (~2 eV) wide band gap perovskite single junction solar cells. For all measurements used in this chapter, the solar cells were fabricated using the novel DMF/DMAX crystallization method with the device stack optimized for performance, as detailed in Chapter 5. Solar cells were measured using Fourier-transform photocurrent spectroscopy (FTPS), external quantum efficiency (EQE), photoluminescence quantum efficiency (PLQE), and electroluminescence quantum

efficiency (ELQE) techniques. FTPS, PLQE, and ELQE measurements were conducted over a period of 120 minutes of continuous solar cell operation.

V_{OC} loss mechanisms were calculated based on these measurements. It is shown that non-radiative recombination processes, rather than halide segregation, dominate V_{OC} losses that can be accounted for from these measurements in 1.97 eV wide band gap perovskite solar cells. These results indicate that, compared to previously published estimates, halide segregation has a less substantial effect on V_{OC} loss mechanisms in 1.97 eV perovskite solar cells fabricated using the DMF/DMAX crystallization method.

To tune the perovskite absorber band gap to ~2 eV, mixed halide compositions are required. Typically, the $AB(Br_xI_{1-x})_3$ composition with $Br \geq 0.6$ is used. At such high bromide content, mixed bromide-iodide perovskite absorbers often exhibit a phenomenon known as halide segregation. It is widely accepted in the field that such mixed bromide-iodide perovskites form small iodide-rich domains with a narrower band gap than the initial mixed bromide-iodide phase under illumination or charge injection.[1-4] Chen et al. proposed a unified theory that analyzed the compositional Helholtz free energy of mixed bromide-iodide perovskites into stable and metastable regions on phase diagrams. They noted large metastable regions under illumination and explained that the difference in band gap energy between the mixed bromide-iodide and iodide-rich domains is the driving force for halide segregation. By funneling to the lower band gap energy iodide-rich domains under excitation, charge carriers favorably lower their free energy. This energetic incentive therefore drives the nucleation and growth of the iodide-rich domains.[3]

Halide segregation from illumination experienced in a solar cell is most evident in time-dependent photoluminescence (PL) measurements. Halide segregation from

charge injection typically experienced in a light emitting diode is most evident in time-dependent electroluminescence (EL) measurements.[1,5] Due to charge funneling from wide band gap mixed bromide-iodide (unsegregated) domains to narrower band gap iodide-rich (segregated) domains, a longer wavelength segregated peak tends to grow with much greater intensity than the mixed bromide-iodide unsegregated peak. Although the iodide-rich domains are only estimated to make up about 1% of a halide segregated-film by volume, they have a markedly outsized impact on luminescence intensity relative to the approximately 99% by volume mixed bromide-iodide domains that remain.[1] In the absence of an excitation source, the halide segregation phenomenon is reversible due to entropic mixing of the halides. Rates of halide segregation in mixed bromide-iodide perovskites have been observed to accelerate with increasing bromide content.

For this thesis, 1.97 eV perovskite thin films were fabricated using the DMF/DMAX crystallization method and stored in a dark nitrogen atmosphere. As shown by PL spectra under continuous illumination in Figure 6.1, these 1.97 eV thin films halide segregated upon illumination over the course of a few minutes. PLQE increased strongly with the formation of iodide-rich domains as a result of halide segregation, signaling the increased radiative efficiency of the segregated domains.

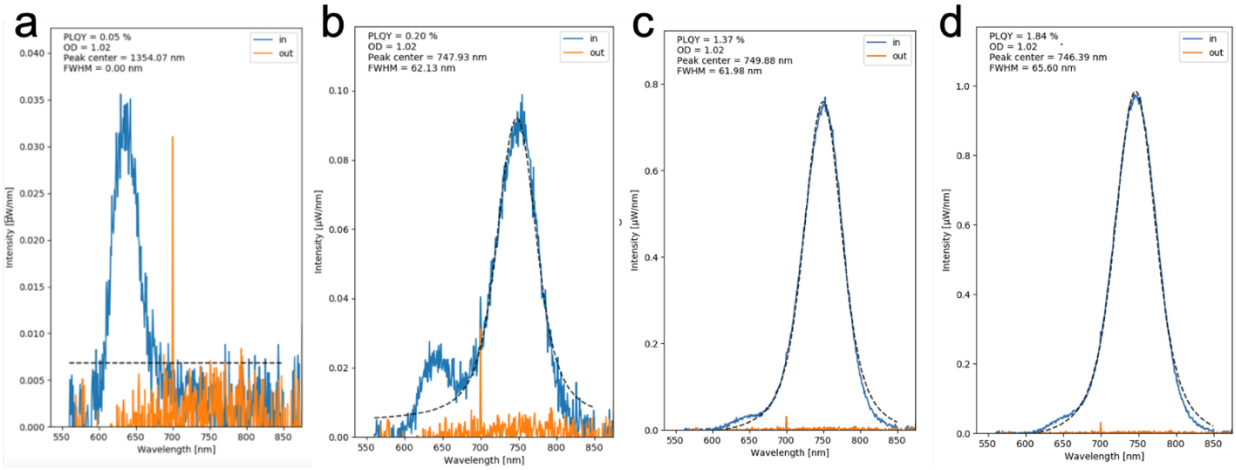

Figure 6.1. PL spectra of 1.97 eV thin film at a) 0 minutes (initial exposure to illumination) b) 1 minute c) 5 minutes and d) 15 minutes of illumination from a 445 nm laser at 1-sun intensity. Iodide-rich domains grew rapidly and become more emissive (PL intensity increases) over time. PLQE of the film increased 36.8-fold from 0 minutes (0.05%) to 15 minutes (1.84%) of illumination.

Due to its reversibility in the dark, halide segregation is not an obvious long-term degradation effect. The main practical consequence of halide segregation is its immediate effect on the performance of the solar cell at the start of and during operation, especially V_{OC}. As discussed in Chapter 5, ~2 eV band gap perovskite solar cells record V_{OC} values hundreds of mV lower than the theoretical maximum.

Mahesh et al. estimated halide segregation to cause a V_{OC} loss of approximately 100 mV in 2 eV band gap perovskite solar cells. These increased radiative recombination losses are due to more sub-band gap absorption from the segregated iodide-rich phases in the absorber. Mahesh et al. also estimated about 400 mV V_{OC} losses from non-radiative recombination processes in the bulk perovskite and at its interfaces.[6] In a later study, Peña-Camargo et al. found that high interfacial defect density in the unsegregated mixed bromide-iodide domains – not emission from iodide-rich domains as a result of halide segregation – becomes the increasingly dominant factor for V_{OC} losses with more bromide content in the perovskite composition for a band gap as wide as 1.9 eV studied.[7]

Neither study, however, fabricated high performance solar cells to quantitatively measure the impact of these factors at very wide ~2 eV band gap perovskite absorber compositions. For this thesis, 1.97 eV perovskite solar cells were fabricated and measured.

6.2 – V_{OC} Loss Mechanism Measurements and Calculations

1.97 eV perovskite single junction solar cells were fabricated with absorbers made using the DMF/DMAX crystallization method detailed in Chapter 5 and tested using Fourier-transform photocurrent spectroscopy, external quantum efficiency, photoluminescence quantum efficiency, and electroluminescence quantum efficiency measurement techniques in an attempt to quantify specific V_{OC} loss mechanisms during 120 minutes of continuous operation.

6.2.1 – Fourier-Transform Photocurrent Spectroscopy and $V_{OC, rad}$

As discussed in Section 6.1, halide segregation is the principal V_{OC} loss mechanism from radiative recombination when wide band gap perovskite solar cells are illuminated. External quantum efficiency and Fourier-transform photocurrent spectroscopy measurements of a 1.97 eV wide band gap perovskite solar cell were first conducted to quantify dark radiative recombination current ($J_{0, rad}$) over illumination time. This, in turn, allows us to quantify radiative recombination losses to V_{OC} during operation of the solar cell through the principle of detailed balance: in an equilibrium state, the absorbed photon current is equal to the emitted photon current. We can then calculate $J_{0, rad}$, the dark radiative recombination current, by taking the overlap integral of the solar cell EQE_{PV} with the blackbody spectrum:

$$J_{0,\,\mathrm{rad}} = \int EQE_{PV}(E)\Phi_{BB}(E)\,dE \qquad (6.1)$$

$EQE_{PV}(E)$ is the measured external quantum efficiency of the solar cell and Φ_{BB} is the blackbody radiation spectrum at 300K temperature.

With $J_{0,\,rad}$ calculated, we can then also calculate the open-circuit voltage of the solar cell taking radiative recombination losses as a function of illumination time into account:

$$V_{OC,\,rad} = \frac{k_B T}{q} * \ln\left(\frac{J_{SC}}{J_0} + 1\right) \qquad (6.2)$$

k_B is Boltzmann's constant (1.38 x 10^{-23} J/K), T is temperature (300K for this measurement), q is the charge, and J_{SC} is the short-circuit current. J_{SC} is estimated by the overlap integral of the AM 1.5G spectrum with the measured EQE_{PV} of the solar cell, referred to hereafter as the integrated J_{SC}.

$$J_{SC} = \int EQE_{PV}(E)\Phi_{AM\,1.5G}(E)dE \qquad (6.3)$$

Based on the EQE_{PV} measurement of the solar cell shown in Figure 6.2, the integrated J_{SC} of the 1.97 eV perovskite solar cell used for the FTPS measurements was calculated.

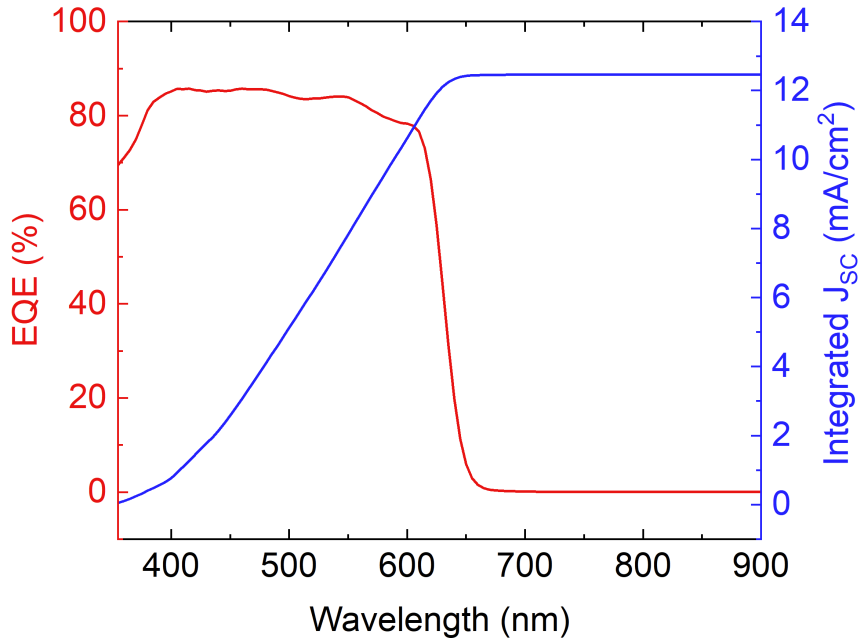

Figure 6.2. EQE_{PV} spectrum of the 1.97 eV solar cell measured for V_{OC} loss calculations. An integrated J_{SC} value of 12.46 mA/cm^2 was calculated and used for the FTPS measurements.

Fourier-transform photocurrent spectroscopy (FTPS) measurements were performed to examine the sub-band gap EQE spectra under a prolonged period of irradiance from a simulated near 1-sun intensity AM 1.5G spectrum from a xenon lamp. Before the measurement, the 1.97 eV solar cell was stored in the dark to ensure virtually no halide segregation occurred beforehand. Figure 6.3 elucidates that after 120 minutes of continuous illumination, there was only a small change in band-edge features of the solar cell.

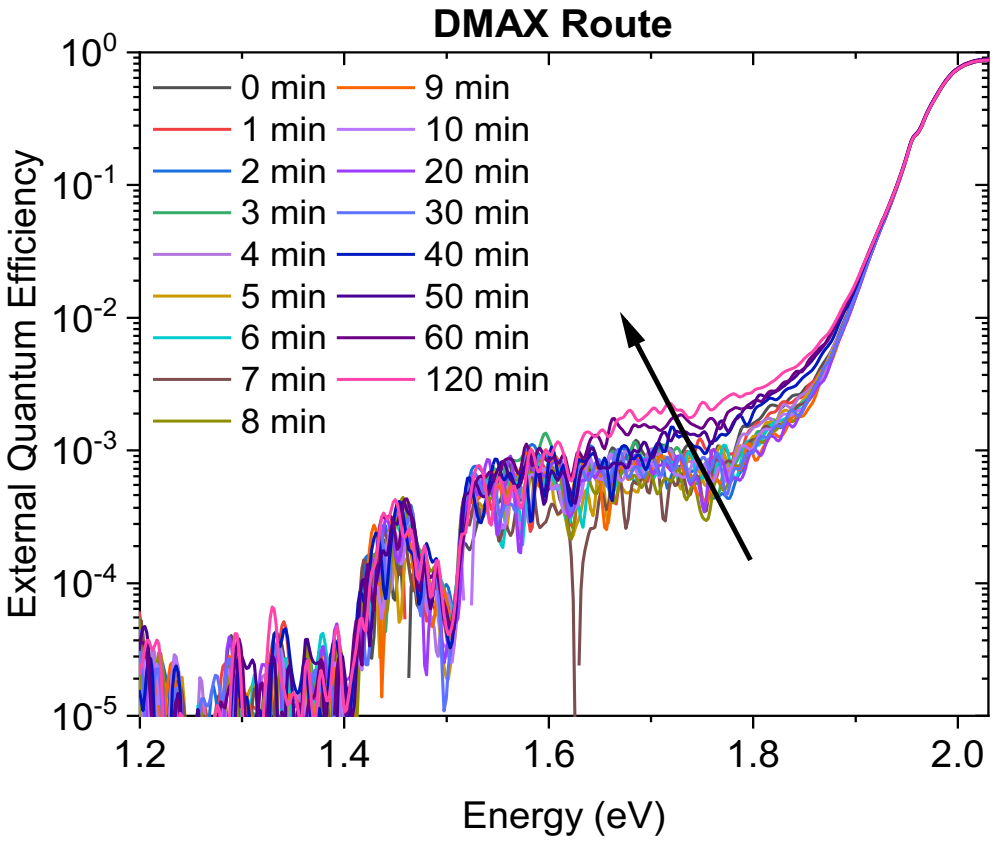

Figure 6.3. FTPS measurements at discrete amounts of time for the 1.97 eV solar cell. Only a slight increase in sub-band gap absorption is observed after 120 minutes of continuous illumination. FTPS measurements and plot created by Qimu Yuan, University of Oxford.

From this data, $J_{0,\,rad}$ and in turn $V_{OC,\,rad}$ were calculated at discrete time points during operation. $V_{OC,\,rad}$ values calculated from these FTPS measurements are plotted in Figure 6.4 with little loss after 120 minutes. Only 20 mV $V_{OC,\,rad}$ loss during operation of the 1.97 eV perovskite solar cell was calculated – five times lower than the ~100 mV loss from halide segregation predicted by Mahesh et al.[6]

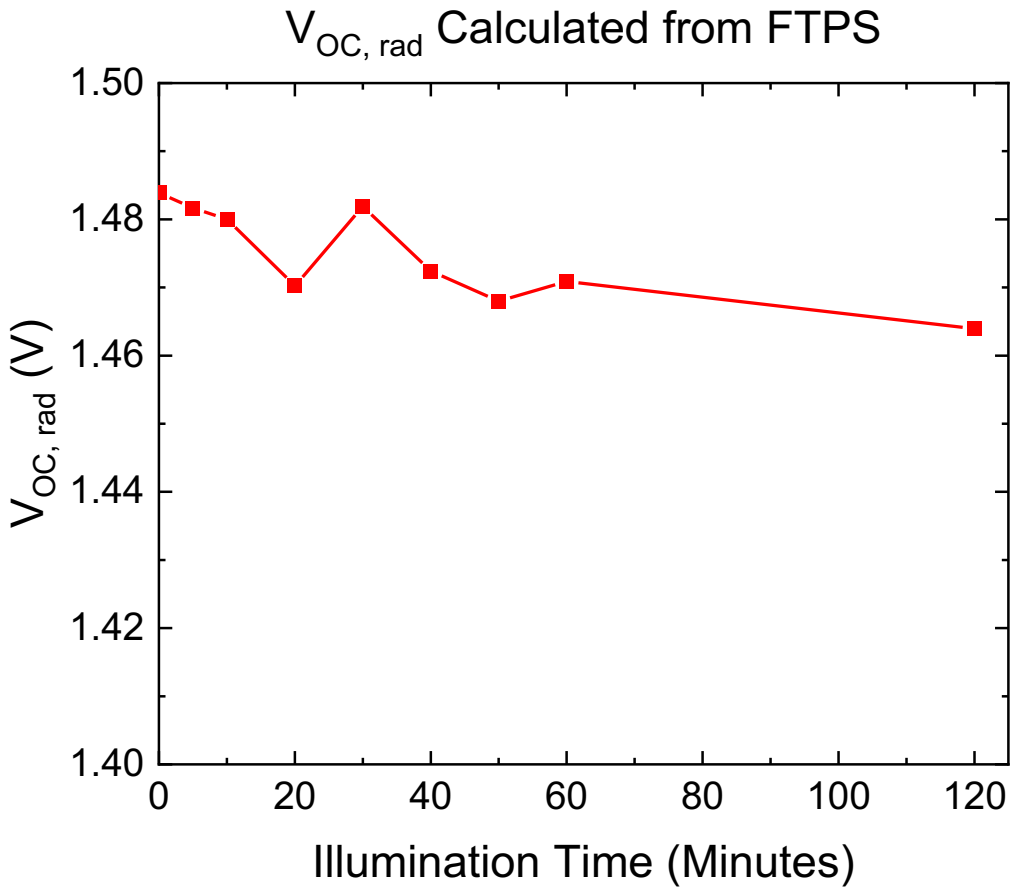

Figure 6.4. $V_{OC, rad}$ values calculated from FTPS measurements over 120 minutes of continuous illumination. After 120 minutes of continuous illumination in the FTPS setup, $V_{OC, rad}$ decreased by only 20 mV in the 1.97 eV solar cell. $V_{OC, rad}$ calculations made using a program coded by Akash Dasgupta, University of Oxford.

In addition to $V_{OC, rad}$, the Urbach energy (E_u) of the solar cell was calculated. E_u can be extracted from the steep gradient near the absorption onset in the EQE spectrum and corresponds to the collection of photocurrent from absorption just below the band gap of the intrinsic absorber. E_u offers valuable information on the relative degree of electronic and energetic disorder in the perovskite crystal.[8,9] For the 1.97 eV solar cell, an E_u value of 20.5 meV was measured at the beginning of the FTPS measurement. Only a slight 1 meV increase in E_u was observed when the solar cell was illuminated for 120 minutes as shown in Figure 6.5.

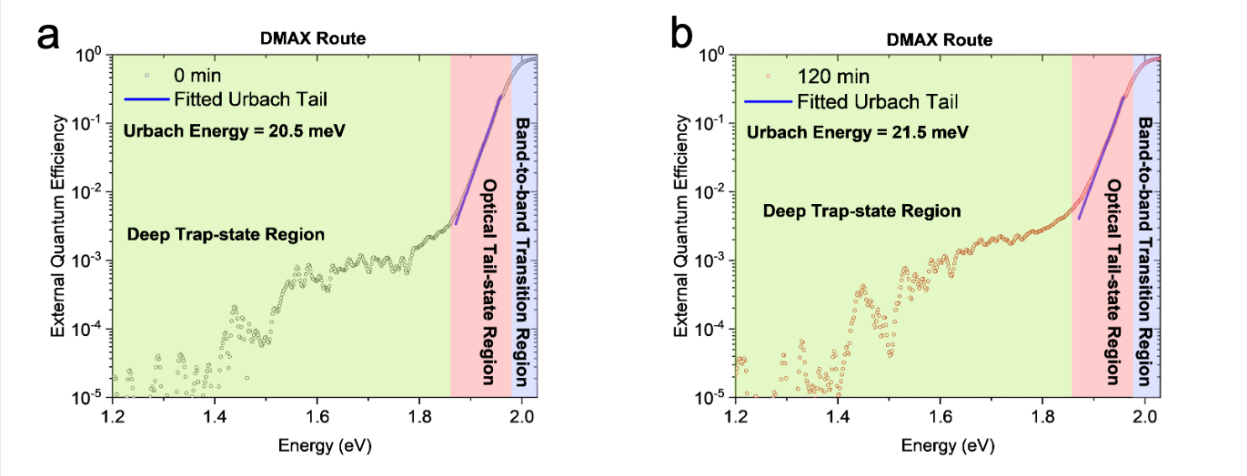

Figure 6.5. EQE spectra measured via FTPS of the same 1.97 eV solar cell and under continuous illumination for a) 0 minutes (start), and b) 120 minutes. A section of the EQE spectrum in the Urbach tail-state region, near the absorption onset, is fitted to extract the Urbach energy at different times. Background colors highlight different spectral regions corresponding to the EQE spectrum. Analysis and plots created by Qimu Yuan, University of Oxford.

A weak but significant photocurrent signal arising from the deep trap-state region was also evident, suggesting the existence of secondary phases. These defect states were photoactive with EQE spectra between 1.6 eV and 1.8 eV and increased by an order of magnitude after 120 minutes of illumination. The enhanced absorption could possibly be related to the increasing density of electron-trapping defects from bromide interstitials due to partial phase segregation or decomposition.[10-12]

6.2.2 – Photoluminescence Quantum Efficiency and $V_{OC, PLQE}$

In an intrinsic semiconductor under steady-state conditions, the Fermi level represents the distribution of intrinsic charge carriers located in the middle of the band gap between the valence band and conduction band. When the semiconductor is illuminated as in a solar cell, the intrinsic population of charge carriers shifts due to the creation of photoexcited charge carriers. Quasi-Fermi levels for the electrons (E_{FN}) and holes (E_{FP}) better describe the population levels of electrons and holes under illumination.

The difference in energy between E_{FN} and E_{FP} is termed the quasi-Fermi level splitting (QFLS).[13] QFLS is sometimes referred to as the "internal voltage" of the semiconductor material because it assumes no contact losses in the solar cell such that the maximum possible voltage is extracted.

Using photoluminescence quantum efficiency (PLQE) measurements, we can calculate the QFLS of a solar cell, hereafter referred to as $V_{OC,\,PLQE}$ in this thesis.

$$V_{OC,\,PLQE} = V_{OC,\,rad} + \frac{k_B T}{q} * \ln(PLQE) \qquad (6.4)$$

With the $V_{OC,\,rad}$ values at certain time points known from FTPS measurements, only PLQE measurements of the 1.97 eV solar cell were required to calculate $V_{OC,\,PLQE}$.

The 1.97 eV solar cell was illuminated continuously for 120 minutes by a 1-sun intensity 445 nm laser and PLQE values were measured at discrete time points. As Figure 6.6 highlights, the resultant $V_{OC,\,PLQE}$ values increased over time indicating enhanced radiative efficiency of the solar cell.

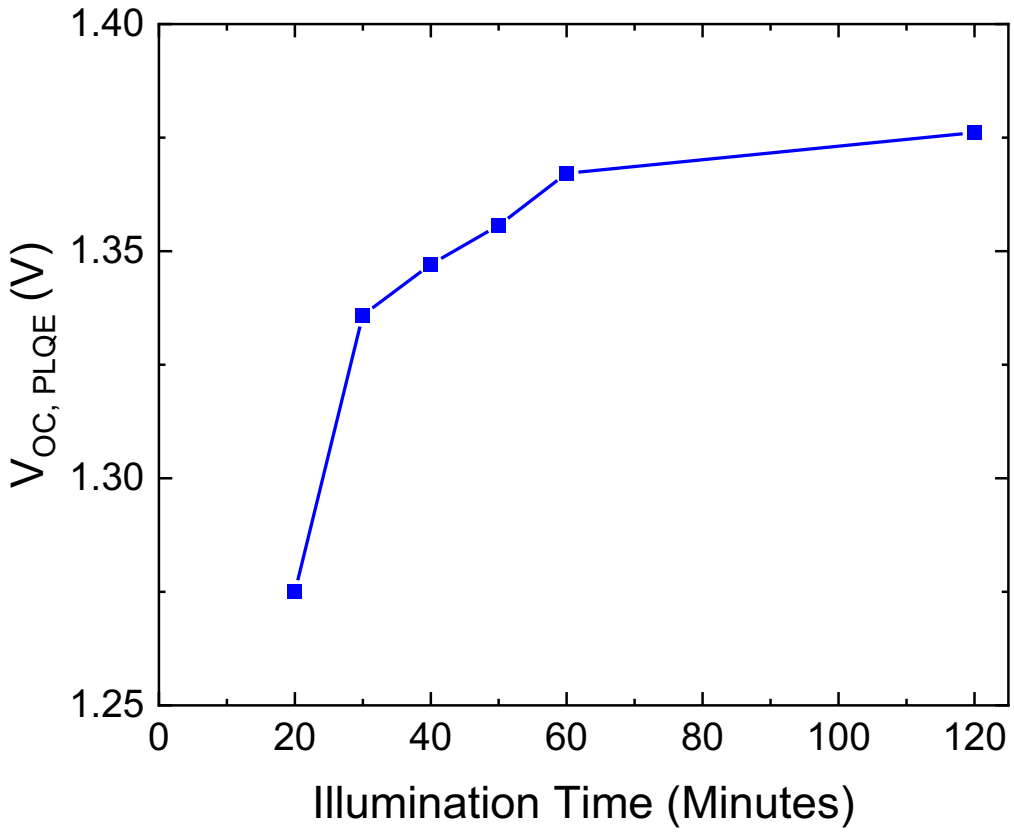

Figure 6.6. $V_{OC, PLQE}$ values calculated from PLQE measurements of the 1.97 eV solar cell over 120 minutes of continuous 1-sun intensity illumination from a 445 nm laser. Reliable PLQE measurements were not picked up until after 20 minutes of illumination with halide segregation.

Note that no $V_{OC, PLQE}$ values could be calculated until after 20 minutes of illumination due to the very low initial mixed bromide-iodide PLQE values below the 0.01% value that could not be reliably measured above noise by the detector. By 20 minutes, halide segregation had occurred in the solar cell with an iodide-rich domain emission peak around 775 nm (1.6 eV) that grew continuously for the remainder of the measurement. After 120 minutes, the PLQE of the solar cell had increased from < 0.01% (dominated by unsegregated mixed bromide-iodide domains) to 3.27% (dominated by segregated iodide-rich domains).

Although the segregated iodide-rich domains have a lower band gap energy around 1.6 eV, this was compensated by the enhanced and continuously improving radiative efficiency of these domains compared to the initial unsegregated mixed bromide-iodide domains. The increased radiative efficiency of the segregated iodide-rich domains was highlighted by their increased PLQE and resultant $V_{OC,\ PLQE}$ with illumination. Over time, the unsegregated mixed bromide-iodide and segregated iodide-rich QFLS seem to align as depicted in Figure 6.7 for effective charge funneling to the segregated iodide-rich domains.

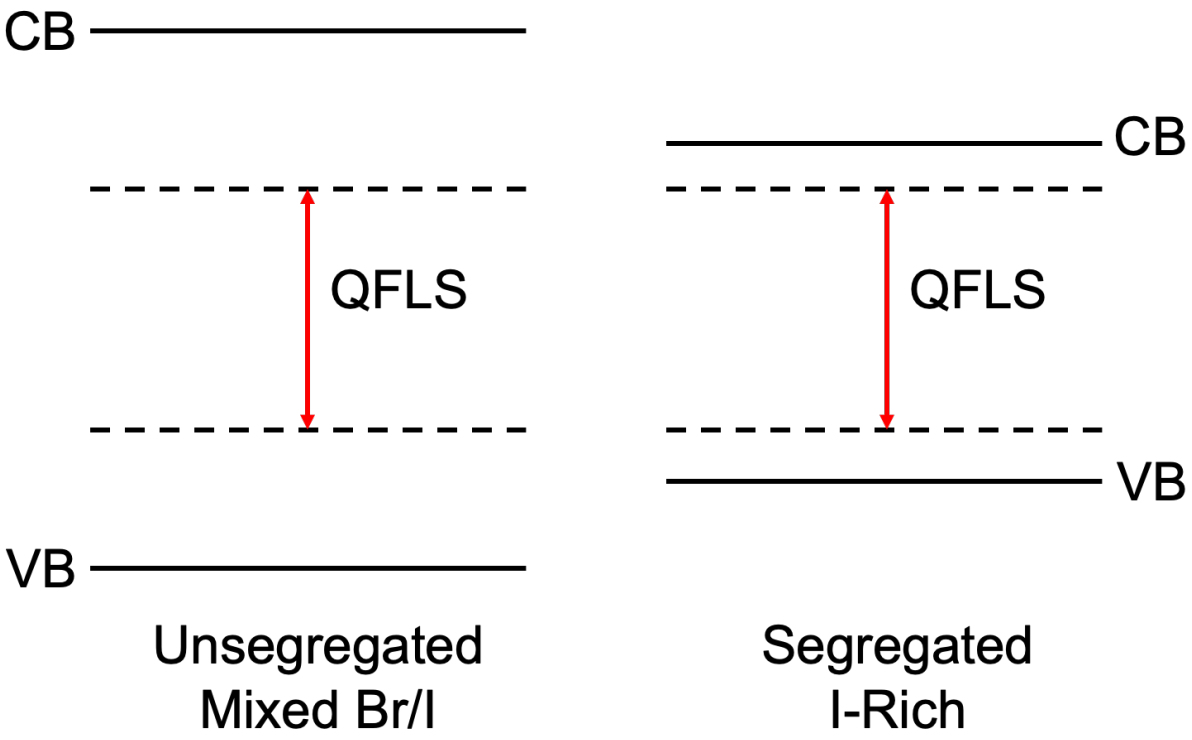

Figure 6.7. Potential QFLS alignment between wide band gap unsegregated mixed bromide-iodide domains and narrower band gap segregated iodide-rich domains that may explain increased radiative efficiency and $V_{OC,\ PLQE}$ of the 1.97 eV solar cell over 120 minutes of illumination time.

The growth of segregated iodide-rich domains in the 1.97 eV perovskite solar cell did not harm $V_{OC,\ PLQE}$ over illumination time. Instead, $V_{OC,\ PLQE}$ increased ~100 mV over

the course of measurement as the iodide-rich domains became more emissive with continued illumination.

6.2.3 – Electroluminescence Quantum Efficiency and $V_{OC, ELQE}$

It is useful to drive current through a solar cell and measure its electroluminescence (EL) to determine non-radiative recombination losses of the solar cell.[14] For this thesis, the 1.97 eV perovskite single junction solar cell was injected with 12 mA/cm^2 current density (which is the same as the J_{SC} value to modulate the same current density in the solar cell during operating condition) for 120 minutes with EL intensity measured. Effectively, this solar cell was treated like a light emitting diode, with halide segregation readily apparent as seen in Figure 6.8. After 120 minutes, the segregated iodide-rich domains were approximately ten times more emissive than the initial unsegregated mixed bromide-iodide domains at J_{SC} current injection condition.

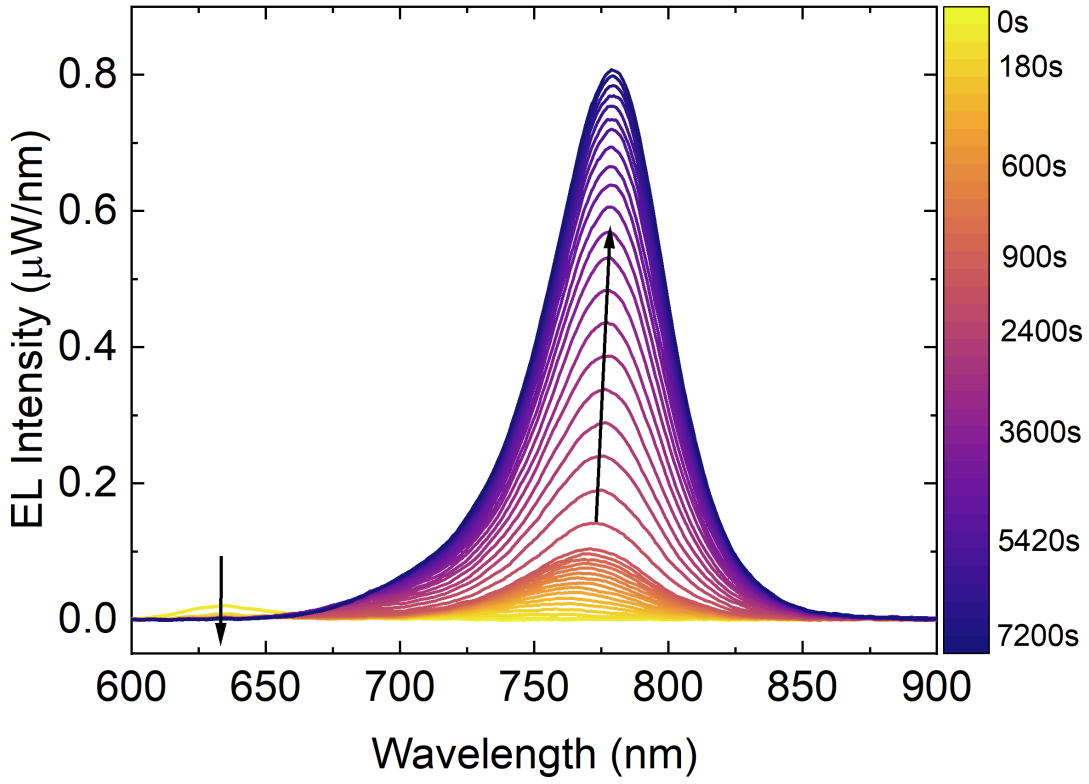

Figure 6.8. EL intensity of 1.97 eV solar cell over 120 minutes of 12 mA/cm^2 current injection (J_{SC} condition). After a few minutes, the initial mixed bromide-iodide domain signal disappeared while the iodide-rich domain signal continuously grew in intensity. Measurement performed by Dr. Zhongcheng Yuan, University of Oxford.

Electroluminescence quantum efficiency (EQE_{EL} or ELQE) is defined as the ratio of radiative recombination current to the total (radiative and non-radiative) recombination current.

$$EQE_{EL} = \frac{J_{0,rad}}{J_0} = \frac{J_{0,rad}}{J_{0,rad} + J_{0,non-rad}} \qquad (6.5)$$

In the context of the measurement setup, EQE_{EL} is equivalent to the ratio of the number of photons emitted to the number of electrons injected.

Rau's second reciprocity theorem establishes the relation between V_{OC} and EQE_{EL}, whereby J_0 can be calculated by including EQE_{EL} as a scaling factor[15]:

$$J_{SC} = \frac{J_{0,rad}}{EQE_{EL}} = \frac{q}{EQE_{EL}} \int_0^{\infty} EQE_{PV}(E)\Phi_{BB}(E)dE \qquad (6.6)$$

With known value of both EQE_{PV} and EQE_{EL} of a solar cell, the V_{OC} of the solar cell can be calculated taking into account non-radiative recombination losses in the bulk and at the interfaces with the perovskite absorber. This value is termed $V_{OC,\ ELQE}$ in this thesis:

$$V_{OC,\ ELQE} = V_{OC,\ rad} + \frac{k_B T}{q} * \ln\left(EQE_{EL}\right) \qquad (6.7)$$

$V_{OC,\ rad}$ is calculated from FTPS measurements of the solar cell discussed in Section 6.2.1.

$V_{OC,\ ELQE}$ values for the 1.97 eV solar cell based on measurements described in the ELQE setup at discrete time points were calculated. As shown in Figure 6.9, $V_{OC,\ ELQE}$ values increased over 120 minutes of continuous current injection. The significant increase in $V_{OC,\ ELQE}$ values over time seems to indicate a reduction in non-radiative recombination losses across the film.

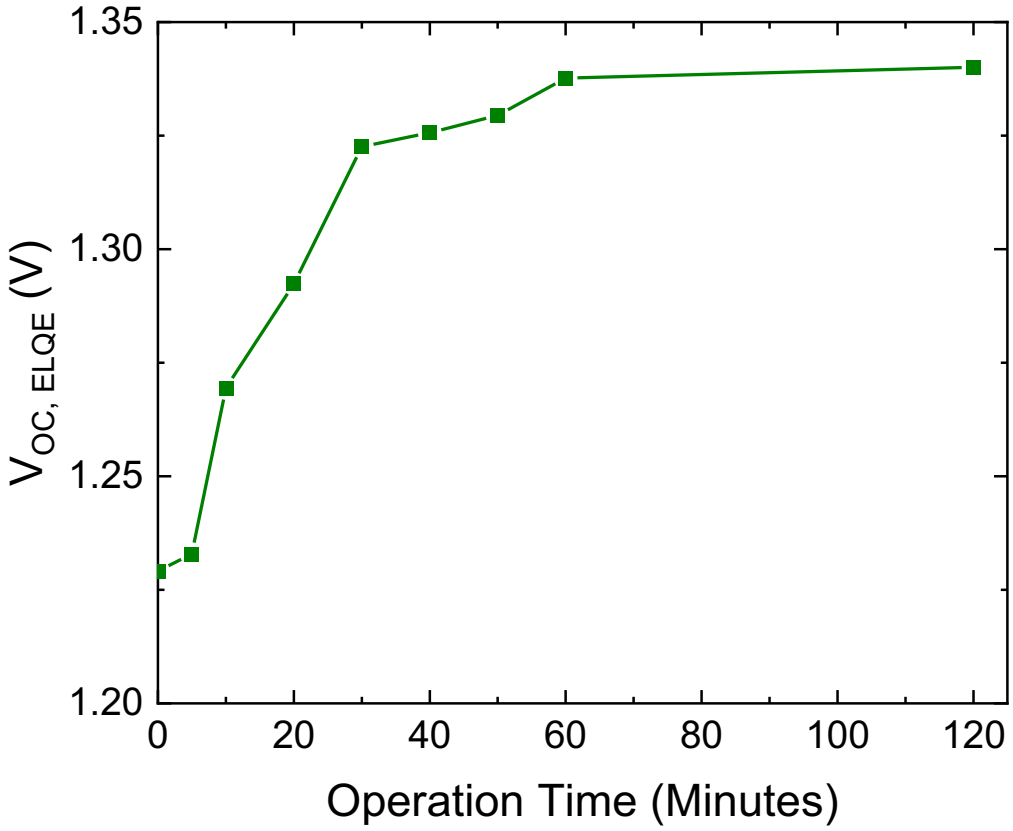

Figure 6.9. $V_{OC, ELQE}$ values calculated from ELQE measurements over 120 minutes of continuous 12 mA/cm^2 current injection. $V_{OC, ELQE}$ values increased ~100 mV over 120 minutes, with the majority of the increase during the first 30 minutes.

After halide segregation occurred, the associated $V_{OC, ELQE}$ values calculated may not be accurate due to the shifted emission spectra. Based on the PLQE measurements of the same solar cell in Section 6.2.2, the radiative efficiency of the segregated iodide-rich domains increased under illumination. The higher EQE_{EL} values from the more emissive segregated iodide-rich domains observed in Figure 6.8 support that the radiative efficiency of these domains also increased under current injection conditions.

Because it is impossible to distinguish the ratio of electrons injected into the unsegregated and segregated (by charge funnelling from the unsegregated mixed bromide-iodide perovskite) domains, the $V_{OC, ELQE}$ of the unsegregated mixed bromide-

iodide perovskite alone cannot be calculated. The non-radiative recombination losses that affect V_{OC} of the initial unsegregated mixed bromide-iodide perovskite therefore cannot be calculated with certainty. V_{OC} loss calculations from ELQE may potentially be less accurate than those from FTPS because ELQE relies on emission while FTPS relies on absorption. Even if we assume 1% of the 1.97 eV perovskite film volume contained segregated domains with illumination/current injection, the more emissive minority phase can saturate the measurement.

Absorption weights the volume of the film more representatively than emission. Because absorption captures light, the entire volume of the film is engaged with absorption. Because emission depends more strongly on the quality of the materials in the film, small volumes with much higher radiative efficiency can dominate the measurement.

$V_{OC,\ ELQE}$ calculations remain accurate for the entire perovskite solar cell system, nonetheless, because the ELQE measurement in this thesis captures both unsegregated and segregated domains. The ELQE measurements show that two signals appeared over time during the 1.97 eV perovskite single junction solar cell operation – unsegregated and segregated – and that the radiative recombination efficiency of the segregated phase increased over time. As current injection time increased, charge carriers in the unsegregated mixed bromide-iodide domains may either have been collected in an unsegregated domain trap state or charge funneled to segregated iodide-rich domains where they radiatively recombined – increasing $V_{OC,\ ELQE}$ over time.

6.3 – Interpreted Results

The $V_{OC,\ rad}$, $V_{OC,\ PLQE}$, and $V_{OC,\ ELQE}$ calculations over 120 minutes of operation time detailed in Section 6.2 are plotted together, along with a 120-minute steady-state V_{OC} measurement of the 1.97 eV perovskite single junction solar cell in the solar simulator. The results are plotted in Figure 6.10, showing 20 mV V_{OC} loss from radiative recombination due to halide segregation ($V_{OC,\ rad}$).

This 20 mV $V_{OC,\ rad}$ loss is five times less than the ~100 mV loss from halide segregation estimated by Mahesh et al.[6] This leaves non-radiative recombination processes, rather than halide segregation, to account for most V_{OC} losses. However, non-radiative recombination losses for the solar cell appeared to decrease with increased $V_{OC,\ PLQE}$ and $V_{OC,\ ELQE}$. While calculated $V_{OC,\ ELQE}$ for the halide segregated 1.97 eV solar cell may not be entirely accurate, ELQE is ultimately a measurement of efficiency under charge injection while $V_{OC,\ Solar\ Simulator}$ is a measurement of charge extraction efficiency.

ELQE treats the solar cell that is being measured under current injection as a light emitting diode while, in reality, it is a solar cell that operates under illumination. For the 1.97 eV perovskite single junction solar cell, Figure 6.10 shows $V_{OC,\ ELQE}$ values under current injection as the green plot, with $V_{OC,\ ELQE}$ increasing with longer current injection time compared to $V_{OC,\ Solar\ Simulator}$ under the same illumination time period, which may in part be explained by the factors discussed herein.

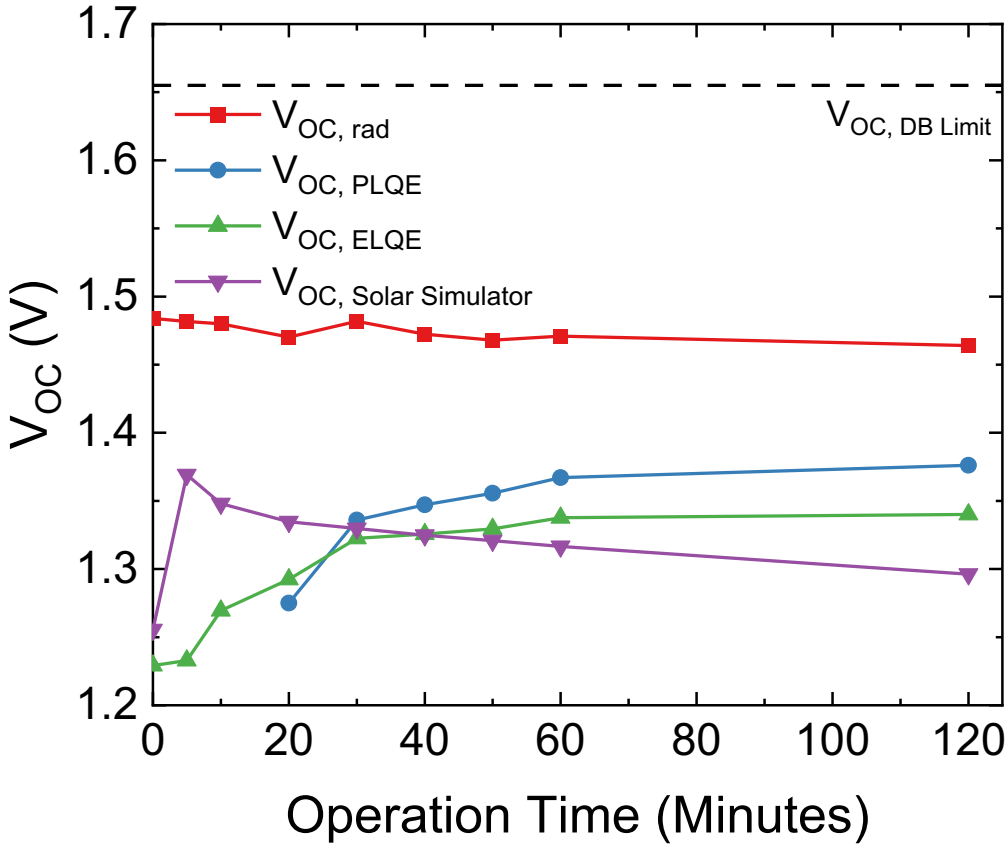

Figure 6.10. Calculated solar cell V_{OC} values over 120 minutes of continuous operation from FTPS ($V_{OC,\ rad}$), PLQE ($V_{OC,\ PLQE}$), and ELQE ($V_{OC,\ ELQE}$) measurements. PLQE values were too low to be reliably detected and calculated before 20 minutes into measurement. Steady-state V_{OC} values from the solar simulator ($V_{OC,\ Solar\ Simulator}$) were measured directly in the setup under 1-sun intensity AM 1.5G illumination. The dashed line represents the detailed balance limit V_{OC} of 1.655 V for a 1.97 eV band gap semiconductor.

$V_{OC,\ Solar\ Simulator}$ decreased from its maximum value at 5 minutes over the course of steady-state measurement. No calculated V_{OC} values from FTPS, PLQE, or ELQE measurements are equivalent to that of $V_{OC,\ Solar\ Simulator}$ after 120 minutes of continuous operation. As such, other V_{OC} loss mechanisms may be at work in the solar cell that were not studied. Three additional potential V_{OC} loss mechanisms during operation of the 1.97 eV perovskite single junction solar cell are: potential buildup of bromide or iodide halide ions at different interfaces with the perovskite absorber resulting from halide segregation;

altered charge selectivity at the charge transport layers due to halide segregation in the absorber; and degradation of the charge transport layers themselves.

Future experimental designs to attempt to reduce these V_{OC} losses, both initially and over time, include better energetically aligned hole transport layers, bulk materials of superior crystalline quality, and potentially more stable non-fullerene organic electron transport layers.[7,15,16]

6.4 – Conclusion

1.97 eV wide band gap perovskite single junction solar cells fabricated using the optimized DMF/DMAX crystallization and device stack developed in Chapter 5 were measured using Fourier-transform photocurrent spectroscopy (FTPS), external quantum efficiency (EQE), photoluminescence quantum efficiency (PLQE), and electroluminescence quantum efficiency (ELQE) techniques. Open-circuit voltage values were calculated from FTPS, PLQE, and ELQE measurements conducted over a period of 120 minutes of continuous solar cell operation. The 20 mV V_{OC} loss from radiative recombination due to halide segregation ($V_{OC,\ rad}$) measured is five times less than the published estimate of ~100 mV loss. These results indicate that, compared to estimates, halide segregation has a less substantial effect on V_{OC} loss mechanisms in the 1.97 eV perovskite solar cells fabricated using DMF/DMAX. These results were promising for incorporation of the 1.97 eV wide band gap perovskite absorber as the top subcell in an all-perovskite triple junction tandem solar cell that must maintain high voltage output for high efficiency during continuous operation, as achieved in Chapter 7.

Chapter 6 References

1. Hoke, E. T. et al. Reversible photo-induced trap formation in mixed-halide hybrid perovskites for photovoltaics". *Chem. Sci.*, **6**, 1, 613–617 (2015).

2. J. Knight and L. M. Herz, "Preventing phase segregation in mixed-halide perovskites: a perspective," Energy Environ. Sci., vol. 13, no. 7, pp. 2024–2046, 2020.

3. Chen, Z. et al. Unified theory for light-induced halide segregation in mixed halide perovskites. *Nature Communications*, **12**, 2687 (2021).

4. Unger, E. L. et al. Roadmap and roadblocks for the band gap tunability of metal halide perovskites. *J. Mater. Chem. A*, **5**, 23, 11401–11409 (2017).

5. Braly, I. L. et al. Current-Induced Phase Segregation in Mixed Halide Hybrid Perovskites and its Impact on Two-Terminal Tandem Solar Cell Design. *ACS Energy Lett.*, **2**, 1841–1847 (2017).

6. Mahesh, S. et al. Revealing the origin of voltage loss in mixed-halide perovskite solar cells. *Energy Environ. Sci.*, **13**, 1, 258–267 (2020).

7. Peña-Camargo, F. et al. Halide Segregation versus Interfacial Recombination in Bromide-Rich Wide-Gap Perovskite Solar Cells. *ACS Energy Lett.*, **5**, 2728–2736 (2020).

8. Zeiske, S. et al. Static disorder in lead halide perovskites. *J. Phys. Chem. Lett.*, **13***,* 31, 7280-7285 (2022).

9. McMeekin, D.P. et al. Intermediate-phase engineering via dimethylammonium cation additive for stable perovskite solar cells. *Nature Materials*, **22**, 73-83 (2023).

10. Motti, S. G. et al. Defect activity in lead halide perovskites. *Adv. Mater.*, **31**, 47, 1901183 (2019).

11. Ulatowski, A. M. et al. Charge-carrier trapping dynamics in bismuth-doped thin films of $MAPbBr_3$ perovskite. *J. Phys. Chem. Lett.*, **11**, 9, 3681-3688 (2020).

12. Sutter-Fella, C. M. et al. Band tailing and deep defect states in $CH_3NH_3Pb(I_{1-x}Br_x)_3$ perovskites as revealed by sub-bandgap photocurrent. *ACS Energy Lett.*, **2**, 3, 709-715 (2017).

13. Caprioglio, P. et al. On the Relation between the Open-Circuit Voltage and Quasi-Fermi Level Splitting in Efficient Perovskite Solar Cells. *Adv. Energy Mater.*, **9**, 1901631 (2019).

14. Rau, U. Reciprocity relation between photovoltaic quantum efficiency and electroluminescent emission of solar cells. *Phys. Rev. B*, **76**, 1-8 (2007).

15. Wang, F. et al. Defects engineering for high-performance perovskite solar cells. *Flexible Electronics*, **22** (2018).

16. Wang, D., Ye, T. and Zhang, Y. Recent advances of non-fullerene organic electron transport materials in perovskite solar cells. *J. Mater. Chem. A*, **8**, 20819-20848 (2020).

Chapter 7

All-Perovskite Multijunction Tandem Solar Cells

7.1 – Introduction

In this chapter, all-perovskite multijunction tandem solar cells utilizing the 1.97 eV $FA_{0.9}Cs_{0.1}Pb(Br_{0.68}I_{0.32})_3$ wide band gap absorber detailed in Chapters 5 and 6 are fabricated and tested, achieving a champion solar cell with 27.3% maximum power point tracked efficiency and 3.37 V steady-state open-circuit voltage at 1 cm^2 area. This 27.3% efficiency is the highest of any known all-perovskite triple junction tandem solar cell efficiency published to date and identical to the highest known reported efficiency of 27.3% for a single junction crystalline silicon solar cell.

Three batches of all-perovskite multijunction tandem solar cells are fabricated and tested, one double junction batch with band gap absorbers of 1.97 eV/1.61 eV and two triple junction batches with band gap absorbers of 1.97 eV/1.61 eV/1.25 eV. Effective architectures and interlayers utilizing 1.61 eV middle band gap and 1.25 eV narrow band gap subcell absorbers are developed and implemented for monolithic, all-perovskite triple junction tandem solar cell application. High performance all-perovskite triple junction tandem solar cells are successfully fabricated demonstrating the increased efficiency resulting from such tandems.

Stability is tested using one of these all-perovskite triple junction solar cells, resulting in the solar cell retaining 99.3% of its initial efficiency after 120 minutes of continuous maximum power point tracking under 1-sun intensity AM 1.5G illumination.

Multijunction solar cells offer the opportunity to exceed the theoretical efficiency limit of single junction solar cells because multiple semiconductor absorbers add to the overall efficiency. The use of multiple semiconductor absorber layers stacked on top of one another is the foundational principle of multijunction solar cells. The different absorber layers contribute in tandem to the overall solar cell efficiency.

In theory, an infinite junction stack of semiconductor layers with different band gaps to absorb each wavelength of incident solar irradiation can achieve a power conversion efficiency of 67% at 1-sun intensity. In practice, the cost of each semiconductor layer and substantial parasitic losses from recombination layers that accumulate with a high number of junctions typically limit multijunction tandem solar cells to 2-4 junctions. Under 1-sun intensity from the AM 1.5G spectrum, double, triple, and quadruple junction tandem solar cells have a theoretical maximum efficiency of 45%, 51%, and 55%, respectively, compared to 33.7% for a single junction solar cell.[1-3]

Multijunction tandem solar cells are typically constructed using either 4-terminal or 2-terminal architectures illustrated in Figure 7.1. In a 4-terminal architecture, semiconductor junctions are fabricated separately into distinct solar cells, each with their own set of two terminal electrodes. These solar cells are then mechanically stacked on top of one another and are independently electrically connected. The power output of a 4-terminal architecture tandem is the sum of the power of each independent subcell. In this architecture, each subcell can generate different current values at their junction and operate independently from one another. Although the theoretical maximum efficiency of a 4-terminal tandem is slightly higher than that of a 2-terminal tandem, they are likely to incur higher overall costs.[4] 4-terminal tandems require more terminals (conductive

substrates and transparent, laterally conductive oxide layers) to function, increasing material cost. The additional terminals may increase parasitic absorption losses in the device stack and therefore decrease the efficiency of the solar cell. To function properly, 4-terminal tandem solar cells require more sophisticated wiring – another source of added cost.

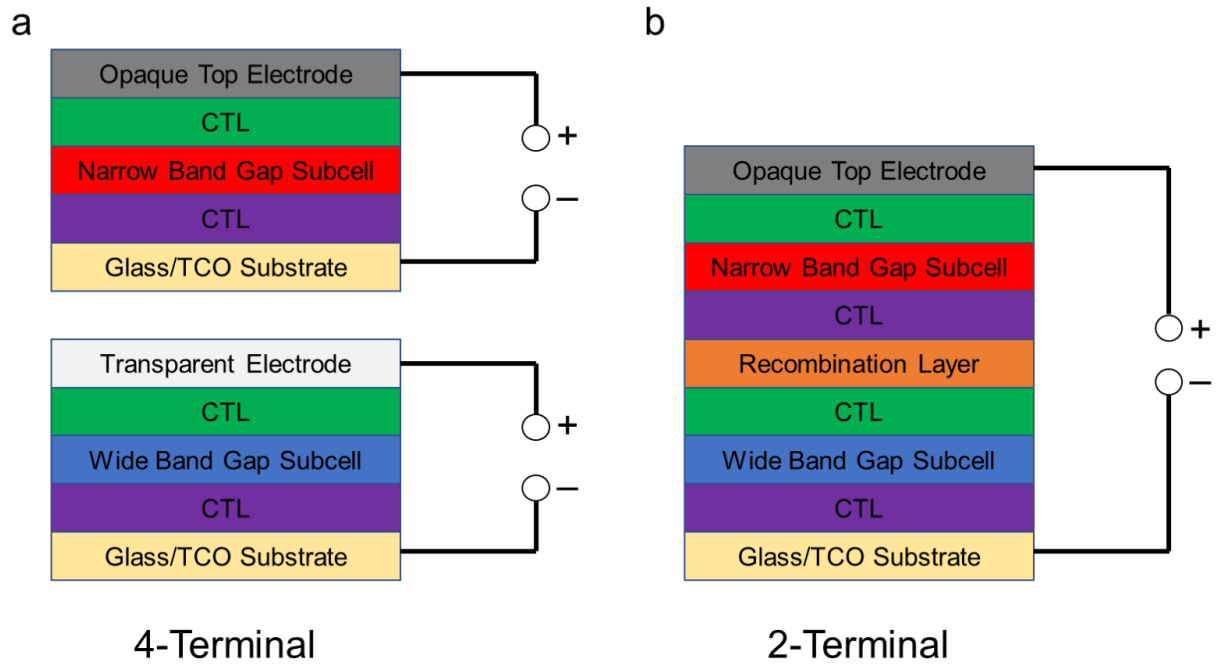

Figure 7.1. Schematics of a) 4-terminal and b) 2-terminal tandem architectures for a double junction tandem solar cell. In a 4-terminal tandem, the subcells are electrically independent and the total power is calculated: $P_{Total} = (J_{Wide}V_{Wide}) + (J_{Narrow}V_{Narrow})$. In a 2-terminal tandem, the subcells are electrically connected in series so the current is limited by the minimum subcell current output, such that the total power is calculated: $P_{Total} = J_{Minimum}\ (V_{Wide} + V_{Narrow})$.

In the 2-terminal architecture, semiconductor absorber layers are fabricated directly on top of each other and mechanically stacked so the junctions are connected in series and integrated into a single, monolithic device.[4] The 2-terminal architecture reduces cost because only two terminals are required for the entire device stack. Instead

of separate electrode connections, 2-terminal tandem solar cells use recombination layers that electrically connect the subcells in series.

Although recombination layers offer the promise of reduced costs, they introduce the challenge of current matching: the current output of each subcell must be equal otherwise the overall tandem current will be limited by the subcell with the minimum current output.[5] To address the challenge of current matching, subcell absorbers with carefully tuned band gaps must be employed. This band gap restriction limits the kinds of semiconductor absorbers that can be used to make 2-terminal tandem solar cells. Because the subcells in a 2-terminal tandem solar cell are connected in series and thus electrically interdependent, each subcell must be fabricated on top of the other in a single stack. It is imperative that the depositions of successive layers in a 2-terminal tandem solar cell – which can impose different chemical environments, solvents, and processing temperatures – do not damage previous layers underneath in the stack. If one subcell does not function as a result of damage at some point during fabrication, the 2-terminal tandem solar cell performance will be reduced.[6]

Notwithstanding the additional challenges that must be considered during fabrication, 2-terminal tandems offer the promise of substantially reduced overall cost if they can be overcome. Perovskites are particularly attractive for 2-terminal architectures – and achieving necessary current matching – due to their tunable wide, middle, and narrow band gap absorbers. The monolithic, 2-terminal architecture was used for all multijunction tandem solar cells fabricated for this thesis.

A multijunction solar cell utilizing Group III-V semiconductors has achieved the highest power conversion efficiency of any solar cell – a quadruple junction

GaInP/AlGaAs/GaInAsP/GaInAs tandem reached 47.6% record efficiency at 665-suns intensity – demonstrating the increased efficiency resulting from tandems.[7] This quadruple junction tandem solar cell, however, is cost-prohibitive because it requires epitaxially grown semiconductor materials with a module minimum sustainable price in the range of $77/W.[8]

More practically, multijunction solar cells utilizing perovskites offer the promise of power conversion efficiencies exceeding 30% and less expensive, scalable fabrication techniques. As noted in Section 2.3.2, a minimum sustainable price of $0.18/W has been estimated for an all-perovskite double junction tandem module at 30% efficiency.[8]

7.2 – All-Perovskite Triple Junction Tandem Solar Cells

All-perovskite triple junction tandem solar cells have the potential to exceed 30% efficiency. Due to their complexity, however, only five articles have published performance results for all-perovskite triple junction tandem solar cells. As discussed in Chapter 5, Hörantner et al. simulated a possible 36.6% PCE all-perovskite triple junction tandem solar cell with approximately 2.0/1.55/1.22 eV wide/middle/narrow band gap subcell absorbers. Although an encouraging possibility, all-perovskite triple junction tandem solar cells have not yet approached this efficiency.[9]

Instead, the published PCE results for all-perovskite triple junction tandem solar cells range from 6.7% to 25.1%, as presented in Table 7.1. Notably, improved wide band gap perovskite subcells for these triple junctions increased tandem V_{OC} and PCE above 20%. ~2 eV wide band gap subcells with V_{OC} > 1.3 V produced tandem V_{OC} values exceeding 3 V and PCE values well beyond 20%.

WBG/MBG/NBG Subcell Absorbers	PCE (%)	V_{OC} (V)	Active Area (cm^2)	Publication Year	Institution
1.94/1.57/1.34 eV	6.7	2.70	0.0919	2019[10]	University of Oxford
1.99/1.60/1.22 eV	16.8	2.78	0.0676	2020[11]	Eindhoven University of Technology
1.73/1.57/1.23 eV	20.1	2.802	0.049	2020[12]	Nanjing University
1.97/1.61/1.25 eV	24.3	3.21	0.049	2023[13]	University of Toronto
2.00/1.60/1.22 eV	25.1	3.33	0.049	2023[14]	University of Toronto

Table 7.1. All-perovskite triple junction tandem solar cells published prior to this thesis. Until the 27.3% efficiency achieved in this thesis, the highest known published all-perovskite triple junction tandem solar cell efficiency was 25.1%. In addition, all active areas were smaller than 1 cm^2 active area of the 27.3% efficiency champion in this thesis.

The published results to date, shown in Table 7.1, indicate high quality, high voltage 2 eV wide band gap subcell absorbers and effective interlayers are crucial for the improvement of all-perovskite triple junction tandem solar cells.

7.3 – Development of All-Perovskite Tandem Solar Cells

For this thesis, three batches of all-perovskite multijunction tandem solar cells were fabricated and tested – one double junction batch and two triple junction batches. The all-perovskite triple junction tandem solar cell batches use a unique device stack featuring an ICBA electron transport layer for the wide band gap subcell and IZO recombination

layers. The double junctions have band gap absorbers of 1.97 eV and 1.61 eV. The triple junctions use the same band gap absorbers of 1.97 eV, 1.61 eV, and 1.25 eV but have different precursor concentrations and different recombination layer materials. The 27.3% efficiency champion solar cell is an all-perovskite triple junction tandem solar cell with band gap absorbers of 1.97 eV, 1.61 eV, and 1.25 eV, 0.9 M concentration for the 1.97 eV perovskite precursor, and IZO recombination layers.

7.3.1 – All-Perovskite Double Junction Tandem Solar Cells with 1.97 eV and 1.61 eV Band Gap Absorbers

All-perovskite double junction tandem solar cells with 1.97 eV wide band gap and 1.61 eV middle band gap subcell absorbers first were fabricated to test recombination layers before proceeding to triple junctions. The purpose of the recombination layer is to electrically connect the subcells in 2-terminal architecture tandem solar cells. Efficient recombination of majority charge carriers, accumulated on either side of the recombination layer from the subcells, enables charge carriers generated in each subcell to ultimately be collected at the contacts of the tandem solar cell. Testing recombination layers in double junctions is easier than in triple junctions because only one recombination layer is varied instead of two. For these double junctions, the 1.97 eV wide band gap subcell was combined with the 1.61 eV middle band gap perovskite subcell fabricated by Dr. Junke Wang, University of Oxford. Gold (Au) and sputtered indium doped zinc oxide (IZO) were tested as recombination layer materials. The device stack for these all-perovskite double junction tandem solar cells was fabricated as illustrated in Figure 7.2, showing the recombination layer between the 1.97 eV and 1.61 eV subcells was fabricated using either Au or IZO.

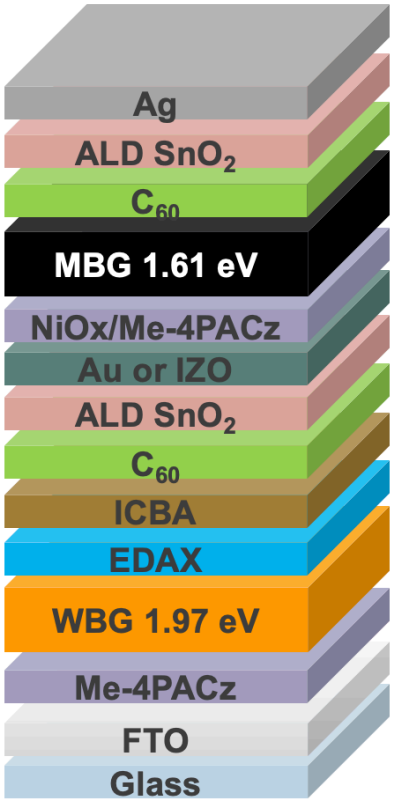

Figure 7.2. All-perovskite double junction tandem solar cell device stack with either Au or IZO recombination layer material between the 1.97 eV and 1.61 eV subcells.

1 nm of Au was thermally evaporated. A variety of thicknesses of IZO (5, 10, 15, and 20 nm) were sputtered. Figure 7.3 presents all double junction tandem solar cells fabricated in this experiment, showing significant J_{SC} enhancement with sputtered IZO recombination layers.

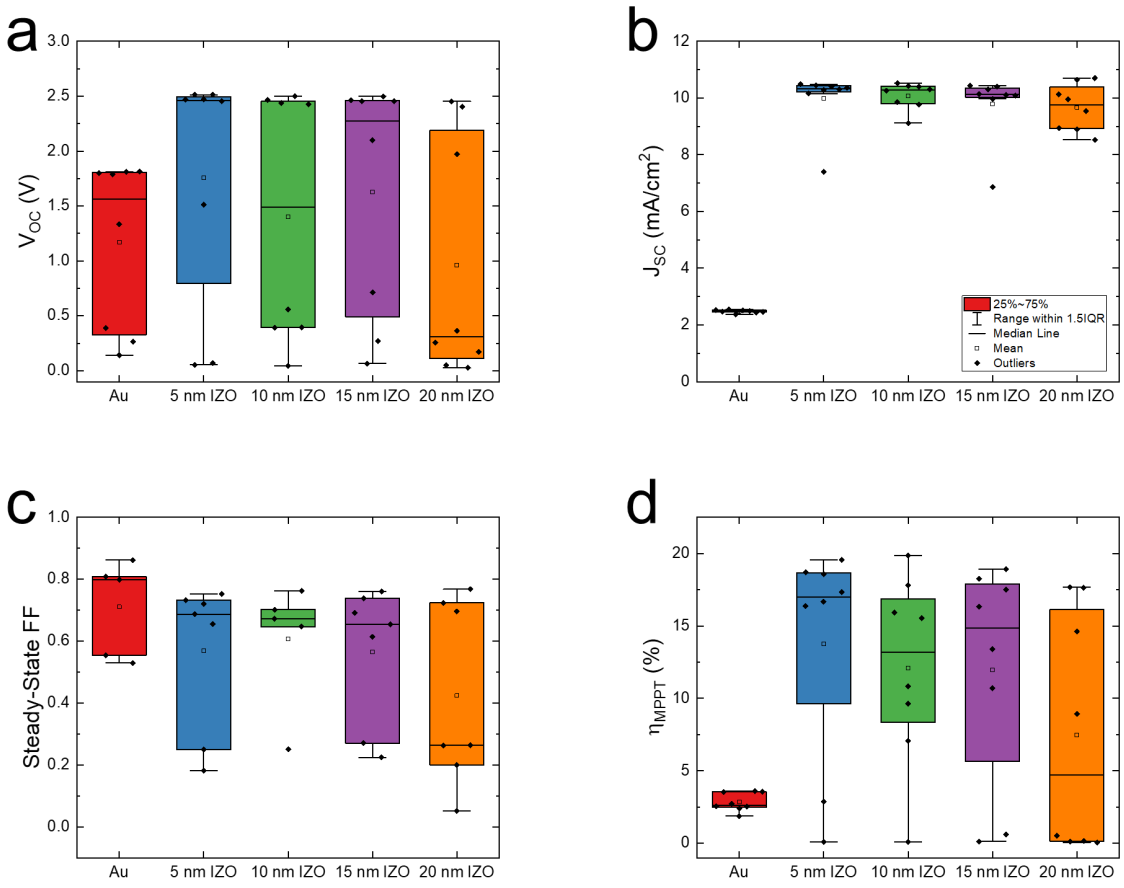

Figure 7.3. Solar cell performance parameter statistics of steady-state a) open-circuit voltage b) short circuit current c) fill factor and d) maximum power point tracked efficiency. The solar cells with a sputtered IZO recombination layer exhibited greatly enhanced J_{SC}. 8 solar cells (6 of 0.25 cm^2 area and 2 of 1 cm^2 area) were fabricated and measured per recombination layer condition.

The evaporated gold recombination layer hindered both acceptable V_{OC} and especially J_{SC}. The sputtered IZO recombination layer, by contrast, improved these parameters, consistently achieving J_{SC} around the desirable value of 10 mA/cm^2. While there is substantial spread for steady-state V_{OC} and fill factor, overall solar cell performance improved with a sputtered IZO recombination layer. Performance decreased at 20 nm IZO thickness, potentially due to more shunt losses as conductivity continued to increase. Performance increased at 10 nm IZO thickness, reducing parasitic

absorption and resultant optical losses farther down the device stack in the 1.61 eV subcell.

The champion double junction solar cells of each recombination layer condition are shown in Table 7.2, ranging from 3.6% to 19.9% maximum power point tracked efficiency.

Champion All-Perovskite Double Junction Tandem Solar Cells

Recombination Layer and Thickness	V_{OC} (V)	J_{SC} (mA/cm^2)	FF (%)	η_{MPPT} (%)
Au 1 nm	1.80	2.48	80.1	3.6
IZO 5 nm	2.51	10.36	75.1	19.5
IZO 10 nm	2.50	10.43	76.2	19.9
IZO 15 nm	2.50	9.97	76.0	18.9
IZO 20 nm	2.45	9.96	72.4	17.7

Table 7.2. Champion all-perovskite double junction tandem solar cells per recombination layer condition showing 10 nm thick IZO recombination layer condition yielded the highest performing solar cell of the batch with maximum power point tracked efficiency of 19.9%.

7.3.2 – All-Perovskite Triple Junction Tandem Solar Cells with 1.97 eV, 1.61 eV, and 1.25 eV Band Gap Absorbers, 1.0 M Concentration of 1.97 eV Perovskite Precursor, and Recombination Layer of Au or IZO for 1.61 eV/1.25 eV Subcells

All-perovskite triple junction tandem solar cells were fabricated and tested with 1.97 eV, 1.61 eV, and 1.25 eV band gap absorbers, 1.0 M concentration of 1.97 eV

perovskite precursor, and a recombination layer of Au or IZO for the 1.61 eV/1.25 eV subcells. For IZO, 10 nm was used after determining this as the optimal thickness for the 1.97 eV/1.61 eV recombination layer in double junction tandem solar cells discussed above. The device stack for these all-perovskite triple junction tandem solar cells was fabricated as illustrated in Figure 7.4, showing the recombination layer between the 1.61 eV and 1.25 eV subcells was fabricated in two ways – using either Au or IZO – to test the efficiency of both.

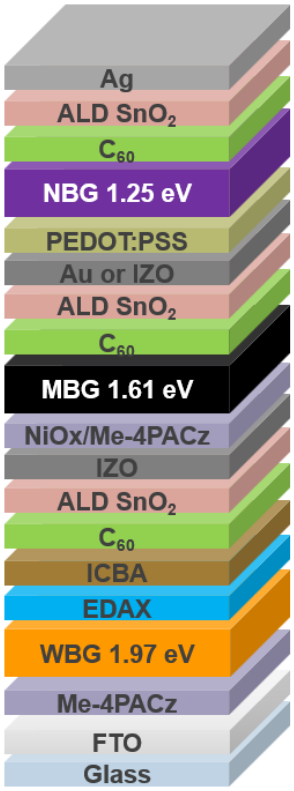

Figure 7.4. All-perovskite triple junction tandem solar cell device stack with either Au or IZO recombination layer material between the 1.61 eV and 1.25 eV subcells.

For these triple junctions, the 1.97 eV wide band gap absorber subcell was combined with the 1.61 eV middle band gap perovskite absorber subcell fabricated by Dr. Junke Wang, University of Oxford, and the 1.25 eV narrow band gap perovskite absorber

fabricated by Dr. Shuaifeng Hu, University of Oxford. Figure 7.5 presents all triple junction tandem solar cells fabricated in this experiment, showing improved steady-state J_{SC} and fill factor with sputtered IZO recombination layers.

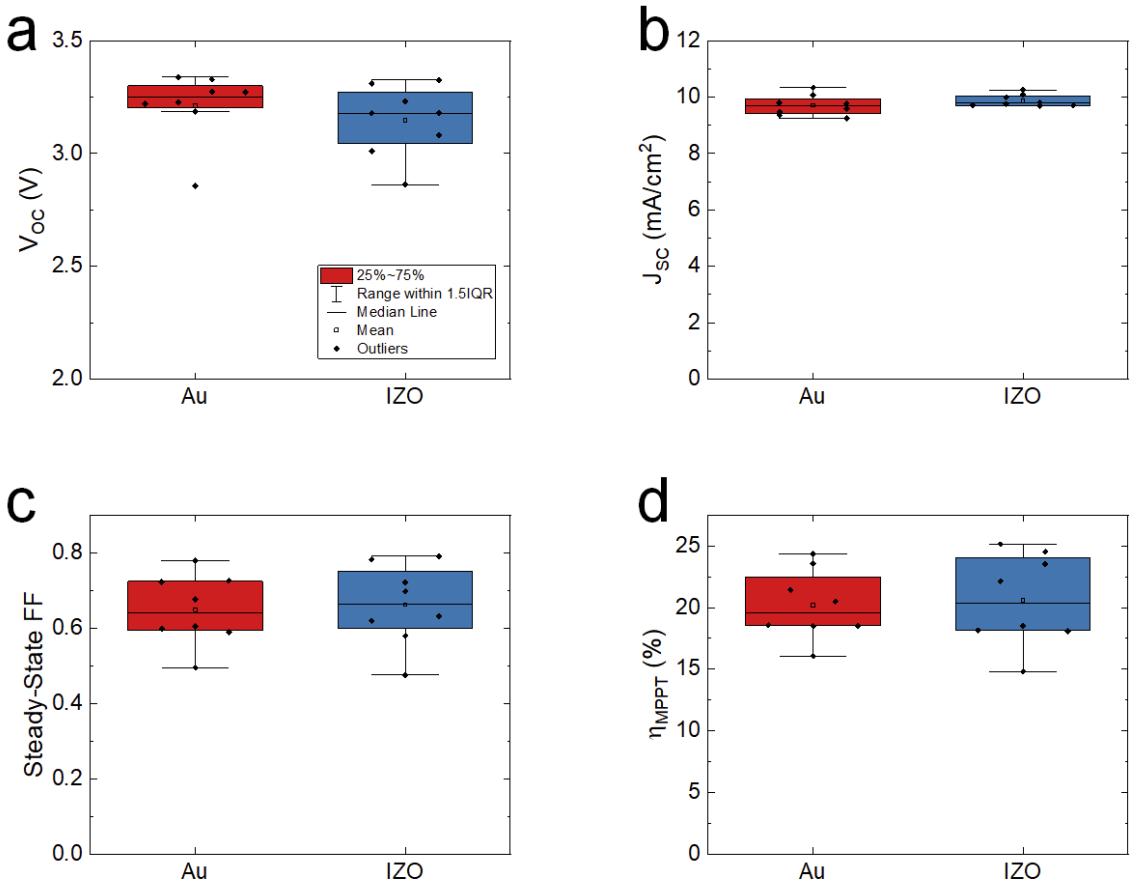

Figure 7.5. Solar cell performance parameter statistics of steady-state a) open-circuit voltage b) short-circuit current c) fill factor and d) maximum power point tracked efficiency. The solar cells with a sputtered IZO recombination layer exhibited enhanced steady-state J_{SC} and fill factor for higher median efficiency. 8 solar cells (6 of 0.25 cm^2 area and 2 of 1 cm^2 area) were fabricated and measured per recombination layer condition.

Solar cell efficiency improved with a sputtered IZO recombination layer. The champion triple junction solar cells of the Au and IZO recombination layer conditions are shown in Table 7.3, ranging from 24.3% to 25.1% maximum power point tracked efficiency.

Au and IZO Recombination Layer Champions of All-Perovskite Triple Junction Tandem Solar Cells with 1.97 eV, 1.61 eV, and 1.25 eV Band Gap Absorbers and 1.0 M Concentration of 1.97 eV Perovskite Precursor

Recombination Layer and Thickness	V_{OC} (V)	J_{SC} (mA/cm^2)	FF (%)	η_{MPPT} (%)
Au 1 nm	3.34	9.36	77.8	24.3
IZO 10 nm	3.31	9.70	78.2	25.1

Table 7.3. Champion all-perovskite triple junction tandem solar cells per Au and IZO recombination layer materials showing 10 nm thick IZO recombination layer condition yielded the highest performing solar cell with maximum power point tracked efficiency of 25.1%.

The highest performing all-perovskite triple junction tandem solar cell of this batch achieved a maximum power point tracked efficiency of 25.1%, equaling the highest PCE of any known all-perovskite triple junction tandem solar cell in published literature. Although the champion 25.1% maximum power point tracked efficiency was encouraging, significant current mismatch occurred, with the triple junction tandem solar cell current limited by the middle band gap subcell as shown in Figure 7.6. Improved current matching was investigated.

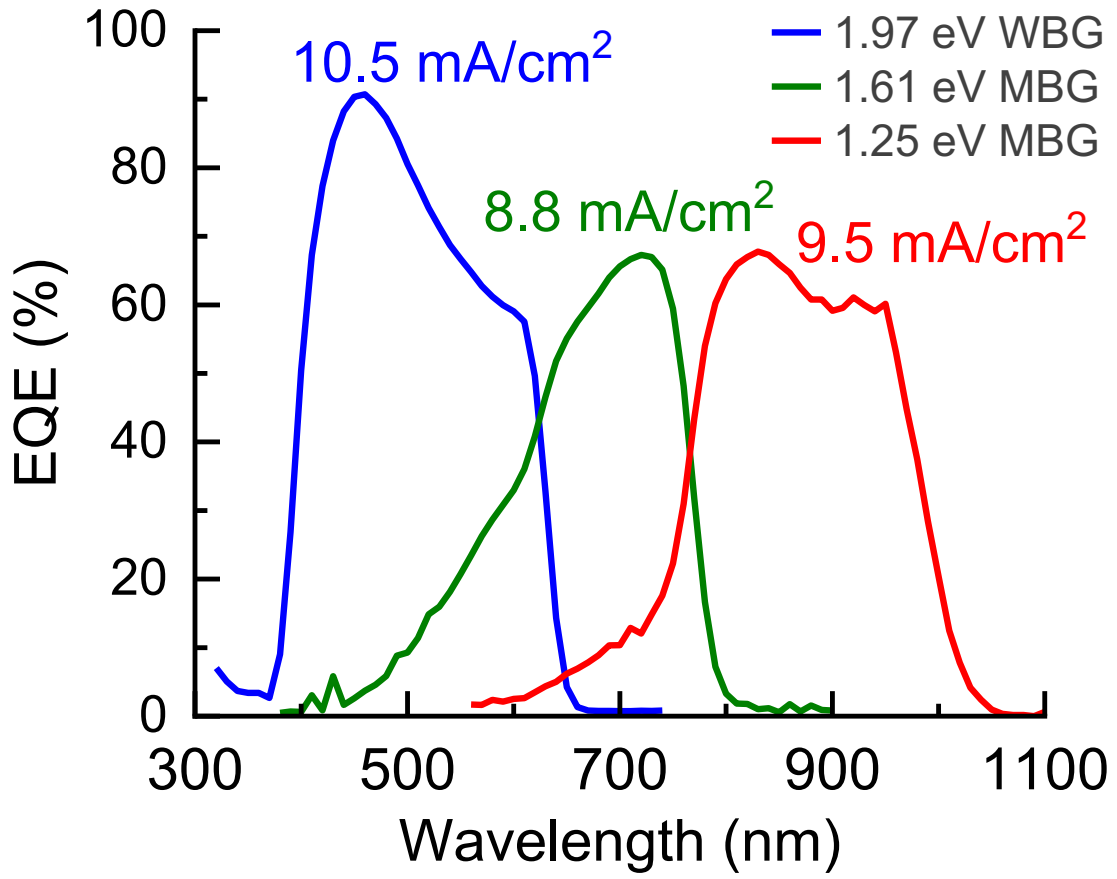

Figure 7.6. EQE spectrum of highest performing 1.97/1.61/1.25 eV all-perovskite triple junction tandem solar cell with IZO recombination layers. The 1.61 eV subcell was current limiting with an integrated J_{SC} of 8.8 mA/cm^2. EQE measurement conducted by Dr. Junke Wang and Dr. Shuaifeng Hu, University of Oxford.

7.3.3 – All-Perovskite Triple Junction Tandem Solar Cells with 1.97 eV, 1.61 eV, and 1.25 eV Band Gap Absorbers, 0.8, 0.9, and 1.0 M Concentration of 1.97 eV Perovskite Precursor, and IZO Recombination Layers

To improve current matching, another batch of all-perovskite triple junction tandem solar cells was fabricated using a unique device stack featuring IZO recombination layers and lower concentrations of 1.97 eV perovskite precursor. For IZO, 10 nm continued to be used as the optimal thickness for both recombination layers. These optimized triple junctions were tested with the same 1.97 eV, 1.61 eV, and 1.25 eV band gap absorbers.

7.4 – Optimized All-Perovskite Triple Junction Tandem Solar Cell Achieves 27.3% Maximum Power Point Tracked Efficiency at 1cm^2 Area

To improve current matching, optimized all-perovskite triple junction tandem solar cells with 1.97 eV, 1.61 eV, and 1.25 eV band gap absorbers, 0.8, 0.9, and 1.0 M concentration of 1.97 eV perovskite precursor, and IZO recombination layers were fabricated and tested, achieving a champion maximum power point tracked efficiency of 27.3% at 1 cm^2 area.

The all-perovskite double junction and triple junction tandem solar cells discussed in Sections 7.3.1 and 7.3.2 were fabricated using 1.0 M concentration 1.97 eV perovskite precursor solutions. While good for single junction performance, 1.0 M concentration of the 1.97 eV perovskite precursor did not appear ideal for current matching in the all-perovskite triple junction tandem solar cells based upon the current mismatch shown in Figure 7.5. At 1.0 M thickness, the 1.97 eV subcell may absorb more light than should be optimally transmitted to the narrower band gap subcells to utilize. To test this, different 1.97 eV perovskite precursor solution concentrations (0.8, 0.9, and 1.0 M) were prepared and used for the wide band gap subcell. Thickness was controlled with molar concentration instead of spin speed to avoid any changes to the formation of intermediate phases during the spincoating and antisolvent quenching stages.

To optimize for current matching, all-perovskite triple junction tandem solar cells with lower 1.97 eV perovskite precursor solution concentrations of 0.8 M and 0.9 M were fabricated according to the unique device stack shown in Figure 7.7, featuring IZO as the material for both recombination layers.

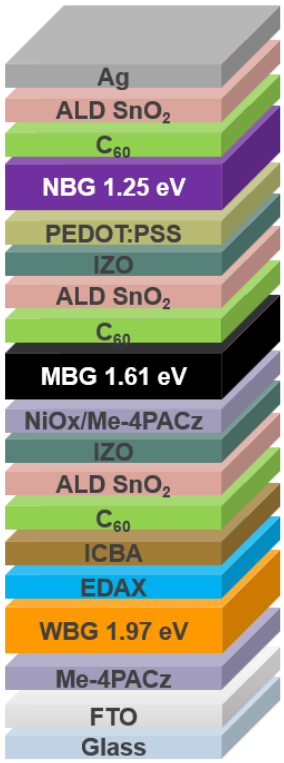

Figure 7.7. All-perovskite triple junction tandem solar cell device stack with IZO as the material for both recombination layers between the 1.97 eV and 1.61 eV subcells and the 1.61 eV and 1.25 eV subcells.

For these optimized triple junctions, the 1.97 eV wide band gap absorber subcell was combined with the 1.61 eV middle band gap absorber subcell fabricated by Dr. Junke Wang, University of Oxford, and the 1.25 eV narrow band gap absorber subcell fabricated by Dr. Shuaifeng Hu, University of Oxford. Figure 7.8 presents all triple junction tandem solar cells fabricated in this experiment, showing that the 0.9 M 1.97 eV perovskite precursor resulted in the highest efficiencies with improved steady-state V_{OC} and J_{SC}.

The champion solar cell achieved 27.3% maximum power point tracked efficiency at 1 cm^2 area, the highest efficiency of any known all-perovskite triple junction tandem solar cell published to date. The 1 cm^2 area is 10-20 times larger than the active area of any known published all-perovskite triple junction tandem solar cell of any efficiency.

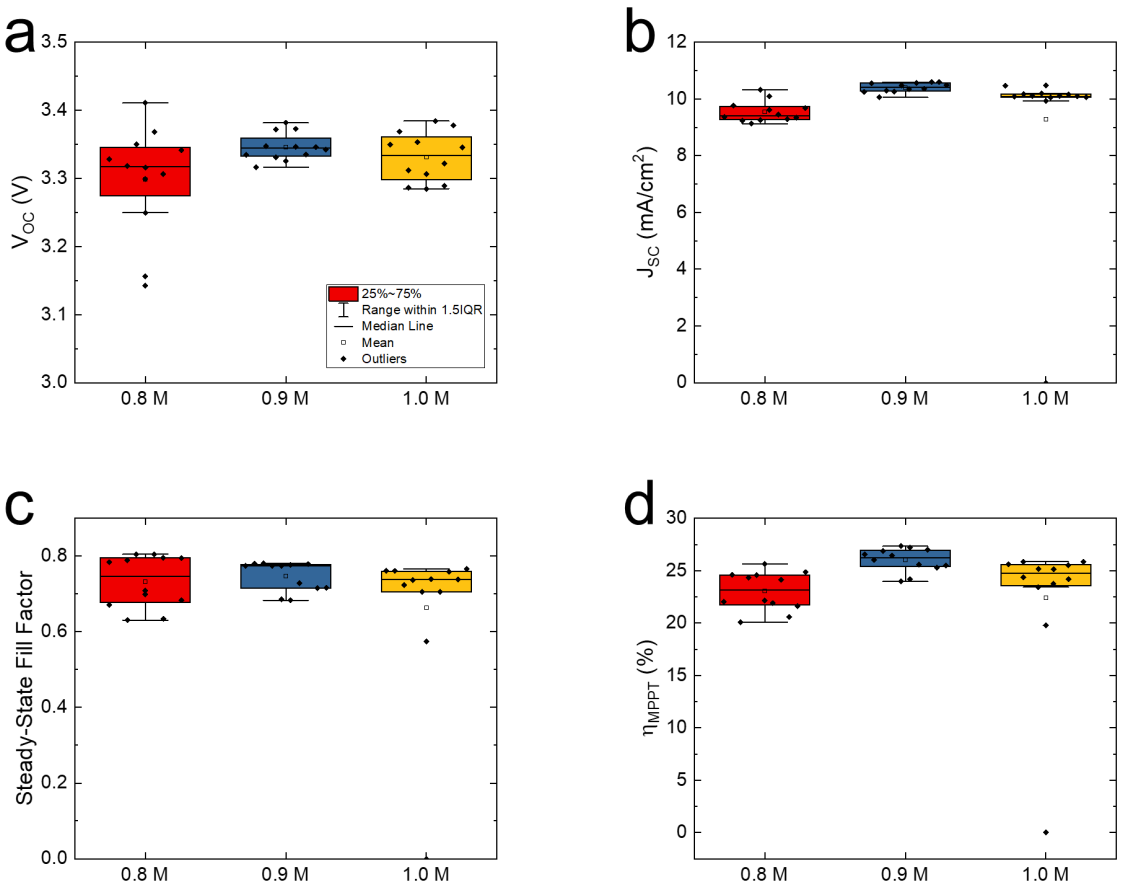

Figure 7.8. Solar cell performance parameter statistics of steady-state a) open-circuit voltage b) short-circuit current c) fill factor and d) maximum power point tracked efficiency. The solar cells with the 0.9 M concentration for the 1.97 eV perovskite precursor yielded the highest all-perovskite triple junction tandem solar cell efficiencies, including a highest recorded efficiency of 27.3%. Significant boosts in steady-state open-circuit voltage and short-circuit current were observed. 12 solar cells (9 of 0.25 cm^2 area and 3 of 1cm^2 area) were fabricated per concentration.

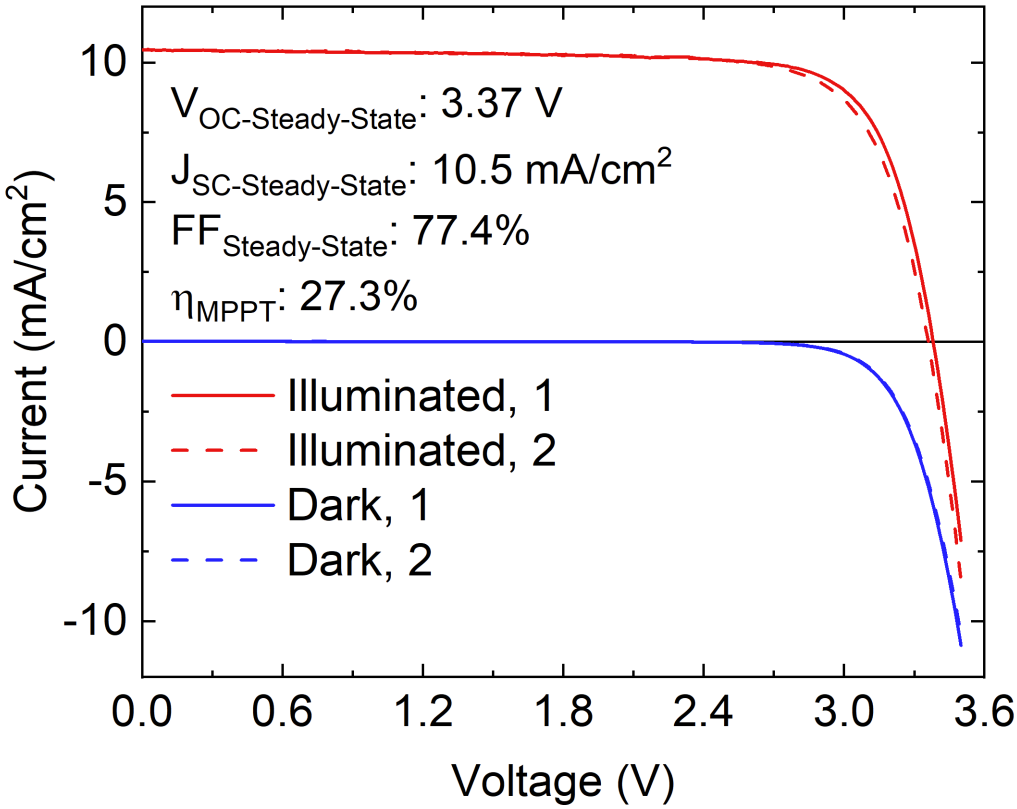

Figure 7.9. J-V curve of champion 1 cm^2 area all-perovskite triple junction tandem solar cell with 27.3% maximum power point tracked efficiency, 3.37 V steady-state V_{OC}, 10.5 mA/cm^2 steady-state J_{SC}, and 77.4% steady-state fill factor.

Near current matching was achieved for the champion all-perovskite triple junction tandem solar cell with 27.3% maximum power point tracked efficiency. The EQE-integrated J_{SC} values for the 1.97, 1.61, and 1.25 eV absorber subcells were 10.2, 10.1, and 10.3 mA/cm^2 respectively. The champion all-perovskite triple junction tandem solar cell demonstrated both near current matching and improved efficiency.

Figure 7.10 shows minimal current mismatch for the champion all-perovskite triple junction tandem solar cell with the middle band gap subcell ultimately limiting the J_{SC} of the tandem solar cell. The only variable changed in the optimized all-perovskite triple junction tandem solar cell batch, including the champion, was lowering the 1.97 eV

perovskite precursor concentration from the 1.0 M used in the triple junctions discussed in Section 7.3.2. This indicates that the 0.9 M concentration of the 1.97 eV perovskite precursor in the champion all-perovskite triple junction tandem solar cell improved current matching and improved efficiency.

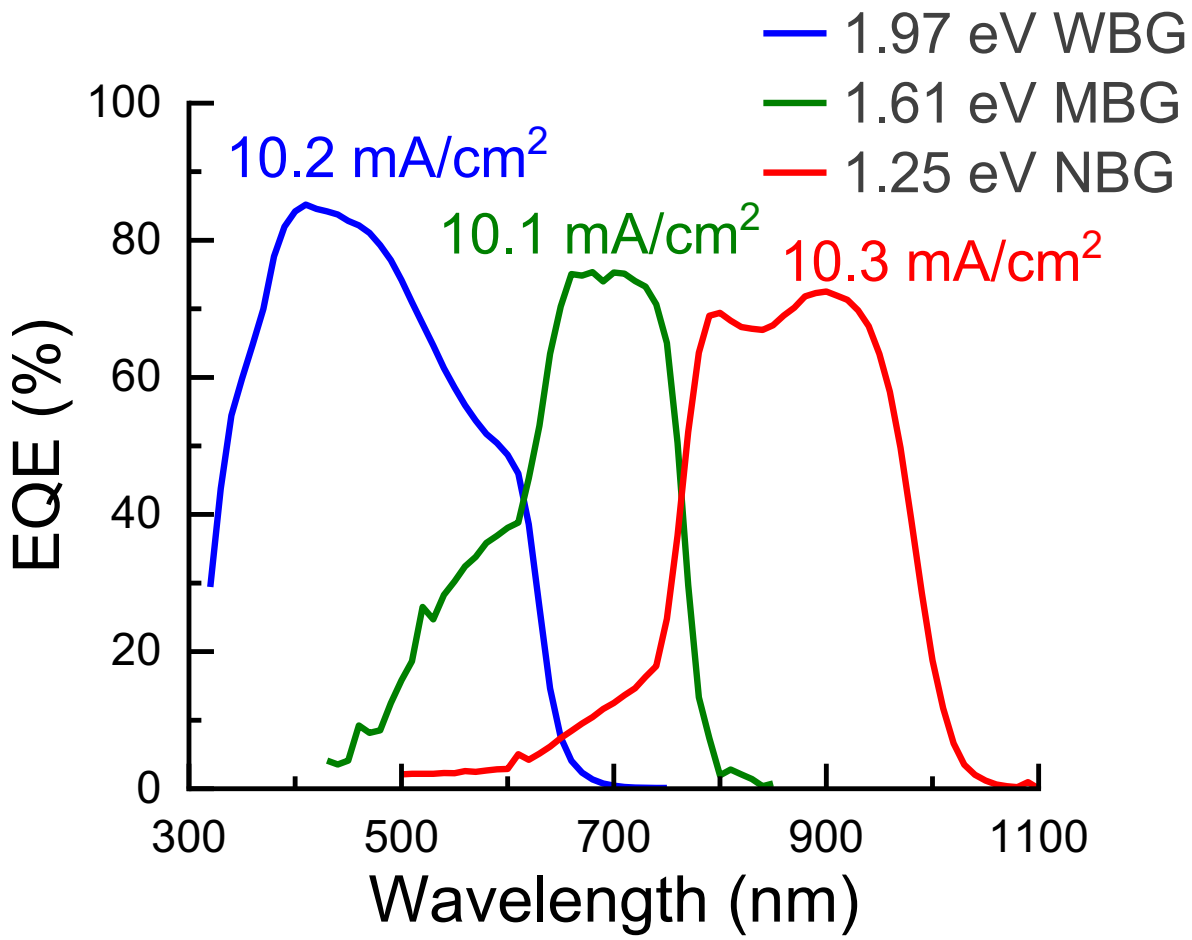

Figure 7.10. EQE spectrum of champion 1.97/1.61/1.25 eV all-perovskite triple junction tandem solar cell with near current matching. EQE measurement conducted by Dr. Junke Wang and Dr. Shuaifeng Hu, University of Oxford.

A cross-sectional SEM image of an all-perovskite triple junction solar cell in Figure 7.11 reveals the growth of conformal perovskite absorber layers in each subcell, indicating quality crystalline growth for each perovskite absorber layer in the device stack. The

thicknesses of the 1.97 eV, 1.61 eV, and 1.25 eV band gap absorber layers were estimated as 210, 640, and 1050 nm respectively from this cross-sectional SEM image.

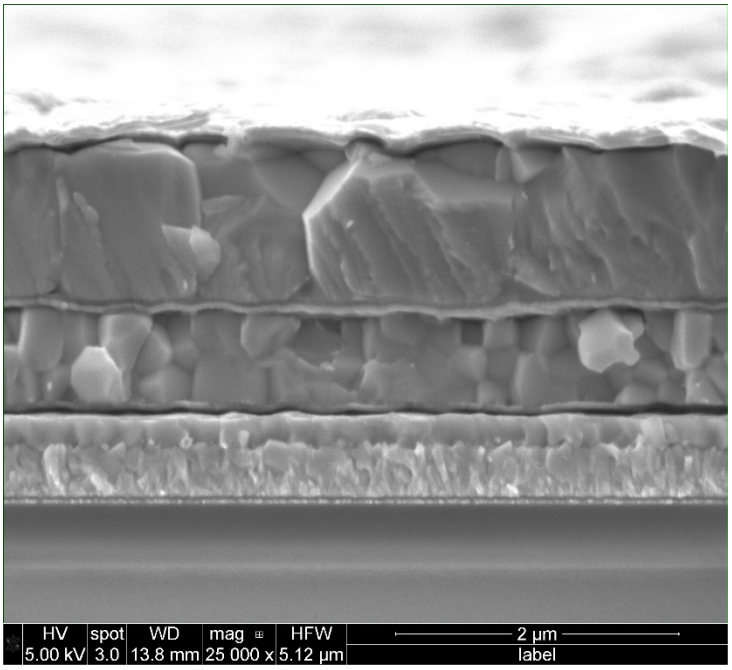

Figure 7.11. Cross-sectional SEM image of all-perovskite triple junction tandem solar cell with 0.9 M concentration 1.97 eV wide band gap absorber. Cross-sectional SEM image produced by Dr. Shuaifeng Hu, University of Oxford. Thicknesses of subcell absorber layers were approximated using ImageJ software based on a median value of 20 measurements per absorber.

7.5 – Stability Testing of All-Perovskite Triple Junction Tandem Solar Cell

Stability was tested using one of the all-perovskite triple junction tandem solar cells of 1.97 eV, 1.61 eV, and 1.25 eV band gap absorbers, 0.8 M concentration of 1.97 eV perovskite precursor, and IZO recombination layers discussed in Section 7.4. For the stability test, the encapsulated solar cell was illuminated continuously under 1-sun intensity AM 1.5G conditions in the solar simulator in the lab. As shown in Figure 7.12, the solar cell retained 99.3% of its initial efficiency after 120 minutes of continuous maximum power point tracking under this illumination.

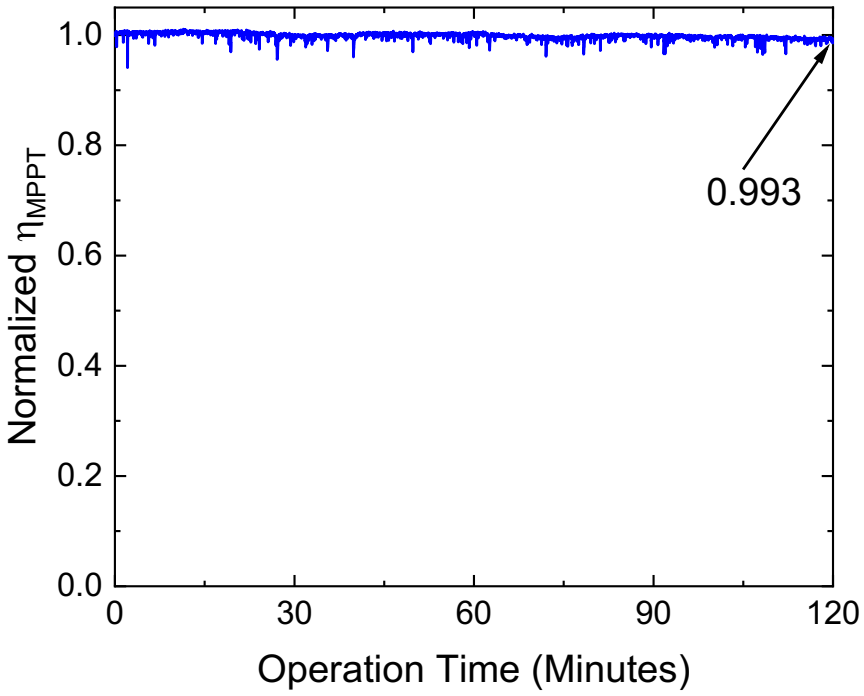

Figure 7.12. Encapsulated all-perovskite triple junction tandem solar cell continuously operated at maximum power point under 1-sun intensity AM 1.5G illumination for 120 minutes, retaining 99.3% of its initial efficiency. A slight current decay of 0.065 mA/cm^2 at J_{MPPT} and slight voltage increase of 2.67 mV at V_{MPPT} occurred after 120 minutes.

This all-perovskite triple junction tandem solar cell incorporating a 1.97 eV band gap absorber is more operationally stable than the single junction 1.97 eV wide band gap perovskite solar cells discussed in Section 5.3.3. This enhanced all-perovskite triple junction tandem solar cell operational stability may be due to the more stable voltage output from the middle and narrow band gap absorber subcells, which could dilute some of the effect of voltage loss in the 1.97 eV band gap absorber subcell over 120 minutes. Future modifications to the device stack, including top electrodes more stable than silver and better surface passivation materials, should be investigated further for all-perovskite triple junction tandem solar cells to replicate such stability under harsher aging conditions experienced in the field.

7.6 – Conclusion

Overall, the all-perovskite triple junction tandem solar cells using a unique device stack incorporating an ICBA electron transport layer and IZO recombination layers with 1.97 eV, 1.61 eV, and 1.25 eV band gap absorbers demonstrated improved efficiency – the champion achieved 27.3% maximum power point tracked efficiency and 3.37 V steady-state open-circuit voltage at 1 cm^2 area – and operational stability. More improvement is possible. Further optimization of perovskite subcell absorber layer thicknesses, reduction of defects in the bulk of the perovskite subcell absorbers, and improved energetic alignment from different charge transport layers could yield continued improvement in efficiencies of all-perovskite triple junction tandem solar cells.

Chapter 7 References

1. Peters, I. M et al. Practical limits of multijunction solar cells. *Progress in Photovoltaics*, **31**, 1006-1015 (2023).

2. Philipps, S. P. and Bett, A. W. III-V Multi-junction solar cells and concentrating photovoltaic (CPV) systems. *Adv. Opt. Techn.*, **3**, 469-478 (2014).

3. Shockley, W. and Queisser, H.J. Detailed Balance Limit of Efficiency of pn Junction Solar Cells. *J. Appl. Phys.* **32**, 510 (1961).

4. Zhu, Z., Mao, K., and Xu, J. Perovskite tandem solar cells with improved efficiency and stability. *J. Energy Chem.*, **58**, 219-232 (2021).

5. Köhnen, E. et al. Highly efficient monolithic perovskite silicon tandem solar cells: analyzing the influence of current mismatch on device performance. *Sustainable Energy Fuels*, **3**, 1995-2005 (2019).

6. Cheng, Y. and Ding, L. Perovskite/Si tandem solar cells: Fundamentals, advances, challenges, and novel applications. *SusMat.*, **1**, 324-344 (2021).

7. Fraunhofer Institute for Solar Energy Systems ISE. *Fraunhofer ISE Develops the World's Most Efficient Solar Cell with 47.6 Percent Efficiency - Fraunhofer ISE*. 30 May 2022, https://www.ise.fraunhofer.de/en/press-media/press-releases/2022/fraunhoferise-develops-the-worlds-most-efficient-solar-cell-with-47-comma-6-percentefficiency.html.

8. Smith, B. et al. *Photovoltaic (PV) Module Technologies: 2020 Benchmark Costs and Technology Evolution Framework Results.* National Renewable Energy Laboratory (2021).

9. Hörantner, M. et al. The Potential of Multijunction Perovskite Solar Cells. *ACS Energy Lett.*, **2**, 10, 2506-2513 (2017).

10. McMeekin, D.P. et al. Solution-Processed All-Perovskite Multi-Junction Solar Cells. *Joule*, **3**, 1-15 (2019).

11. Wang, J. et al. 16.8% Monolithic all-perovskite triple-junction solar cells via a universal two-step solution process. *Nature Communications*, **11**, 5254 (2020).

12. Xiao, K. et al. Solution-Processed Monolithic All-Perovskite Triple-Junction Solar Cells with Efficiency Exceeding 20%. *ACS Energy Lett.*, **5**, 2819-2826 (2020).

13. Wang, J. et al. Halide homogenization for low energy loss in 2-eV-bandgap perovskites and increased efficiency in all-perovskite triple-junction solar cells. *Nature Energy*, **9**, 70-80 (2023).

14. Wang, Z. et al. Suppressed phase segregation for triple-junction perovskite solar cells. *Nature*, **618**, 74-79 (2023).

Chapter 8

Conclusion

Energy advancements have powered human development throughout history. Today, the burning of fossil fuels continues to dominate our energy supply but has rapidly increased greenhouse gas concentrations in the atmosphere and contributed to climate change dangerous to humanity, including more extreme weather events, increased ocean acidification, higher storm surges, and rising sea levels.

Last year was the hottest year in recorded history and this year is on track to be even hotter. At the same time, global demand for energy continues to grow.

Sunlight offers the greatest potential to meet our need for increased energy and decreased greenhouse gas emissions. The amount of solar energy from sunlight striking the land surface of the Earth every year is 15 times greater than the total energy of all non-renewable reserves remaining and 180 times greater than the annual energy potential of all other renewable energy sources combined. In less than eight hours, enough solar energy strikes the land surface of the Earth to meet current global energy demand for an entire year.

Solar energy has not yet realized this immense potential. In 2023, only about 2.5% of global primary energy production was from solar energy. Crystalline silicon has been the dominant solar cell technology for 70 years. The newer solar cell technology of perovskites provides potentially higher efficiencies and lower costs than crystalline silicon because of superior light absorption, tunable band gap absorbers, lower formation

energies, greater defect tolerance, and lower cost industrially scalable fabrication techniques.

These advantages have been projected to provide the potential for all-perovskite tandem solar cells to be fabricated at costs as much as 50% lower than crystalline silicon. For perovskites to deliver on the promise of more efficient and lower cost commercial solar cells, however, stability, efficiency, and scalability must improve.

Perovskites are more adaptable in their fabrication than crystalline silicon and low-cost, high-throughput roll-to-roll perovskite processing is a promising pathway to scalable fabrication. Yet, efficiencies must continue to improve.

The development of efficient and reproducible perovskite absorbers for all-perovskite triple junction tandem solar cells is advanced by this thesis. Improvements to efficiency, reproducibility, and stability are investigated and achieved for three principal study areas: 1) representative middle band gap perovskite absorber relevant for all-perovskite triple junction tandem solar cells; 2) all-perovskite triple junction tandem solar cells using a novel crystallization method for the 1.97 eV wide band gap absorber layer involving dimethylammonium bromide and dimethylammonium iodide (DMAX); and 3) all-perovskite triple junction tandem solar cells using a unique device stack incorporating an ICBA electron transport layer and IZO recombination layers with the 1.97 eV wide band gap absorber layer.

For practical and widespread use, solar cells must be stable and efficient. Perovskite solar cells are not yet as stable as crystalline silicon solar cells. For all-perovskite triple junction tandem solar cells to survive aging conditions in the field, the stability of each absorber subcell – wide, middle, and narrow – must be improved.

For this thesis, 1.55 eV $FA_{0.8}Cs_{0.2}PbI_3$ single junction perovskite solar cells were studied as a representative middle band gap subcell absorber relevant for all-perovskite triple junction tandem solar cells. Improvements to stability, reproducibility, and efficiency were achieved.

The incorporation of a benzylammonium thiocyanate bulk additive and the use of a C_{60}/ALD SnO_2 top contact device stack yielded efficient and reproducible $FA_{0.8}Cs_{0.2}PbI_3$ solar cells, with a maximum power point tracked efficiency of 21.2% reached. Further modification to a C_{60}/ALD SnO_2/IZO/Au device stability stack increased solar cell reproducibility in a tandem-relevant context. $EDAI_2$ surface passivation and excess PbI_2 perovskite precursor stoichiometry improved the stability of 1.55 eV $FA_{0.8}Cs_{0.2}PbI_3$ single junction perovskite solar cells in a tandem-relevant C_{60}/ALD SnO_2/IZO/Au top contact device stack under 85°C light aging.

For perovskite absorbers with similar band gaps to $FA_{0.8}Cs_{0.2}PbI_3$, these stability enhancements may be transferrable.

All-perovskite triple junction tandem solar cells have higher theoretical efficiencies than crystalline silicon because perovskites use wide, middle, and narrow band gap absorbers – ranging from 1.22 eV to 3.5 eV – to absorb different portions of the solar irradiance spectrum. The band gap of a perovskite can be easily modified – or tuned – within its range. Crystalline silicon has a fixed band gap at 1.12 eV, limiting the spectrum it can absorb.

All-perovskite tandem solar cells of 30% or higher efficiency are required to exceed the 29.8% modified practical limit of crystalline silicon. In practice, the highest reported efficiency for a single junction crystalline silicon solar cell is 27.3%. Prior to this thesis,

the highest published efficiency for an all-perovskite triple junction tandem solar cell was 25.1%.

The most important solar cell performance parameter for a 2 eV wide band gap subcell is open-circuit voltage because the 2 eV subcell must be the largest voltage contributor among the three perovskite subcells to create high efficiency triple junction tandem solar cells. To realize the efficiency potential of all-perovskite triple junction tandem solar cells, the 2 eV band gap top subcell must produce V_{OC} greater than 1.5 V. Yet, to date, only one published result has exceeded even 1.4 V.

For this thesis, a novel crystallization method was developed to create efficient and reproducible solution-processed ~2 eV (1.97 eV) wide band gap perovskite absorbers and single junction solar cells. This crystallization method involves a novel 68 mol%:32 mol% stoichiometric mixture of dimethylammonium bromide (DMABr) and dimethylammonium iodide (DMAI) additive salts – DMAX – to a 1.97 eV $FA_{0.9}Cs_{0.1}Pb(Br_{0.68}I_{0.32})_3$ perovskite precursor solution in neat DMF solvent. These DMAX salts replace the DMSO solvent used in standard perovskite precursor solutions dissolved in DMF and DMSO.

The perovskite thin films crystallized using the DMF/DMAX method exhibit larger median apparent grain sizes, more homogeneous morphology, and longer carrier lifetimes compared to DMF/DMSO. The 1.97 eV perovskite single junction solar cells fabricated using DMF/DMAX demonstrated improved median maximum power point tracked efficiency, reproducibility, and operational stability compared to DMF/DMSO.

The champion 1.97 eV single junction perovskite solar cell fabricated using the DMF/DMAX crystallization method – and further optimized utilizing the 1 mg/mL ICBA

electron transport layer – achieved near-record 1.42 V steady-state open-circuit voltage and 13.7% maximum power point tracked efficiency.

Based on the detailed balance limit, the performance parameters of this champion are more than 80% of the theoretical maximums for V_{OC}, J_{SC}, and FF and 58.9% of the theoretical maximum efficiency. The DMF/DMAX crystallization method improved operational stability, with the DMF/DMAX 1.97 eV solar cell retaining 93.4% of its initial efficiency compared to 82.1% for the DMF/DMSO 1.97 eV solar cell. Compared to the DMF/DMSO control, DMF/DMAX achieved more reproducible 1.97 eV perovskite single junction solar cells, as demonstrated by more consistent performance parameter results.

For 1.97 eV wide band gap perovskite solar cells fabricated using DMF/DMAX, non-radiative recombination processes, rather than halide segregation, dominate V_{OC} losses that can be accounted for from measurements in this thesis. The 20 mV V_{OC} loss from radiative recombination due to halide segregation ($V_{OC, rad}$) measured is five times less than the published estimate of ~100 mV loss. These results indicate that, compared to estimates, halide segregation has a less substantial effect on V_{OC} loss mechanisms in the 1.97 eV perovskite solar cells fabricated using DMF/DMAX.

Future experimental designs to attempt to reduce these V_{OC} losses, both initially and over time, include better energetically aligned hole transport layers, bulk materials of superior crystalline quality, and potentially more stable non-fullerene organic electron transport layers.

Although all-perovskite triple junction tandem solar cells have the potential to exceed 30% efficiency, due to their complexity including the challenge of current matching three subcells, only five articles have published performance results for all-perovskite

triple junction tandem solar cells. The published PCE results for all-perovskite triple junction tandem solar cells range from 6.7% to 25.1%.

For this thesis, three batches of all-perovskite multijunction tandem solar cells were fabricated and tested – one double junction batch and two triple junction batches – using the DMF/DMAX crystallization method for the 1.97 eV wide band gap absorber and a unique device stack featuring an ICBA electron transport layer and IZO recombination layers.

Band gaps of 1.97 eV and 1.61 eV were used for the double junction batch. The triple junction batches both used the same band gaps of 1.97 eV, 1.61 eV, and 1.25 eV but had different precursor concentrations and different recombination layer materials.

The all-perovskite double junction tandem solar cells showed significant J_{SC} enhancement with sputtered IZO recombination layers, improving both acceptable V_{OC} and J_{SC} and consistently achieving J_{SC} around the desirable value of 10 mA/cm^2. Performance increased at 10 nm IZO thickness, reducing parasitic absorption and resultant optical losses farther down the device stack in the 1.61 eV subcell. The champion all-perovskite double junction tandem solar cell with a 10 nm thick IZO recombination layer yielded a maximum power point tracked efficiency of 19.9%.

The first batch of all-perovskite triple junction tandem solar cells were fabricated and tested with 1.97 eV, 1.61 eV, and 1.25 eV band gap absorbers, 1.0 M concentration of 1.97 eV perovskite precursor, and a recombination layer of Au or IZO for the 1.61 eV/1.25 eV subcells. For IZO, 10 nm was used after determining this as the optimal thickness for the 1.97 eV/1.61 eV recombination layer in the all-perovskite double junction tandem solar cells.

For these all-perovskite triple junction tandem solar cells, the recombination layer between the 1.61 eV and 1.25 eV subcells was fabricated in two ways – using either Au or IZO – to test the efficiency of both. Steady-state J_{SC}, fill factor, and overall solar cell efficiency improved with sputtered IZO recombination layers. The champion triple junction solar cells of the Au and IZO recombination layer conditions ranged from 24.3% to 25.1% maximum power point tracked efficiency.

The highest performing all-perovskite triple junction tandem solar cell of this batch achieved a maximum power point tracked efficiency of 25.1%, equaling the highest PCE of any known all-perovskite triple junction tandem solar cell in published literature.

Although this 25.1% maximum power point tracked efficiency was encouraging, significant current mismatch occurred, with the triple junction tandem solar cell current limited by the middle band gap subcell.

To improve current matching, a second batch of all-perovskite triple junction tandem solar cells with the same 1.97 eV, 1.61 eV, and 1.25 eV band gap absorbers was fabricated using the DMF/DMAX crystallization method and a unique device stack featuring 10 nm IZO recombination layers and 0.8 M and 0.9 M concentrations of 1.97 eV perovskite precursor.

For these optimized triple junctions, the 0.9 M 1.97 eV perovskite precursor resulted in the highest efficiencies with improved steady-state V_{OC} and J_{SC}. The champion all-perovskite triple junction tandem solar cell achieved 27.3% maximum power point tracked efficiency and 3.37 V steady-state open-circuit voltage at 1 cm^2 area.

This 27.3% efficiency is the highest of any known all-perovskite triple junction tandem solar cell published to date and identical to the highest known reported efficiency of 27.3% for a single junction crystalline silicon solar cell. The 1 cm^2 solar cell active area is 10-20 times larger than any other known published all-perovskite triple junction tandem solar cell of any efficiency.

Near current matching was achieved for the champion all-perovskite triple junction tandem solar cell with 27.3% maximum power point tracked efficiency. The EQE-integrated J_{SC} values for the 1.97, 1.61, and 1.25 eV subcells were 10.2, 10.1, and 10.3 mA/cm^2 respectively.

One of the all-perovskite triple junction tandem solar cells – fabricated with 1.97 eV, 1.61 eV, and 1.25 eV band gap absorbers, 0.8 M concentration of 1.97 eV perovskite precursor, and IZO recombination layers – was stability tested and retained 99.3% of its initial efficiency after 120 minutes of continuous maximum power point tracking under 1-sun intensity AM 1.5G illumination. This all-perovskite triple junction tandem solar cell incorporating the 1.97 eV band gap absorber was more operationally stable than the single junction 1.97 eV wide band gap perovskite solar cells fabricated and tested.

Future modifications to the device stack, such as top electrodes more stable than silver and better surface passivation materials, should be investigated further for all-perovskite triple junction tandem solar cells to replicate such stability under harsher aging conditions experienced in the field.

Overall, the all-perovskite triple junction tandem solar cells fabricated with 1.97 eV, 1.61 eV, and 1.25 eV band gap absorbers using the novel DMF/DMAX crystallization method, 0.9 M concentration of the 1.97 eV perovskite precursor, and unique device stack

featuring an ICBA electron transport layer for the wide band gap subcell and IZO recombination layers improved efficiency and operational stability.

Higher efficiencies from all-perovskite triple junction tandem solar cells are needed and potentially possible. Continuous, high voltage output from ~2 eV wide band gap absorber top subcells and quality recombination layers for monolithic, 2-terminal architectures are some of the challenges that must be addressed to achieve higher efficiencies for all-perovskite triple junction tandem solar cells.

Further optimization of perovskite subcell absorber layer thicknesses, reduction of defects in the bulk of the perovskite subcell absorbers, and improved energetic alignment from different charge transport layers could yield continued improvement in efficiencies of all-perovskite triple junction tandem solar cells. With the promise of higher efficiencies and lower costs than crystalline silicon, stable all-perovskite triple junction tandem solar cells have the potential to power our world into a better tomorrow.

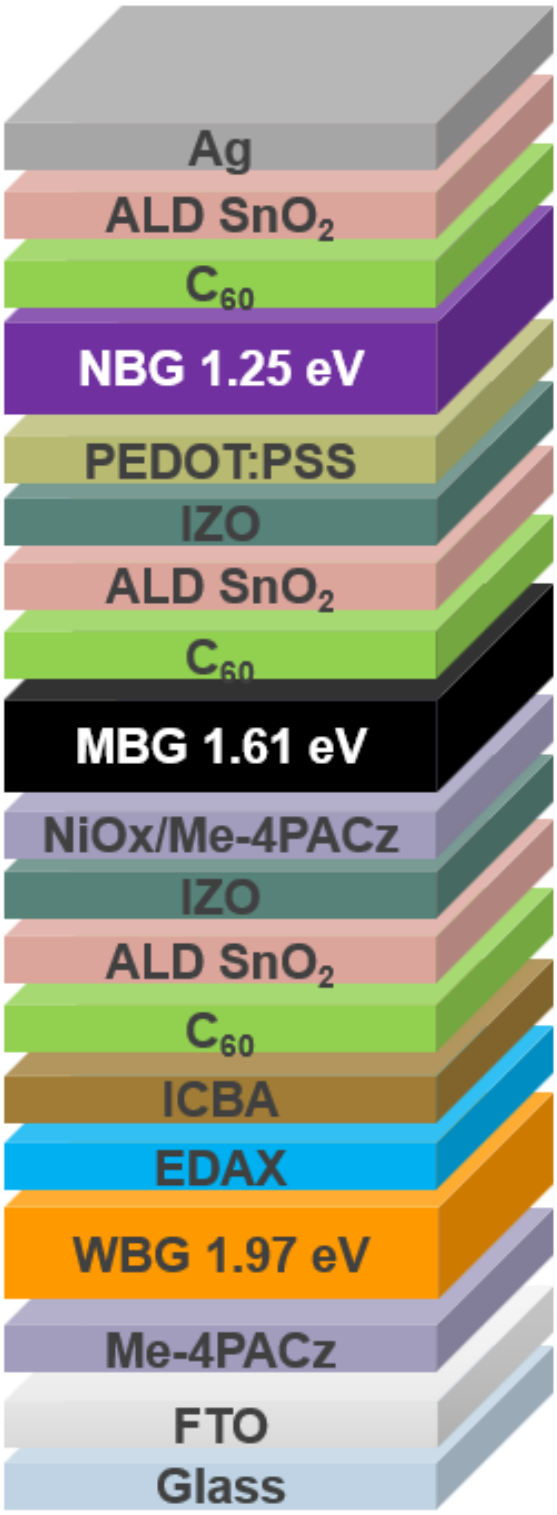

The 27.3% efficiency champion all-perovskite triple junction tandem solar cell using DMF/DMAX crystallization method for the 1.97 eV perovskite absorber with 1.97 eV/1.61 eV/1.25 eV band gaps, 0.9 M 1.97 eV perovskite precursor, and IZO recombination layers